THE UNIVERSITY OF CHICAGO

METAL-ORGANIC NANOSENSITIZERS FOR DRUG DELIVERY AND CANCER THERAPY

A DISSERTATION SUBMITTED TO

THE FACULTY OF THE DIVISION OF THE PHYSICAL SCIENCES

IN CANDIDACY FOR THE DEGREE OF

DOCTOR OF PHILOSOPHY

DEPARTMENT OF CHEMISTRY

BY

TAOKUN LUO

CHICAGO, ILLINOIS

AUGUST 2023

TABLE OF CONTENTS

LIST OF FIGURES

LIST OF TABLES

LIST OF ABBREVIATIONS

·OH	Hydroxyl radicals
$^1O_2$	Singlet oxygen
2-D	Two-dimensional
3-D	Three-dimensional
$^3O_2$	Ground-state oxygen
AA	Acetic acid
ACK	Ammonium-Chloride-Potassium
ADU-S100	Bisphosphorothioate analog of c-di-AMP, Rp isomers
AEC	Amino-9-ethylcarbazole
AFM	Atomic force microscopy
AH1	SPSYVYHQF
ALA	5-aminolevulinic acid
ALS	Artificial leukocytoid structure
ANOVA	Analysis of Variance
AO	Acridine orange
APC	Antigen-presenting cell
APF	Aminophenyl fluorescein assay

ATCC	American Type Culture Collection
AUC	Area under the curve
BMDC	Bone marrow-derived dendritic cell
BMDM	Bone marrow-derived macrophage
BMPO	5-tert-butoxycarbonyl 5-methyl-1-pyrroline N-oxide
BSA	Bovine serum albumin
C3ar1	Complement component 3a receptor 1
CCDC	Cambridge Crystallographic Data Centre
Ccl	C-C chemokine ligand
Ccrl	Chemokine receptor-like
CD	Cluster of differentiation
$CDCl_3$	Deuterated chloroform
CFSE	Carboxyfluorescein succinimidyl ester
cGAMP	2’,3’-cyclic guanosine monophosphate–adenosine monophosphate
CLSM	Confocal laser scanning microscopy
COVID	Coronavirus disease 2019
CRT	Calreticulin
CTL	Cytotoxic lymphocyte

CV	Cyclic voltammogram
Cxcl	C-X-C chemokine ligand
Cxcr	C-X-C chemokine receptor
Cy5	Cyanine5
D_2O	Deuterium oxide
D_2O	Deuterium oxide
D_3PO_4	Deuterium$_3$-phosphoric acid
D_6-DMSO	Deuterium$_6$-dimethyl sulfoxide
DAB	Diaminobenzidine
DAMP	Danger-associated molecular patterns
DBB	4,4’-di(4-benzoato)-2,2’-bipyridine
DC	Dendritic cell
DCF-DA	2',7'-dichlorodihydrofluorescein diacetate
dF(CF_3)ppy	2-(2,4-difluorophenyl)-5-(trifluoromethyl)pyridine
DFT	Density functional theory
DLS	Dynamic light scattering
DMEM	Dulbecco's modified eagles medium
DMF	*N,N*-dimethylformamide

DMSO	Dimethyl sulfoxide
DNA	Deoxyribonucleic acid
DPPA	Diphenylphosphinic acid
DTT	Dithiothreitol
e.q.	Equivalent
EC_{50}	Half-maximal effective concentration
ECL	Electrochemiluminescence
ELISA	Enzyme-linked immunosorbent assay
ELISpot	Enzyme-linked immunospot
EnT	Energy transfer
EPR	Enhanced permeability and retention
ER	Endoplasmic reticulum
ESR	Electron spin resonance
ET	Electron transfer
Et_2O	Diethyl ether
EtOH	Ethanol
F(ab')2	Bivalent antigen-binding fragment
FACS	Fluorescence-activated cell sorting

FBS	Fetal bovine serum
FDA	U.S. Food and Drug Administration
FFPE	Formalin-fixed-paraffin-embedded
FFT	Fast Fourier transform
FITC	Fluorescein isothiocyanate
GA	2’,3’-cyclic guanosine monophosphate–adenosine monophosphate
$GIF_{10\%}$	Growth inhibition factor at 10% growth rate
GM-CSF	Granulocyte-macrophage colony-stimulating factor
GMP	Gemcitabine monophosphate
GR	Growth rate
GRI	Growth rate inhibition index
GSA	Gene Set Analysis
Gy	Gray
H&E	Hematoxylin-eosin
H+L	Heavy chain + light chain
H_2O_2	Hydrogen peroxide
H_3PO_4	Phosphoric acid
HCl	Hydrochloric acid

hcp	Hexagonal close-packed
HNO_3	Nitric acid
HOMO	Highest occupied molecular orbital
HPLC	High-performance liquid chromatography
HR-MS	High-resolution mass spectrometry
HRP	Horseradish peroxidase
HR-TEM	High-resolution transmission electron microscopy
HTS	High throughput screening
i.p.	Intraperitoneal
i.t.	Intratumoral
IBA-1	Ionized calcium-binding adaptor molecule 1
IC_{50}	Inhibitory concentration at 50% level
ICB	Immune checkpoint blockade
ICD	Immunogenic cell death
ICP-MS	Inductively coupled plasma-mass spectrometry
IFN	Interferon
IgG	Immunoglobulin G
IHC	Immunohistochemistry

IL	Interleukin
Il1r2	IL1 receptor type 2
IP	Immunoprecipitation
Irak3	IL1 receptor-associated kinase 3
IRF	Interferon regulatory factor
Ir-PS	DBB-Ir photosensitizer
Isg	IFN-stimulated gene
ISRE	Interferon-stimulated response element
ITC	Isothermal titration calorimetry
IVIS	In Vivo Imaging Systems
Ka	Association constant
Kdr	Kinase insert domain receptor
kgd	Kagome dual
KO	Knock out
KSP	KSPWFTTL peptide
LC-MS	Liquid chromatography-mass spectrometry
LDS	Lithiumdodecyl sulfate
LED	Light-emitting diode

LINCS	Linear Constraint Solver
LMP	Lysosomal membrane permeabilization
LN	Lymph node
LUMO	Lowest unoccupied molecular orbital
MD	Molecule dynamics
MDSC	Myeloid-derived suppressor cells
MeOH	Methanol
MHCII	Major histocompatibility complex class II
MMP	Mitochondrial membrane permeabilization
MON	Metal-organic nanosensitizer
MTS	3-(4,5-dimethylthiazol-2-yl)-5-(3-carboxymethoxyphenyl)-2-(4-sulfophenyl)-2H-tetrazolium
MyD	Myeloid differentiation
NC	Negative control
NF-κβ	Nuclear factor kappa-light-chain-enhancer of activated B cells
NH_4OH	Ammonium hydroxide
NK	Natural killer
Nlrp3	NLR family pyrin domain containing 3

nMOF	Nanoscale metal-organic framework
nMOL	Nanoscale metal-organic layer
NMR	Nuclear magnetic resonance
Nos2	Nitric oxide synthase 2
NVT	Constant-number, constant-volume, and constant-temperature ensemble
O_2^-	Superoxide
OAc	Acetate group
OCT	Optimal cutting temperature
PA	Propionic acid
p_{adj}	Adjacent *p* values
PBS	Phosphate-buffered saline
PC	Positive control
PCN	Porous coordination network
PD-1	Programmed cell death protein 1
PD-L1	Programmed cell death ligand 1
PDT	Photodynamic therapy
PE	Phycoerythrin

PFA	Paraformaldehyde
p-IRF-3	phosphorylated of IRF-3
PK	Pharmacokinetics
$PO(OMe)_3$	Trimethyl phosphate
$POCl_3$	Phosphoryl chloride
PPA	Phenylphosphonic acid
ppb	Parts per billion
Ppbp	Pro-platelet basic protein
PpIX	Protoporphyrin IX
ppm	Parts per million
PS	Photosensitizer
p-STING	Phosphorylated of STING
PTT	Photothermal therapy
PVDF	Poly(vinylidene fluoride)
PXRD	Powder X-ray diffraction pattern
RDF	Radial distribution function
RIPA	Radioimmunoprecipitation assay
RNA	Ribonucleic acid

ROS	Reactive oxygen species
RPMI	Roswell Park Memorial Institute 1640
Rsad2	Radical S-adenosyl methionine domain-containing protein 2
RT-RDT	Radiotherapy-radiodynamic therapy
RT-RDT	Radiotherapy
SBU	Secondary building units
SD	Standard deviation
SFC	Spot-forming cell
Slc11a1	Solute carrier family 11-member 1
SOSG	Singlet oxygen sensor green assay
STING	Stimulator of interferon genes
$STING^{-/-}$	STING-knockout
TAA	Tumor-associated antigens
TBB	5,10,15,20-tetra(p-benzoato)bacteriochlorin
TBC	5,10,15,20-tetra(*p*-benzoato)chlorin
TBK	TANK-binding kinase
TBP	5,10,15,20-tetra(*p*-benzoato)porphyrin
TBS	Tris-buffered saline

TBST	Tris-buffered saline with 0.1% Tween-20 detergent
TDLN	Tumor draining lymph nodes
TEM	Transmission electron microscopy
TFA	Trifluoroacetate
TFA-TMS	Trimethylsilyl trifluoroacetate
TGF-β	Transforming growth factor β
Thbd	Thrombomodulin
TLR	Toll-like receptor
TME	Tumor microenvironment
TNF	Tumor necrosis factor
TPDC	Tetraphenyl dicarboxylate
T_{reg}	Regulatory T cell
TS	Transition state
$TsNHNH_2$	p-toluenesulfonyl hydrazide
TUNEL	Terminal deoxynucleotidyl transferase biotin-dUTP nick end labeling
UFF	Universal Force Field
UHPLC	Ultra high-performance liquid chromatography
UV-Vis	Ultraviolet-visible

WT	Wild-type
αPD-L1	anti-PD-L1
γ-H2AX	Phosphorylated histone H2A.X
ΔG	Gibbs free energy change
$\Delta G^{\neq}$	Gibbs energy of activation
ε	Molar extinction coefficient

ABSTRACT

Taokun Luo: Metal-Organic Nanosensitizers for Drug Delivery and Cancer Therapy

Under Direction of Professor Wenbin Lin

Metal-organic nanosensitizers (MONs), including nanoscale metal-organic frameworks (nMOFs) and nanoscale metal-organic layers (nMOLs), are emerging nanoplatforms for biomedical applications, including photodynamic therapy (PDT), radiotherapy-radiodynamic therapy (RT-RDT), immunotherapy, sonodynamic therapy, photothermal therapy (PTT), drug delivery, imaging, and sensing. MON is a crystalline, porous, and supramolecular material consisting of bridging organic molecules (ligands) and metal or metal-oxo nodes (primary or secondary building units). MONs can achieve efficient mass transport for drug delivery and energy transfer to sensitize the generation of reactive oxygen species (ROS), respectively. Because of the component hierarchy in MONs, we can incorporate photosensitizing molecules into the ligands for PDT or stabilize unstable drugs by framework rigidity. We can use heavy metals in the secondary building units (SBUs) to enhance radiotherapy (RT) or conjugate hydrophilic drugs to SBUs for a sustained release under physiological conditions. The insoluble, hydrophobic drugs can be loaded into the hydrophobic channels of MOFs for delivery or spatial isolation to avoid aggregation-induced quenching of photosensitizers (PSs).

The research of MONs for drug delivery and cancer therapy is a cross-disciplinary research standing at the intersection of physics, chemistry, and biology. Physics is used to study the energy transfer and sensitization mechanisms as exemplified by how low-energy or high-energy photons

interact with photosensitizers or heavy metal SBUs, respectively. Chemistry is used to efficiently synthesize and characterize MON materials with crystallinity, appropriate pore dimensions, and suitable particle sizes, and to modify MONs with suitable therapeutic motifs. Biology and immunology are used to identify target applications, analyze treatment outcomes, and inform MON optimization for enhanced biological effects.

My Ph.D. thesis research further leveraged the properties of MON materials, such as the rigid framework, open channels, Lewis acidic SBUs, and material dimensionality to maximize their anticancer efficacy. Starting from molecular design and material engineering, my research interest gradually shifted to the biomedical applications of MONs and addressing the limitations of existing anticancer drugs, such as instability, limited water solubility, and poor pharmacokinetics. My graduate research demonstrates MONs as a powerful nanoplatform for rescuing unfavorable drug candidates to enhance cancer therapy, including PDT, RT-RDT, chemotherapy, and immunotherapy.

ACKNOWLEDGEMENT

The five years of my graduate study at the University of Chicago, although less than 20% of the total length of my life, was one of the longest, and as paradoxical as it sounds, the fastest period of my life. It was long enough because during my doctoral studies, I re-evaluated myself, including my life goals, my self-worth, and the gap between my academic aspirations and reality, so much so that I ended up re-planning the next phase of my life. The reason for the rapid pace is that the world has been swiftly evolving these days, marked by significant events such as the COVID-19 pandemic, military conflicts, and the rise of generative AI. It felt as though I was a young boy standing on a subway platform, holding books, watching trains speeding by, yet unable to take a step forward. During my Ph.D., I did my best to try to make contributions to my research field. However, these achievements were not solely mine but belonged to all those who guided, inspired, supported, critiqued, and helped me. In the following acknowledgments, I would like to recall and thank each individual who assisted me.

First and foremost, I would like to express my most sincere gratitude to my academic advisor, Prof. Wenbin Lin. The most fortunate and valuable aspect of my five years at the University of Chicago was pursuing my research interests in his group.

Why do I consider doing research in Wenbin’s lab fortunate? Despite having an inorganic chemistry background and considerable interest in coordination chemistry, my fascination with biology started in junior high school. During my time at Tsinghua University, I frequently pondered issues related to cancer. This interest arose not only because cancer is one of humanity's most severe public health challenges, causing immense suffering by taking away our loved ones, but also because cancer cells, like stem cells, represent life's closest pursuit of immortality. Researching these seemingly perilous life forms is invaluable in exploring the mysteries of life

and the significance of human existence. The research topics in Wenbin's lab offered the ideal entry path for someone with a chemistry background (especially in MOF-related fields) like me to transition into cancer research. Under his guidance and support, I successfully and fortunately redirected my research focus from inorganic chemistry to biomedical science.

Why do I consider working with Wenbin the most valuable experience? Because I learned so much from him. As a person, he is just, decisive, straightforward, down-to-earth, smart, and persistent. He cared for and educated me as he would do to his own children. Nowadays, academic communities are plagued with superficiality. Even within the ivory tower, peer reviews, academic conferences, and awards have become vehicles for sweet-talking, networking, and building connections. However, Wenbin stands out as a pure stream, never compromising his principles and constantly evaluating his and others' work based on his unique values rather than social expectations. This is rare and highly commendable. In today's complex socio-political environment, everyone fears for their own reputations and tries to keep silent. Many renowned professors dare not directly criticize wrongdoings, even hesitant to speak frankly to their own graduate students, for fear of breaking taboos and causing trouble. However, Wenbin never contemplates using flowery language to disguise his thoughts; he speaks directly and frankly. This is the most efficient form of communication and the essence of education. If everyone were to package themselves in hypocrisy, academia would eventually breed a group of pretentious gentlemen and sophisticated egoists, judging science based on the so called political/social correctness rather than logical and scientific correctness. Such an approach would lead to the collapse of the scientific community.

As a scientist, Wenbin is a profound philosopher with meticulous and detailed thinking, and a daring innovator. Regardless of his own rich academic achievements, when working with us in

scientific research, he always provides feedback and unique insights in a highly responsible and timely manner. Looking back at my email records from the past five years, I was ashamed to realize that Wenbin often responded to emails much more promptly and attentively than I did. Opening the revision history of the papers we published in the past five years, I could see Wenbin's careful revisions and annotations throughout the manuscript. In the early stages, it is not an exaggeration to say that the word counts of his revisions and comments are more than that of my original text. He would also personally verify the data in the article for accuracy and rigor. He always leads by example and demands strict work discipline and attitude from us. I consider myself inherently not paying enough attention to details, but working with Wenbin has helped me change many bad habits, which has greatly benefited me. We often discuss research ideas and experimental progress together, whether it's in his office, the laboratory, in front of my bench, or in front of the whiteboard. The intense discussions and collisions of thoughts often result in tangible scientific achievements or guidelines for future research. We learn together, inspire each other, and progress together. His many unique and innovative ideas have been repeatedly guiding and inspiring me. He often teaches me to cultivate critical thinking instead of simply following the crowd because science is not a democratic election but a process where the majority follows the minority. Great science often involves refutation rather than affirmation. Instead of mindlessly following hot research topics or admiring the work of big names, it is better to calm down, think carefully, reflect, and criticize. Many doctoral students have limited opportunities to meet with their advisors, and their interactions are scarce. In stark contrast, the timely feedback and face-to-face communication I have had with Wenbin throughout my Ph.D. life give me more confidence in my work and allow me to obtain the most timely experience and suggestions, greatly boosting my research efficiency.

From the perspective of career planning and laboratory management, Wenbin practices a flat management style that allows each of us to have the opportunity to communicate ideas directly with him. Despite the fact that it would require more of his energy and time, he has never complained and always tried to solve everyone's difficulties. Complex interpersonal relationships can form even in a group of a dozen people. However, Wenbin never judges a person's scientific research ability based on personal matters, nor does he make judgments based on one-sided opinions. He silently protects us and handles the complex interpersonal and interest relationships within the group. Over the past five years, I have also witnessed the various challenges faced by a principal investigator. Many times, what may seem unreasonable from our perspective is actually the result of weighing various pros and cons, and as group members, it is difficult for us to fully understand the whole picture. In the face of crises, Wenbin never gets discouraged and handles negative things with a positive attitude. At the same time, Wenbin is a courageous entrepreneur and idealist. He has always adhered to the concept of practicality and believes that science should not be limited to literature and ivory towers but should give back to society and benefit humanity. He has put in unimaginable effort and persistence to realize his dreams. I not only greatly admire his actions, but also hope that what I have learned and achieved can make a small contribution to his current great endeavors.

In my opinion, Wenbin is the most outstanding scientist I have ever met. He is the lighthouse that illuminates my path in the sea of knowledge, the role model for my future research career, the caring parent who watches over me silently, and the friend with whom I learn and grow together. My gratitude and admiration for Wenbin cannot be encapsulated in limited words. I only hope that in the future, when I have the opportunity to share a drink with Wenbin, I can live up to his guidance and appreciation and become someone he can be proud of.

Throughout my Ph.D. journey, I feel fortunate to engage in discussions with distinguished and world-renowned faculties, and I am grateful for their guidance and support in my research work. I would like to thank Prof. Chuan he and Prof. Stephen J. Kron for serving on my dissertation committee, reading through my thesis, giving me helpful suggestions on my research, and generously sharing research resources with me. I would like to thank Prof. Joseph Piccirilli, Prof. Stephen B. H. Kent, and Prof. Raymond E. Moellering for serving on my candidacy committee and guiding me in my early Ph.D. research. I can still remember Prof. Kent telling me how to keep a positive mind and happy mood in Chicago, where there is a long and depressing winter: get more light bulbs, open up windows, and get more sunshine. I would like to thank Prof. John S. Anderson, Prof. Bozhi Tian, and Dr. Ralph R. Weichselbaum for their help and support not only for my Ph.D. research but also for my future career development. I would like to thank Dr. Aditya Juloori and Dr. Alexander T. Pearson for their expertise in histology and clinical study. I would like to thank Prof. Howard J. Halpern for his guidance and sharing of experiments related to radiotherapy. I would also like to thank Prof. Makoto Fujita for guiding me into the field of MOF chemistry, accepting my invitation to give a Closs lecture, and providing me with numerous constructive suggestions for my current research.

During my five years at the University of Chicago, I had the privilege of working with peers with the most brilliant minds in the world. Whether it was collaborating on research projects, discussing scientific questions, or even having fun tother, being in their company was fulfilling and greatly enjoyable to me.

I would like to thank Dr. Xiaomin Jiang, my most trusted research partner and my best friend in private. Xiaomin's mastery of experimental techniques and attention to experimental details can only be described as extraordinary. Many experiments he conduted were flawless and impeccable.

Xiaomin is an outstanding researcher who excels at critical thinking and reflection. Together, we have discussed and resolved various challenging experimental issues. Working with him always inspires me and gives me innovative insights. In laboratory management, Xiaomin takes care of tasks beyond his responsibilities, ensuring a well-functioning and conducive lab setting. In our personal lives, as roommates for three years, Xiaomin not only cooked for both of us but also helped me develop many good habits. For example, he introduced me to classical music and encouraged me to engage in fitness activities. Besides research achievements, my greatest accomplishment at the University of Chicago was losing more than 80 pounds, and Xiaomin definitely played a significant role in guiding and assisting me throughout this journey.

I would like to thank Geoffrey T. Nash, one of my earliest collaborators and my best friends. In our group, we always form a chem-bio pair to accelerate the progress of projects. I had a tough start at the beginning of my Ph.D. because I had zero background in biological studies. Geoffrey is always willing to trust me unconditionally and provides me with his high-quality synthesis and solid chemistry knowledge. We collaborated twice during our third year, and both experiences were enjoyable and highly efficient. His trust and support made me more confident in the lab, and collaborating with him was incredibly reassuring because I did not have to worry about synthesis-related issues and could focus solely on my assigned tasks. I really appreciate his professionalism and expertise in both chemical synthesis and laboratory safety management. His carefree and liberated attitude toward life is worth emulating and learning from. Collaborating with Geoffrey provided me with the best start to my Ph.D. research.

I would like to thank Dr. Guangxu Lan, a great scientist and mentor. Guangxu is undoubtedly a genius in MOF synthesis. Furthermore, he is good at teaching and willing to share his knowledge with all of us. In fact, most of my research is based on his discovery. He is also a problem solver

and can efficiently tackle experimental challenges. I am grateful that I have worked with him and learned a lot from him.

I would like to thank all my collaborators in Lin lab, including Yingjie Fan for his talented synthetic skills, Ziwan Xu for her fantastic and inspiring simulations and synthesis, Jianming Mao for his simulation, synthesis, and diligent help with biological experiments, Jinhong Li for his simulation and hard synthetic work, Dr. Wenyao Zhen for her expertise in nanotechnology and perfect control of all experimental details, Dr. Gan Lin for his expertise in sonodynamic therapy, and Dr. Luciana Albano for her expertise in head and neck cancer and proteomics. Together, we accomplished remarkable research projects, which would have been impossible without their knowledge, expertise, and hard work.

I would like to thank three of my undergraduate mentees, August Culbert, Michael Kaufmann, and Eric Yuan. Although I am officially guiding them, in reality, we are learning, researching, and progressing together. They are all extremely diligent and intelligent individuals. I am often inspired by them during our collaboration, whether it be in project design, research ideas, or experimental details. Their research efforts have helped me to complete projects more efficiently. Eric, who has worked with me for two years, is an incredibly smart, efficient, and hardworking undergraduate researcher. He can accurately reproduce any experiment I have only explained once, and he often provides insightful thoughts and perspectives after performing experiments. He has a deep understanding of our research system, and it is not an exaggeration to say that his thinking ability and experimental skills are on par with those of an outstanding graduate student.

I would like to thank many senior group members, including Dr. Kuangda Lu, Dr. Wenbo Han, Dr. Kaiyuan Ni, Dr. Nining Guo, Dr. Xuanyu Feng, Dr. Yang Song, Dr. Zhe Li, Dr. Yingying Li, Dr. Christina Chan, Dr. Wenjie Shi, Dr. Zekai Lin, and Dr. Chunbai He. When I first joined

the laboratory, they provided me with a lot of help with experimental techniques, research experience, and my personal life. With their help and guidance, I quickly adapted to life at the University of Chicago and efficiently embarked on my research journey in the Lin lab.

I would like to thank other Lin lab members, Dr. Haifeng Zheng, Dr. Dong Won Kang, Dr. Pengfei Ji, Dr. Yuanyuan Zhu, Dr. Xiaopin Duan, Dr. Yangjian Quan, Dr. Qingyun Guo, Dr. Deyan Gong, Dr. Xiang Ling, Dr. Jing Liu, Dr. Tasha Drake, Dr. Yunhong Pi, Youyou Li, Jianqiao Liu, Zitong Wang, Junjie Xia, Langston Tillman, Yibin Mao, Maolin Wang, Samuel Veroneau, Eric You, Justin Chen, Morten Lee, Caroline McCleary, Megan Rodriguez, Pierce Yeary, Steven Labalme, Tomas Germanas, Abbie Blenko, for their help with my research during my Ph.D. study and for their support of my research assistantship.

Besides my chemist fellows, the assistance provided by the staff working in the core facilities is indispensable for my research work. With their expertise in their respective fields, the quality and efficiency of my research have improved greatly. I would like to thank Dr. Christine Labno, Shirley Bond, and Dr. Vytas Bindokas at the Integrated Light Microscopy Core for helping with confocal imaging and whole slide scanning. I would like to thank Dr. Shihong Li, Can Gong, Xin Jiang, Ming Chen, Christy Schmehl, Haiqing Luo, Brittany Grantham, and others at the Human Tissue Resource Center for help with the histology study. I would like to thank Dr. Siquan Chen, Dr. Carman Ka Man Ip, Dr. Eugene Xu, and Chun-yi Chiang at the Cellular Screening Center for help with live imaging. I would like to thank Hongyuan Jiao and Dr. Yuanyuan Zha at the Human Immunologic Monitoring Facility for their help with NanoString. I would like to thank David Leclerc at the Cytometry and Antibody Technology Core Facility for help with flow cytometry. I would like to thank Yimei Chen and Dr. Qiti Guo at the Advanced Electron Microscopy Core for their help with TEM and AFM. I would like to thank Dr. C. Jin Qin and Guangchang Zhou at the

Mass Spectrometry Facility for their help with LC-MS. I would like to thank Dr. Josh Kurutz at the NMR Facility for helping with NMR experiments. I would like to thank Dr. Alexander Filatov at the X-ray facilities for his help with PXRD. I would like to thank Dr. Erik Pearson, Gene Barth, and John Lukens at the Department of Radiation and Cellular Oncology for their help with radiotherapy-related experiments. I would like to thank James Marsicek for the guidance on radiation safety. I would like to thank Karin Kelly, Sara Kusch, Mindy Nguyen, Courtney Losser, Aniruddhsingh Solankim, and many others at the Animal Resource Center for help with rodent experiments. I would like to thank Dr. Yu-Sheng Chen at the Argonne National for help with crystallography.

The greatness of the Department of Chemistry at the University of Chicago is not only attributed to its exceptional faculties but also to the outstanding staff who silently serve. I would like to thank Dr. Vera Dragisich for her guidance as the program director and for caring for our mental health and lab environment. I would like to thank Melinda Moore for her dedication to student service. I would like to thank Debrah Morgan and Laura Luburich for their efforts in organizing seminars, particularly for their great support during my planning of the Closs lecture. I would also like to thank Dr. Meishan Zhao for guiding and helping with my teaching assistantship during my first year. I am deeply impressed by his conscientious and responsible work attitude in teaching.

I would like to thank several other friends at the University of Chicago, including but not limited to Dr. Kaiting Yang, Dr. András Piffkó, Siddhartha Sohoni, Zeyu Qiao, Zhongyu Zou, Dr. Tong Wu, Haoqi Wu, Tong Lan, Dr. Cheng Peng, Dr. Shusuke Ochi, and Dr. Ge Zhang. Their invaluable assistance in research, insightful discussions, and unwavering support have been instrumental in my academic journey. I would like to thank Jiakun Zhao and his mother, Xiaowei

Tang, for their unwavering care and immense support throughout my initial two years. I would like to thank Zuofu Wang for traveling around the United States with me.Finally, I would like to express my sincerest and most loving gratitude to my family. Since middle school, despite the majority of our time being filled with silence and the periods of separation being much shorter than our reunions, I deeply understand that my family will always love me, support me, and silently cheer me on, praying and blessing me. Similarly, I am constantly thinking of my beloved family, who loves me deeply. My parents are both great educators, selfless contributors, and hardworking individuals. I deeply regret not being able to be with my family for the past five years. I know how worried and stressed my family must have felt when they saw unfavorable things happening on the other side of the earth. I know how excited and thrilled my family was when they heard about my achievements. I know that my parents have managed the entire family well enough, ensuring that I have no worries behind. My parents once told me that home is an everlasting harbor where I can take a breath regardless of success or failure in my career. And I want to say that I aspire to become their harbor in the future, to be their support, to be their pride. Please wait for me a little longer, so we can embrace each other once again.

Chapter 1. Metal-Organic Nanosensitizers for Cancer Therapy

1.1 Nanomaterials for Cancer Therapy

Cancer is a complex and potentially terminal disease that affects millions of people worldwide.[1] It is characterized by uncontrolled growth and spread of malignant cells in the body.[2-3] These cells have the ability to invade and destroy surrounding tissues, leading to the formation of tumors and metastases.[4-5]

The management of cancer in the clinic typically involves a multidisciplinary approach, including surgery, radiotherapy (RT), chemotherapy, targeted therapy, hormone therapy, immunotherapy, and other emerging treatment modalities (**Figure 1-1**).[6-7] These therapies either use a form of energy to destroy tumor cells or use pharmacologically active therapeutics to kill tumor cells directly or indirectly. However, energy deposition in the surrounding normal tissues and non-specific therapeutic delivery lead to severe side effects for a majority of cancer patients.[8-9] Improving the efficacy of existing modalities and developing new treatment strategies are at the forefront of cancer research.[10]

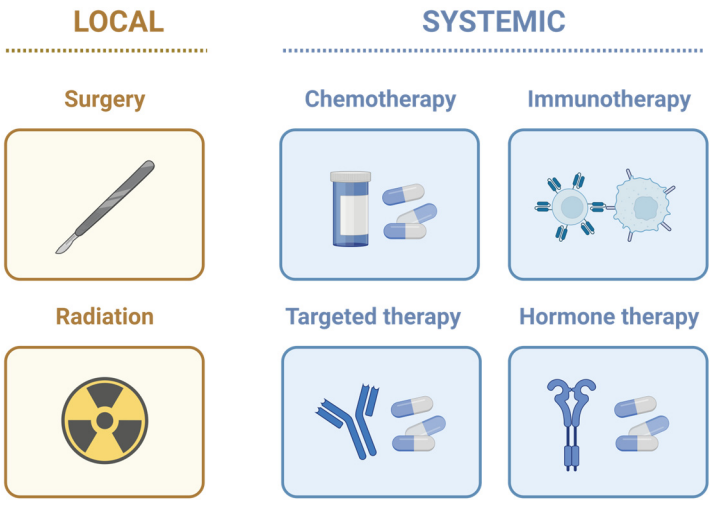

Figure 1-1. General treatment regimens for cancer. The scheme is created with Biorender.com.

Nanoparticles, typically between 1 and 100 nm in sizes, exhibit unique and sometime unexpected properties compared to their bulk counterparts. The reduction of physical dimensions to the nanoscale results in altered physical, chemical, optical, and biological properties. Nanoparticles can be designed from a variety of different materials, including metals, semiconductors, oxides, polymers, lipids, and carbon-based structures (**Figure 1-2**). A prominent feature of nanoparticles is their high surface-to-volume ratios, leading to enhanced reactivity and interactions with their surroundings and offering new opportunities for further manipulation and control. Size-dependent behaviors of nanomaterials, including quantum confinement, plasmon resonance, and surface enhancement effects, have found applications in many scientific fields.

Nanomedicine, the application of nanotechnology in medicine, harnesses the unique properties of nanoparticles to enhance the diagnosis, treatment, and monitoring of cancer.[11] Nanoparticles, with their tailored size, surface characteristics, and functionalization, enable precise and targeted delivery of therapeutic agents while minimizing damage to healthy tissues.[12] As a drug carrier and a condensed state of matter, the nanoparticle can stabilize the payload, improve the pharmacokinetics (PK), and prolong the circulation time. Nanomedicines have proven to be an effective means of delivering therapeutics, especially for vaccines during the COVID-19 pandemic.[13] Additionally, nanoparticle-based imaging agents have contributed to medical diagnostics, providing high-resolution imaging and early disease detection.[14]

In the field of cancer therapy, nanomedicines have been extensively explored for the delivery of chemotherapeutics in the past three decades, largely motivated by the postulation of the enhanced permeability and retention (EPR) effect in tumors.[15] It is believed that the leaky neovasculature and ineffective lymphatic drainage in tumors can increase tumor deposition of drug payloads in long-circulating nanotherapeutics.[16-20] Despite extensive efforts, only several

nanotherapeutics have been approved by U.S. Food and Drug Administration (FDA) for cancer treatment.[21-23] Accumulating evidence indicates that EPR-mediated nanoparticle deposition in tumors is limited by the heterogeneity of pathophysiological parameters, especially in human tumors.[24-27] Research in nanomedicines should be directed toward improving tumor targeting when administered systemically or seeking to utilize their unique features in other clinical scenarios, such as local treatments and multimodal treatments.

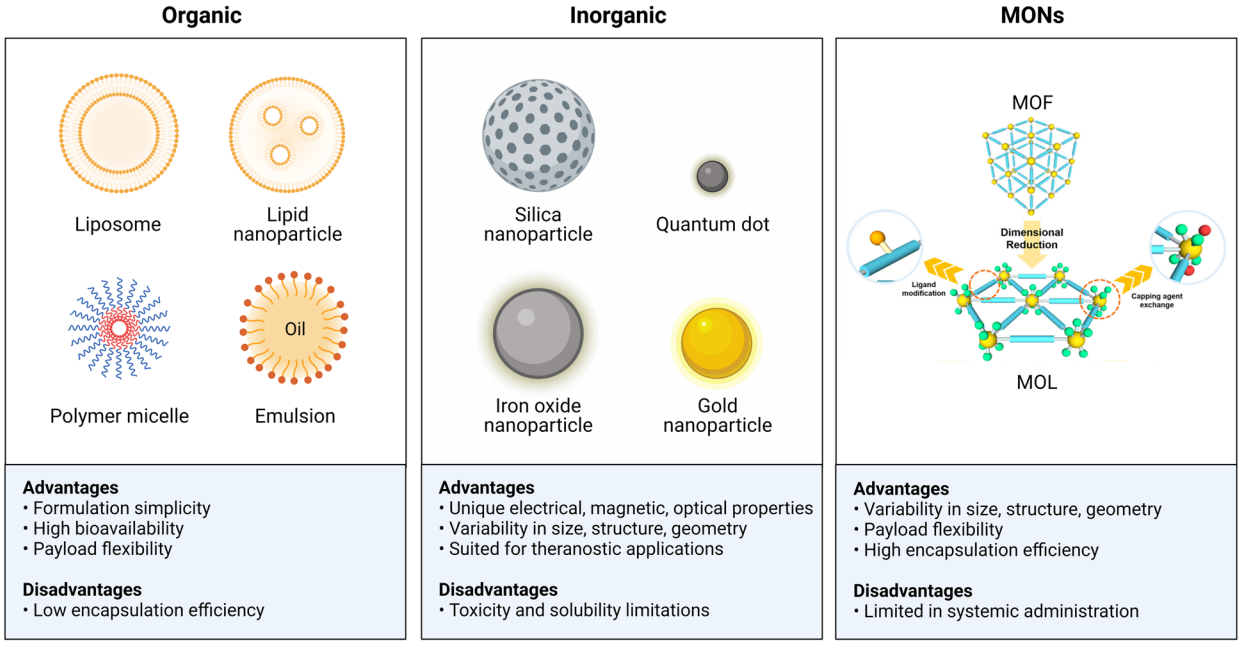

Figure 1-2. Different classes of nanoparticles and their biomedical applications. The scheme is created with BioRender.com.

1.2 Metal-Organic Nanosensitizers for cancer therapy

1.2.1 Introduction

Metal-organic nanosensitizers (MONs) have recently emerged as a novel class of nanotherapeutics for photodynamic therapy (PDT), radiotherapy-radiodynamic therapy (RT-RDT), chemotherapy, and immunotherapy of cancer.[28-29] MONs are hybrid, porous, and crystalline materials made of metals and organic linkers with hydrodynamic sizes around 100 nm. In MONs

for biomedical applications, organic sensitizers/drugs are periodically arranged as ligands in the crystalline frameworks to afford high drug payloads, and they are spatially isolated by metal−oxo secondary building units (SBUs) to avoid aggregation and other adverse processes.[30-31] The metals in MONs are usually Zirconium or Hafnium. This choice can ensure a relatively stable framework under physiological conditions and minimal toxicity and side effects to patients. Heavy metals can also enhance RT due to their large attenuation coefficients for X-rays. In an ongoing Phase I clinical trial, the MON developed by our lab is well tolerated in patients with no dose-limiting toxicity and significantly enhances local tumor response rates upon low-dose radiation.[32] Furthermore, MONs have dynamic surface chemistry and internal pores to efficiently load and deliver drugs with very different pharmacological properties to solve stability, aggregation, and solubility issues of potential drug candidates (**Figure 1-3**).

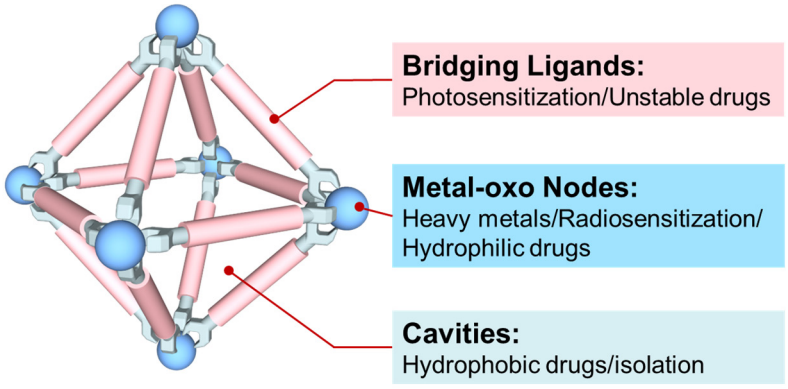

Figure 1-3. Three delivery strategies by nMOFs to address respective pharmacological issues.

At the current stage, MONs can be classified into two categories based on their dimensions, three-dimensional (3-D) nanoscale metal-organic framework (nMOF) and two-dimensional (2-D) nanoscale metal-organic layer (nMOL) (**Figure 1-4**).[33] nMOF synthesis is adapted from solvothermal synthesis of bulk MOF materials. However, the bottom-up synthesis of self-supported nMOL requires suitable coordination modes and organic linkers with proper geometries and careful control of reaction temperature, capping agents, water concentration, and other

parameters.[34-35] That is the reason why there are significantly more reports of nMOFs in biomedical applications than those of nMOLs. nMOLs inherit many attractive features of nMOFs, such as crystalline structure, uniform and hierarchical organization of active sites, and molecular tunability. nMOLs have already been explored for heterogenous catalysis,[36-40] chemical sensing,[41-42] and biomedicine.[43-45] In particular, nMOLs have outperformed nMOFs in catalytic applications, with all of their active sites accessible to organic substrates. In this thesis, I will discuss the anticancer applications of nMOFs in **Chapters 1** and **7**, the advantages of nMOLs over nMOFs in **Chapter 2**, and drug delivery by nMOLs in **Chapters 3**, **4**, **5**, and **6**.

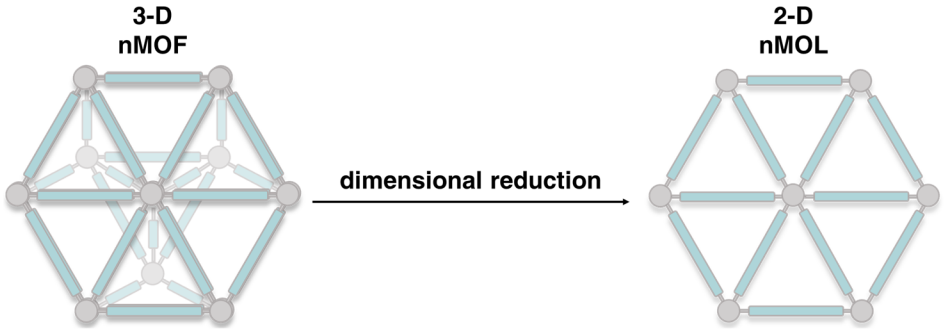

Figure 1-4. Dimensional reduction from 3-D nMOF to 2-D nMOL.

MONs are efficient nanoplatforms for simultaneous mass transport and energy conversion for drug delivery and sensitization, respectively. Efficient mass transport enables protection of drug cargos, high payloads, and controlled and sustained release of therapeutics. Efficient energy conversion allows sensitizing different formats of energy, such as photons, into cytotoxic species, such as reactive oxygen species (ROS), to kill cancer cells.

1.2.2 Mass Transport: Drug Delivery

As a hybrid supramolecular material, MONs can be engineered at different sites for drug delivery. SBUs and ligands themselves can be therapeutic motifs to be transported into cells. Drugs can be conjugated onto ligands via reversible covalent linkages. nMOFs are porous and exhibit large channels for drug loading. Numerous works in the literature have reported utilizing nMOF

channels for drug delivery or nMOF frameworks for encapsulation (**Figure 1-5a**).[46-48] However, the cavities are hydrophobic because most ligands of nMOFs are insoluble in water, thus limiting the loading efficiency of hydrophilic molecules into nMOFs. Most channels of reported nMOFs are below 5 nm, which are difficult to load macromolecules like proteins and nucleic acids.[49]

Meanwhile, both nMOFs and nMOLs exhibit Lewis acidic SBUs with large surface-volume ratios.[50] However, the surface of MONs is usually inert since the SBUs are capped with carboxylate capping groups such as benzoate, formate, and acetate. Lin and coworkers previously found that SBUs on MONs can be modified for further functionalization.[38, 51] Capping agents occupying vertical coordination sites can be replaced with other monocarboxylates to introduce new functionalities into MONs. There is a dynamic equilibrium between the coordination of the capping reagents and SBUs, so we can disrupt this equilibrium by modulating the nucleophilic strength and stoichiometry of targeted molecules to allow the replacement of the capping reagent. This strategy can be utilized for drug loading onto MON surface.[52]

We developed a trifluoroacetate (TFA) modification method to exchange inert capping agents into more labile TFA groups.[52-53] For capping agent exchange in polar solvents, the rate-limiting step is the nucleophilic substitution itself. Because TFA is a weak Lewis base, TFA-modified SBUs can be easily substituted by other carboxylate- or phosphate-containing molecules to load target molecules onto MONs in a thermodynamically favorable way (**Figure 1-5b**). To synthesize these thermodynamically unfavorable TFA-capped MONs from any MONs, we designed a reaction between MONs and trimethylsilyl trifluoroacetate (TFA-TMS) in non-polar solvents. Solvation of modulator acids in a non-polar solvent such as benzene is difficult, which makes nucleophilic reaction in benzene very slow. The rate-limiting step becomes the solvation, which leads to the leveling effect in benzene, making both TFA and capping acids neither good

nucleophilic agents. An excess amount of TFA can kinetically drive the substitution reaction to afford TFA-capped MONs (**Figure 1-5b**). Nevertheless, this strategy also has its limitation as it requires the target drugs to have carboxylate or phosphate groups for coordination onto SBUs.[54]

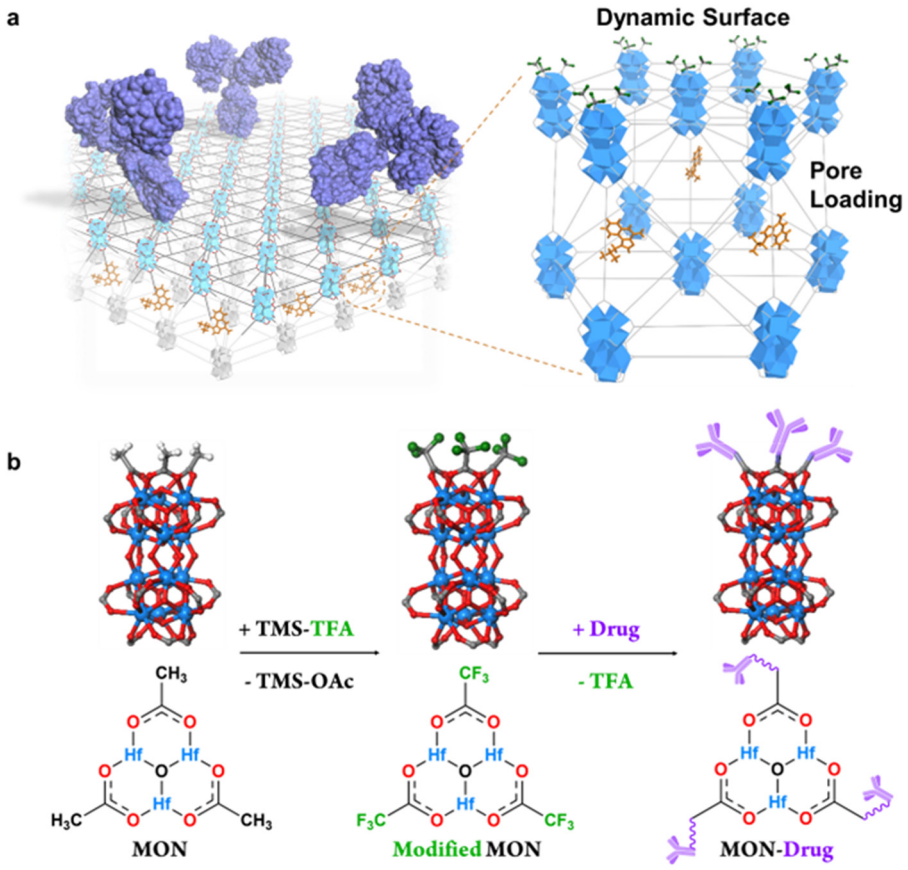

Figure 1-5. Drug delivery by channels and SBUs. (a) Schematic showing drug delivery strategies by MONs: channel loading of hydrophobic small molecules (orange) and surface conjugation of carboxylate/phosphate containing small molecules (green) and macromolecules (purple). (b) Synthetic scheme of TFA modification of MONs, and drug loading onto TFA-modified MONs.

There are three aspects to consider before loading drugs to MONs:

First, is this drug targeting endo/lysosomes, or can this drug penetrate the plasma/organelle membrane? (**Figure 1-6a**) Based on our observation (**Figure 1-6b**) and literature reports, the majority of MONs are endocytosed into endo/lysosomes via macropinocytosis, clathrin- or caveolae-mediated pathways.[55] Bare MONs are not able to penetrate the lipid bilayer. Therefore,

it is difficult to deliver drugs to the cytoplasm or other organelles if the drug itself cannot escape endo/lysosomes. Examples of successful targets include cell membrane receptors by antibodies, toll-like receptors (TLR) on endolysosomal membrane by CpG oligodeoxynucleotide and imiquimod, metabolic pathways by endogenous precursors (**Chapter 4**), DNA synthesis by chemotherapeutics (**Chapter 5**), and stimulator of interferon genes (STING) by cyclic dinucleotides which can across lipid bilayer by themselves (**Chapter 6** and **Chapter 7**). Failed candidates include double-stranded DNA targeting STING and nucleic acids for transfection.

Second, is this drug targeting tumors cell or immune cells? One issue that cannot be avoided in nanomedicine is the uptake of nanoparticles by different cell populations. Particularly for MONs as foreign particles, the phagocytosis and clearance by immune cells cannot be overlooked.[56] If delivering cytotoxic reagents, the toxicity to immune cells should be carefully studied. If targeting immune cells by certain agonists, the distribution of a MON among different cell types and the immune effects induced by the MON itself should be identified (**Chapter 7**).

Third, what is the minimal effective concentration of the drug? This problem not only relates to the *in vitro* effective concentration, but also raises questions about the administration routes of MONs. Each MON has a limit on loading efficiency for a specific drug type, and the MON has its own upper limit of dosage. If a maximally loaded drug reaches the toxic concentration of MONs but still fails to reach its minimum concentration of action, then it is not ideal for delivery by MONs. Similarly, if a drug requires high local concentration to be effective, for example, radiosensitizers, or is too toxic when administered systemically, such as immunotherapeutics, then local injection could be a more appropriate way to maximize treatment efficacy and minimize side effects.

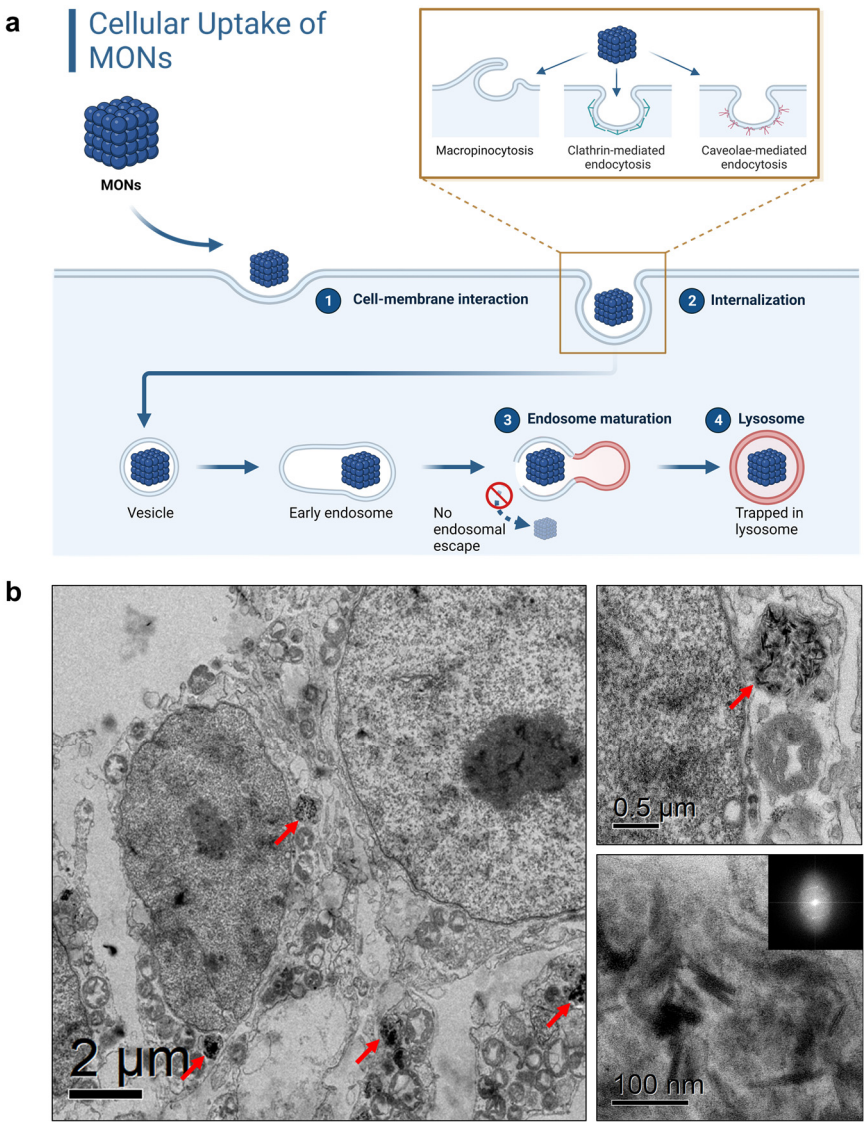

Figure 1-6. Cellular uptake of MONs. (a) Endocytosis pathways and limited endosomal escape of MONs. (b) Transmission electron microscopy images showing MONs trapped in lysosomes of CT26 cells 24 hours after incubation.

1.2.3 Energy Conversion: Sensitization

Besides drug delivery, MONs and their building blocks can have therapeutic functions by converting energy into cytotoxic species, particularly upon external stimulation with visible light or X-rays (**Figure 1-7**). This sensitization capability is a unique feature of MONs to integrate multiple treatment regimens in one single nanoplatform. In a stable MON platform, the therapeutic

components can remain intact in MOFs for their biological functions under physiological conditions, which is in stark contrast to conventional molecular nanocarriers, whose primary purpose is cargo transport and release after delivery to the target tissue.

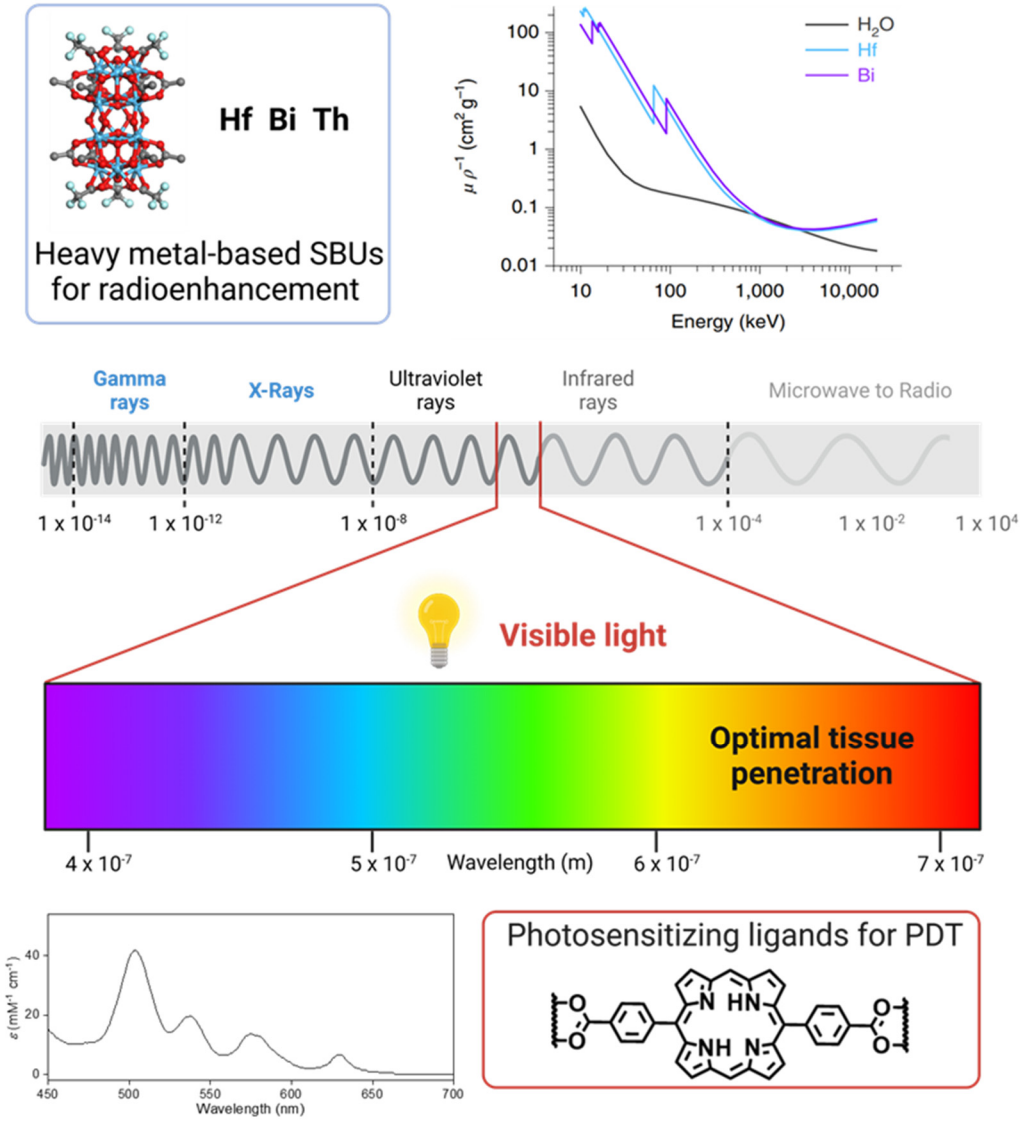

Figure 1-7. Energy scheme for photon sensitization by MONs. Photons are accessible energy sources for MONs. Heavy metal-based SBUs can efficiently absorb X-rays to deposit more energy near MONs for more ionization events and stronger radiosensitization than irradiation alone. PS-based ligands can convert visible light, preferably photons within the optimal tissue penetration range, to generate highly cytotoxic ROS to eradicate cancer cells for PDT applications. The scheme is created with BioRender.com.

The sensitizing organic motifs, usually photosensitizers (PSs), can be embedded directly as ligands if their symmetry allows for MON synthesis, conjugated to ligands or SBUs by post-synthetic modifications, or loaded into pores for spatial isolation. These PS molecules are highly coherent with photons in the visible wavelength band and can efficiently absorb the photons and bring themselves into the excited state. On the one hand, the elevated energy levels can be emitted through radiative processes such as fluorescence and phosphorescence to release photons or undergo vibrational relaxation through internal conversion, which leads to nonradiative photothermal conversion to generate heat for photothermal therapy. However, this process is not efficient and requires high power of photon sources which are beyond the clinical threshold. On the other hand, the excited states can also be quenched by external molecules and transfer energy to other molecules, such as oxygen, to generate highly cytotoxic ROS for PDT.

Lin and coworkers first reported efficient PDT with MONs built from photosensitizing ligands.[57] Clinically used PSs are derivatives of porphyrins and phthalocyanines because they have high ROS quantum yield and strong absorption at optimal penetration wavelength. However, with highly conjugated structures, PSs such as porphyrins and phthalocyanines are sparingly soluble in aqueous environments and prone to aggregation-induced quenching under physiological conditions. By incorporating PSs into the frameworks, we showed that MONs could overcome the drawbacks of traditional PSs and act at the molecular level as nanophotosensitizers *in vivo*.[58-59] By tuning SBUs and ligands, MONs were shown to generate various types of ROS for both type-I and type-II PDT.[60-61] Isolation of PSs on SBUs or in MON channels provides another strategy to formulate MOF-based nanophotosensitizers.[44, 62] Despite the excellent photosensitizing efficacy of MONs, the clinical use of PDT is limited by the shallow penetration of light and photosensitivity side effects.

Compared to visible light, X-ray can reach deeply seated tumors and is widely used in clinical practice. However, these high-energy photons can also deposit energy in the healthy tissue on their tracks, causing severe side effects. High-Z metal-based nanoparticles have been investigated for decades to enhance RT efficacy and lower X-ray dose. In MONs, the metals within SBUs can be heavy elements (Hf, Bi, Th) exhibiting large X-ray attenuation coefficients to enhance X-ray energy deposition and increase local ionization events for radiosensitization. Lin and coworkers disclosed hafnium-porphyrin-based MOFs as a powerful nano-radiosensitizer to enhance low-dose X-ray radiation via a unique RT-RDT process in 2018.[63] During RT-RDT, heavy metal-based SBUs efficiently intercepted and absorbed X-ray radiation, and deposited energy to directly excite the coordinated photosensitizers to generate $^1O_2$. In a recent Monte-Carlo simulation study, we found periodic arrays of SBUs in MONs are better radiosensitizers than non-porous NPs in terms of physical dose enhancement regardless of the radiation source and particle size.[64] Though the mechanism of RT-RDT is not fully understood, the up-to-date experiments and simulations indicate that MONs may act as a photon decelerator: the X-ray photons with high kinetic energy may interact, scatter, and even be trapped inside the porous, electron-dense, and crystalline MON framework. These elastic and inelastic interactions enabled by MONs reduce incident photon energy and increase mass attenuation coefficients of surrounding matters. Photons decelerated by MONs thus have higher chances to interact with surrounding substrates, including PSs embedded in the gaps and water, for enhanced photosensitization and more radiolysis, respectively.

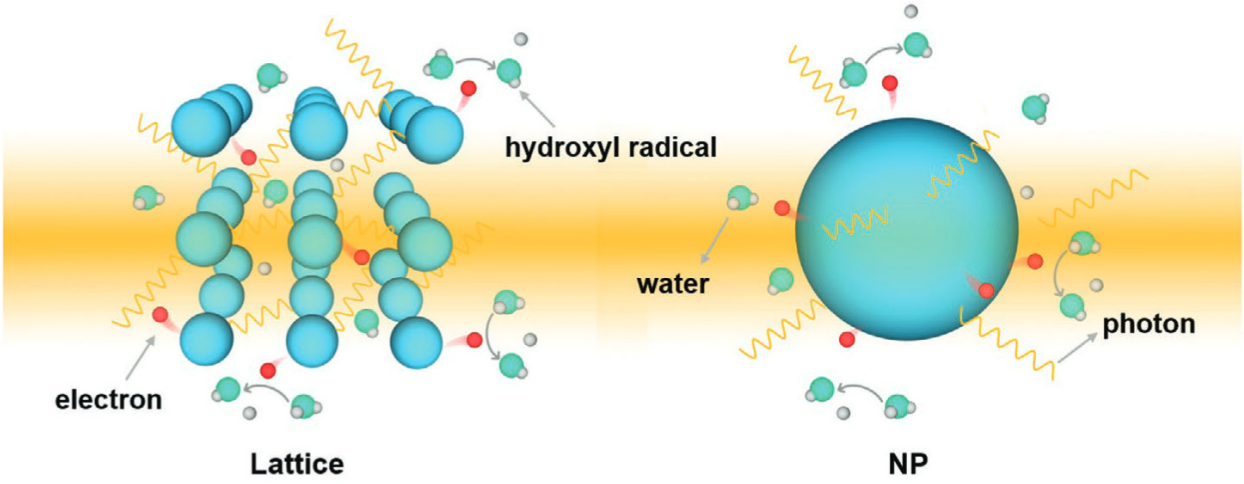

Figure 1-8. Schematic showing radiation-induced reactions in crystalline MON (left) and a NP (right).

1.2.4 Combining drug delivery and sensitization by MONs for new avenues in cancer treatments

Lin and coworkers have combined immunotherapy with MON-mediated PDT or RT-RDT.[59, 63, 65] MON-based nanosensitizers generate cytotoxic ROS to induce local antitumor effects that produce immunogenic cell death and inflammatory tumor microenvironment. MON-mediated exposure of tumor antigens and proinflammatory markers stimulates antigen presentation and T-cell infiltration. Consequently, the combination of immune checkpoint blockade not only enhances local treatment effects but also elicits abscopal effects in murine models, which extends the scope of MON-mediated local therapy to systemic immune responses. MONs also possess porous structures and dynamic surface chemistry to deliver small molecules and biomacromolecules as immune agonists and cancer vaccines to confer antitumor immunity to the host. [28, 54, 61, 66]

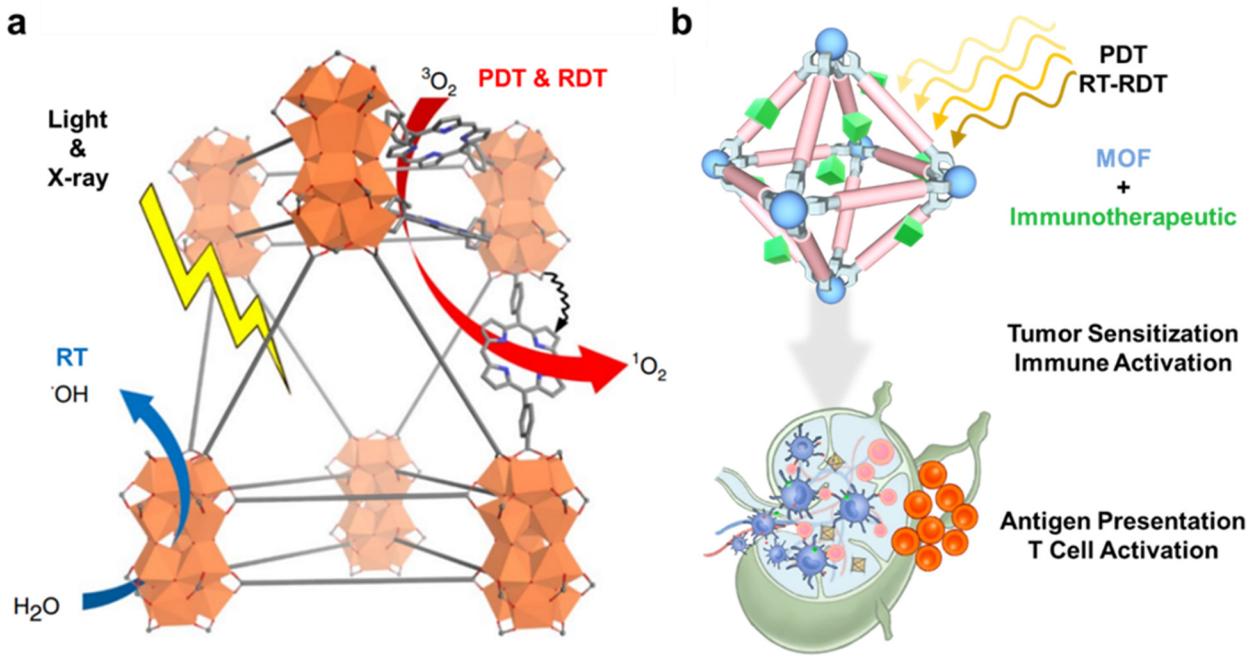

Figure 1-9. Combination of drug delivery and sensitization enabled by MONs. (a) Modes of actions of PDT and RT-RDT enabled by MONs. (b) Schematic showing the synergy between MON-based local therapies and delivered immunotherapeutics for systemic antitumor responses.

Chapter 1 of this thesis broadly discusses the development of drug delivery nanoplatforms and current challenges in the clinic. As an emerging nanocarrier and sensitizing reagent, MONs achieve efficient mass transport and energy conversion for drug delivery and ROS generation, respectively. Thus, MONs present an ideal platform for the development of advanced nanosensitizers and for integrating multiple treatment regimens, including PDT (**Chapter 2-4**), chemotherapy (**Chapter 5**), RT-RDT (**Chapter 5-7**), and immunotherapy (**Chapter 6-7**), to afford unique combination nanotherapeutics for preclinical exploration and clinical translation.

Chapter 2 discusses the use of the framework rigidity of nMOFs to stabilize unstable photosensitizing ligands for PDT. A number of highly potent PSs, such as bacteriochlorin derivatives, are limited in PDT application due to their intrinsic instability toward oxidation and photobleaching. The rationally designed Zr-TBB nMOF stabilizes 5,10,15,20-tetra(p-benzoato)bacteriochlorin (TBB) ligands toward oxygen and light via geometrical constraint of the

framework. Zr-TBB nMOF protects the TBB ligand from photodegradation and efficiently generates type-I and type-II ROS to afford significant inhibition of colorectal and breast tumors. nMOFs thus offer a unique nanoplatform to protect and deliver bacteriochlorins and other unstable photosensitizing molecules for PDT.

Chapter 3 reveals a dimensional reduction strategy to significantly enhance PDT efficacy of MONs. By adjusting the coordination strength of the monocarboxylate modulator, M-DBP nMOFs and nMOLs (M = Zr, Hf) based on M_{12}−oxo SBUs and 5,15-di-p-benzoatoporphyrin (DBP) ligands are rationally synthesized. Molecule dynamics (MD) simulations and experimental studies show that the nMOLs enhance ROS generation and exhibit more than an order of magnitude higher cytotoxicity than the nMOFs. As a result, 2-D nMOLs significantly outperform 3-D nMOFs in PDT, leading to enhanced tumor regression, higher cure rates, and reduced metastasis in mouse models. This dimensional reduction strategy can be generalized to the design of other nanophotosensitizers for potent PDT.

Chapter 4 describes surface modification of the 2-D nMOL-based nanophotosensitizer to conjugate a mitochondria-targeted drug, 5-aminolevulinic acid (ALA), to afford ALA/Hf-MOL for dual-organelle-targeted PDT. Upon endocytosis, ALA/Hf-MOL enhances ALA delivery and protoporphyrin IX (PpIX) synthesis in mitochondria, and traps the Hf-MOL comprising DBP ligands in lysosomes. Light irradiation at 630 nm simultaneously excites PpIX and DBP to generate ROS and rapidly damage both mitochondria and lysosomes, leading to synergistic enhancement of the PDT efficacy. 2-D nMOL presents a unique nanophotosensitizer with the capacity for multi-drug delivery.

Chapter 5 presents the rational design of a 2-D nMOL for simultaneous chemotherapeutic delivery and RT-RDT. A Hf_{12}-Ir nMOL comprising Ir-based PSs and Hf_{12} SBUs is synthesized

and verified as a potent nanoradiosensitizer. Coordination of phosphate-containing drugs onto SBUs prolongs their intratumoral retention, allowing for continuous release of gemcitabine monophosphate (GMP) for effective localized chemotherapy. GMP/MOL serves as a reservoir for the slow release of chemotherapeutics as well as a 2-D nanoradiosensitizer for amplifying the antitumor effects of radiotherapy. 2-D nMOLs provide a new treatment paradigm for combining radiotherapy and localized chemotherapy with a single nanoplatform.

Chapter 6 discusses the rational design of the 2-D nanoplatform cGAMP/MOL via conjugating 2',3'-cyclic guanosine monophosphate–adenosine monophosphate (cGAMP) to Hf_{12}-DBB-Ir nMOL for simultaneous activation of stimulator of interferon genes (STING) and radiosensitization. The MOL not only exhibits strong radiosensitization effects for enhanced cancer killing and induction of immunogenic cell death but also retains cGAMP in tumors for sustained STING activation in a phosphate-dependent manner. Compared to free cGAMP, cGAMP/MOL elicits stronger STING activation and regresses local tumors upon X-ray irradiation. Further combination with an immune checkpoint inhibitor bridges innate and adaptive immune systems by activating the tumor microenvironment to elicit systemic antitumor responses. MOLs provide an integrated nanoplatform for the delivery of immunotherapeutics with non-ideal pharmacokinetic behavior and high systemic toxicity.

Chapter 7 discusses the formation of artificial leukocytoid structures (ALS) induced by intratumoral injection of MONs and its long-term immune effects. A robust nanoplatform, cGAMP/MOF, was developed by conjugating cGAMP on nMOFs for synergistic radiosensitization and STING activation. cGAMP/MOF demonstrated strong anticancer efficacy and induced the formation of an immune cell-rich nodule, ALS. ALS transforms into an immunostimulatory "hotspot" by low-dose RT. Combining cGAMP/MOF with immune

checkpoint blockade suppressed distant tumors through systemic immune activation. These findings not only demonstrate the potent radiosensitizing efficacy of cGAMP/MOF, but also provide insights into the immune mechanism for the design of locally administered nanoradiosensitizers.

1.3 References

(1) Siegel, R. L.; Miller, K. D.; Fuchs, H. E.; Jemal, A., Cancer statistics, 2022. *CA. Cancer J. Clin.* **2022,** *72* (1), 7-33.

(2) Dawson, Mark A.; Kouzarides, T., Cancer Epigenetics: From Mechanism to Therapy. *Cell* **2012,** *150* (1), 12-27.

(3) Martinez-Outschoorn, U. E.; Peiris-Pagés, M.; Pestell, R. G.; Sotgia, F.; Lisanti, M. P., Cancer metabolism: a therapeutic perspective. *Nat. Rev. Clin. Oncol.* **2017,** *14* (1), 11-31.

(4) Fares, J.; Fares, M. Y.; Khachfe, H. H.; Salhab, H. A.; Fares, Y., Molecular principles of metastasis: a hallmark of cancer revisited. *Signal Transduct. Target. Ther.* **2020,** *5* (1), 28.

(5) Hanahan, D., Hallmarks of Cancer: New Dimensions. *Cancer Discov.* **2022,** *12* (1), 31-46.

(6) Scott, E. C.; Baines, A. C.; Gong, Y.; Moore, R.; Pamuk, G. E.; Saber, H.; Subedee, A.; Thompson, M. D.; Xiao, W.; Pazdur, R.; Rao, V. A.; Schneider, J.; Beaver, J. A., Trends in the approval of cancer therapies by the FDA in the twenty-first century. *Nat. Rev. Drug Discovery* **2023**.

(7) Miller, K. D.; Nogueira, L.; Devasia, T.; Mariotto, A. B.; Yabroff, K. R.; Jemal, A.; Kramer, J.; Siegel, R. L., Cancer treatment and survivorship statistics, 2022. *CA. Cancer J. Clin.* **2022,** *72* (5), 409-436.

(8) Schaue, D.; McBride, W. H., Opportunities and challenges of radiotherapy for treating cancer. *Nat. Rev. Clin. Oncol.* **2015,** *12* (9), 527-540.

(9) Schirrmacher, V., From chemotherapy to biological therapy: A review of novel concepts to reduce the side effects of systemic cancer treatment (Review). *Int. J. Oncol.* **2019,** *54* (2), 407-419.

(10) Galluzzi, L.; Aryankalayil, M. J.; Coleman, C. N.; Formenti, S. C., Emerging evidence for adapting radiotherapy to immunotherapy. *Nat. Rev. Clin. Oncol.* **2023**.

(11) Davis, M. E.; Chen, Z.; Shin, D. M., Nanoparticle therapeutics: an emerging treatment modality for cancer. *Nat. Rev. Drug Discovery* **2008,** *7* (9), 771-782.

(12) Blanco, E.; Shen, H.; Ferrari, M., Principles of nanoparticle design for overcoming biological barriers to drug delivery. *Nat. Biotechnol.* **2015,** *33* (9), 941-951.

(13) Guerrini, G.; Magrì, D.; Gioria, S.; Medaglini, D.; Calzolai, L., Characterization of nanoparticles-based vaccines for COVID-19. *Nat. Nanotechnol.* **2022,** *17* (6), 570-576.

(14) Anselmo, A. C.; Mitragotri, S., Nanoparticles in the clinic: An update. *Bioeng. transl. med.* **2019,** *4* (3), e10143.

(15) Wilhelm, S.; Tavares, A. J.; Dai, Q.; Ohta, S.; Audet, J.; Dvorak, H. F.; Chan, W. C. W., Analysis of nanoparticle delivery to tumours. *Nat. Rev. Mater.* **2016,** *1* (5), 16014.

(16) Matsumura, Y.; Maeda, H., A New Concept for Macromolecular Therapeutics in Cancer Chemotherapy: Mechanism of Tumoritropic Accumulation of Proteins and the Antitumor Agent Smancs1. *Cancer Res.* **1986,** *46* (12_Part_1), 6387-6392.

(17) Davis, M. E.; Chen, Z. G.; Shin, D. M., Nanoparticle therapeutics: an emerging treatment modality for cancer. *Nat. Rev. Drug Discov.* **2008,** *7* (9), 771-82.

(18) Chapman, S.; Dobrovolskaia, M.; Farahani, K.; Goodwin, A.; Joshi, A.; Lee, H.; Meade, T.; Pomper, M.; Ptak, K.; Rao, J.; Singh, R.; Sridhar, S.; Stern, S.; Wang, A.; Weaver, J. B.; Woloschak, G.; Yang, L., Nanoparticles for cancer imaging: The good, the bad, and the promise. *Nano Today* **2013,** *8* (5), 454-460.

(19) Zhang, G.; Yang, Z.; Lu, W.; Zhang, R.; Huang, Q.; Tian, M.; Li, L.; Liang, D.; Li, C., Influence of anchoring ligands and particle size on the colloidal stability and in vivo biodistribution of polyethylene glycol-coated gold nanoparticles in tumor-xenografted mice. *Biomater.* **2009,** *30* (10), 1928-1936.

(20) Liu, D.; Poon, C.; Lu, K.; He, C.; Lin, W., Self-assembled nanoscale coordination polymers with trigger release properties for effective anticancer therapy. *Nat. Commun.* **2014,** *5* (1), 4182.

(21) Bobo, D.; Robinson, K. J.; Islam, J.; Thurecht, K. J.; Corrie, S. R., Nanoparticle-Based Medicines: A Review of FDA-Approved Materials and Clinical Trials to Date. *Pharm. Res.* **2016,** *33* (10), 2373-2387.

(22) Yang, J.; Wang, X.; Wang, B.; Park, K.; Wooley, K.; Zhang, S., Challenging the fundamental conjectures in nanoparticle drug delivery for chemotherapy treatment of solid cancers. *Adv. Drug Delivery Rev.* **2022,** *190*, 114525.

(23) Min, Y.; Caster, J. M.; Eblan, M. J.; Wang, A. Z., Clinical Translation of Nanomedicine. *Chem. Rev.* **2015,** *115* (19), 11147-11190.

(24) Chauhan, V. P.; Stylianopoulos, T.; Boucher, Y.; Jain, R. K., Delivery of Molecular and Nanoscale Medicine to Tumors: Transport Barriers and Strategies. *Annu. Rev. Chem. Biomol. Eng.* **2011,** *2* (1), 281-298.

(25) Subhan, M. A.; Yalamarty, S. S.; Filipczak, N.; Parveen, F.; Torchilin, V. P., Recent Advances in Tumor Targeting via EPR Effect for Cancer Treatment. *J. Pers. Med.* **2021,** *11* (6).

(26) Minchinton, A. I.; Tannock, I. F., Drug penetration in solid tumours. *Nat. Rev. Cancer* **2006,** *6* (8), 583-592.

(27) Heldin, C.-H.; Rubin, K.; Pietras, K.; Östman, A., High interstitial fluid pressure — an obstacle in cancer therapy. *Nat. Rev. Cancer* **2004,** *4* (10), 806-813.

(28) Ni, K.; Luo, T.; Nash, G. T.; Lin, W., Nanoscale Metal–Organic Frameworks for Cancer Immunotherapy. *Acc. Chem. Res.* **2020,** *53* (9), 1739-1748.

(29) Ni, K.; Lan, G.; Lin, W., Nanoscale Metal–Organic Frameworks Generate Reactive Oxygen Species for Cancer Therapy. *ACS Cent. Sci.* **2020,** *6* (6), 861-868.

(30) Lan, G.; Ni, K.; Lin, W., Nanoscale metal–organic frameworks for phototherapy of cancer. *Coord. Chem. Rev.* **2019,** *379*, 65-81.

(31) Lu, K.; Aung, T.; Guo, N.; Weichselbaum, R.; Lin, W., Nanoscale Metal–Organic Frameworks for Therapeutic, Imaging, and Sensing Applications. *Adv. Mater.* **2018,** *30* (37), 1707634.

(32) Spiotto, M.; Feldman, L. E.; Luke, J. J.; Fleming, G. F.; Olson, D.; Moroney, J. W.; Nanda, R.; Rosenberg, A.; Pearson, A. T.; Juloori, A.; Weinberg, F.; Ray, C.; Gaba, R. C.; Chang, P. J.; Janisch, L. A.; Xu, Z.-Q.; Lin, W.; Weichselbaum, R. R.; Chmura, S. J., A phase 1 dose-escalation study of RiMO-301 with palliative radiation in advanced tumors. *J. Clin. Oncol.* **2023,** *41* (16_suppl), 2527-2527.

(33) Xu, Z.; Luo, T.; Lin, W., Nanoscale Metal–Organic Layers for Biomedical Applications. *Acc. Mater. Res.* **2021,** *2* (10), 944-953.

(34) Cao, L.; Wang, C., Metal–Organic Layers for Electrocatalysis and Photocatalysis. *ACS Cent. Sci.* **2020,** *6* (12), 2149-2158.

(35) Cao, L.; Wang, T.; Wang, C., Synthetic Strategies for Constructing Two-Dimensional Metal-Organic Layers (MOLs): A Tutorial Review. *Chin. J. Chem.* **2018,** *36* (8), 754-764.

(36) Song, Y.; Pi, Y.; Feng, X.; Ni, K.; Xu, Z.; Chen, J. S.; Li, Z.; Lin, W., Cerium-Based Metal–Organic Layers Catalyze Hydrogen Evolution Reaction through Dual Photoexcitation. *J. Am. Chem. Soc.* **2020,** *142* (15), 6866-6871.

(37) Cao, L.; Lin, Z.; Shi, W.; Wang, Z.; Zhang, C.; Hu, X.; Wang, C.; Lin, W., Exciton Migration and Amplified Quenching on Two-Dimensional Metal–Organic Layers. *J. Am. Chem. Soc.* **2017,** *139* (20), 7020-7029.

(38) Lan, G.; Li, Z.; Veroneau, S. S.; Zhu, Y.-Y.; Xu, Z.; Wang, C.; Lin, W., Photosensitizing Metal–Organic Layers for Efficient Sunlight-Driven Carbon Dioxide Reduction. *J. Am. Chem. Soc.* **2018,** *140* (39), 12369-12373.

(39) Lin, Z.; Thacker, N. C.; Sawano, T.; Drake, T.; Ji, P.; Lan, G.; Cao, L.; Liu, S.; Wang, C.; Lin, W., Metal–organic layers stabilize earth-abundant metal–terpyridine diradical complexes for catalytic C–H activation. *Chem. Sci.* **2018,** *9* (1), 143-151.

(40) Guo, Y.; Shi, W.; Yang, H.; He, Q.; Zeng, Z.; Ye, J.-y.; He, X.; Huang, R.; Wang, C.; Lin, W., Cooperative Stabilization of the [Pyridinium-CO2-Co] Adduct on a Metal–Organic Layer Enhances Electrocatalytic CO2 Reduction. *J. Am. Chem. Soc.* **2019,** *141* (44), 17875-17883.

(41) Lan, G.; Ni, K.; You, E.; Wang, M.; Culbert, A.; Jiang, X.; Lin, W., Multifunctional Nanoscale Metal–Organic Layers for Ratiometric pH and Oxygen Sensing. *J. Am. Chem. Soc.* **2019,** *141* (48), 18964-18969.

(42) Ling, X.; Gong, D.; Shi, W.; Xu, Z.; Han, W.; Lan, G.; Li, Y.; Qin, W.; Lin, W., Nanoscale Metal–Organic Layers Detect Mitochondrial Dysregulation and Chemoresistance via Ratiometric Sensing of Glutathione and pH. *J. Am. Chem. Soc.* **2021,** *143* (3), 1284-1289.

(43) Lan, G.; Ni, K.; Xu, R.; Lu, K.; Lin, Z.; Chan, C.; Lin, W., Nanoscale Metal–Organic Layers for Deeply Penetrating X-ray-Induced Photodynamic Therapy. *Angew. Chem. Int. Ed.* **2017,** *56* (40), 12102-12106.

(44) Nash, G. T.; Luo, T.; Lan, G.; Ni, K.; Kaufmann, M.; Lin, W., Nanoscale Metal–Organic Layer Isolates Phthalocyanines for Efficient Mitochondria-Targeted Photodynamic Therapy. *J. Am. Chem. Soc.* **2021,** *143* (5), 2194-2199.

(45) Lan, G.; Ni, K.; Veroneau, S. S.; Song, Y.; Lin, W., Nanoscale Metal–Organic Layers for Radiotherapy–Radiodynamic Therapy. *J. Am. Chem. Soc.* **2018,** *140* (49), 16971-16975.

(46) Wu, M.-X.; Yang, Y.-W., Metal–Organic Framework (MOF)-Based Drug/Cargo Delivery and Cancer Therapy. *Adv. Mater.* **2017,** *29* (23), 1606134.

(47) Wang, L.; Zheng, M.; Xie, Z., Nanoscale metal–organic frameworks for drug delivery: a conventional platform with new promise. *J. Mater. Chem. B* **2018,** *6* (5), 707-717.

(48) Mallakpour, S.; Nikkhoo, E.; Hussain, C. M., Application of MOF materials as drug delivery systems for cancer therapy and dermal treatment. *Coord. Chem. Rev.* **2022,** *451*, 214262.

(49) Peng, S.; Bie, B.; Sun, Y.; Liu, M.; Cong, H.; Zhou, W.; Xia, Y.; Tang, H.; Deng, H.; Zhou, X., Metal-organic frameworks for precise inclusion of single-stranded DNA and transfection in immune cells. *Nat. Commun.* **2018,** *9* (1), 1293.

(50) Feng, X.; Song, Y.; Lin, W., Dimensional Reduction of Lewis Acidic Metal–Organic Frameworks for Multicomponent Reactions. *J. Am. Chem. Soc.* **2021,** *143* (21), 8184-8192.

(51) Quan, Y.; Shi, W.; Song, Y.; Jiang, X.; Wang, C.; Lin, W., Bifunctional Metal–Organic Layer with Organic Dyes and Iron Centers for Synergistic Photoredox Catalysis. *J. Am. Chem. Soc.* **2021,** *143* (8), 3075-3080.

(52) Ni, K.; Luo, T.; Culbert, A.; Kaufmann, M.; Jiang, X.; Lin, W., Nanoscale Metal–Organic Framework Co-delivers TLR-7 Agonists and Anti-CD47 Antibodies to Modulate Macrophages and Orchestrate Cancer Immunotherapy. *J. Am. Chem. Soc.* **2020,** *142* (29), 12579-12584.

(53) Luo, T.; Fan, Y.; Mao, J.; Jiang, X.; Albano, L.; Yuan, E.; Germanas, T.; Lin, W., Metal-Organic Layer Delivers 5-Aminolevulinic Acid and Porphyrin for Dual-Organelle-Targeted Photodynamic Therapy. *Angew. Chem. Int. Ed.* **2023,** *62* (22), e202301910.

(54) Luo, T.; Nash, G. T.; Jiang, X.; Feng, X.; Mao, J.; Liu, J.; Juloori, A.; Pearson, A. T.; Lin, W., A 2D Nanoradiosensitizer Enhances Radiotherapy and Delivers STING Agonists to Potentiate Cancer Immunotherapy. *Adv. Mater.* **2022,** *34* (39), 2110588.

(55) Linnane, E.; Haddad, S.; Melle, F.; Mei, Z.; Fairen-Jimenez, D., The uptake of metal–organic frameworks: a journey into the cell. *Chem. Soc. Rev.* **2022,** *51* (14), 6065-6086.

(56) Durymanov, M.; Permyakova, A.; Sene, S.; Guo, A.; Kroll, C.; Giménez-Marqués, M.; Serre, C.; Reineke, J., Cellular Uptake, Intracellular Trafficking, and Stability of Biocompatible Metal-Organic Framework (MOF) Particles in Kupffer Cells. *Mol. Pharm.* **2019,** *16* (6), 2315-2325.

(57) Lu, K.; He, C.; Lin, W., Nanoscale Metal–Organic Framework for Highly Effective Photodynamic Therapy of Resistant Head and Neck Cancer. *J. Am. Chem. Soc.* **2014,** *136* (48), 16712-16715.

(58) Lu, K.; He, C.; Lin, W., A Chlorin-Based Nanoscale Metal–Organic Framework for Photodynamic Therapy of Colon Cancers. *J. Am. Chem. Soc.* **2015,** *137* (24), 7600-7603.

(59) Lu, K.; He, C.; Guo, N.; Chan, C.; Ni, K.; Weichselbaum, R. R.; Lin, W., Chlorin-Based Nanoscale Metal–Organic Framework Systemically Rejects Colorectal Cancers via Synergistic Photodynamic Therapy and Checkpoint Blockade Immunotherapy. *J. Am. Chem. Soc.* **2016,** *138* (38), 12502-12510.

(60) Lan, G.; Ni, K.; Veroneau, S. S.; Feng, X.; Nash, G. T.; Luo, T.; Xu, Z.; Lin, W., Titanium-Based Nanoscale Metal–Organic Framework for Type I Photodynamic Therapy. *J. Am. Chem. Soc.* **2019,** *141* (10), 4204-4208.

(61) Luo, T.; Ni, K.; Culbert, A.; Lan, G.; Li, Z.; Jiang, X.; Kaufmann, M.; Lin, W., Nanoscale Metal–Organic Frameworks Stabilize Bacteriochlorins for Type I and Type II Photodynamic Therapy. *J. Am. Chem. Soc.* **2020,** *142* (16), 7334-7339.

(62) Luo, T.; Nash, G. T.; Xu, Z.; Jiang, X.; Liu, J.; Lin, W., Nanoscale Metal–Organic Framework Confines Zinc-Phthalocyanine Photosensitizers for Enhanced Photodynamic Therapy. *J. Am. Chem. Soc.* **2021,** *143* (34), 13519-13524.

(63) Lu, K.; He, C.; Guo, N.; Chan, C.; Ni, K.; Lan, G.; Tang, H.; Pelizzari, C.; Fu, Y.-X.; Spiotto, M. T.; Weichselbaum, R. R.; Lin, W., Low-dose X-ray radiotherapy–radiodynamic therapy via nanoscale metal–organic frameworks enhances checkpoint blockade immunotherapy. *Nat. Biomed. Eng.* **2018,** *2* (8), 600-610.

(64) Xu, Z.; Ni, K.; Mao, J.; Luo, T.; Lin, W., Monte Carlo Simulations Reveal New Design Principles for Efficient Nanoradiosensitizers Based on Nanoscale Metal–Organic Frameworks. *Adv. Mater.* **2021,** *33* (40), 2104249.

(65) Ni, K.; Lan, G.; Chan, C.; Quigley, B.; Lu, K.; Aung, T.; Guo, N.; La Riviere, P.; Weichselbaum, R. R.; Lin, W., Nanoscale metal-organic frameworks enhance radiotherapy to potentiate checkpoint blockade immunotherapy. *Nat. Commun.* **2018,** *9* (1), 2351.

(66) Ni, K.; Lan, G.; Guo, N.; Culbert, A.; Luo, T.; Wu, T.; Weichselbaum, R. R.; Lin, W., Nanoscale metal-organic frameworks for x-ray activated in situ cancer vaccination. *Sci. Adv.* **2020,** *6* (40), eabb5223.

Chapter 2. Nanoscale Metal-Organic Frameworks Stabilize Bacteriochlorins for Type-I and Type-II Photodynamic Therapy

2.1 Introduction

PDT is a minimally invasive and effective local therapy for some cancers,[1-5] but its clinical utility is limited by side effects from photosensitivity caused by residual PSs in normal tissues, shallow light penetration, and low oxygen concentrations in hypoxic tumors.[6-8] As highly reduced derivatives of porphyrins and chlorins, bacteriochlorins possess several distinct features to overcome the challenges faced by conventional PSs: 1) weak absorption in the visible spectrum minimizes photosensitivity from ambient light, 2) strong absorption in the near-infrared region (700-850 nm) increases PDT efficacy, and 3) type-I PDT tolerates hypoxia.[9-11] Padeliporfin, a Pd-coordinated bacteriochlorin, was approved in Europe for PDT treatment of prostate cancer.[12] However, bacteriochlorins are unstable toward oxygen and light,[13-15] significantly reducing their potency in PDT.[16-18]

In this chapter, we report the use of nMOFs to stabilize bacteriochlorins for effective PDT. Experimental and computational studies demonstrated the stabilization of 5,10,15,20-tetra(*p*-benzoato)bacteriochlorin (TBB) ligands in the Zr-TBB nMOF toward oxygen and light owing to geometrical constraint by the framework. Zr-TBB mediated effective PDT via both type-I and type-II mechanisms by generating various ROS, including superoxide anion (O_2^-), hydrogen peroxide (H_2O_2), hydroxyl radicals (·OH), and singlet oxygen ($^1O_2$), upon irradiation at 740 nm (**Figure 2-1**). Zr-TBB showed superb *in vivo* antitumor efficacy on 4T1 and MC38 mouse models of breast and colon cancers to afford cure rates of 40% and 60%, respectively.

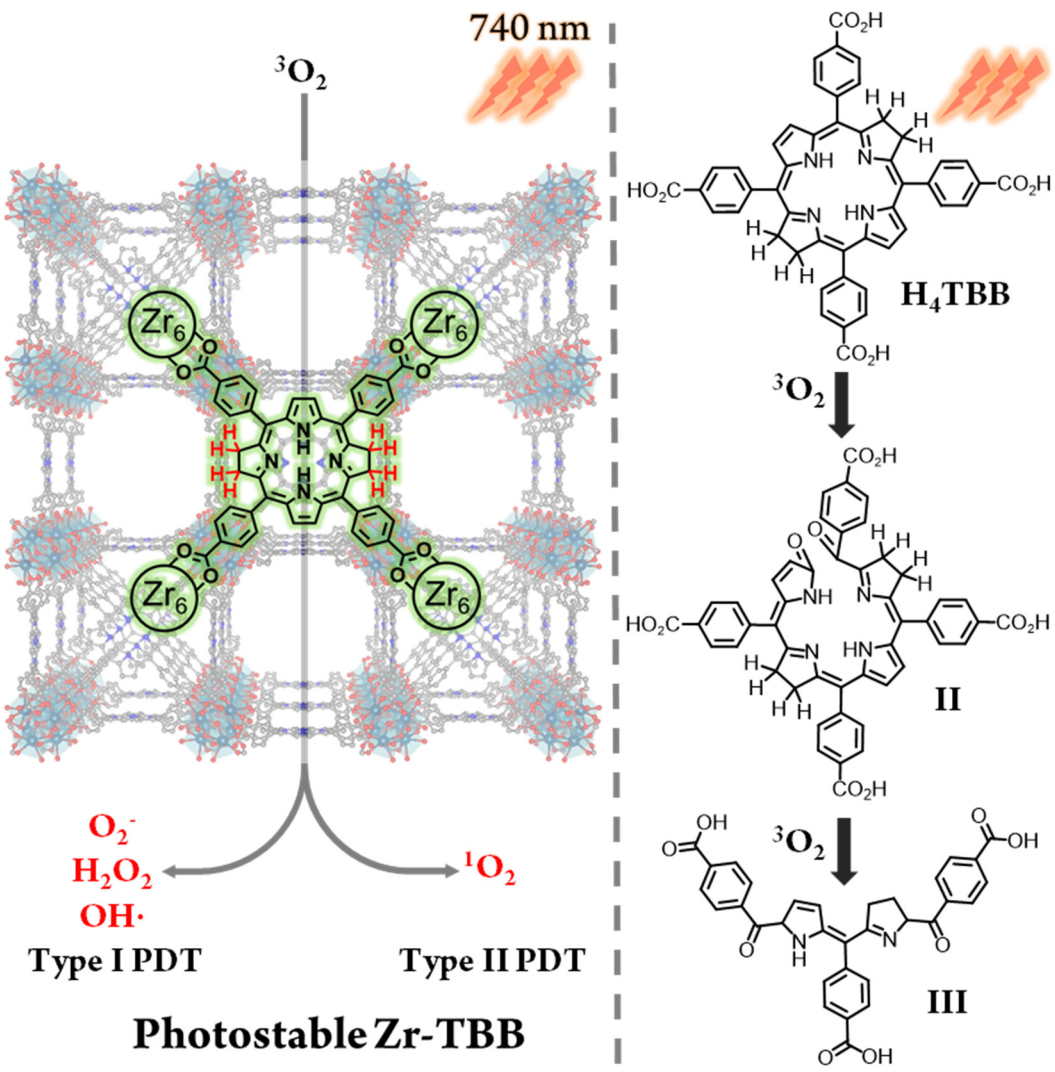

Figure 2-1. Stabilization of bacteriochlorin in nMOF for type-I and type-II PDT.

2.2 Results and Discussion

2.2.1 Synthesis and Characterization of H_4TBB

The new bacteriochlorin H_4TBB was synthesized via solvent-free reduction of 5,10,15,20-tetra(*p*-benzoato)porphyrin (H_4TBP) with *p*-toluenesulfonyl hydrazide (**Figure 2-2a,b**).[19] The ultraviolet-visible (UV-Vis) spectrum of H_4TBB in *N,N*-dimethylformamide (DMF) exhibited four major peaks (**Figure 2-2c**) assignable to the transitions from two HOMOs (HOMO-1 and HOMO)

to two LUMOs (LUMO and LUMO+1) based on the four-orbital model.[20] For H_4TBB, the B_y peak at λ_{max} = 361 nm had a molar extinction coefficient (ε) of 70.4 $mM^{-1}\cdot cm^{-1}$ whereas the B_x peak at λ_{max} = 377 nm had an ε of 73.4 $mM^{-1}\cdot cm^{-1}$. These ε values are ~4 times lower than those of Soret bands in H_4TBP (ε_{420} = 460 $mM^{-1}\cdot cm^{-1}$) and 5,10,15,20-tetra(*p*-benzoato)chlorin (H_4TBC, ε_{420} = 381 $mM^{-1}\cdot cm^{-1}$), suggesting that H_4TBB might alleviate photosensitivity side effects from ambient light.[21] The Q_x and Q_y peaks of H_4TBB had an ε_{521} of 32.4 $mM^{-1}\cdot cm^{-1}$ and an ε_{742} of 58.4$mM^{-1}\cdot cm^{-1}$, respectively. The Q_y peak of H_4TBB at 742 nm is nearly ideal for tissue penetration, and H_4TBB has ~12 and ~2 times higher ε values than those of H_4TBP and H_4TBC, respectively.[21] H_4TBB is thus a superior PS over H_4TBP and H_4TBC with an optimal Q_y wavelength and a much higher ε.[22]

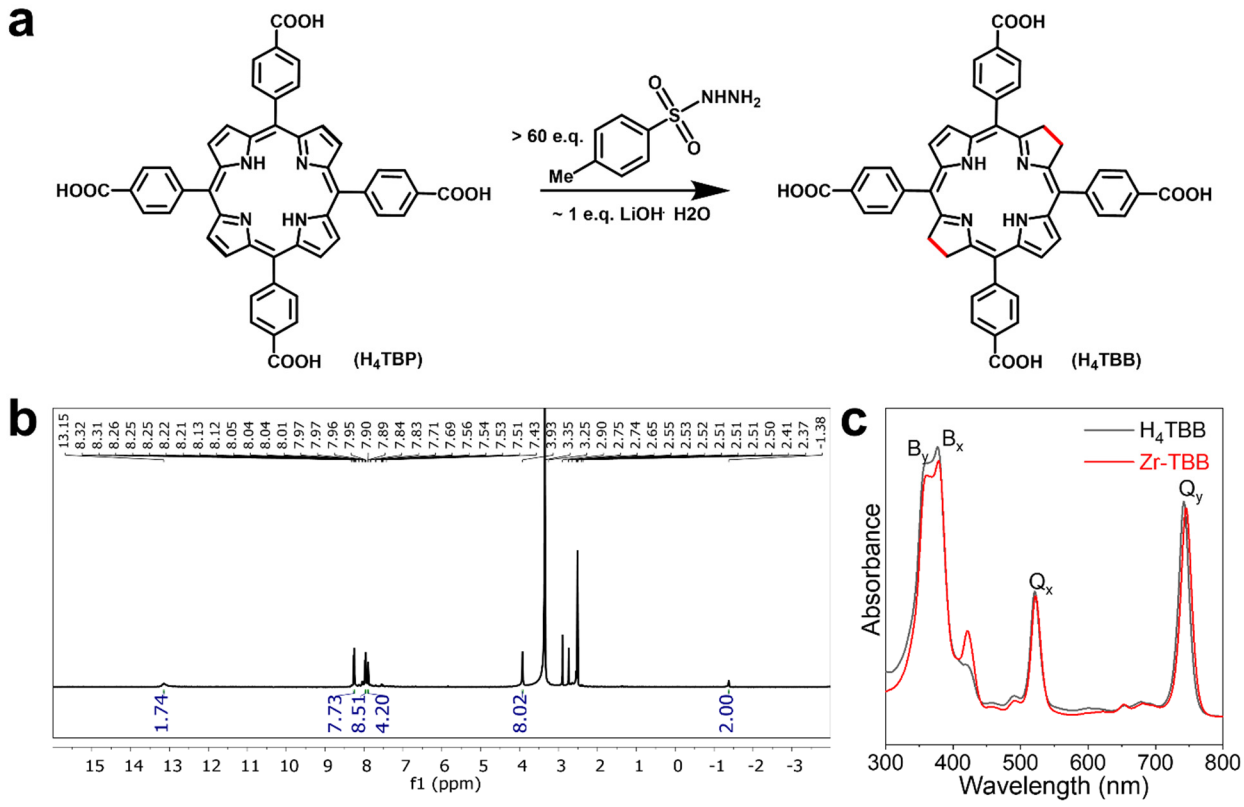

Figure 2-2. Synthesis and characterization of H_4TBB. (a) Synthesis of H_4TBB. (b) ^{1}H-Nuclear magnetic resonance (NMR) spectra of H_4TBB in D_6-dimethyl sulfoxide (D_6-DMSO). (c) UV-Vis spectra of H_4TBB and Zr-TBB in DMF.

2.2.2 Synthesis and Characterization of Zr-TBB nMOF

Zr-TBB was synthesized via a solvothermal reaction of $ZrCl_4$, H_4TBB, and 88% formic acid in DMF at 100 ℃ under anaerobic conditions. Single crystal X-ray diffraction of a Zr-TBB analogue, Hf-TBB, revealed a PCN-224 structure in the $Im\bar{3}m$ space group with $Hf_6(\mu_3\text{-}O)_4(\mu_3\text{-}OH)_4$ SBUs linked by TBB ligands to afford a 3-D framework of *she* topology (**Figure 2-3a** and **Table 2-1**).[23] Powder X-ray diffraction pattern (PXRD) studies indicated that Zr-TBB adopted the same structure as the Hf-TBB single crystal (**Figure 2-3b**) with a formula of $[Zr_6(\mu_3\text{-}O)_4(\mu_3\text{-}OH)_4(OH)_6(H_2O)_6]_2(TBB)_3$. Inductively coupled plasma-mass spectrometry (ICP-MS) and UV-Vis spectra gave a Zr to TBB ratio of 4.22, which is slightly lower than the theoretical ratio of 4, likely due to the presence of defects in the nMOF and slight decomposition of TBB ligands during nMOF synthesis.

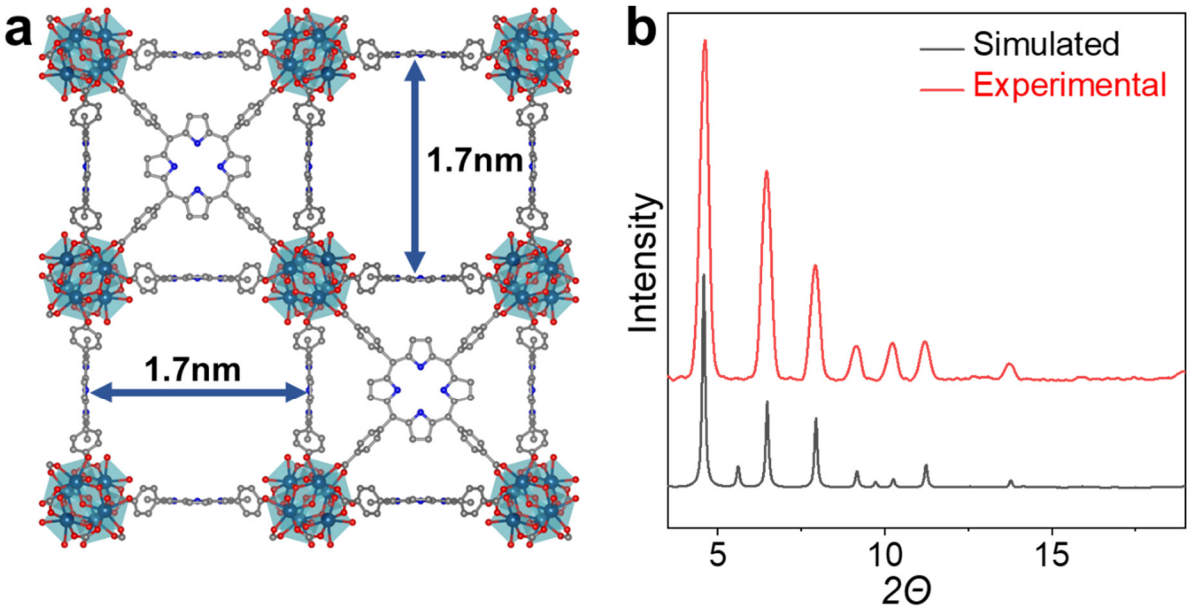

Figure 2-3. Structure and PXRD of Zr-TBB. (a) X-ray crystal structure of Zr-TBB (Cyan: Hf, red: O, gray: C, blue: N). (b) PXRD pattern of Zr-TBB and simulated PCN-224 structure.

Table 2-1. Crystallographic information of Hf-TBB

Name	**Hf-TBB**
Empirical formula	$C_{72}H_{45}Hf_6N_6O_{32}$
Formula weight	2577.08
Temperature/K	100
Crystal system	trigonal
Space group	$Im\bar{3}m$
a/Å	38.585(10)
b/Å	38.585 (10)
c/Å	38.585(10)
α/°	90
β/°	90
γ/°	90
Volume/Å^3	57444(43)
Z	8
ρ_{calc}g/cm^3	0.596
μ/mm^{-1}	0.550
F(000)	9608.0
2Θ range for data collection/°	1.504 to 17.752
Index ranges	$-28 \leq h \leq 28$, $-28 \leq k \leq 28$, $-27 \leq l \leq 28$
Reflections collected	1458115
Independent reflections	1252 [R_{int} = 0.1618, R_{sigma} = 0.0235]
Data/restraints/parameters	11100/1137/658
Goodness-of-fit on F^2	1.187
Final R indexes [I>=2σ (I)]	R_1 = 0.1041, wR_2 = 0.2388
Final R indexes [all data]	R_1 = 0.1104, wR_2 = 0.2417
Largest diff. peak/hole / e Å^{-3}	1.28/-0.92
CCDC No.	1985562

Dynamic light scattering (DLS) of Zr-TBB revealed a number-averaged size of 117.9 ± 1.4 nm, with a polydispersity index of 0.09 (**Figure 2-4a**). Transmission electron microscopy (TEM) imaging (**Figure 2-4b**) revealed spherical/cubic morphology for Zr-TBB with a diameter of approximately 100 nm. High-resolution TEM (HR-TEM) imaging gave a lattice spacing of 1.7 nm for Zr-TBB, while the fast Fourier transform (FFT) patterns (**Figure 2-4c**) revealed the tetragonal symmetry, consistent with projection down the crystallographic axis (**Figure 2-3a**). Additionally, the UV-Vis spectrum of Zr-TBB showed the same number of peaks as H_4TBB (**Figure 2-2c**), with the appearance of a small TBC Soret peak at ~422 nm due to slight oxidation of TBB (4%) during nMOF synthesis.

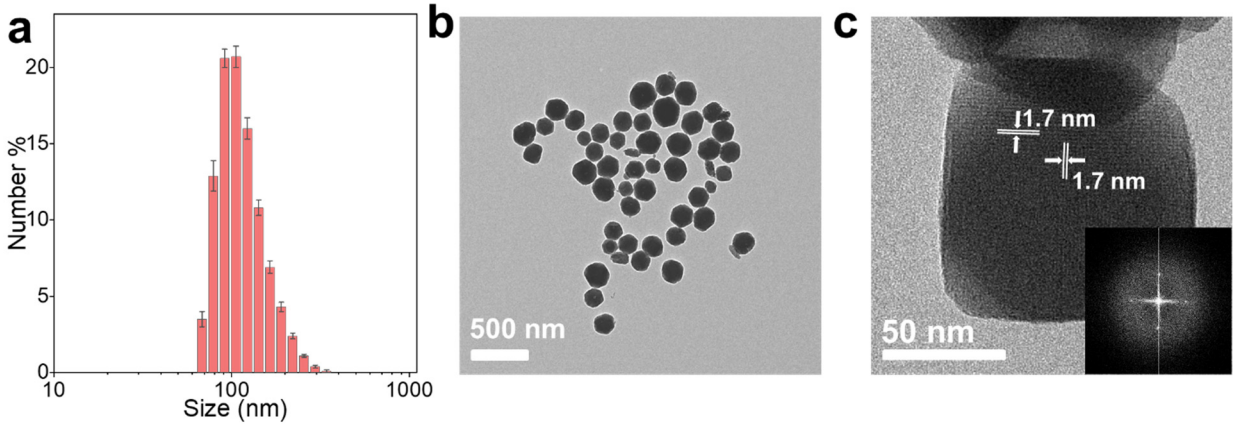

Figure 2-4. DLS and TEM of Zr-TBB. (a) Number-averaged diameter of Zr-TBB in ethanol by DLS. (b) TEM image and (c) HR-TEM image and FFT pattern (inset).

2.2.3 Stabilization of Bacteriochlorin by Zr-TBB nMOF

Photostability of H_4TBB and Zr-TBB was tested in air-saturated DMF at a 5 μM TBB concentration at 740 nm (100 mW·cm^{-2}). After irradiation for 5 minutes, the Q_y peak absorbance of H_4TBB dropped to <4% of the original value, indicating its severe photobleaching (**Figure 2-5**). In contrast, Zr-TBB retained 73% and 65% of the Q_y peak absorbance after light irradiation for 15 and 30 minutes, respectively, indicating its much-enhanced photostability over H_4TBB.

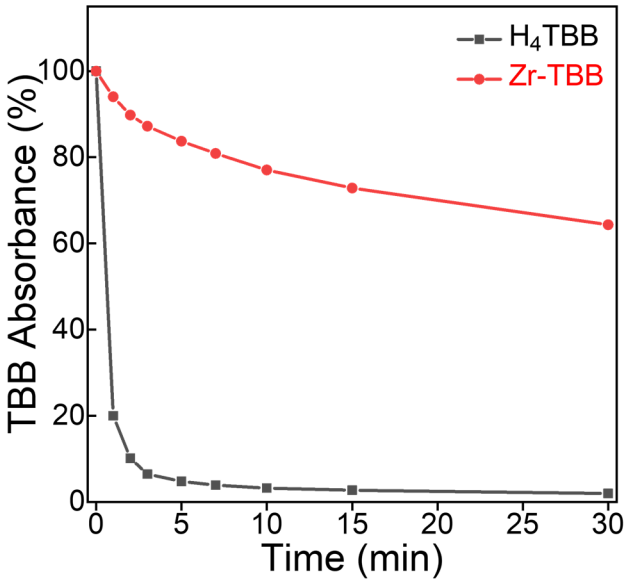

Figure 2-5. Time-dependent UV-Vis absorbance after light irradiation in air-saturated DMF.

The photodecomposition quantum yield of Zr-TBB ($\Phi_{pd} = 8.14 \times 10^{-4}$) was 14 times lower than that of H4TBB ($\Phi_{pd} = 1.15 \times 10^{-2}$, **Table 2-2**). The improved TBB stability of Zr-TBB can be attributed to the spatial constraint of the nMOF framework, which prevents TBB from undergoing structural changes before photooxidation can occur, and the site isolation effect of Zr-TBB which prevents TBB ligands from biomolecular decomposition. [24] We found photostability of Zr-TBB and H4TBB was much improved in oxygen-free conditions (**Table 2-2**), which indicates that photobleaching of TBB is oxygen-dependent.

Table 2-2. $\boldsymbol{\Phi_{pd}}$ and photostability of Zr-TBB and H4TBB in air-saturated conditions or N_2-degassed conditions.

	Zr-TBB air	**H4TBB air**	**Zr-TBB N_2**	**H4TBB N_2**
$\boldsymbol{\Phi_{pd}}$	8.14×10^{-4}	1.15×10^{-2}	3.47×10^{-7}	9.63×10^{-5}
%TBB (90 J/cm^2)	72.9	2.71	98.5	97.3
%TBB (180 J/cm^2)	64.3	1.93	94.7	91.5

We used high-resolution mass spectrometry (HR-MS) to characterize the photobleaching products of Zr-TBB and H_4TBB after 740 nm irradiation (100 mW·cm^{-2}) in air-saturated DMF for 4 h. Photo-irradiated Zr-TBB was digested with 10% H_3PO_4 in DMSO before HR-MS analysis. For H_4TBB, the [H_4TBB+H^+] peak at m/Z=795.2 disappeared with the appearance of [M+H^+] at 563.5 assignable to (Z)-4-(2-((5-(4-carboxy-benzoyl)-1H-pyrrol-2-yl)(4-carboxy-phenyl) methylene)-3,4-dihydro-2H-pyrrole-5-carbonyl)benzoic acid (**III**, **Figure 2-1** and **Figure 2-6**), a known fragmentation product from bacteriochlorin photobleaching.[25] The fragmentation of H_4TBB during photooxidation was supported by the UV-vis spectrum, which showed two new peaks at 327 nm and 406 nm for **III** and the disappearance of all peaks corresponding to H_4TBB (**Figure 2-7a,b**). In contrast, only H_4TBC at m/Z=793.3 ([M+H^+]) was recovered from the digested photo-irradiated Zr-TBB with no evidence of known photo-fragments. TBC can be generated by direct oxidization of the pyrroline ring of TBB without significant structural change on the bacteriochlorin.

UV-Vis spectroscopy was used to quantify photobleaching products of H_4TBB (**Figure 2-7c**) and Zr-TBB (**Figure 2-7d**) after light irradiation for 1-30 minutes. H_4TBB was nearly completely photobleached (95%) within 5 minutes to generate mostly fragmentation product **III** (95%) and a negligible amount of H_4TBC (<0.1%). In contrast, Zr-TBB retained 84% TBB in 5 minutes with the formation of 4% TBC. Only 12% of TBB decomposed into unknown photoproducts. As TBC is also a good PS, TBB retained 80% and 74% PDT efficacy after light irradiation for 15 and 30 minutes, respectively.

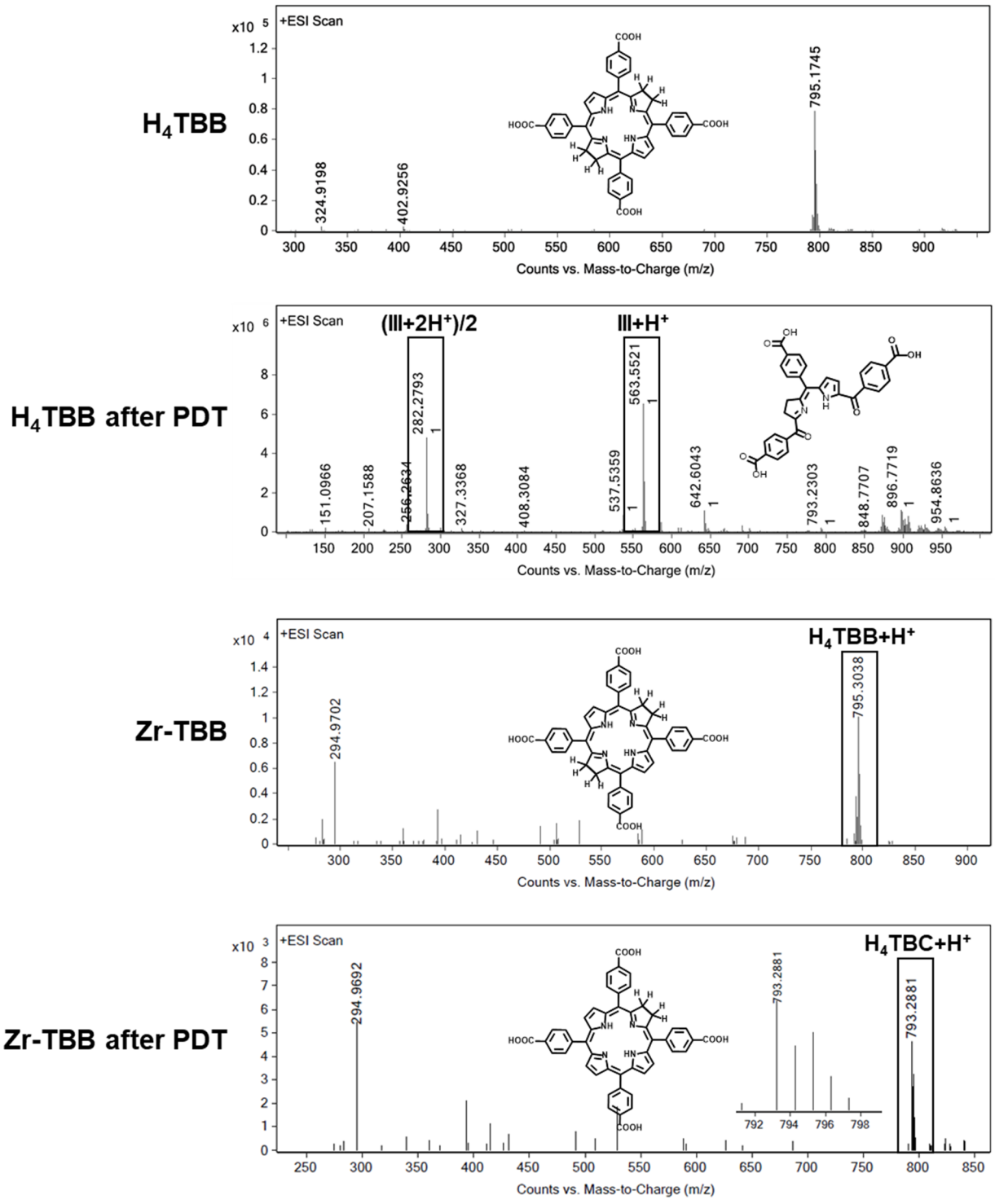

Figure 2-6. MS spectra of photoproducts with or without photobleaching.

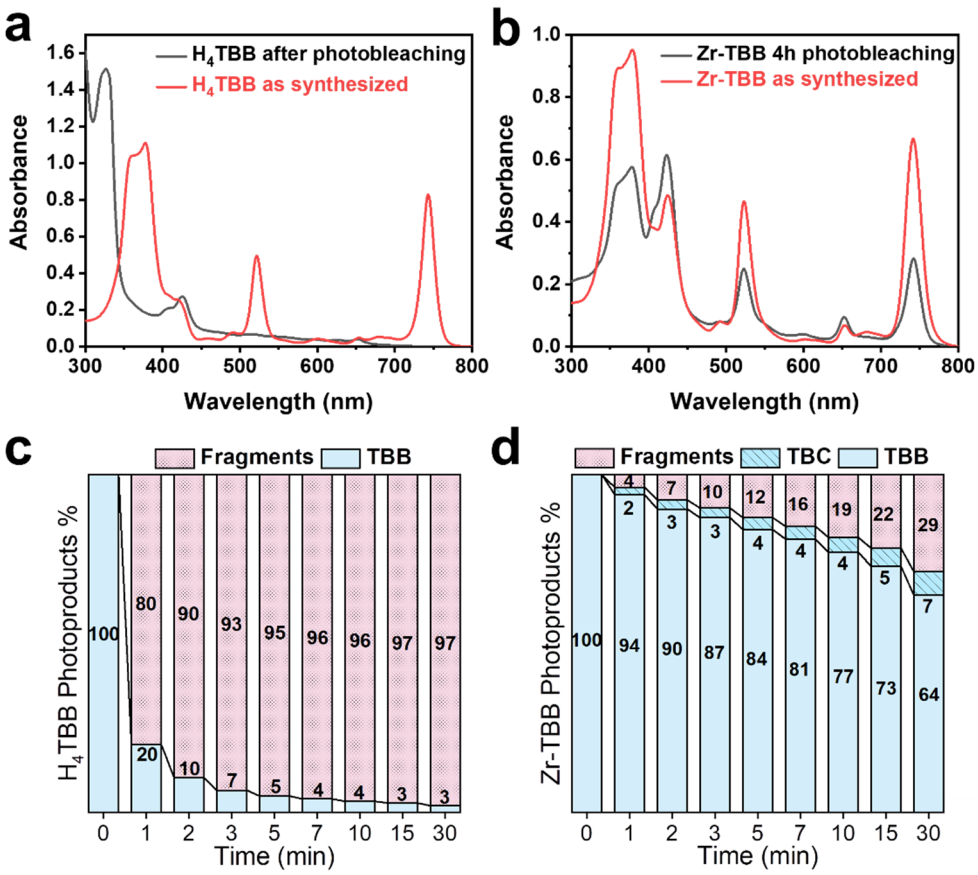

Figure 2-7. Photobleaching of H_4TBB and Zr-TBB. (a) UV-Vis spectra of H_4TBB and its photoproducts. (b) UV-Vis spectra of Zr-TBB and its photoproducts after 4 hours of light irradiation (740 nm, 100 mW cm^{-2}). Percentages of photoproducts (TBB, TBC, fragments) of (c) H_4TBB and (d) Zr-TBB throughout 30-minute light irradiation (740 nm, 100 mW cm^{-2}).

Photobleaching of bacteriochlorins typically starts with [2+2] peroxidation reaction between C=C double bonds and O_2 (**Figure 2-8**).[26] The peroxidized intermediate **I** breaks the Π-conjugated bacteriochlorin ring and converts sp^2-carbons into sp^3-carbons, leading to significant distortion from the planar structure of TBB. The peroxide bridge is cleaved into two ketones in intermediate **II** via retro-[2+2] cyclization. Successive peroxidation and retro-[2+2] cyclization form fragmentation product **III**. However, the rigid framework of Zr-TBB prohibits TBB ligands from undergoing large structural changes, shutting down light-mediated peroxidation pathway. The

pyrroline rings of the bacteriochlorin can still be oxidized to form TBC ligands without disturbing π-conjugation.

Density functional theory (DFT) calculations were performed to support the photostability difference of bacteriochlorins in H_4TBB and Zr-TBB (**Figure 2-8**). The crystal structure of Zr-TBB was used, and the structures of the carboxylate groups were frozen during DFT optimization to mimic spatial constraints in the nMOF. In the calculated energy profiles, H_4TBB displayed a $\Delta G^{\neq}$ of 30.6 kcal/mol (1.33 eV), while the constrained TBB in Zr-TBB exhibited a much higher $\Delta G^{\neq}$ of 39.2 kcal/mol (1.70 eV). The 1.69 eV energy in the 740 nm light source was thus sufficient to overcome the $\Delta G^{\neq}$ in H_4TBB but insufficient to overcome the $\Delta G^{\neq}$ in Zr-TBB, which explained the resistance of Zr-TBB to peroxidation and photo-fragmentation.

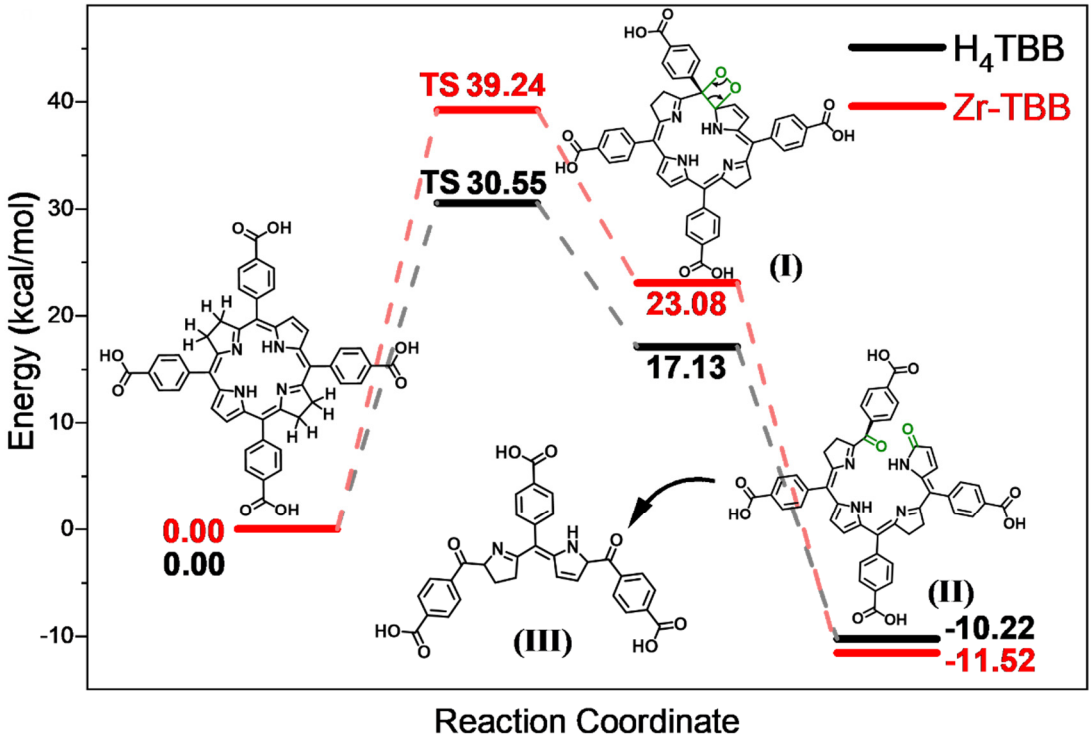

Figure 2-8. Energy profiles of TBB photo-fragmentation calculated by DFT. TS=transition state.

2.2.4 Type-I and Type-II ROS generation

Bacteriochlorins can generate multiple ROS via both type-I (O_2^-, H_2O_2, and ·OH) and type-II ($^1O_2$) mechanisms (**Figure 2-9**).[27] The generation of O_2^-, H_2O_2, ·OH, and $^1O_2$ by H_4TBB and Zr-TBB was confirmed by electron spin resonance (ESR, **Figure 2-10a**), hydrogen peroxide detection (**Figure 2-10b**), aminophenyl fluorescein assay (APF) (**Figure 2-10c**), and singlet oxygen sensor green assay (SOSG) (**Figure 2-10d**), respectively. Due to photobleaching, H_4TBB showed much weaker signals of type-I ROS than Zr-TBB. Similarly, $^1O_2$ generation of H_4TBB reached a plateau within 1 minute of light irradiation, while Zr-TBB showed a linear increase of $^1O_2$ signal throughout the 15-minute experiment.

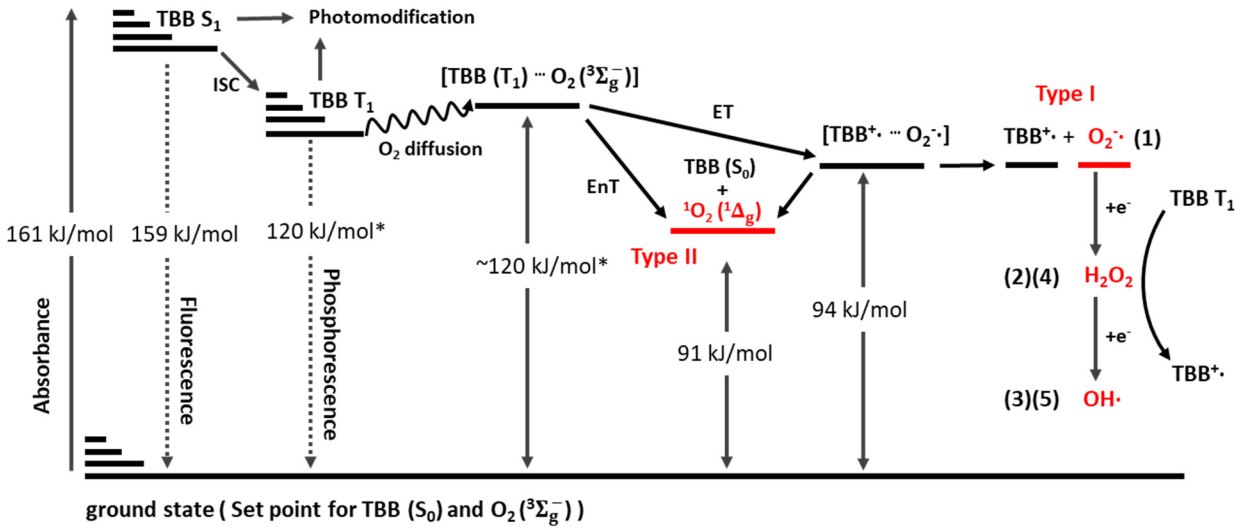

Figure 2-9. Modified Jablonski diagram with type-I and type-II PDT mechanisms for TBB. ET = electron transfer; EnT = energy transfer. The energy levels of TBB S_1, TBB T_1, [TBB (T_1) ··· O_2], [TBB^{+}· ··· O_2^-·], $^1O_2$ are determined by fluorescence, phosphorescence, cyclic voltammogram (CV) of H_4TBB and phosphorescence of singlet oxygen, respectively. (*The phosphorescence of H_4TBB was not observed in this case, thus the value of a similar derivative was used as a reference.[28])

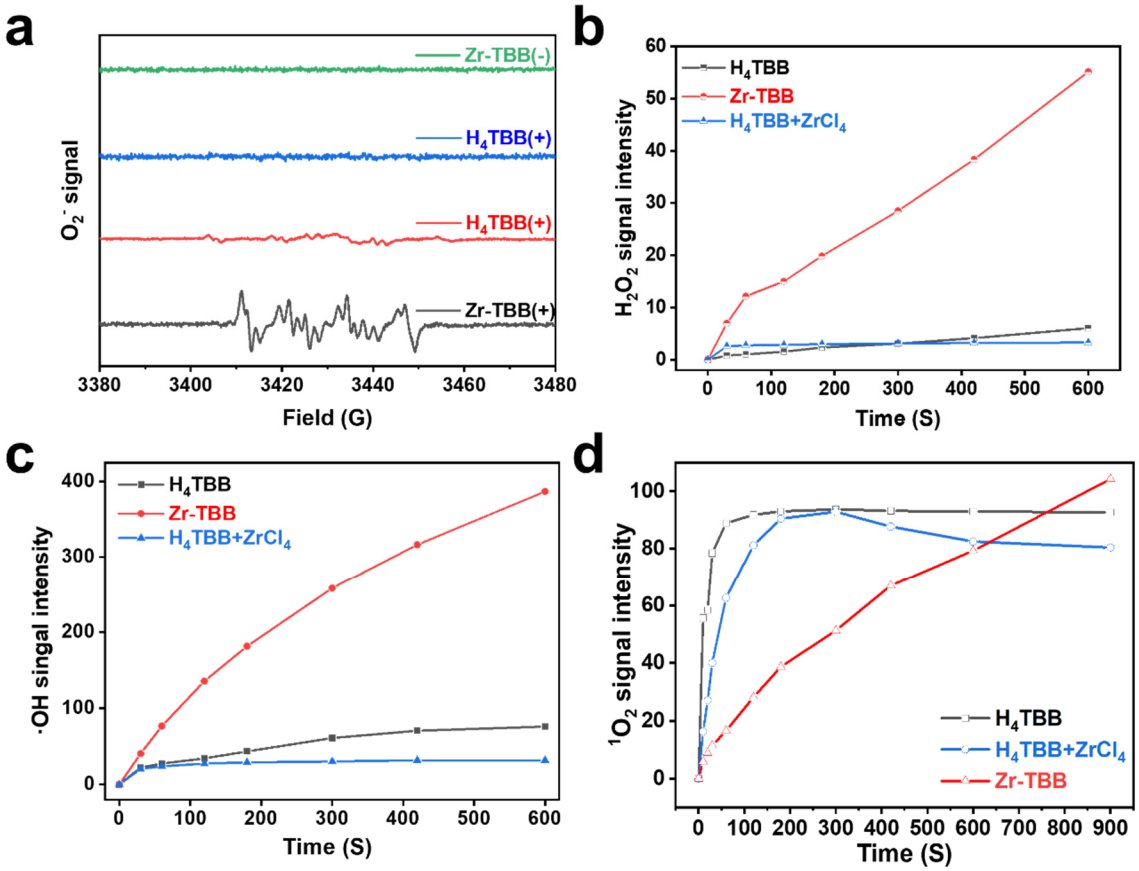

Figure 2-10. Type-I and type-II ROS generation in test tube. (a) ESR signals of 5-tert-butoxycarbonyl 5-methyl-1-pyrroline N-oxide (BMPO) adduct of O_2^{-}. (b) Time-dependent generation of H_2O_2 detected by the hydrogen peroxide detection kit. (c) Time-dependent generation of ·OH detected by APF assay. (d) Time-dependent generation of $^1O_2$ detected by SOSG assay.

The *in vitro* generation of O_2^{-}, H_2O_2, ·OH, and $^1O_2$ by Zr-TBB plus light irradiation [denoted Zr-TBB(+)] was detected under confocal laser scanning microscopy (CLSM) with superoxide detection, intracellular hydrogen peroxide, coumarin-3-carboxylic acid assay and SOSG assay kits, respectively, in murine triple-negative breast cancer 4T1 cells (**Figure 2-11**). The generation of $^1O_2$ and O_2^{-} by Zr-TBB(+) was also confirmed by flow cytometric analyses. H_4TBB(+) generated much less ROS than Zr-TBB(+), likely due to oxidation and photobleaching. Zr-TBB(+) efficiently generated four different kinds of ROS to facilitate type-I and type-II PDT.

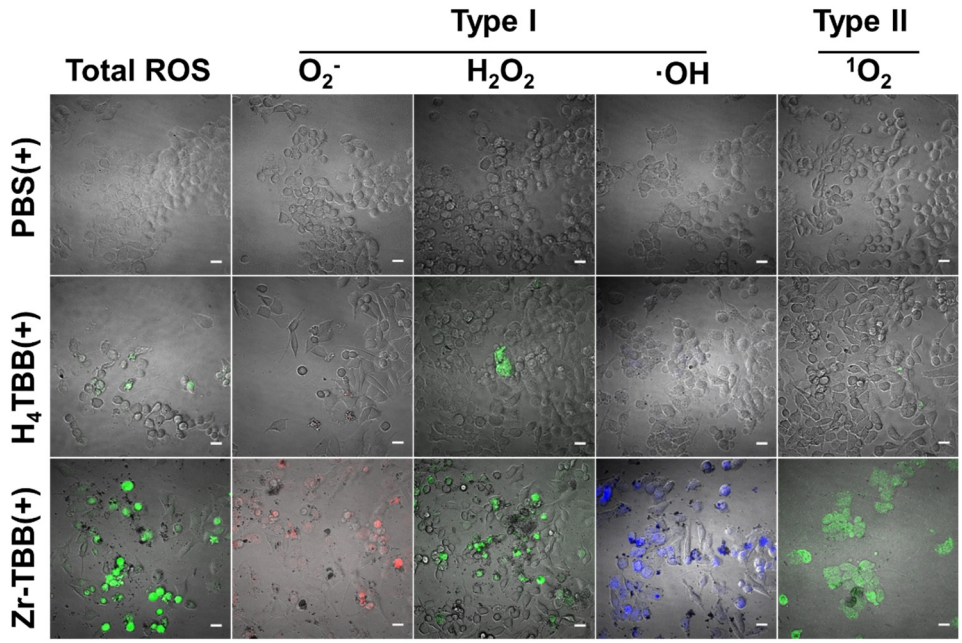

Figure 2-11. Type-I and type-II ROS generation *in vitro*. CLSM images of various ROS species generated in 4T1 cells after light irradiation. Total ROS was detected by 2',7'-dichlorodihydrofluorescein diacetate (DCF-DA) assay. Scale bar is 20 μm. PBS is phosphate-buffered saline.

2.2.5 *In Vitro* Cell Killing under Hypoxia

The cytotoxicity of Zr-TBB(+) was determined by 3-(4,5- dimethylthiazol-2-yl)-5-(3-carboxymethoxyphenyl)-2-(4-sulfo-phenyl)-2H-tetrazolium (MTS) assay. Under normoxic conditions, Zr-TBB(+) exhibited an IC_{50} of 0.91±0.77 μM on 4T1 cells, while H_4TBB(+) did not show any cytotoxicity at ≤20 μM (**Figure 2-12a**). Under hypoxic conditions, the IC_{50} values of Zr-TBB(+) and H_4TBB(+) on 4T1 cells were 2.94±0.76 and 19.50±0.82 μM, respectively (**Figure 2-12b**). The increased cytotoxicity of H_4TBB(+) under hypoxia likely resulted from reduced photobleaching at low O_2 concentration.

The apoptosis of 4T1 cells after PDT treatments was evaluated by flow cytometry with Annexin-V and propidium iodide (PI) staining. Zr-TBB(+) treated cells gave significantly stronger apoptosis signals than those treated with H_4TBB(+) and PBS(+) (**Figure 2-12c**).

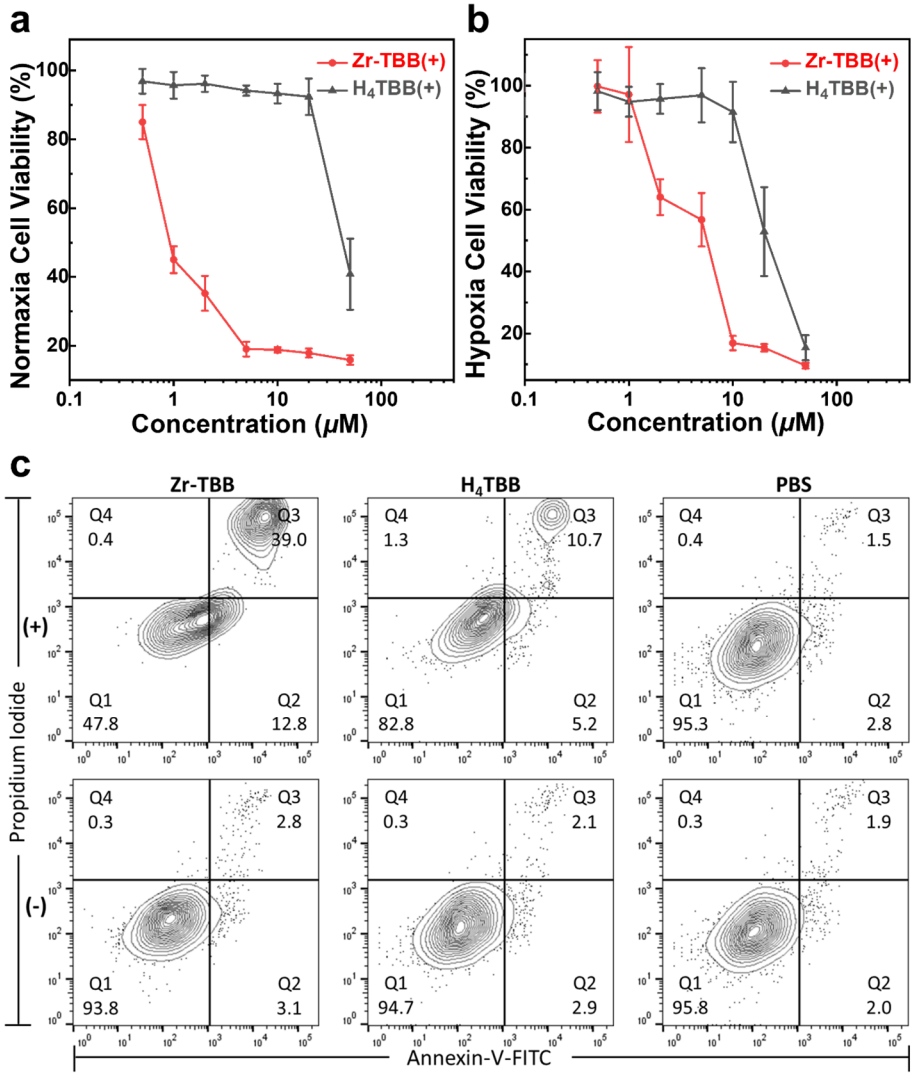

Figure 2-12. *In vitro* cytotoxicity and apoptosis. MTS assays of Zr-TBB(+) and H_4TBB(+)-treated 4T1 cells under (a) normoxic and (b) hypoxic conditions. (c) Flow cytometry analysis of apoptosis status of 4T1 cells 24 hours after irradiation. Q1, Q2, Q3, and Q4 indicate normal, early apoptotic, late apoptotic, and necrotic populations among 4T1 cells, respectively. The percentages of each population are shown in each quadrant.

2.2.6 *In Vivo* Antitumor Efficacy

The *in vivo* anti-tumor efficacy was investigated on subcutaneous 4T1 tumor-bearing BALB/c mice and murine colon carcinoma MC38 tumor-bearing C57BL/6 mice. Zr-TBB(+) exhibited excellent therapeutic effects to afford 91% tumor growth inhibition and a 40% cure rate on the

4T1 model (**Figure 2-13a**) and 97% tumor growth inhibition and a 60% cure rate on the MC38 model (**Figure 2-13b**). Hematoxylin-eosin (H&E) staining showed severe necrosis in Zr-TBB(+) treated 4T1 tumors. Terminal deoxynucleotidyl transferase biotin-dUTP nick end labeling (TUNEL) and Calreticulin (CRT) expression (**Figure 2-13c**) assays by CLSM showed strong apoptosis and immunogenic cell death (ICD) induced by Zr-TBB(+) treatment. Finally, steady body weight indicated that Zr-TBB had no systematic toxicity on BALB/c and C57BL/6 mice (**Figure 2-14**).

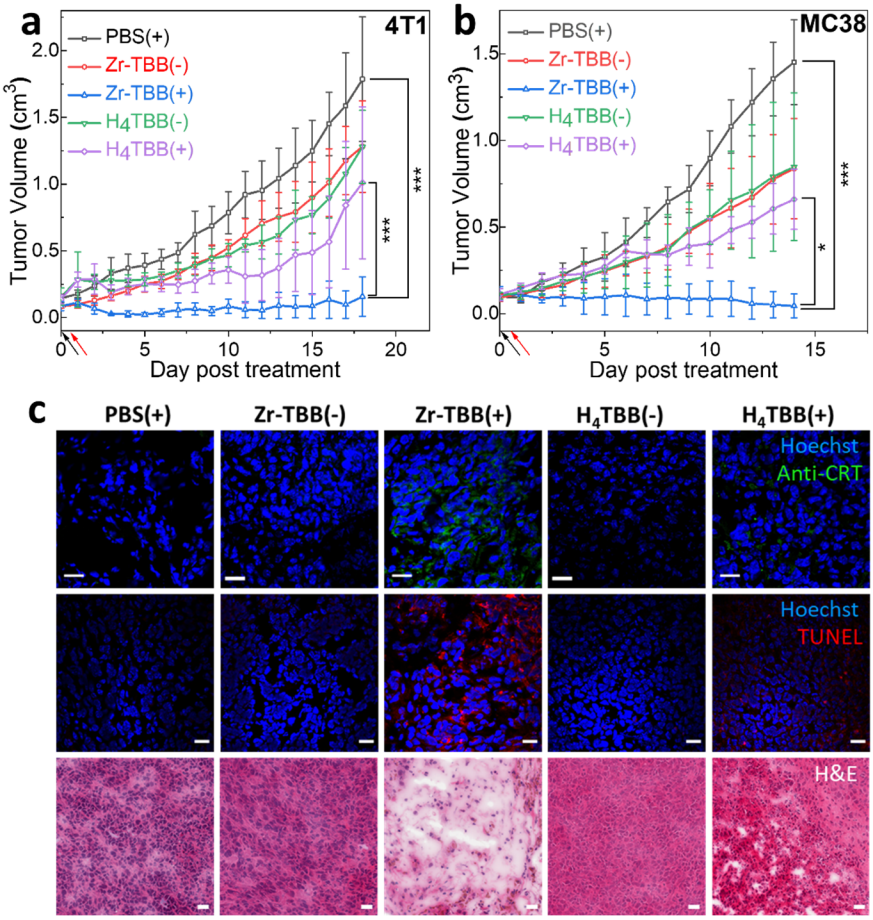

Figure 2-13**.** *In vivo* antitumor efficacy. Antitumor efficacy on (a) 4T1 bearing BALB/c mice and (b) MC38 bearing C57BL/6 mice (*N*=5, the black arrow indicates particle injection, and the red arrow indicates PDT treatment). (c) CLSM imaging of cell surface CRT (top) and cell apoptosis (middle) and H&E staining showing severe apoptosis and necrosis (bottom) after Zr-TBB(+) treatment on 4T1 tumors. Scale bar is 20 μm.

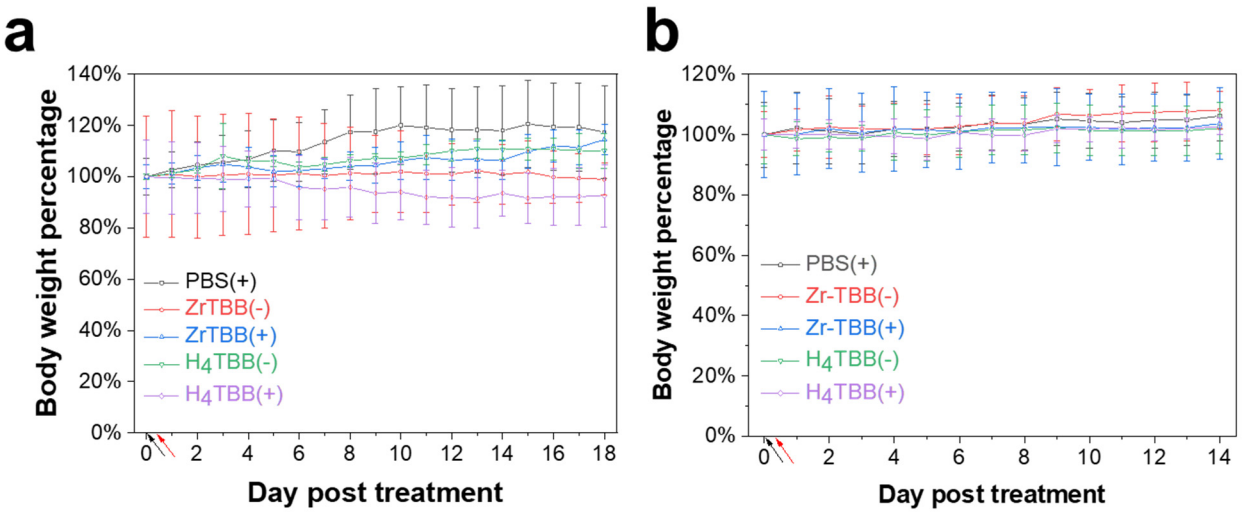

Figure 2-14. Body weights of tumor-bearing mice after treatment. (a) Relative body weights of treated BALB/c mice. (b) Relative body weights of treated C57BL/6 mice (The black arrow indicates injection of particles, and the red arrow indicates 740nm 100 mW cm^{-2} light-emitting diode (LED) light irradiation for 15 minutes).

2.3 Conclusion

In this Chapter, we report the use of Zr-TBB framework to stabilize bacteriochlorins toward oxygen and light irradiation. Zr-TBB mediated effective PDT by generating O_2^-, H_2O_2, ·OH, and $^1O_2$ via both type-I and type-II mechanisms. Zr-TBB showed superb *in vivo* antitumor efficacy on mouse tumor models of breast and colon cancers to afford cure rates of 40% and 60%, respectively. nMOFs thus present a unique platform to design novel nanophotosensitizers based on bacteriochlorins and other unstable photosensitizing molecules.

2.4 Methods

Synthesis of H_4TBB. H_4TBP was synthesized as previously reported with modifications.[21] Inside a glove box, 0.90 g of H_4TBP, 6.30 g of p-toluenesulfonyl hydrazide ($TsNHNH_2$) (~30 e.q.), and 46 mg of $LiOH·H_2O$ (1 e.q.) were mixed and ground into fine powder (gray). The solid was

added into a Schlenk flask and sealed with a rubber stopper. The flask was taken out of the glove box and evacuated for 4 hours. The mixture was then covered with Al foil and heated at 133 °C in an oil bath under vacuum for 12 hours. After the reaction mixture cooled to room temperature, an additional 6.3 g of $TsNHNH_2$ (~30 e.q.) was added into the flask and sealed, evacuated, and heated in the same fashion as the previous step. The black and sticky crude product was dispersed in dichloromethane/acetone (1:3 V/V). The suspension was degassed with N_2 and stirred for 2 hours in the dark and then vacuum filtered. The solid was again dispersed in 1 M HCl, degassed with N_2 and stirred in the dark for 2 hours, and then collected by centrifugation. The product was washed with 1 M N_2-degassed HCl by repeating sonication and centrifugation cycles three times. The product was dried under vacuum and in the dark for 3 days to afford 0.65g (72% yield) of H_4TBB. The purity of thus obtained H_4TBB was 93% with 7% H_4TBC. The powdery sample of H_4TBB was stored without exposing to light in a glovebox at room temperature.

Synthesis of Zr-TBB nMOF. DMF solutions of 1.8 mg/mL $ZrCl_4$ and 2.4 mg/mL H_4TBB were prepared and degassed with N_2. Inside a glovebox, 0.5 mL of each of the above-prepared $ZrCl_4$ and H_4TBB solutions and 20 μL of 88% HCOOH (N_2 degassed) were added to a 1-dram glass vial. The vial was sealed tightly and kept at 100 ℃ for 60 hours. Dark brown Zr-TBB nMOF suspension was obtained and washed with N_2 degassed DMF, 1% triethylamine in EtOH, and EtOH sequentially. The nMOF was dispersed in EtOH, and the yield was 34.7% based on ICP-MS analysis. The percentage of TBC was calculated as 11% from the Q peak of TBC and TBB by UV-Vis spectroscopy, which indicates ~4% TBB was oxidized during nMOF growth.

Synthesis of Hf-TBB single crystals. DMF solutions of 2.0 mg/mL $HfCl_4$ and 2.4 mg/mL H_4TBB were prepared and degassed with N_2. Inside a glovebox, 0.5 mL of each of the above-prepared $HfCl_4$ and H_4TBB solutions and 200 μL 88% HCOOH (N_2 degassed) were added to a 1-

dram glass vial. The vial was sealed tightly and kept at 100 ℃ for 5 days. Dark red square-shaped crystals formed at the bottom of the vial to afford 0.13 mg of Hf-TBB single crystals (5.8% yield). Single crystals of Zr-TBB were obtained similarly but did not diffract X-ray well.

Stabilization of TBB ligands in Zr-TBB. The photostability of Zr-TBB and H_4TBB was studied by UV-Vis spectroscopy and mass spectrometry. Zr-TBB and H_4TBB were dissolved in air-saturated DMF at a TBB concentration of 5 μM. The samples were irradiated under ambient conditions with 100 mW·cm^{-2} 740 nm LED light for 0, 1, 2, 3, 5, 7, 10, 15, and 30 min, and Q_y peak at 742 nm was monitored by UV-Vis spectroscopy, which provided a sensitive measure of relative TBB concentrations. The TBC amount was calculated by the last Q peak of TBC at 653 nm with $\varepsilon_{653,\,TBC}$ = 44.6 mM^{-1}·cm^{-1}. The pre-existed TBC (7% in H_4TBB, 11% in Zr-TBB) were subtracted from the calculation of photoproducts. H_4TBB gave negligible TBC generation during photobleaching (calculated to be less than 0.1%). For oxygen-free conditions, the solution was degassed with nitrogen gas for 1 hour and sealed tightly. The N_2-degassed Zr-TBB and H_4TBB solutions were irradiated with 100 mW·cm^{-2} 740 nm LED light for 0, 5, 10, 15, and 30 min, and the Q_y peaks at 742 nm were monitored.

To further identify the photoproducts by UV- Vis spectra and MS spectra, Zr-TBB and H_4TBB DMF solutions were irradiated with 740 nm LED light (100 mW·cm^{-2}) for 4 hours to reach a thorough photobleaching. The photoproducts were then lyophilized and dispersed in DMSO / 5% H_3PO_4 for the acquisition of MS spectra and UV-Vis spectra. The photodecomposition quantum yield (Φ_{pd}) was calculated by Equation 2-1:

$$\Phi_{pd} = \frac{initial\ rate\ of\ photosensitizer\ disappearance}{initial\ rate\ of\ photon\ absorption} \qquad \text{Eq. } 2-1$$

Where the initial rate of photosensitizer disappearance was calculated from absorbance difference with molar extinction coefficient of TBB, and the initial rate of photon absorption was calculated with initial absorbance and the LED power of 100 $mW \cdot cm^{-2}$.

ROS generation in test tubes. (1) Superoxide generation: Zr-TBB and H_4TBB were respectively suspended in benzyl alcohol at TBB concentrations of 200 μM in the presence of 25 mM BMPO. 500 μL of each suspension was added to ESR tubes and irradiated by 740 nm LED light (100$mW \cdot cm^{-2}$) for 10 mins. The ESR signal of each sample was collected immediately (frequency = 9.6331 GHz) at 293 K on the ESR spectrometer. (2) Hydrogen peroxide generation: A hydrogen peroxide fluorescence detection kit was used to test H_2O_2 generation in an aqueous solution (Emission/Excitation Maximum 490nm/520nm). Zr-TBB, H_4TBB, and H_4TBB plus $ZrCl_4$ (1:1) were dispersed in 2ml water at a TBB concentration of 20 μM in the presence of 1 μL hydrogen peroxide detection kit and then irradiated with 740 nm LED light (100 $mW \cdot cm^{-2}$) for 0, 30, 60, 120, 180, 300, 420, and 600 seconds. Fluorescence intensity was read with a fluorimeter to afford relative concentration for H_2O_2. (3) Hydroxyl radical generation: APF assay was used to test ·OH generation in an aqueous solution (Emission/Excitation Maximum 490nm/515nm). Zr-TBB, H_4TBB, and H_4TBB plus $ZrCl_4$ (1:1) were dispersed in 2 mL water at a TBB concentration of 20 μM and APF at 5 μM, and then irradiated with 740 nm LED light (100 $mW \cdot cm^{-2}$) for 0, 30, 60, 120, 180, 300, 420, 600 seconds. The fluorescence intensity of APF was read by the fluorimeter as ·OH relative intensity. (4) Singlet oxygen generation: SOSG assay was used to test single oxygen generation in an aqueous solution (Emission/Excitation Maximum 504nm/525nm). Zr-TBB, H_4TBB, and H_4TBB plus $ZrCl_4$ (1:1) were dispersed in 2 mL water at a TBB concentration of 20 μM and SOSG at 12.5 μM, and then irradiated with 740nm LED light (100$mW \cdot cm^{-2}$) for 0,

10, 20, 30, 60, 120, 180, 300, 420, 600, and 900 seconds. The fluorescence intensity of SOSG was read by a fluorimeter as $^1O_2$ relative intensity.

ROS generation *in vitro*. Total ROS, singlet oxygen, superoxide, hydrogen peroxide, and hydroxyl radicals were detected by DCF-DA assay, SOSG, superoxide detection kit, intracellular hydrogen peroxide detection kit, and coumarin-3-carboxylic acid, respectively, using confocal laser CLSM imaging. Briefly, 4T1 cells were seeded in a 3.5-cm petri dish and cultured overnight. The cells were incubated with Zr-TBB, H_4TBB, or PBS at a TBB concentration of 20 μM for 4 h, then washed with PBS three times to remove excess Zr-TBB and H_4TBB. Cells were stained with respective dye and incubated for 15 min. The cells were irradiated with LED light (740 nm, 100 mW/cm^2, 15 min). Then the cells were washed with PBS three times to remove excess ROS probes and CLSM was immediately used to visualize various ROS species generated in live cells by detecting the fluorescence signals inside the cells. Singlet oxygen and superoxide generation were also analyzed by flow cytometry with SOSG and superoxide detection kits, respectively.

***In vitro* cytotoxicity.** The cytotoxicity of Zr-TBB and H_4TBB was evaluated by MTS assay (Promega, USA) with or without light irradiation. For the normoxic condition, 4T1 cells were seeded on 96-well plates at 1500 cells/well and further cultured overnight. Zr-TBB or H_4TBB was dispersed in PBS and added to the cells at a TBB ligand dose of 0, 0.5, 1, 2, 5, 10, 20, 50, and 100 μM and incubated for 4 h (N=6), followed by light irradiation (740 nm, 100 mW/cm^2, 15 min). The cells were further incubated for 72 h before determining the cell viability by MTS assay. IC_{50} value of Zr-TBB with light irradiation on the 4T1 model was determined as 0.91±0.77 μM by fitting the dose-response curves. As for H_4TBB with light irradiation, no significant toxicity was found until 20 μM. No obvious dark toxicity was observed for both Zr-TBB and H_4TBB.

To verify that efficient type-I PDT of Zr-TBB can also tolerate hypoxic conditions in cells, a hypoxia-mimicking *in vitro* cytotoxicity assay was performed. 4T1 cells were seeded on 96-well plates at 1500 cells/well and cultured overnight. Then the cells were transferred into the anaerobic chamber and further incubated for 4 hours. Zr-TBB and H_4TBB were added to the cells at a TBB ligand dose of 0, 0.5, 1, 2, 5, 10, 20, 50, and 100 μM and further incubated in the anaerobic chamber for 4 hours. Cells were then irradiated by LED for 15 minutes. After PDT treatment, the cells were further incubated for 72 hours before determining the cell viability by MTS assay. Hypoxic IC_{50} values of Zr-TBB and H_4TBB with light irradiation on the 4T1 model were determined as 2.94±0.76 and 19.50±0.82 μM, respectively, by fitting the dose-response curves.

Apoptotic cell death. The apoptosis after PDT treatment was evaluated by flow cytometry. On two 6-well plates, 4T1 cells were seeded at a density of $5x10^5$ cells/well with full RPMI-1640 medium. After culturing overnight, the cells on both plates were treated with Zr-TBB, H_4TBB, or PBS at a TBB concentration of 20 μM and further incubated for 4 hours. Then one of the plates was irradiated with 740 nm LED light (100 $mW \cdot cm^{-2}$) for 15 min. The cells on both plates were washed with PBS and further incubated for another 24 hours. The cells were stained with AlexaFluor 488 Annexin V/dead cell apoptosis kit and PI for flow cytometry analysis.

***In vivo* anti-cancer efficacy.** 4T1 tumor model was established by inoculating $5x10^6$ cells/mouse subcutaneously to BALB/c mice at day 0. Seven days later, 25 mice with tumor volumes between 100 mm^3 and 150 mm^3 were randomized for PDT treatment. Zr-TBB and H_4TBB were dispersed in PBS and injected intratumorally (*i.t.*) with a TBB dose of 0.2 μmol (N=5). The control group was treated with PBS (N=5). Eight hours later, the mice were anaesthetized with 2.5% (V/V) isoflurane/O_2, and only the tumor area was irradiated with LED light (740 nm, 100mW/cm^2, 15 min). Tumor sizes were measured by an electronic caliper (tumor volume =

length×width^2/2), and body weight was monitored every day. On day 25, the mice were sacrificed, and the tumors were weighed and photographed. Tumors were sectioned for H&E staining. One mouse in H_4TBB (+) treatment group died 4 days after H_4TBB injection.

MC38 tumor model was established by inoculating 5x10^6 cells/mice subcutaneously to C57BL/6 mice at day 0. Seven days later, 25 mice with tumor volumes between 100 mm^3 and 150 mm^3 were randomized for PDT treatment. Zr-TBB and H_4TBB were injected *i.t.* with a TBB dose of 0.2 μmol (N=5). The control group was treated with PBS (N=5). Eight hours later, the mice were anesthetized with 2.5% (V/V) isoflurane/O_2, and only the tumor area was irradiated with LED light (740nm, 100mW/cm^2, 15min). Tumor sizes were measured by an electronic caliper (tumor volume = length×width^2/2), and body weight was monitored every day. On day 21, the mice were sacrificed, and the tumors were weighed and photographed. The tumor growth inhibition index (TGI) was defined by Eq. 2-2:

$$TGI = 1 - \frac{\frac{T_e}{T_s} \Big/ \frac{C_e}{C_s}}{1 - \frac{C_s}{C_e}} \times 100\% \qquad Eq. 2-2$$

where T_e, T_s, C_e, and C_s Represent average tumor volumes of treated mice at the endpoint, treated mice at the starting point, control mice at the endpoint, and control mice at the starting point, respectively.

***In vivo* immunogenicity.** To evaluate in vivo immunogenicity of PDT treatment, we performed CRT assay and TUNEL assay on tumor sections. The excised tumors were sectioned and fixed with 4% paraformaldehyde (PFA) solution for 30 min. For CRT assay, the tumor slides were directly blocked with 3% bovine serum albumin (BSA) and 1% fetal bovine serum (FBS) for 2 hours and then stained with anti-Calreticulin Alexa Fluor 488 (NOVUS) at 4 °C overnight. The slides were washed and mounted for CLSM imaging. For the TUNEL assay, the tumor slides were

permeabilized and blocked with 3% BSA and 0.3% Triton X-100 for 2 hours, and then each slide was added 10-20 μL TUNEL-Mix and then covered with a coverslip. The slides were incubated for 1 hour at 37 °C in a dark and humid environment. Then the slides were washed and stained with Alexa Fluor 488 dye-labeled anti-BrdU antibody for 1 hour at room temperature. The slides were then washed and mounted for CLSM imaging.

DFT Calculations. All DFT calculations were carried out using the Gaussian 09 program.[29] The structures of chemical species in solution-phase and gas-phase were fully optimized by using the B3LYP functional. [30-32] The 6-31G (d, p) basis set was used for all elements (C, H, O, and N). And the corresponding energy calculation was based on def2TZVP basis set to ensure accuracy. The structure of H_4TBB was built using ChemDraw software and then optimized. The TBB structure in the Zr-TBB structure was simulated using the single crystal structure of Hf-TBB, and the structures of all carboxylate groups were frozen during optimization. The transition states (TSs) of TBB photo-oxidation step were found by using the QST3 method and confirmed by the intrinsic reaction coordinate method. All of the TSs were validated by imaginary vibrational frequencies along the reaction coordinates and their reasonable geometries bridging the reactants and products.

2.5 References

(1) Lovell, J. F.; Liu, T. W.; Chen, J.; Zheng, G., Activatable photosensitizers for imaging and therapy. *Chem. Rev.* **2010,** *110* (5), 2839-2857.

(2) Luby, B. M.; Walsh, C. D.; Zheng, G., Advanced photosensitizer activation strategies for smarter photodynamic therapy beacons. *Angew. Chem. Int. Ed.* **2019,** *58* (9), 2558-2569.

(3) Huang, H.-C.; Mallidi, S.; Liu, J.; Chiang, C.-T.; Mai, Z.; Goldschmidt, R.; Ebrahim-Zadeh, N.; Rizvi, I.; Hasan, T., Photodynamic therapy synergizes with irinotecan to overcome compensatory mechanisms and improve treatment outcomes in pancreatic cancer. *Cancer Res.* **2016,** *76* (5), 1066-1077.

(4) Dolmans, D. E.; Fukumura, D.; Jain, R. K., Photodynamic therapy for cancer. *Nat. Rev. Cancer* **2003,** *3* (5), 380-387.

(5) Shao, S.; Rajendiran, V.; Lovell, J. F., Metalloporphyrin nanoparticles: Coordinating diverse theranostic functions. *Coord. Chem. Rev.* **2019,** *379*, 99-120.

(6) Lan, G.; Ni, K.; Xu, Z.; Veroneau, S. S.; Song, Y.; Lin, W., Nanoscale metal–organic framework overcomes hypoxia for photodynamic therapy primed cancer immunotherapy. *J. Am. Chem. Soc.* **2018,** *140* (17), 5670-5673.

(7) Hopper, C., Photodynamic therapy: a clinical reality in the treatment of cancer. *Lancet Oncol.* **2000,** *1* (4), 212-219.

(8) Mallidi, S.; Anbil, S.; Bulin, A.-L.; Obaid, G.; Ichikawa, M.; Hasan, T., Beyond the barriers of light penetration: strategies, perspectives and possibilities for photodynamic therapy. *Theranostics* **2016,** *6* (13), 2458.

(9) Chen, Y.; Li, G.; Pandey, R. K., Synthesis of bacteriochlorins and their potential utility in photodynamic therapy (PDT). *Curr. Org. Chem.* **2004,** *8* (12), 1105-1134.

(10) Zhou, Z.; Song, J.; Nie, L.; Chen, X., Reactive oxygen species generating systems meeting challenges of photodynamic cancer therapy. *Chem. Soc. Rev.* **2016,** *45* (23), 6597-6626.

(11) Lan, G.; Ni, K.; Veroneau, S. S.; Feng, X.; Nash, G. T.; Luo, T.; Xu, Z.; Lin, W., Titanium-Based Nanoscale Metal–Organic Framework for Type I Photodynamic Therapy. *J. Am. Chem. Soc.* **2019,** *141* (10), 4204-4208.

(12) Azzouzi, A.-R.; Vincendeau, S.; Barret, E.; Cicco, A.; Kleinclauss, F.; van der Poel, H. G.; Stief, C. G.; Rassweiler, J.; Salomon, G.; Solsona, E.; Alcaraz, A.; Tammela, T. T.; Rosario, D. J.; Gomez-Veiga, F.; Ahlgren, G.; Benzaghou, F.; Gaillac, B.; Amzal, B.; Debruyne, F. M. J.; Fromont, G.; Gratzke, C.; Emberton, M., Padeliporfin vascular-targeted photodynamic therapy versus active surveillance in men with low-risk prostate cancer (CLIN1001 PCM301): an open-label, phase 3, randomised controlled trial. *Lancet Oncol.* **2017,** *18* (2), 181-191.

(13) Pucelik, B.; Arnaut, L. G.; Stochel, G.; Dąbrowski, J. M., Design of Pluronic-Based Formulation for Enhanced Redaporfin-Photodynamic Therapy against Pigmented Melanoma. *ACS Appl. Mater. Interfaces* **2016,** *8* (34), 22039-22055.

(14) Huang, Y. Y.; Balasubramanian, T.; Yang, E.; Luo, D.; Diers, J. R.; Bocian, D. F.; Lindsey, J. S.; Holten, D.; Hamblin, M. R., Stable synthetic bacteriochlorins for photodynamic therapy: role of dicyano peripheral groups, central metal substitution (2H, Zn, Pd), and Cremophor EL delivery. *ChemMedChem* **2012,** *7* (12), 2155-2167.

(15) Dąbrowski, J. M.; Arnaut, L. G., Photodynamic therapy (PDT) of cancer: from local to systemic treatment. *Photochem. Photobiol. Sci.* **2015,** *14* (10), 1765-1780.

(16) Grahn, M. F.; McGuinness, A.; Benzie, R.; Boyle, R.; de Jode, M. L.; Dilkes, M. G.; Abbas, B.; Williams, N. S., Intracellular uptake, absorption spectrum and stability of the bacteriochlorin photosensitizer 5, 10, 15, 20-tetrakis (m-hydroxyphenyl) bacteriochlorin (mTHPBC). Comparison with 5, 10, 15, 20-tetrakis (m-hydroxyphenyl) chlorin (mTHPC). *J. Photochem. Photobiol., B* **1997,** *37* (3), 261-266.

(17) Huang, L.; Huang, Y.-Y.; Mroz, P.; Tegos, G. P.; Zhiyentayev, T.; Sharma, S. K.; Lu, Z.; Balasubramanian, T.; Krayer, M.; Ruzié, C., Stable synthetic cationic bacteriochlorins as selective antimicrobial photosensitizers. *Antimicrob. Agents Chemother.* **2010,** *54* (9), 3834-3841.

(18) Pandey, R. K.; Constantine, S.; Tsuchida, T.; Zheng, G.; Medforth, C. J.; Aoudia, M.; Kozyrev, A. N.; Rodgers, M. A.; Kato, H.; Smith, K. M., Synthesis, photophysical properties, in vivo photosensitizing efficacy, and human serum albumin binding properties of some novel bacteriochlorins. *J. Med. Chem.* **1997,** *40* (17), 2770-2779.

(19) Pereira, M. M.; Monteiro, C. J. P.; Simões, A. V. C.; Pinto, S. M. A.; Abreu, A. R.; Sá, G. F. F.; Silva, E. F. F.; Rocha, L. B.; Dąbrowski, J. M.; Formosinho, S. J.; Simões, S.; Arnaut, L. G., Synthesis and photophysical characterization of a library of photostable halogenated bacteriochlorins: an access to near infrared chemistry. *Tetrahedron* **2010,** *66* (49), 9545-9551.

(20) Ghosh, A., Theoretical Comparative Study of Free Base Porphyrin, Chlorin, Bacteriochlorin, and Isobacteriochlorin: Evaluation of the Potential Roles of ab Initio Hartree− Fock and Density Functional Theories in Hydroporphyrin Chemistry. *J. Phys. Chem. B* **1997,** *101* (16), 3290-3297.

(21) Lu, K.; He, C.; Guo, N.; Chan, C.; Ni, K.; Weichselbaum, R. R.; Lin, W., Chlorin-based nanoscale metal–organic framework systemically rejects colorectal cancers via synergistic photodynamic therapy and checkpoint blockade immunotherapy. *J. Am. Chem. Soc.* **2016,** *138* (38), 12502-12510.

(22) Bashkatov, A. N.; Berezin, K. V.; Dvoretskiy, K. N.; Chernavina, M. L.; Genina, E. A.; Genin, V. D.; Kochubey, V. I.; Lazareva, E. N.; Pravdin, A. B.; Shvachkina, M. E., Measurement of tissue optical properties in the context of tissue optical clearing. *J. Biomed. Opt.* **2018,** *23* (9), 091416.

(23) Feng, D.; Chung, W.-C.; Wei, Z.; Gu, Z.-Y.; Jiang, H.-L.; Chen, Y.-P.; Darensbourg, D. J.; Zhou, H.-C., Construction of ultrastable porphyrin Zr metal–organic frameworks through linker elimination. *J. Am. Chem. Soc.* **2013,** *135* (45), 17105-17110.

(24) Stratonnikov, A. A.; Meerovich, G. A.; Loschenov, V. B. In *Photobleaching of photosensitizers applied for photodynamic therapy*, Optical Methods for Tumor Treatment and Detection: Mechanisms and Techniques in Photodynamic Therapy IX, International Society for Optics and Photonics: 2000; pp 81-91.

(25) Bonnett, R.; Martínez, G., Photobleaching of compounds of the 5, 10, 15, 20-Tetrakis (m-hydroxyphenyl) porphyrin Series (m-THPP, m-THPC, and m-THPBC). *Org. Lett.* **2002,** *4* (12), 2013-2016.

(26) Bonnett, R.; Martınez, G., Photobleaching of sensitisers used in photodynamic therapy. *Tetrahedron* **2001,** *57* (47), 9513-9547.

(27) Silva, E. F.; Serpa, C.; Dąbrowski, J. M.; Monteiro, C. J.; Formosinho, S. J.; Stochel, G.; Urbanska, K.; Simões, S.; Pereira, M. M.; Arnaut, L. G., Mechanisms of singlet ‐ oxygen and superoxide ‐ ion generation by porphyrins and bacteriochlorins and their implications in photodynamic therapy. *Chem. Eur. J.* **2010,** *16* (30), 9273-9286.

(28) Vakrat-Haglili, Y.; Weiner, L.; Brumfeld, V.; Brandis, A.; Salomon, Y.; McLlroy, B.; Wilson, B. C.; Pawlak, A.; Rozanowska, M.; Sarna, T.; Scherz, A., The Microenvironment Effect on the Generation of Reactive Oxygen Species by Pd−Bacteriopheophorbide. *J. Am. Chem. Soc.* **2005,** *127* (17), 6487-6497.

(29) Frisch, M. J.; Trucks, G. W.; Schlegel, H. B.; Scuseria, G. E.; Robb, M. A.; Cheeseman, J. R.; Scalmani, G.; Barone, V.; Petersson, G. A.; Nakatsuji, H.; Li, X.; Caricato, M.; Marenich, A. V.; Bloino, J.; Janesko, B. G.; Gomperts, R.; Mennucci, B.; Hratchian, H. P.; Ortiz, J. V.; Izmaylov, A. F.; Sonnenberg, J. L.; Williams; Ding, F.; Lipparini, F.; Egidi, F.; Goings, J.; Peng, B.; Petrone, A.; Henderson, T.; Ranasinghe, D.; Zakrzewski, V. G.; Gao, J.; Rega, N.; Zheng, G.; Liang, W.; Hada, M.; Ehara, M.; Toyota, K.; Fukuda, R.; Hasegawa, J.; Ishida, M.; Nakajima, T.; Honda, Y.; Kitao, O.; Nakai, H.; Vreven, T.; Throssell, K.; Montgomery Jr., J. A.; Peralta, J. E.; Ogliaro, F.; Bearpark, M. J.; Heyd, J. J.; Brothers, E. N.; Kudin, K. N.; Staroverov, V. N.; Keith, T. A.; Kobayashi, R.; Normand, J.; Raghavachari, K.; Rendell, A. P.; Burant, J. C.; Iyengar, S. S.; Tomasi, J.; Cossi, M.; Millam, J. M.; Klene, M.; Adamo, C.; Cammi, R.; Ochterski, J. W.; Martin, R. L.; Morokuma, K.; Farkas, O.; Foresman, J. B.; Fox, D. J. *Gaussian, Inc.,*, Wallingford, CT, 2016.

(30) Becke, A. D., Density-functional exchange-energy approximation with correct asymptotic behavior. *Phys. Rev. A* **1988,** *38* (6), 3098-3100.

(31) Lee, C. T.; Yang, W. T.; Parr, R. G., Development of the Colle-Salvetti correlation-energy formula into a functional of the electron density. *Phys. Rev. B* **1988,** *37* (2), 785-789.

(32) Gupta, M.; da Silva, E. F.; Svendsen, H. F., Postcombustion CO2 Capture Solvent Characterization Employing the Explicit Solvation Shell Model and Continuum Solvation Models. *J. Phys. Chem., B* **2016,** *120* (34), 9034-9050.

Chapter 3. Dimensional Reduction Enhances Photodynamic Therapy of Metal-Organic Nanophotosensitizers

3.1 Introduction

In PDT, PSs absorb photons and transfer energy to nearby oxygen and other molecules to ROS.[1-2] The efficacy of PDT depends on the aqueous solubility and ROS generation efficiency of PSs. The most well-known PSs based on porphyrins and phthalocyanines tend to have poor aqueous solubility and severely aggregate under physiological conditions.[3-5] Nanotechnology can overcome unfavorable physicochemical properties of highly conjugated and poorly soluble PSs.[6-9] For example, liposome and micelle formulations have been advanced into the clinic to facilitate the intravenous administration of benzoporphyrin and phthalocyanine.[10-18] Inorganic nanoparticles have also been explored as potential nanocarriers for a wide range of PSs.[19-23]

nMOFs have recently emerged as a novel class of nanophotosensitizers.[24-28] In nMOFs, PSs are periodically arranged as ligands in three-dimensional crystalline frameworks to afford high PS loadings and spatially isolated by metal-oxo SBUs to prevent self-quenching.[29-36] We hypothesized that the PDT performance of nMOFs could be further enhanced via dimensional reduction to increase the energy transfer from photoexcited PSs to oxygen molecules and the diffusion of singlet oxygen ($^1O_2$) from the nanophotosensitizers to intracellular organelles for maximal cytotoxicity.[37-40]

In this Chapter, we report the design of two-dimensional (2-D) metal-organic nanophotosensitizers, and nanoscale metal-organic layers (nMOLs), via dimensional reduction of three-dimensional (3-D) nMOFs. We synthesized Hf-DBP nMOL (Hf-MOL) and Hf-DBP nMOF (Hf-MOF) based on Hf_{12}-SBUs and 5,15-di(p-benzoato)porphyrin (DBP) ligands by using

propionic acid (PA) and acetic acid (AA) modulators, respectively (**Figure 3-1**). Hf-MOL provided fully accessible PSs to O_2 molecules and minimal diffusion barrier for ROS, leading to stronger ROS generation and significantly higher PDT efficacy on colorectal and triple-negative breast cancer in mouse models.

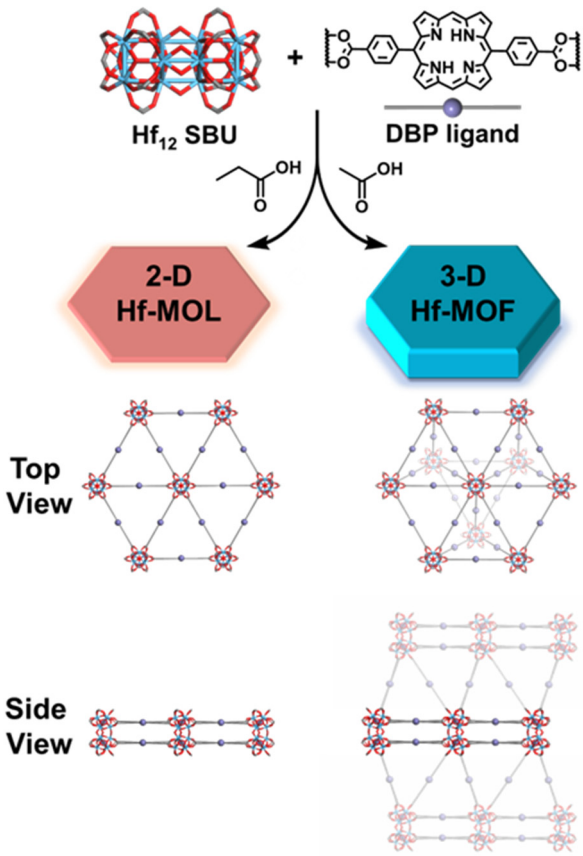

Figure 3-1. Schematic showing structures of Hf-MOL and Hf-MOF with kgd and hcp topology, respectively. Propionate groups cap Hf_{12} SBUs in vertical directions to afford Hf-MOL.

3.2 Results and Discussion

3.2.1 Synthesis and Characterization of 2-D Hf-MOL and 3-D Hf-MOF

Hf-MOL was synthesized through a solvothermal reaction between $HfCl_4$ and H_2DBP in DMF at 80 °C with PA and water as modulators. Hf-MOL was constructed from $Hf_{12}(\mu_3\text{-}O)_8(\mu_3\text{-}OH)_8(\mu_2\text{-}OH)_6$ SBUs and DBP bridging ligands as a monolayer with a 2-D network of kagome dual (**kgd**) topology. The monolayer was vertically capped by propionate groups (via coordination

to the Hf_{12} SBUs to afford a molecular formula of $Hf_{12}(\mu_3\text{-}O)_8(\mu_3\text{-}OH)_8(\mu_2\text{-}OH)_6(DBP)_6(\mu_2\text{-}PA)_6$ (**Figure 3-1**). Analyses of the digested Hf-MOL by UV-vis spectroscopy, ^{1}H-NMR spectroscopy, and ICP-MS revealed a Hf : DBP : PA molar ratio of 2 : 1 : 1 (**Figure 3-2**), which matched the proposed molecular formula.

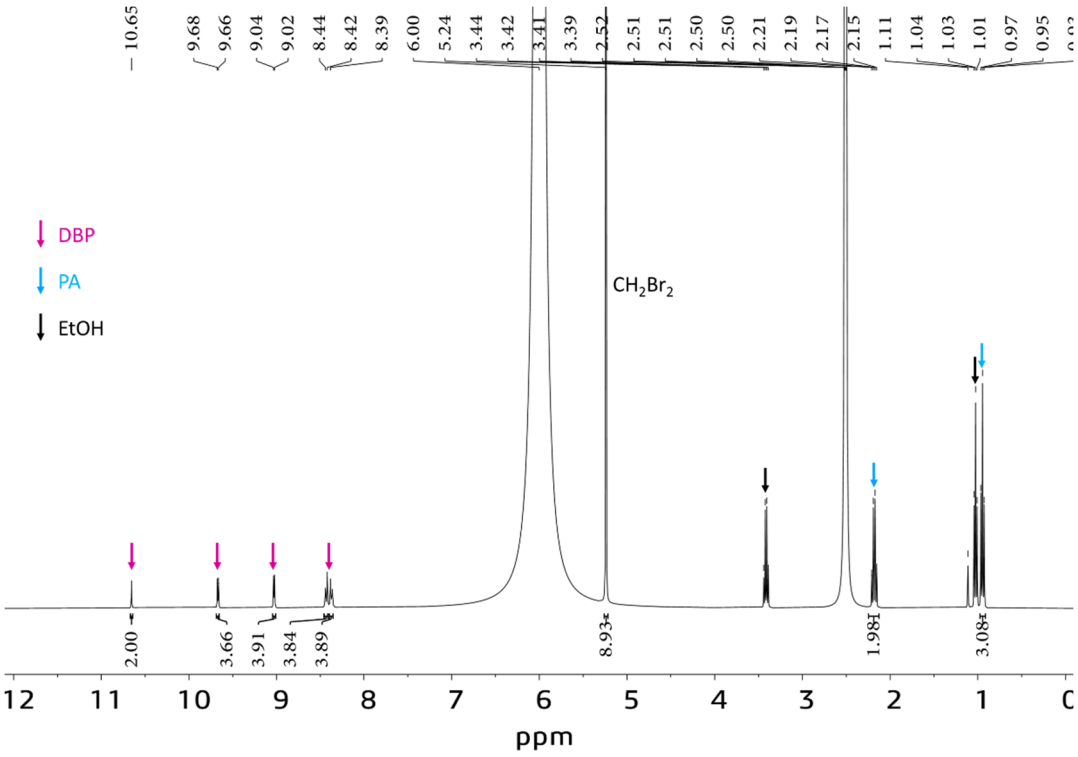

Figure 3-2. ^{1}H-NMR spectrum of digested Hf-MOL.

As a control, Hf-MOF was synthesized through a solvothermal reaction between $HfCl_4$ and H_2DBP with AA and water as modulators.[41] Hf-MOF was similarly constructed from Hf_{12} SBUs and DBP bridging ligands, but with a 3-D network of hexagonal close-packed (**hcp**) topology. Each Hf_{12} SBU was connected to the 12 nearest Hf_{12} SBU by 18 bridging DBP ligands to afford an ideal molecular formula of $Hf_{12}(\mu_3\text{-}O)_8(\mu_3\text{-}OH)_8(\mu_2\text{-}OH)_6(DBP)_9$ (**Figure 3-1**).

TEM showed a nanoplate morphology with a diameter of approximately 200 nm, and atomic force microscopy (AFM) showed a thickness of approximately 1.7 nm for Hf-MOL (**Figure 3-3a,c**). This thickness matched the height of Hf_{12} SBUs capped with propionate groups (**Figure 3-**

3e). In contrast, TEM and AFM of Hf-MOF revealed 3-D hexagonal nanoplates with a diameter of approximately 150 nm and a thickness of approximately 17 nm (**Figure 3-3b,d**).

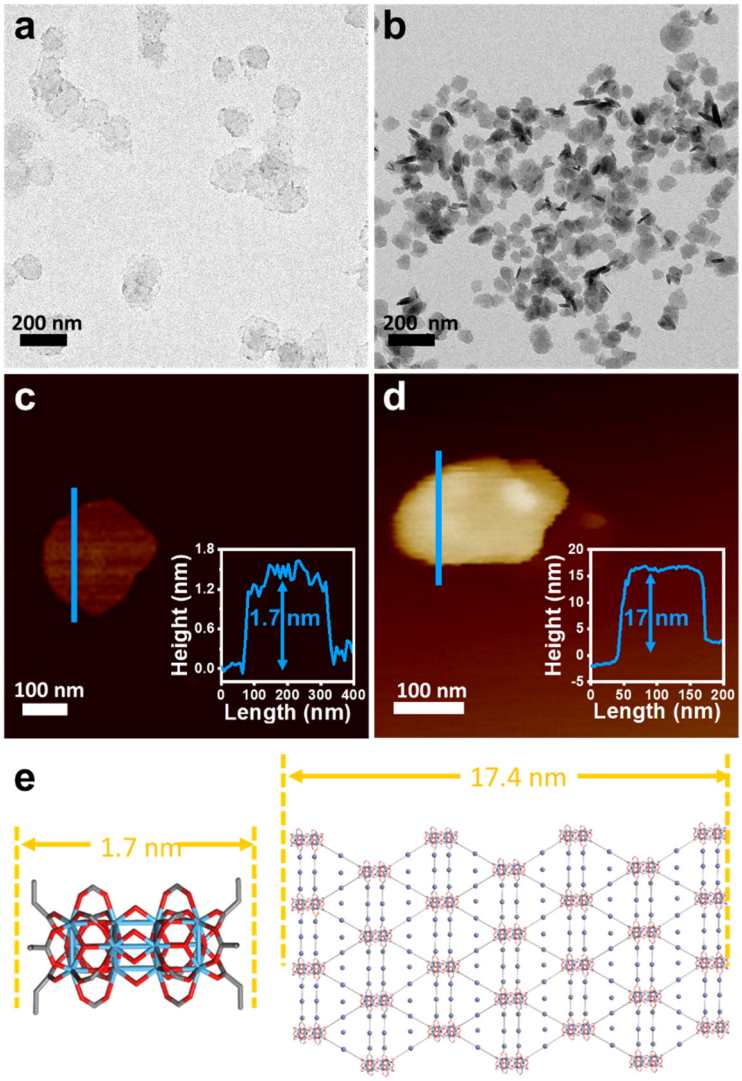

Figure 3-3. Morphology characterization of 2-D Hf-MOL and 3-D Hf-MOF. TEM images of (a) Hf-MOL and (b) Hf-MOF; AFM topography and height profile (inset) of (c) Hf-MOL and (d) Hf-MOF.

HR-TEM images and their FFT patterns revealed a six-fold symmetry consistent with the **kgd** topology for Hf-MOL (**Figure 3-4a**) and hcp topology for Hf-MOF (**Figure 3-4b**). DLS measurements of Hf-MOL and Hf-MOF showed number-average sizes of 192.8 ± 0.7 nm and 201.4 ± 0.9 nm, respectively (**Figure 3-4c**). PXRD patterns of Hf-MOL and Hf-MOF matched

their simulated PXRD patterns, and both materials were stable after incubation in PBS, as demonstrated by the unchanged PXRD patterns (**Figure 3-4d**).

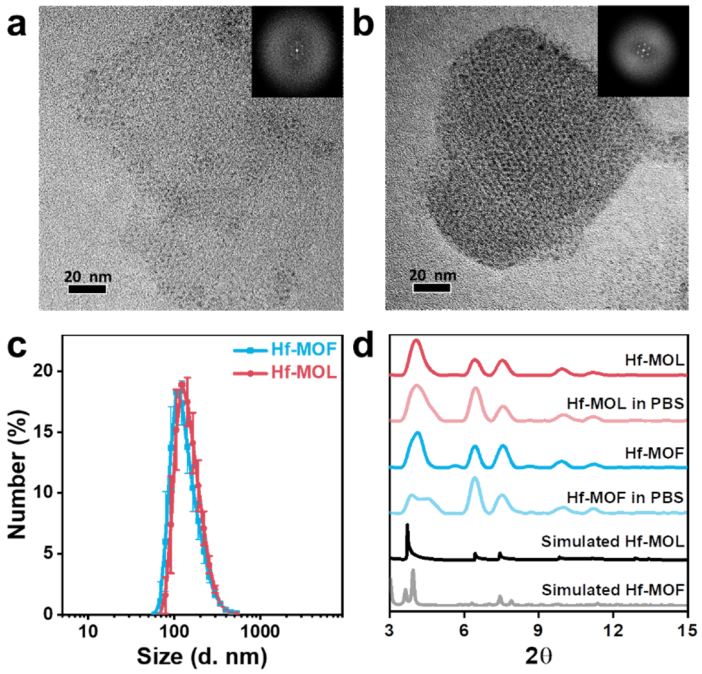

Figure 3-4. High-resolution TEM, DLS, and PXRD of Hf-MOL and Hf-MOF. HR-TEM (FFT in inset) of (a) Hf-MOL and (b) Hf-MOF. (c) Number-average size of Hf-MOL and Hf-MOF in ethanol measured by DLS. (d) PXRD patterns of as-synthesized Hf-MOL and Hf-MOF, Hf-MOL, and Hf-MOF incubated in PBS for 24 hours, along with the simulated PXRD patterns for Hf-MOL and Hf-MOF.

3.2.2 Oxygen Distribution by Molecular Dynamics Simulations

Because energy transfer efficiency decreases drastically as the donor-acceptor distance increases,[42-43] $^1O_2$ generation in PDT requires close encounters between intracellular ground-state oxygen ($^3O_2$) and photoexcited PS.[44-45] We hypothesized that reducing the dimension from 3-D Hf-MOF to 2-D Hf-MOL could promote $^1O_2$ generation by enhancing the interaction between photoexcited DBP and intracellular O_2. We performed molecular dynamics (MD) simulations to investigate the distribution of O_2 around DBP ligands in Hf-MOL or a Hf-MOF model with two layers linked by additional vertical ligands (**Figure 3-5a**). MD simulations showed O_2 enrichment

in the frameworks with a higher density around horizontal DBP ligands, leading to more O_2 molecules per DBP ligand within 5 nm of the DBP nitrogen atoms in Hf-MOL (**Figure 3-5b**). We also calculated the radial distribution function (RDF) of O_2 around the DBP nitrogen atoms. Hf-MOL showed a 2-fold higher RDF value than Hf-MOF in a short range, indicating a higher O_2 density near the DBP ligands in Hf-MOL (**Figure 3-5c**).

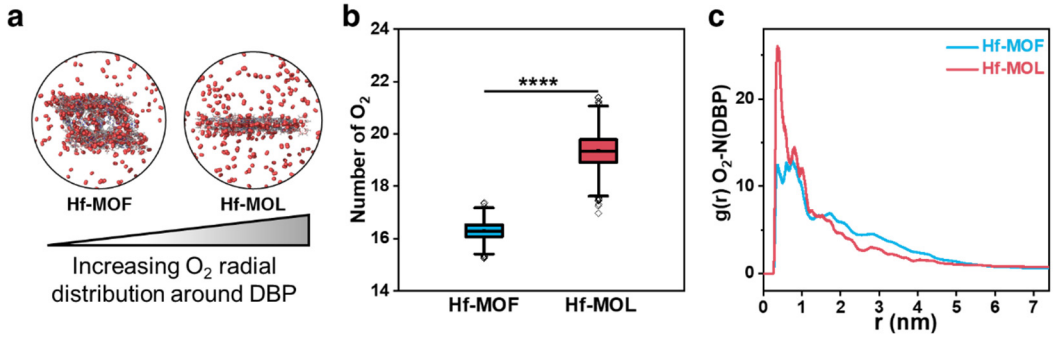

Figure 3-5. MD simulations of O_2 distributions. (a) Schematic showing Hf-MOL with higher O_2 RDF around DBP ligands. Snapshots of O_2 distribution in Hf-MOF (left) and Hf-MOL (right) were captured at 20 ns production run. (b) The number of O_2 molecules within 5 nm vicinity of each DBP ligand (calculated from nitrogen atoms). (c) RDF g(r) of O_2 molecules around DBP nitrogen atoms. The final 10 ns of the whole production run was analyzed.

3.2.3 Singlet Oxygen Generation in Test Tubes

We then experimentally determined $^1O_2$ generation by SOSG assay. Upon irradiation with 630 nm light, Hf-MOL generated 2.5-fold higher $^1O_2$ than Hf-MOF in 15 minutes (**Figure 3-6**). Thus, both simulation and experimental results indicated that dimensional reduction increased $^3O_2$ density around the photosensitizing ligands and $^1O_2$ diffusion out of the channels, leading to enhanced $^1O_2$ generation by Hf-MOL over Hf-MOF or free H_2DBP in test tubes.

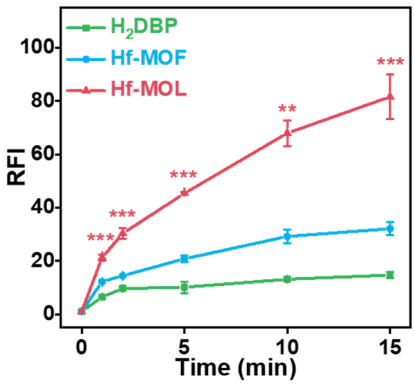

Figure 3-6. $^1O_2$ generated in test tube. SOSG assay showing significantly higher $^1O_2$ generated by Hf-MOL over Hf-MOF or free H_2DBP under 630 nm light with a fluence of 100 mW/cm^2. **p<0.01, ***p<0.001, and ****p<0.0001.

3.2.4 *In Vitro* Cell Killing

MTS assays revealed that Hf-MOL with light irradiation [denoted Hf-MOL(+)] had significantly higher cytotoxicity than Hf-MOF(+) with 14.3-, 10.1-, 11.5-, 8.5-, 4.7-fold lower IC_{50} values on CT26, 4T1, MC38, Panc02, and MDA-MB-231 cell lines, respectively (**Table 3-1**). Meanwhile, Hf-MOL without light irradiation [denoted Hf-MOL(-)] exhibited minimal toxicity at a 50 μM DBP dose *in vitro*, verifying Hf-MOL as a biocompatible and potent nanophotosensitizer with a large therapeutic window.

Table 3-1. IC_{50} values from MTS assays. Cell viability assays of Hf-MOL and Hf-MOF in CT26, 4T1, MC38, Panc02, and MDA-MB-231 cell lines upon light irradiation.

IC_{50}	Hf-MOF(+)	Hf-MOL(+)
CT26	16.2 μM	1.13 μM
4T1	29.7 μM	2.94 μM
MC38	27.3 μM	2.38 μM
Panc02	124.6 μM	14.7 μM
MDA-MB-231	29.5 μM	6.34 μM

3.2.5 *In Vitro* Cell Invasion and Migration

4T1 is an aggressive tumor model that has strong metastatic potential. We used scratch wound assay and clonogenic assay to evaluate if Hf-MOL PDT treatment can more effectively inhibit the migration and invasion potential of 4T1 cells. Scratch wound assays on 4T1 cells 13.5 hours post-PDT treatment showed that Hf-MOL(+) inhibited wound healing and cell invasion 51.1-fold more effectively than Hf-MOF(+) (**Figure 3-7**).

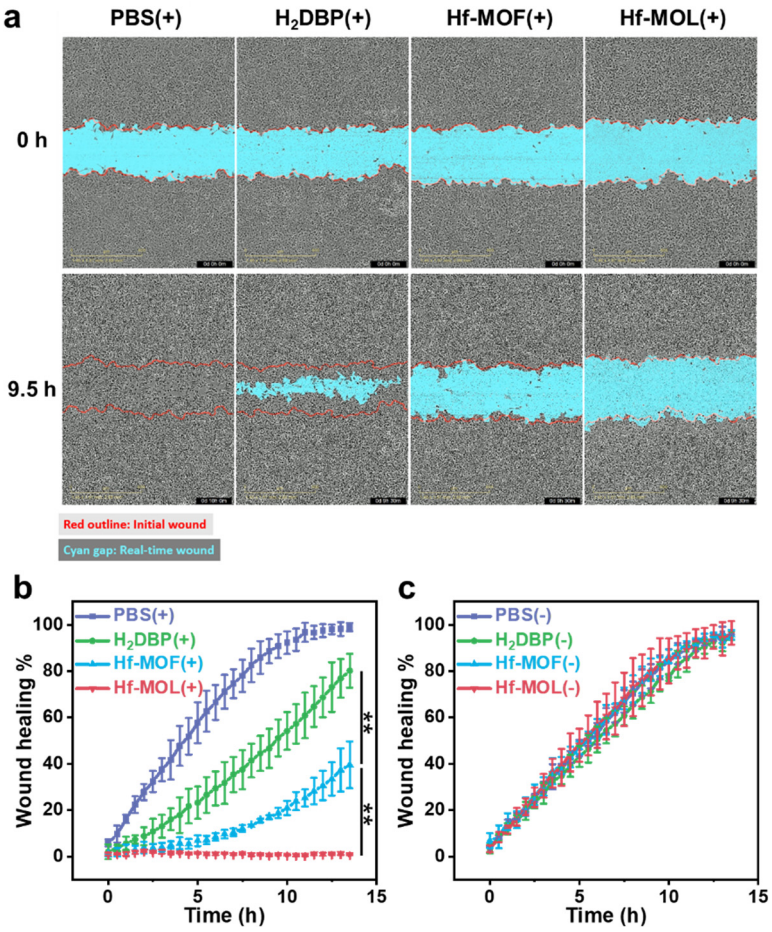

Figure 3-7. Scratch wound healing assay. (a) Representative images of wound healing status at 0 h and 9.5 h post-PDT treatment. The initial wound was marked with a red outline, and the real-time wound was marked by the cyan gap (scale bar = 600 μm). Quantification of wounding healing percentages of different treatment groups in 4T1 cells (b) with or (c) without light irradiation (n = 3).

Clonogenic assays also showed that Hf-MOL(+) reduced surviving fractions of 4T1 cells by a factor of 2.4 over Hf-MOF(+), indicating significant retardation of cancer cell colonization and migration by Hf-MOL(+) *in vitro* (**Figure 3-8**).

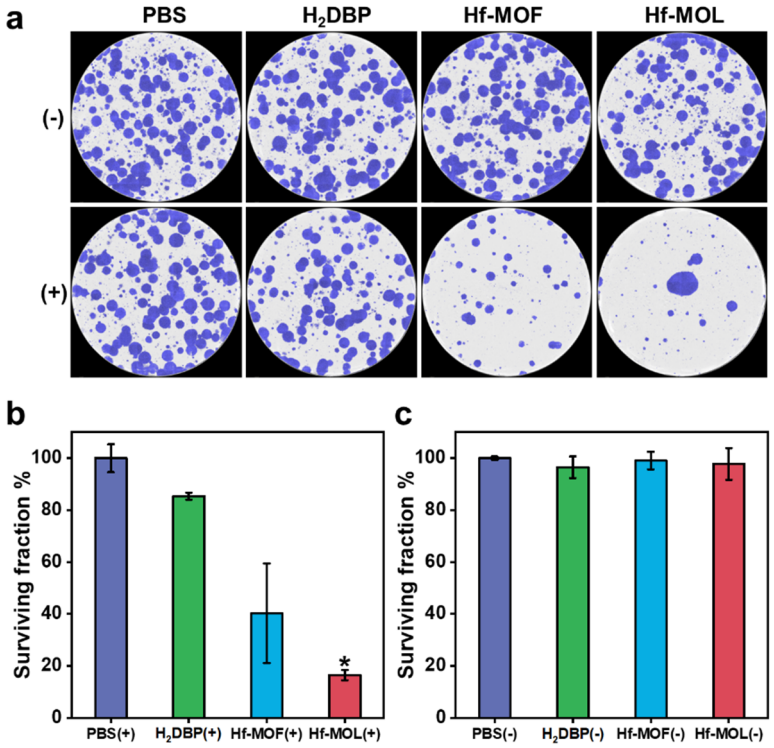

Figure 3-8. Clonogenic assay. (a) Representative colony-forming spots of PDT-treated cells (The diameter of the well is 35 mm). Quantification of surviving fractions of different treatment groups in 4T1 cells (b) with or (c) without light irradiation (n = 3).

3.2.6 Cellular Uptake and Subcellular Localization

Hf-MOL showed a higher cellular uptake than Hf-MOF and H_2DBP, which could contribute to the higher toxicity of Hf-MOL over Hf-MOF (**Figure 3-9a,b**). LysoTracker staining and DBP fluorescence were visualized by CLSM in z-stack mode to assess the subcellular localization of the particles. H_2DBP showed perfect overlap of its signals with lysosomes, while Hf-MOF and Hf-MOL showed partial dislocation of DBP signals with lysosomes (**Figure 3-9c-e**). This difference could be attributed to more active endocytosis of nanoparticles as early endosomes with uptaken

nanoparticles were not acidic enough to be labeled by LysoTracker or lysosomal escape of Hf-MOF and Hf-MOL to cytosol or other organelles.

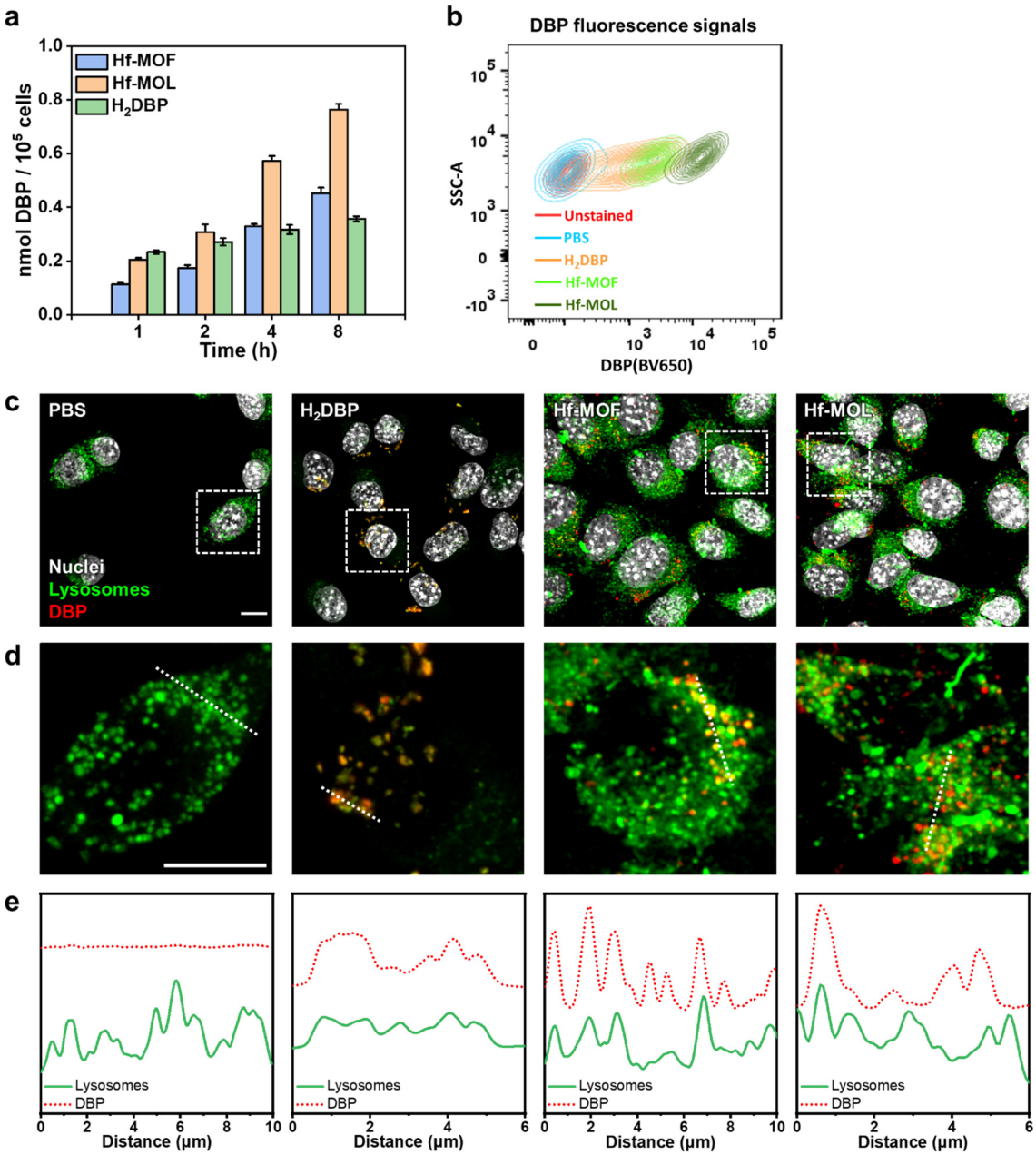

Figure 3-9. Cellular uptake and localization. (a) Time-dependent cellular uptake of H_2DBP, Hf-MOF, and Hf-MOL (n = 3) quantified by UV-Vis. (b) BV650 histograms showing DBP signals of H_2DBP, Hf-MOF, and Hf-MOL-treated cells by flow cytometry. (c) CLSM images showing colocalization of lysosomes (green) and DBP (red) in CT26 cells (nuclei, grey; scale bar = 20 μm). (d) Zoom-in views and (e) intensity histograms of the white dashed lines.

3.2.7 *In vitro* ROS Generation and Immunogenic Cell Death

Despite the selective accumulation of Hf-MOL in lysosomes, the ROS level of Hf-MOL(+) treated CT26 cells significantly increased in most parts of the cells (**Figure 3-10a**). Consistent with the results from MD simulation and ROS generation in test tubes, Hf-MOL(+) showed 2.5- and 11.6-fold more ROS generation in CT26 cells than Hf-MOF(+) and H_2DBP(+), respectively, as quantified by flow cytometry (**Figure 3-11a**).

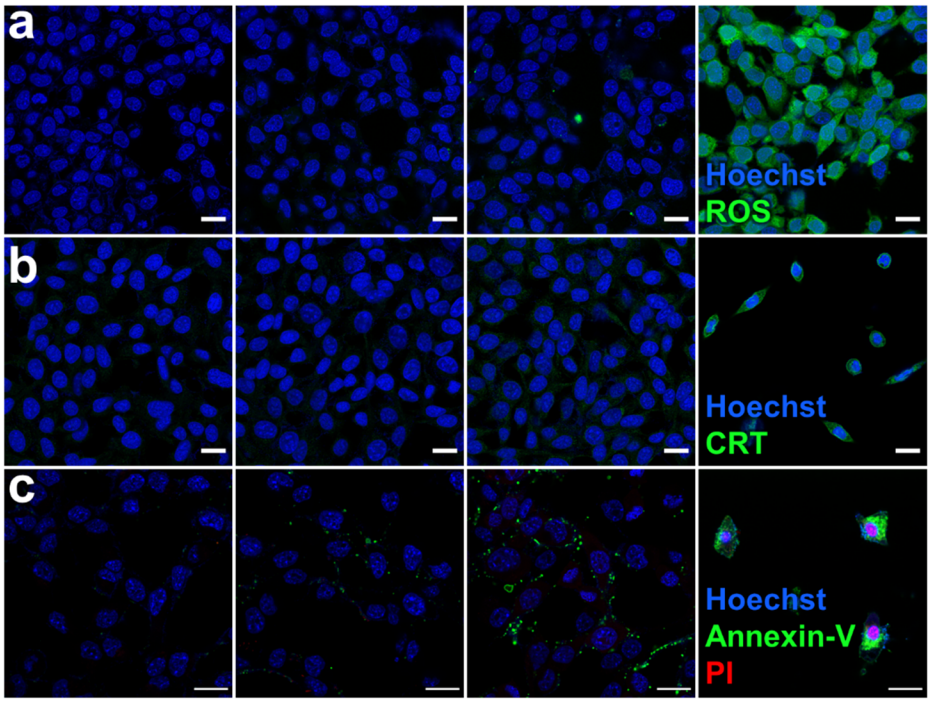

Figure 3-10. CLSM showing ROS generation and ICD. (a) Colocalization of H_2DBP, Hf-MOF, or Hf-MOL (DBP fluorescence in red) with lysosomes (green) in CT26 cells. (b) DCF-DA assay showing total ROS (green) generation in CT26 cells. (c) CRT surface translocation (green) on CT26 cells. (d) Annexin-V (green) and PI (red) double staining of apoptotic CT26 cells. Nuclei were visualized by Hoechst 33342 (blue). All scale bars are 20 μm. A dose of 5 μM DBP and a light dose of 18 J/cm^2 at 630 nm were used.

Hf-MOL(+) also induced stronger immunogenic cell death (ICD) than Hf-MOF(+) by CLSM and flow cytometry. Membrane translocation of calreticulin (CRT) was stained by an anti-CRT antibody as a marker of ICD (**Figure 3-10b**). The surface CRT signal from Hf-MOL(+) treated

cells was upregulated 2.9-fold more than that of Hf-MOF(+) treatment (**Figure 3-11b**), demonstrating enhanced ICD after Hf-MOL(+) treatment.[46]

The apoptotic marker on the cellular membrane was stained by Annexin-V, whereas the compromised membrane function was stained by PI (**Figure 3-10c**). The Annexin-V^+/PI^+ population after Hf-MOL(+) treatment was 23.4-fold more than that after Hf-MOF(+) treatment, indicating significantly more late apoptosis after Hf-MOL(+) treatment (**Figure 3-11c**).

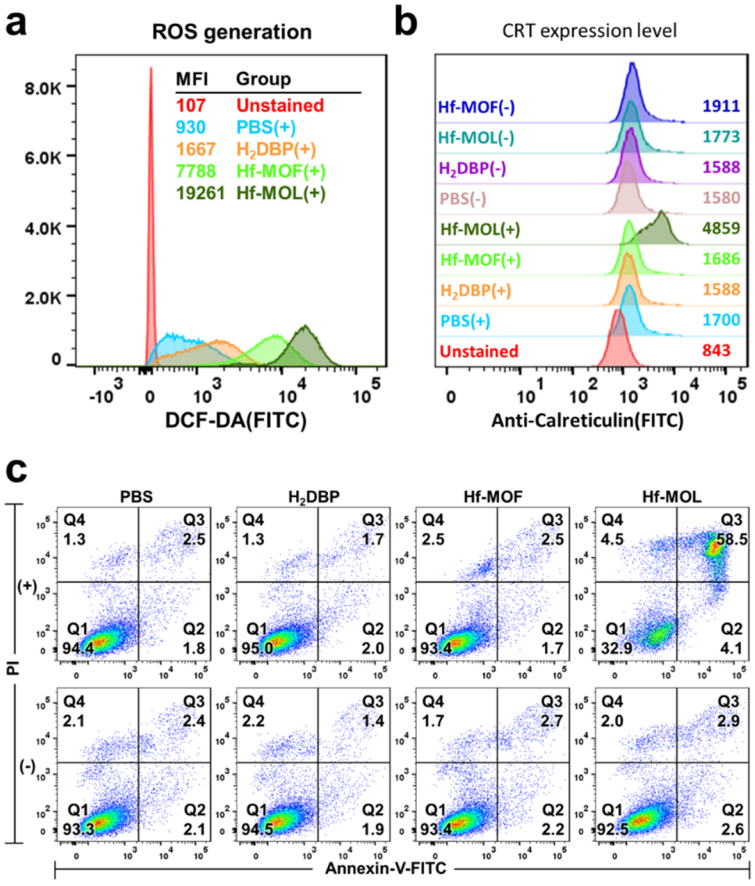

Figure 3-11. Flow cytometry showing ROS generation and ICD. (a) Quantification of histograms of intracellular ROS signals by flow cytometry in CT26 cells. The negative control without staining is shown in red (DCF-DA, FITC channel). (b) Flow cytometry analysis of CRT expression in CT26 cells 24 hours after PDT treatment. The negative control without staining was shown in red (CRT, FITC channel). (c) Flow cytometry analysis of CT26 apoptosis after PDT treatment. Q1, Q2, Q3, and Q4 refer to normal, early apoptotic, late apoptotic, and necrotic populations among CT26 cells, respectively. The percentages of each population are shown in each quadrant.

3.2.8 *In Vivo* Antitumor and Antimetastatic efficacy

We then evaluated the antitumor efficacy of Hf-MOL(+) on a subcutaneous murine colon cancer model CT26 and an orthotopic murine triple-negative breast cancer model 4T1 in BALB/c mice. Compared to PBS(+) control, H_2DBP(+), Hf-MOF(-), and Hf-MOL(-) showed minimal efficacy with TGI values less than 5.0 % on both CT26 and 4T1 models (**Table 3-2**). Hf-MOF(+) moderately inhibited tumor growth with TGI values of 87.3% and 49.2% on CT26 and 4T1 tumors, respectively. Hf-MOL(+) exhibited outstanding tumor regression with TGI values of >98.3% on both models (**Figure 3-12a,b**). Furthermore, Hf-MOL(+) cured 40% and 80% of tumor-bearing mice in CT26 and 4T1 models, respectively (n = 5). H&E and TUNEL staining showed that Hf-MOL(+) treated tumors exhibited sparser nuclear density and more DNA fragmentations (**Figure 3-12c**), demonstrating effective cancer cell killing and enhanced induction of ICD.

Table 3-2. TGI values of CT26-bearing BABL/c mice at day 19 and 4T1-bearing BABL/c mice at day 22.

Treatment	TGI(CT26)	TGI(4T1)
H_2DBP(+)	0.0454	-0.0671
Hf-MOF(+)	0.873	0.492
Hf-MOL(+)	0.988	0.983
H_2DBP(-)	0.0209	N/A
Hf-MOF(-)	0.0253	N/A
Hf-MOL(-)	-0.0941	N/A

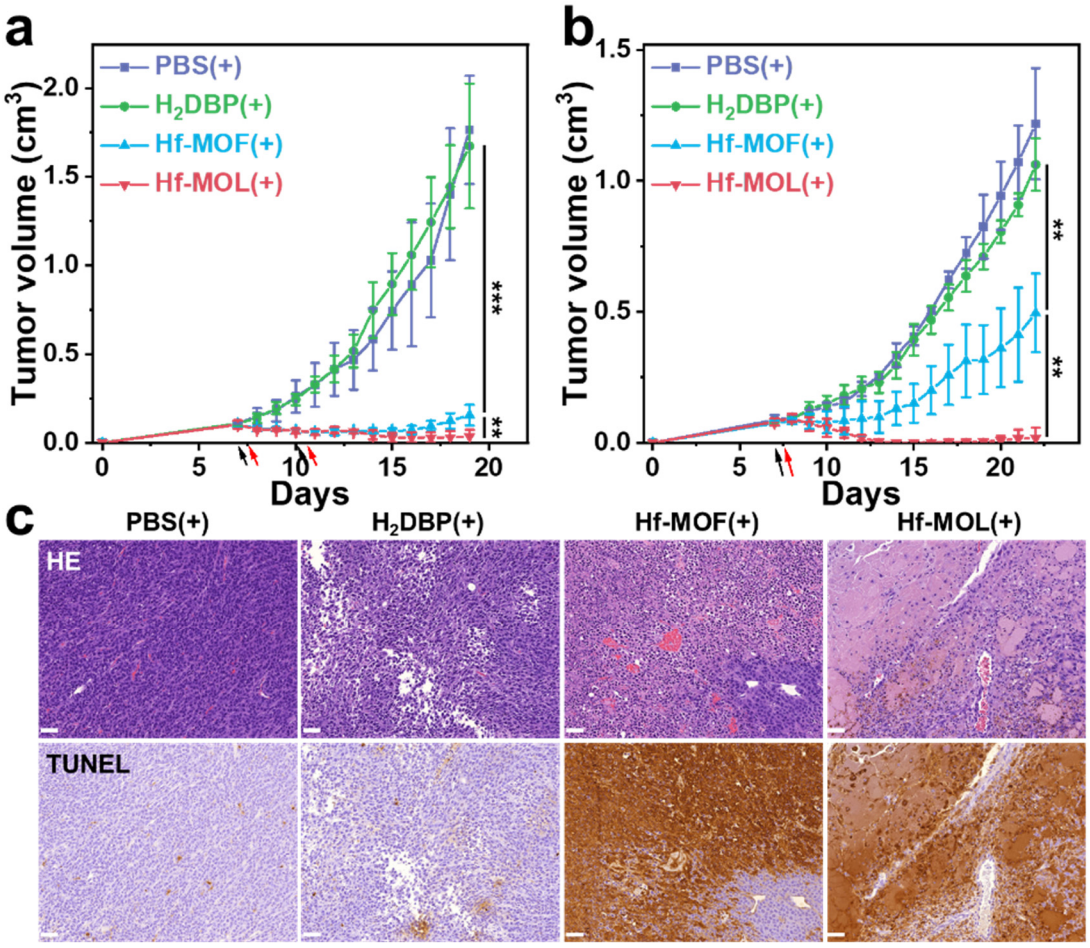

Figure 3-12. Antitumor efficacy. Tumor volume curves of different treatments on subcutaneous CT26 tumor-bearing (a) and orthotopic 4T1 tumor-bearing (b) BALB/c mice (n = 5, black arrows referred to particle administration and red arrows referred to light irradiation of 90 J/cm^2 at 630 nm). (c) H&E and TUNEL staining of excised CT26 tumors (Scale bars = 50 μm). *p<0.05, **p<0.01, and ***p<0.001.

4T1 orthotopic model is known to metastasize to lungs.[47-48] Hf-MOL(+) significantly inhibited lung metastasis of 4T1 tumors with 67.5-, 42.0-, and 16.3-fold fewer metastatic nodules than PBS(+), H2DBP(+), and Hf-MOF(+) groups, respectively (**Figure 3-13**). Thus, Hf-MOL not only elicits superb local PDT efficacy but can also prevent cancer metastasis to distant sites.

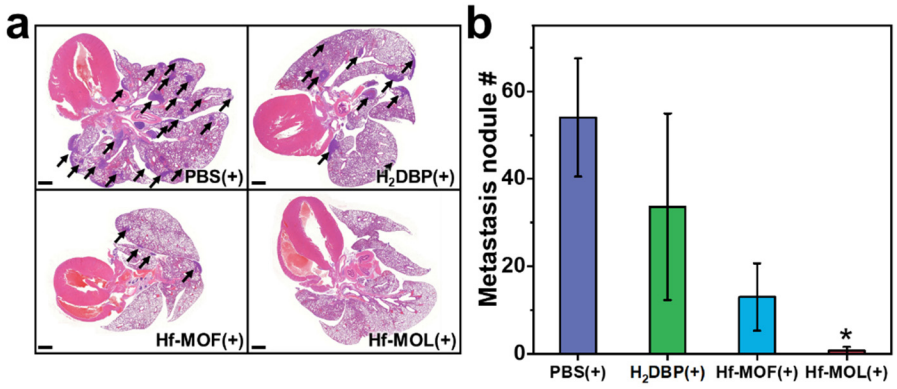

Figure 3-13. Inhibition of lung metastasis.(a) Representative images of H&E staining of lungs after PDT treatment from 4T1 tumor-bearing BALB/c mice (black arrow indicated metastatic nodules). (b) Statistical analysis of lung metastatic nodules in different groups from H&E slides (n = 5). *p<0.05, **p<0.01, and ***p<0.001.

3.3 Conclusion

In this Chapter, we revealed a significant enhancement of PDT efficacy via the dimensional reduction of MOFs. By adjusting the coordination strength of monocarboxylate modulators, we successfully synthesized M-DBP nMOFs and nMOLs (M=Zr and Hf) based on M_{12}-SBUs and DBP ligands. MD simulations and experimental studies showed that the nMOLs enhanced ROS generation and exhibited more than an order of magnitude higher cytotoxicity than the nMOFs. As a result, the nMOLs significantly outperformed the nMOFs in PDT, leading to enhanced tumor regression, higher cure rate, and reduced metastasis in mouse models. The dimensional reduction strategy can be generalized to the design of other nanophotosensitizers for PDT.

3.4 Methods

Synthesis of Hf-MOF and Hf-MOL. H_2DBP and Hf-MOF were synthesized according to literature reports.[29,41] Hf-MOL was synthesized by adding 2 mg $HfCl_4$, 1 mg H_2DBP, 8.5 μL propionic acid (PA), 5 μL H_2O, and 1 mL DMF to a one-dram vial. The vial was placed at 80 °C

oven for 1 day. The resultant purple particles were collected by centrifugation and washed with DMF and ethanol, and stored as ethanol dispersions.

UV-vis spectroscopic analysis of Hf-MOL. 10 μL Hf-MOL dispersion was added to a mixture of 940 μL DMSO and 50 μL H_3PO_4. After a sonication for 10 minutes, a UV-Vis spectrum of the solution was recorded with a Shimadzu UV-2600 UV-Vis spectrophotometer. The concentration of DBP in Hf-MOL dispersion was determined as 6.0 mM based on the established method.[29]

ICP-MS analysis of Hf-MOL. To a mixture of 980 μL HNO_3 and 10 μL HF, 10 μL Hf-DBP dispersion was added. The mixture was sonicated for 10 minutes, kept at room temperature for 3 days and then subjected to ICP-MS analysis using an Agilent 7700x ICP-MS and analyzed using an ICP-MS Mass Hunter version 4.6 C.01.06. Samples were diluted in a 2% HNO_3 matrix and analyzed with ^{159}Tb and internal standards against a 10-point standard curve between 1 ppb and 500 ppb. The correlation was given R>0.999 for all analyses of interest. Data collection was performed in Spectrum Mode with three replicates per sample and 100 sweeps per replicate. The concentration of Hf element in Hf-MOL was determined as 12.3 mM.

NMR analysis of Hf-MOL. To a mixture of 500 μL d_6-DMSO, 50 μL D_3PO_4, and 50 μL D_2O was added 2 mg of dried Hf-MOL particles. The mixture was sonicated for 10 minutes until no solid residue remained. CH_2Br_2 was added as an internal standard, and ^{1}H-NMR was recorded with a Bruker NMR 400 DRX spectrometer at 400 MHz and referenced to the proton resonance resulting from incomplete deuteration of $CDCl_3$ (δ = 7.26) or D_6-DMSO (δ = 2.50). The ratio of DBP to PA was determined to be 1:0.99, and the concentration of DBP and PA in Hf-MOL were determined as 5.6 mM and 5.5 mM, respectively.

MD simulations. The Gromacs 2021.1 package[49] was used for molecular dynamics simulations and data analysis according to a reported procedure.[50] The structures of Hf_{12}-DBP nMOF and nMOL atomistic models were constructed based on the crystal structure of a similar nMOF Zr_{12}-TPDC (TPDC = tetraphenyl dicarboxylate) using BIOVIA Materials Studio.[51] The vacant metal sites were occupied by acetate groups. Charges of the frameworks were calculated by the Qeq protocol.[52-53] The structure of oxygen molecules was optimized by Gaussian16 at the B3LYP/6-31++G(d) level of theory. The topologies were obtained using the OBGMX tool[54] which is based on the Universal Force Field (UFF)[55] to describe the Lennard-Jones, bond, angle, dihedral, and improper torsion potentials. For MD simulations, the nMOF or nMOL model was placed and restrained in the center of a cubic box (a = 15 nm) containing 500 oxygen molecules. The oxygen concentration corresponds to the oxygen in water under atmospheric pressure. Prior to the production run, both systems were allowed to equilibrate for 1 ns in the canonical NVT ensemble. For the production run, long-range electrostatic interactions were treated using the particle-mesh Ewald scheme[56] with a grid spacing of 1.6 Å and a cut-off of 12 Å was applied for the Van der Waals interactions. All hydrogen-related bonds were constrained using the LINCS algorithm. The temperature was maintained at 300 K by V-rescale thermostat using a coupling constant of τ_T = 0.1 ps. The systems were then equilibrated for 20 ns with a time step of 1 fs in the NVT ensemble. The final 10 ns were used for radial distribution function analysis.

Singlet oxygen generation in test tubes. The SOSG assay was used to test time-dependent $^1O_2$ generation of H_2DBP, Hf-MOF, and Hf-MOL upon 630 nm LED irradiation. H_2DBP, Hf-MOF, and Hf-MOL suspensions were prepared with an equivalent dose of 5 μM DBP in water. To 10 mL of each of these suspensions, a SOSG stock solution (25 μL at 5 mM in MeOH) was added (final SOSG concentration = 12.5 μM) before fluorescence measurements. The mixed solution

was exposed to an LED light (630 nm, 100 mW/cm^2) for 0, 1, 2, 5, 10, 15 minutes, and the fluorescence intensity was immediately measured with a Synergy HTX plate reader with a green filter (excitation 485 nm / emission 520 nm).

Cellular uptake. The cellular uptake of H_2DBP, Hf-MOF, and Hf-MOL was evaluated on CT26 cells. The cells were seeded in 6-well plates at a density of 5×10^5/well followed by culturing overnight. H_2DBP, Hf-MOF, and Hf-MOL were added at a DBP concentration of 5 μM in medium (n = 3). The cells were incubated at 37℃ for 1, 2, 4, and 8 hours. At each time point, the medium was aspirated, the cells were washed with PBS three times, trypsinized and collected by centrifugation, and counted by a hemocytometer. The cell pellets were digested with a mixture of DMSO and 10% H_3PO_4 in 1.5 mL Eppendorf tubes for 48 hours with strong vortex and sonication every 12 hours and the DBP concentration was determined by UV-Vis absorbance at 630 nm (ε=341 m$M^{-1} \cdot cm^{-1}$). The relative cellular uptake was also confirmed by flow cytometry and confocal microscopy after 8-hour incubation of CT26 cells with H_2DBP, Hf-MOF, and Hf-MOL. The fluorescence intensity of DBP was monitored by the BV650 channel (ex. 405 nm / em. 645 nm).

Subcellular localization. CT26 cells were seeded in 35 mm glass bottom dishes (MatTek) with a cell density of 1×10^5 cells/mL and cultured overnight. H_2DBP, Hf-MOF, or Hf-MOL was added at an equivalent DBP concentration of 1 μM in medium, together with 200 nM LysoTracker Red DND-99 (Thermo Fisher Scientific, USA) and incubated for 12 hours. The cells were washed with PBS twice and exchanged into fresh warm medium for another 30-minute incubation. Then the cells were washed again with PBS twice and fixed with 4% PFA at room temperature for 15 minutes. The cells were counterstained with Hoechst-33342 (3 μg/mL, Thermo Fisher Scientific, USA) for 5 minutes and observed under a Leica Stellaris 8 microscope with Z-stack mode.

Cell viability assay. The cytotoxicity of H_2DBP, Hf-MOF, and Hf-MOL was evaluated on CT26 cells by MTS assay. Zr-MOF and Zr-MOL were also tested to verify the PDT performance of 2-D nanophotosensitizers. The cells were first seeded on 96-well plates at a density of 1×10^4 cells/mL with 100 μL medium per well and further cultured overnight. H_2DBP, Hf/Zr-MOF, or Hf/Zr-MOL was added to the wells at a DBP concentration of 0, 0.2, 0.5, 1, 2, 5, 10, 20, 50, and 100 μM and incubated for 8 hours (n = 6), followed by light irradiation (630 nm, 50 mW/cm^2, 10 minutes, 30 J/cm^2 as total dose). Then the cells were further incubated for 48 hours, and the cell viability was determined by MTS assay. IC_{50} values of all treatment groups were fit with the dose-response curves in Origin Lab.

Wound healing assay. The wound healing assay was performed to evaluate the invasion and migration ability of 4T1 cells after PDT treatment with H_2DBP, nMOF, or nMOL. The cells were first seeded on an Incucyte Imagelock 96-well plate (Sartorius) at a density of 3×10^5 cells/mL with 100 μL medium per well and further cultured overnight. The wound was first created with an Incucyte 96-well woundmaker tool. The cells were washed with PBS twice, and H_2DBP, nMOF, or nMOL was added to the wells at an equivalent DBP concentration of 5 μM and incubated for 4 hours (n = 3), followed by light irradiation (630 nm, 50 mW/cm^2, 10 minutes, 30 J/cm^2 as total dose). Then the cells were put into IncuCyte S3 for live imaging for up to 14 hours and analyzed with a scratch wound analysis module.

Clonogenic assay. The cells were first seeded on 6-well plates at a density of 5×10^4 cells/mL with 2 mL medium per well and further cultured overnight. H_2DBP, Hf-MOF, or Hf-MOL was added to the wells at a DBP concentration of 5 μM and incubated for 4 hours (n = 3), followed by light irradiation (630 nm, 30 mW/cm^2, 10 min, 18 J/cm^2 as total dose). Then the cells were trypsinized, counted, and reseeded in new 6-well plates at a density of 200 cells per well, with 2.5

mL medium per well. One week later, the plates with visible colonies were scanned on IncuCyte S3 directly without staining. The cells were marked with purple masks.

***In vitro* ROS generation.** The ROS generation of H_2DBP, Hf-MOF, or Hf-MOL during PDT treatment was evaluated on CT26 cells by flow cytometry and CLSM. For flow cytometry analysis, on two 6-well plates, CT26 cells were seeded at a density of 2×10^5 cells/ml with medium and cultured overnight. The cells on both plates were treated with H_2DBP, Hf-MOF, or Hf-MOL at an equivalent DBP concentration of 5 μM and further incubated for 4 hours. 20 μM DCF-DA (Invitrogen) was then added to each well for another 1-hour incubation. Then the plates were irradiated with LED light (630 nm, 30 $mW \cdot cm^{-2}$) for 10 minutes. The cells were then washed with PBS, scraped off, and analyzed by flow cytometry. For CLSM, inside 35 mm glass bottom dishes, CT26 cells were seeded at a density of 1×10^5 cells/mL with 2 mL medium and cultured overnight. The cells were treated in the same way as flow cytometry but not detached. The cells were washed with PBS three times, exchanged with warm phenol-red-free RPMI-1640 medium, and mounted for confocal imaging immediately using a Leica Stellaris 8 microscope.

Apoptotic cell death. The apoptosis after PDT treatment was evaluated on CT26 cells by flow cytometry and confocal laser scanning microscopy (CLSM). For flow cytometry analysis, on two 6-well plates, CT26 cells were seeded at a density of 2×10^5 cells/ml with medium and cultured overnight. The cells on both plates were treated with H_2DBP, Hf-MOF, or Hf-MOL at a DBP concentration of 5 μM and further incubated for 8 hours. Then the plates were irradiated with LED light (630 nm, 30 $mW \cdot cm^{-2}$) for 10 minutes. The cells on both plates were washed with PBS, exchanged to warm fresh medium, and further incubated overnight. The cells were then scraped off and stained with Alexa Fluor 488 Annexin V/dead cell apoptosis kit (Thermo Fisher Scientific, USA) following the vendor's protocol for flow cytometry analysis. For CLSM analysis, inside 35

mm glass bottom dishes, CT26 cells were seeded at a density of 1×10^5 cells/ml with medium and cultured overnight. Then the treatment and staining were the same with flow cytometry except for a counterstain step of Hoechst-33342 3 μg/mL 5 minutes at room temperature and fixation by 2% PFA (in $1 \times Ca^{2+}$ containing binding buffer). The dishes were then washed with PBS and added with 1 mL 1x binding buffer and observed by a Leica Stellaris 8 microscope immediately.

CRT expression. CRT expression level was evaluated by flow cytometry and CLSM after PDT treatment. For flow cytometry analysis, CT26 cells were seeded on 6-well plates at a density of 2.5×10^5 cells/mL with 2 mL medium and cultured overnight. The cells were treated with H_2DBP, Hf-MOF, or Hf-MOL at a DBP concentration of 5 μM and further incubated for 8 hours. Then one of the plates was irradiated with LED light (630 nm, 30 $mW \cdot cm^{-2}$) for 10 minutes. The cells on both plates were washed with PBS and exchanged with warm fresh medium, and further incubated overnight. The medium was then discarded, and cells were washed with PBS and scraped off to obtain cell suspensions. The cells were stained with anti-Calreticulin Alexa Fluor 488 (NOVUS) (1:150 dilution in 0.5% BSA PBS solution) on ice for 30 minutes, washed with PBS once, and resuspended in 0.5% BSA PBS solution for flow cytometry analysis. For CLSM analysis, the PDT treatment procedure was the same with flow cytometry, except CT26 cells were seeded with a coverslip in each well with a cell density diluted to 1×10^5 cells/mL. The cells were fixed with -20 ℃ methanol for 5 minutes, blocked with 3% BSA and 1% FBS at room temperature for 1 hour, and then stained with anti-Calreticulin Alexa Fluor 488 (NOVUS) (1:150 dilution in 0.5% BSA PBS solution) at 4 ℃ overnight. The cells were washed with PBS and counterstained with Hoechst (3 μg/mL 5 minutes at room temperature), and the coverslips were mounted on glass slides with ProLong™ Glass Antifade Mountant, cured for 6 hours, and sealed for confocal imaging under a Leica Stellaris 8 microscope.

***In vivo* anti-cancer efficacy.** To evaluate *in vivo* PDT efficacy of Hf-MOF and Hf-MOL, subcutaneous CT26 and orthotopic 4T1 tumor models were established on BALB/c mice by inoculating 2×10^6 cells/mouse subcutaneously or 1×10^6 cells/mouse into the 3rd mammary pad of females at day 0, respectively. At day 7, the mice with tumor volume around 100 mm^3 were randomized for PDT treatment. PBS, H_2DBP, Hf-MOF, or Hf-MOL was injected *i.t.* with an equivalent DBP dose of 0.2 μmol (n = 5). Eight hours later, the mice were anesthetized with 2.5% (V/V) isoflurane/O_2 and covered by a black cloth. The tumor area was exposed and irradiated with LED light (630 nm, 100 mW/cm^2, 15 minutes, the CT26 model received the other dose of 90 J/cm^2 at day 10). Tumor sizes were measured with an electronic caliper (tumor volume = length×$width^2$/2) and body weight was monitored with an electronic scale. At day 19 and day 22 for subcutaneous CT26 and orthotopic 4T1 model, respectively, the mice were euthanized, and the tumors were weighed, photographed and sectioned for H&E and TUNEL staining. Major organs were sectioned for H&E staining to evaluate general toxicity. The lung sections from 4T1-bearing BALB/c mice were stained by H&E, and metastatic nodules were counted for statistical analysis.

TUNEL assay. Tumors were fixed in 4% PFA (freshly prepared and pH=7.1) for 1 day and 70% ethanol for 1 day. Tissues were embedded in paraffin, sectioned, and stained for TUNEL assay by the Human Tissue Resource Center at the University of Chicago.[57] The slides were then sealed and scanned on a CRi Pannoramic SCAN 40x whole slide scanner by Integrated Light Microscopy Core at the University of Chicago. The images were viewed and analyzed by QuPath-0.2.3 software.[58]

3.5 References

(1) Dolmans, D. E. J. G. J.; Fukumura, D.; Jain, R. K., Photodynamic therapy for cancer. *Nat. Rev. Cancer* **2003,** *3* (5), 380-387.

(2) Castano, A. P.; Mroz, P.; Hamblin, M. R., Photodynamic therapy and anti-tumour immunity. *Nat. Rev. Cancer* **2006,** *6* (7), 535-545.

(3) Pham, T. C.; Nguyen, V.-N.; Choi, Y.; Lee, S.; Yoon, J., Recent Strategies to Develop Innovative Photosensitizers for Enhanced Photodynamic Therapy. *Chem. Rev.* **2021,** *121* (21), 13454-13619.

(4) Lovell, J. F.; Liu, T. W. B.; Chen, J.; Zheng, G., Activatable Photosensitizers for Imaging and Therapy. *Chem. Rev.* **2010,** *110* (5), 2839-2857.

(5) Sorrin, A. J.; Kemal Ruhi, M.; Ferlic, N. A.; Karimnia, V.; Polacheck, W. J.; Celli, J. P.; Huang, H.-C.; Rizvi, I., Photodynamic Therapy and the Biophysics of the Tumor Microenvironment. *Photochem. Photobiol.* **2020,** *96* (2), 232-259.

(6) Dai, X.; Du, T.; Han, K., Engineering Nanoparticles for Optimized Photodynamic Therapy. *ACS Biomater. Sci. Eng.* **2019,** *5* (12), 6342-6354.

(7) Lucky, S. S.; Soo, K. C.; Zhang, Y., Nanoparticles in Photodynamic Therapy. *Chem. Rev.* **2015,** *115* (4), 1990-2042.

(8) dos Santos, A. F.; Arini, G. S.; de Almeida, D. R. Q.; Labriola, L., Nanophotosensitizers for cancer therapy: a promising technology? *J. Phys. Mater.* **2021,** *4* (3), 032006.

(9) Chitgupi, U.; Qin, Y.; Lovell, J. F., Targeted Nanomaterials for Phototherapy. *Nanotheranostics* **2017,** *1* (1), 38-58.

(10) Obaid, G.; Jin, W.; Bano, S.; Kessel, D.; Hasan, T., Nanolipid Formulations of Benzoporphyrin Derivative: Exploring the Dependence of Nanoconstruct Photophysics and Photochemistry on Their Therapeutic Index in Ovarian Cancer Cells. *Photochem. Photobiol.* **2019,** *95* (1), 364-377.

(11) Yu, W.; Ye, M.; Zhu, J.; Wang, Y.; Liang, C.; Tang, J.; Tao, H.; Shen, Y., Zinc phthalocyanine encapsulated in polymer micelles as a potent photosensitizer for the photodynamic therapy of osteosarcoma. *Nanomedicine* **2018,** *14* (4), 1099-1110.

(12) Macháček, M.; Carter, K. A.; Kostelanský, F.; Miranda, D.; Seffouh, A.; Ortega, J.; Šimůnek, T.; Zimčík, P.; Lovell, J. F., Binding of an amphiphilic phthalocyanine to pre-formed liposomes confers light-triggered cargo release. *J. Mater. Chem. B* **2018,** *6* (44), 7298-7305.

(13) Kramer, M.; Miller, J. W.; Michaud, N.; Moulton, R. S.; Hasan, T.; Flotte, T. J.; Gragoudas, E. S., Liposomal Benzoporphyrin Derivative Verteporfin Photodynamic Therapy: Selective Treatment of Choroidal Neovascularization in Monkeys. *Ophthalmology* **1996,** *103* (3), 427-438.

(14) de Oliveira, D. C. S.; de Freitas, C. F.; Calori, I. R.; Goncalves, R. S.; Cardinali, C. A. E. F.; Malacarne, L. C.; Ravanelli, M. I.; de Oliveira, H. P. M.; Tedesco, A. C.; Caetano, W.; Hioka, N.; Tessaro, A. L., Theranostic verteporfin- loaded lipid-polymer liposome for photodynamic applications. *J. Photochem. Photobiol., B* **2020,** *212*, 112039.

(15) Ghosh, S.; Carter, K. A.; Lovell, J. F., Liposomal formulations of photosensitizers. *Biomater.* **2019,** *218*, 119341.

(16) Charron, D. M.; Yousefalizadeh, G.; Buzzá, H. H.; Rajora, M. A.; Chen, J.; Stamplecoskie, K. G.; Zheng, G., Photophysics of J-Aggregating Porphyrin-Lipid Photosensitizers in Liposomes: Impact of Lipid Saturation. *Langmuir* **2020,** *36* (19), 5385-5393.

(17) Rizvi, I.; Nath, S.; Obaid, G.; Ruhi, M. K.; Moore, K.; Bano, S.; Kessel, D.; Hasan, T., A Combination of Visudyne and a Lipid-anchored Liposomal Formulation of Benzoporphyrin Derivative Enhances Photodynamic Therapy Efficacy in a 3D Model for Ovarian Cancer. *Photochem. Photobiol.* **2019,** *95* (1), 419-429.

(18) Mallidi, S.; Anbil, S.; Bulin, A.-L.; Obaid, G.; Ichikawa, M.; Hasan, T., Beyond the barriers of light penetration: strategies, perspectives and possibilities for photodynamic therapy. *Theranostics* **2016,** *6* (13), 2458.

(19) Zhao, L.; Kim, T.-H.; Kim, H.-W.; Ahn, J.-C.; Kim, S. Y., Enhanced cellular uptake and phototoxicity of Verteporfin-conjugated gold nanoparticles as theranostic nanocarriers for targeted photodynamic therapy and imaging of cancers. *Mater. Sci. Eng. C* **2016,** *67*, 611-622.

(20) Liu, H.; Hu, Y.; Sun, Y.; Wan, C.; Zhang, Z.; Dai, X.; Lin, Z.; He, Q.; Yang, Z.; Huang, P.; Xiong, Y.; Cao, J.; Chen, X.; Chen, Q.; Lovell, J. F.; Xu, Z.; Jin, H.; Yang, K., Co-delivery of Bee Venom Melittin and a Photosensitizer with an Organic–Inorganic Hybrid Nanocarrier for Photodynamic Therapy and Immunotherapy. *ACS Nano* **2019,** *13* (11), 12638-12652.

(21) Qiu, H.; Tan, M.; Ohulchanskyy, T. Y.; Lovell, J. F.; Chen, G., Recent Progress in Upconversion Photodynamic Therapy. *Nanomaterials* **2018,** *8* (5), 344.

(22) Liu, Y.; Zhu, D.; Xie, Z., Ir(III) Complex Dimer Nanoparticles for Photodynamic Therapy. *ACS Med. Chem. Lett.* **2021,** *12* (9), 1374-1379.

(23) Wang, D.; Wu, H.; Phua, S. Z. F.; Yang, G.; Qi Lim, W.; Gu, L.; Qian, C.; Wang, H.; Guo, Z.; Chen, H.; Zhao, Y., Self-assembled single-atom nanozyme for enhanced photodynamic therapy treatment of tumor. *Nat. Commun.* **2020,** *11* (1), 357.

(24) Lan, G.; Ni, K.; Lin, W., Nanoscale metal–organic frameworks for phototherapy of cancer. *Coord. Chem. Rev.* **2019,** *379*, 65-81.

(25) Lismont, M.; Dreesen, L.; Wuttke, S., Metal-Organic Framework Nanoparticles in Photodynamic Therapy: Current Status and Perspectives. *Adv. Funct. Mater.* **2017,** *27* (14), 1606314.

(26) Song, Y.; Wang, L.; Xie, Z., Metal–Organic Frameworks for Photodynamic Therapy: Emerging Synergistic Cancer Therapy. *Biotechnol. J.* **2021,** *16* (2), 1900382.

(27) Zhou, J.; Li, Y.; Wang, L.; Xie, Z., Structural diversity of nanoscale zirconium porphyrin MOFs and their photoactivities and biological performances. *J. Mater. Chem. B* **2021,** *9* (37), 7760-7770.

(28) Zhong, X.-f.; Sun, X., Nanomedicines based on nanoscale metal-organic frameworks for cancer immunotherapy. *Acta Pharmacol. Sin.* **2020,** *41* (7), 928-935.

(29) Lu, K.; He, C.; Lin, W., Nanoscale Metal–Organic Framework for Highly Effective Photodynamic Therapy of Resistant Head and Neck Cancer. *J. Am. Chem. Soc.* **2014,** *136* (48), 16712-16715.

(30) Lu, K.; He, C.; Guo, N.; Chan, C.; Ni, K.; Weichselbaum, R. R.; Lin, W., Chlorin-Based Nanoscale Metal–Organic Framework Systemically Rejects Colorectal Cancers via Synergistic Photodynamic Therapy and Checkpoint Blockade Immunotherapy. *J. Am. Chem. Soc.* **2016,** *138* (38), 12502-12510.

(31) Luo, T.; Ni, K.; Culbert, A.; Lan, G.; Li, Z.; Jiang, X.; Kaufmann, M.; Lin, W., Nanoscale Metal–Organic Frameworks Stabilize Bacteriochlorins for Type I and Type II Photodynamic Therapy. *J. Am. Chem. Soc.* **2020,** *142* (16), 7334-7339.

(32) Rajasree, S. S.; Li, X.; Deria, P., Physical properties of porphyrin-based crystalline metal–organic frameworks. *Commun. Chem.* **2021,** *4* (1), 47.

(33) Zheng, X.; Wang, L.; Pei, Q.; He, S.; Liu, S.; Xie, Z., Metal–Organic Framework@Porous Organic Polymer Nanocomposite for Photodynamic Therapy. *Chem. Mater.* **2017,** *29* (5), 2374-2381.

(34) Park, J.; Jiang, Q.; Feng, D.; Mao, L.; Zhou, H.-C., Size-Controlled Synthesis of Porphyrinic Metal–Organic Framework and Functionalization for Targeted Photodynamic Therapy. *J. Am. Chem. Soc.* **2016,** *138* (10), 3518-3525.

(35) Alves, S. R.; Calori, I. R.; Tedesco, A. C., Photosensitizer-based metal-organic frameworks for highly effective photodynamic therapy. *Mater. Sci. Eng. C* **2021,** *131*, 112514.

(36) Wang, L.; Zheng, M.; Xie, Z., Nanoscale metal–organic frameworks for drug delivery: a conventional platform with new promise. *J. Mater. Chem. B* **2018,** *6* (5), 707-717.

(37) Feng, X.; Song, Y.; Lin, W., Dimensional Reduction of Lewis Acidic Metal–Organic Frameworks for Multicomponent Reactions. *J. Am. Chem. Soc.* **2021,** *143* (21), 8184-8192.

(38) Feng, X.; Lin, W., From 3D to 2D: Multifunctional metal-organic layers for organic synthesis. *Matter* **2021,** *4* (8), 2683-2685.

(39) Xu, Z.; Luo, T.; Lin, W., Nanoscale Metal–Organic Layers for Biomedical Applications. *Acc. Mater. Res.* **2021,** *2* (10), 944-953.

(40) McNicholas, K.; MacGregor, M. N.; Gleadle, J. M., In order for the light to shine so brightly, the darkness must be present—why do cancers fluoresce with 5-aminolaevulinic acid? *Br. J. Cancer* **2019,** *121* (8), 631-639.

(41) Lu, K.; He, C.; Guo, N.; Chan, C.; Ni, K.; Lan, G.; Tang, H.; Pelizzari, C.; Fu, Y.-X.; Spiotto, M. T.; Weichselbaum, R. R.; Lin, W., Low-dose X-ray radiotherapy–radiodynamic therapy via

nanoscale metal–organic frameworks enhances checkpoint blockade immunotherapy. *Nat. Biomed. Eng.* **2018,** *2* (8), 600-610.

(42) Melle, S.; Calderón, O. G.; Laurenti, M.; Mendez-Gonzalez, D.; Egatz-Gómez, A.; López-Cabarcos, E.; Cabrera-Granado, E.; Díaz, E.; Rubio-Retama, J., Förster Resonance Energy Transfer Distance Dependence from Upconverting Nanoparticles to Quantum Dots. *J. Phys. Chem. C* **2018,** *122* (32), 18751-18758.

(43) Blum, N. T.; Zhang, Y.; Qu, J.; Lin, J.; Huang, P., Recent Advances in Self-Exciting Photodynamic Therapy. *Front. Bioeng. Biotechnol.* **2020,** *8* (1136).

(44) Wu, W.; Shao, X.; Zhao, J.; Wu, M., Controllable Photodynamic Therapy Implemented by Regulating Singlet Oxygen Efficiency. *Adv. Sci.* **2017,** *4* (7), 1700113.

(45) Silva, E. F. F.; Serpa, C.; Dąbrowski, J. M.; Monteiro, C. J. P.; Formosinho, S. J.; Stochel, G.; Urbanska, K.; Simões, S.; Pereira, M. M.; Arnaut, L. G., Mechanisms of Singlet-Oxygen and Superoxide-Ion Generation by Porphyrins and Bacteriochlorins and their Implications in Photodynamic Therapy. *Chem. Eur. J* **2010,** *16* (30), 9273-9286.

(46) Krysko, D. V.; Garg, A. D.; Kaczmarek, A.; Krysko, O.; Agostinis, P.; Vandenabeele, P., Immunogenic cell death and DAMPs in cancer therapy. *Nat. Rev. Cancer* **2012,** *12* (12), 860-875.

(47) Yang, L.; Yong, L.; Zhu, X.; Feng, Y.; Fu, Y.; Kong, D.; Lu, W.; Zhou, T.-y., Disease progression model of 4T1 metastatic breast cancer. *J. Pharmacokinet. Pharmacodyn.* **2020,** *47* (1), 105-116.

(48) Wang, X.; Hu, J.; Wang, P.; Zhang, S.; Liu, Y.; Xiong, W.; Liu, Q., Analysis of the *In Vivo* and *In Vitro* Effects of Photodynamic Therapy on Breast Cancer by Using a Sensitizer, Sinoporphyrin Sodium. *Theranostics* **2015,** *5* (7), 772-786.

(49) Abraham, M. J.; Murtola, T.; Schulz, R.; Páll, S.; Smith, J. C.; Hess, B.; Lindahl, E., GROMACS: High performance molecular simulations through multi-level parallelism from laptops to supercomputers. *SoftwareX* **2015,** *1-2*, 19-25.

(50) Chen, X.; Zhuang, Y.; Rampal, N.; Hewitt, R.; Divitini, G.; O'Keefe, C. A.; Liu, X.; Whitaker, D. J.; Wills, J. W.; Jugdaohsingh, R.; Powell, J. J.; Yu, H.; Grey, C. P.; Scherman, O. A.; Fairen-Jimenez, D., Formulation of Metal–Organic Framework-Based Drug Carriers by Controlled Coordination of Methoxy PEG Phosphate: Boosting Colloidal Stability and Redispersibility. *J. Am. Chem. Soc.* **2021,** *143* (34), 13557-13572.

(51) Ji, P.; Manna, K.; Lin, Z.; Feng, X.; Urban, A.; Song, Y.; Lin, W., Single-Site Cobalt Catalysts at New Zr12(μ3-O)8(μ3-OH)8(μ2-OH)6 Metal–Organic Framework Nodes for Highly Active Hydrogenation of Nitroarenes, Nitriles, and Isocyanides. *J. Am. Chem. Soc.* **2017,** *139* (20), 7004-7011.

(52) Rappe, A. K.; Goddard, W. A., Charge equilibration for molecular dynamics simulations. *The Journal of Physical Chemistry* **1991,** *95* (8), 3358-3363.

(53) Ongari, D.; Boyd, P. G.; Kadioglu, O.; Mace, A. K.; Keskin, S.; Smit, B., Evaluating Charge Equilibration Methods To Generate Electrostatic Fields in Nanoporous Materials. *J. Chem. Theory Comput.* **2019,** *15* (1), 382-401.

(54) Garberoglio, G., OBGMX: A web-based generator of GROMACS topologies for molecular and periodic systems using the universal force field. *J. Comput. Chem.* **2012,** *33* (27), 2204-2208.

(55) Rappe, A. K.; Casewit, C. J.; Colwell, K. S.; Goddard, W. A.; Skiff, W. M., UFF, a full periodic table force field for molecular mechanics and molecular dynamics simulations. *J. Am. Chem. Soc.* **1992,** *114* (25), 10024-10035.

(56) Essmann, U.; Perera, L.; Berkowitz, M. L.; Darden, T.; Lee, H.; Pedersen, L. G., A smooth particle mesh Ewald method. *J. Chem. Phys.* **1995,** *103* (19), 8577-8593.

(57) Luo, T.; Nash, G. T.; Xu, Z.; Jiang, X.; Liu, J.; Lin, W., Nanoscale Metal–Organic Framework Confines Zinc-Phthalocyanine Photosensitizers for Enhanced Photodynamic Therapy. *J. Am. Chem. Soc.* **2021,** *143* (34), 13519-13524.

(58) Bankhead, P.; Loughrey, M. B.; Fernández, J. A.; Dombrowski, Y.; McArt, D. G.; Dunne, P. D.; McQuaid, S.; Gray, R. T.; Murray, L. J.; Coleman, H. G.; James, J. A.; Salto-Tellez, M.; Hamilton, P. W., QuPath: Open source software for digital pathology image analysis. *Sci. Rep.* **2017,** *7* (1), 16878.

Chapter 4. Metal-Organic Layer Delivers 5-Aminolevulinic Acid and Porphyrin for Dual-Organelle-Targeted Photodynamic Therapy

4.1 Introduction

In the previous chapter, we disclosed 2-D nMOL comprising PSs as a novel and efficient class of nanophotosensitizers.[1-3] The 2-D MOL spatially isolates PSs by SBUs to prevent self-quenching while maximizing the accessibility of PSs to $^3O_2$ for efficient energy transfer and $^1O_2$ generation.[4-5] Since the generated ROS can only diffuse in the submicron range in biological systems,[6-9] PDT efficacy strongly depends on the subcellular localization of PSs.[10-12]

Subcellular organelles are cornerstones of cells and play vital roles in regulating and maintaining cell functions. Some PSs can localize in specific organelles such as endo/lysosomes, endoplasmic reticulums, and mitochondria.[13-15] PDT causes damage to these organelles by excessive oxidative stress, membrane permeabilization, and expression of proapoptotic factors to initiate cell apoptosis.[16-17] The destruction of specific organelles can elicit more lethal cell damage.[18-19] We posited that nanophotosensitizers with the ability to target multiple organelles could synergistically enhance cell death to provide potent PDT efficacy.

5-aminolevulinic acid (ALA), an endogenous metabolite in the heme synthesis pathway, has received FDA approval for PDT of actinic keratosis and fluorescence-guided visualization of malignant tissues during glioma surgery.[20-22] ALA selectively accumulates in mitochondria and produces photosensitizing protoporphyrin IX (PpIX).[23-25] However, the low bioavailability and irreversible dimerization of ALA under physiological conditions limit its clinical performance.[26-27]

In this Chapter, we report a dual-organelle-targeted nanoparticle platform, ALA/Hf-MOL, for enhanced PDT of cancer. ALA/Hf-MOL was synthesized by grafting ALA to Hf-MOL via Hf-carboxylate coordination. ALA/Hf-MOL enhanced ALA delivery and PpIX synthesis in mitochondria while trapping the Hf-MOL comprising DBP photosensitizing ligands in endo/lysosomes. Light irradiation at 630 nm simultaneously excited PpIX and DBP to generate singlet oxygen and cause mitochondrial membrane permeabilization (MMP) and lysosomal membrane permeabilization (LMP), respectively, in cancer cells, leading to the concomitant release of cytochrome C and cathepsin B, respectively (**Figure 4-1**). The dual-organelle-targeted PDT by ALA/Hf-MOL enhanced cell death *in vitro* and PDT efficacy in a murine colon cancer model *in vivo*.

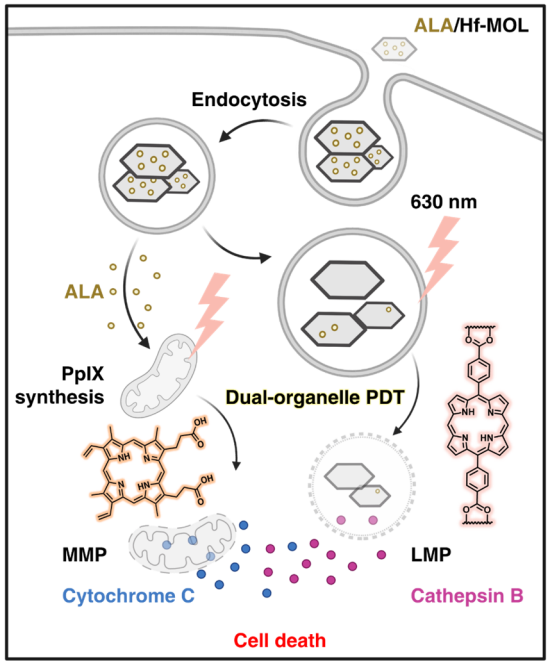

Figure 4-1. Schematic showing dual-organelle-targeted PDT by ALA/Hf-MOL. After endocytosis, ALA is released from Hf-MOL via the phosphate concentration gradient and enables PpIX synthesis in mitochondria, while Hf-MOL is trapped in endo/lysosomes. The ROS generated from light irradiation causes membrane permeabilization of both lysosomes and mitochondria to release cathepsin B and cytochrome C, respectively, which synergistically elicits potent cell death.

4.2 Results and Discussions

4.2.1 Synthesis and Characterization of ALA/Hf-MOL

Hf-MOL was synthesized by heating H_2DBP and $HfCl_4$ in DMF at 80 ºC with water and PA as modulators.[5] The capping PA was subsequently replaced by TFA, as confirmed by the decrease of the PA intensity in the ^{1}H-NMR spectrum and the appearance of the TFA peak in the ^{19}F-NMR spectrum (**Figure 4-2a,b**). ALA/Hf-MOL was synthesized by carboxylate exchange in DMF at room temperature. The ALA to DBP ratio in ALA/Hf-MOL was 74.5% by ^{1}H-NMR (**Figure 4-2c**), affording a chemical formula of $Hf_{12}(\mu_3\text{-}O)_8(\mu_3\text{-}OH)_8(\mu_2\text{-}OH)_6(DBP)_6(\mu_2\text{-}ALA)_{4.47}(\mu_2\text{-}TFA)_{1.53}$.

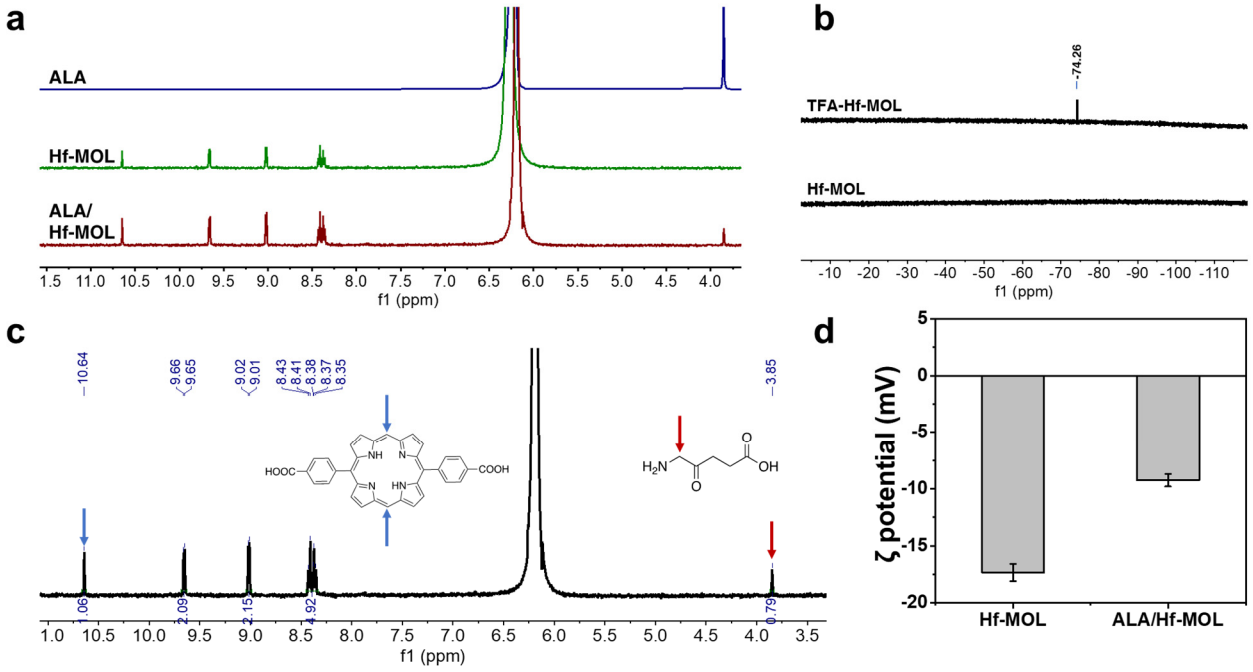

Figure 4-2. Synthesis of ALA/Hf-MOL. (a) ^{1}H-NMR spectra of ALA, digested Hf-MOL, and digested ALA/Hf-MOL. (b) ^{19}F NMR spectra of digested Hf-MOL and TFA-Hf-MOL. (c) The loading efficiency of ALA was calculated by dividing the integral of ALA by that of DBP. (d) ζ-potentials of Hf-MOL and ALA/Hf-MOL in water (mean ± SD).

TEM images showed that ALA/Hf-MOL retained the nanoplate morphology with a size of ~200 nm (**Figure 4-3a,b**). DLS measurements of Hf-MOL and ALA/Hf-MOL showed comparable number-average sizes of 208.4 ± 4.5 nm and 202.4 ± 5.6 nm, and polydispersity indices of 0.061 and 0.088, respectively (**Figure 4-3c**). PXRD studies indicated that ALA/Hf-MOL retained the crystalline framework after ALA loading and incubation with PBS (**Figure 4-3d**).

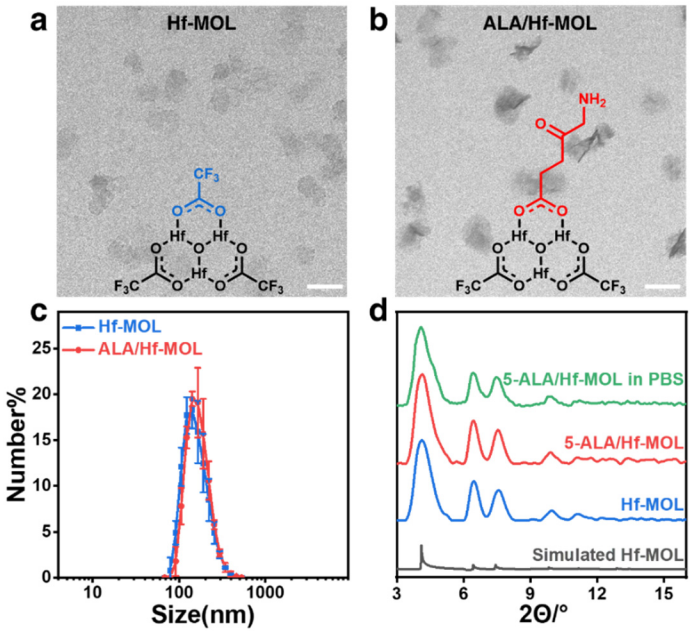

Figure 4-3. Characterization of ALA/Hf-MOL. TEM images of (a) Hf-MOL after TFA modification and (b) ALA/Hf-MOL. Scale bar = 200 nm. The coordination of TFA and ALA to Hf_{12} SBUs is also shown. (c) Number-averaged sizes and (d) PXRD patterns of Hf-MOL and ALA/Hf-MOL.

4.2.2 Release Profiles of ALA

Liquid chromatography-mass spectrometry (LC-MS) analysis indicated that ALA could be released from ALA/Hf-MOL in a pH-independent but phosphate concentration-dependent manner (**Figure 4-4**). As Hf-MOL is stable in PBS (~10 mM phosphate), the release of ALA is likely caused by the substitution of ALA on Hf_{12} SBUs by phosphate anions in the physiological environment. Furthermore, as the cytoplasm has ~10-fold higher free phosphate concentration

(~10 mM phosphate) than the interstitial fluid or plasma (~1 mM phosphate),[28-32] ALA/Hf-MOL can retain ALA in the extracellular space but rapidly release ALA upon uptake by cells with a higher phosphate concentration.[33]

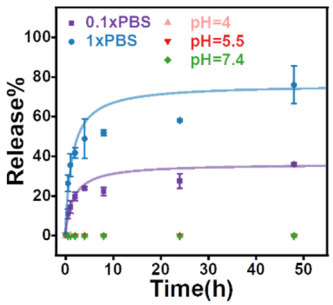

Figure 4-4. Release profiles of ALA/Hf-MOL. (1x PBS ≈ 10 mM phosphate, 0.1 x PBS ≈ 1 mM phosphate)

4.2.3 ROS Generation and Cell Viability Assays

The SOSG assay showed similar $^1O_2$ generation by Hf-MOL and ALA/Hf-MOL under 630 nm light irradiation, indicating that conjugation of ALA to Hf-MOL did not impact $^1O_2$ generation from Hf-MOL (**Figure 4-5a**). However, cell viability assays revealed that ALA/Hf-MOL with 630 nm light irradiation [denoted ALA/Hf-MOL(+)] exhibited an IC_{50} value of 0.28 ± 0.13 μM in CT26 cells, which was 2.7-fold lower than that of Hf-MOL(+) (0.76 ± 0.13 μM, **Figure 4-5b**). ALA(+) showed negligible cytotoxicity. No dark toxicity was observed in all treatment groups (**Figure 4-5c-e**). A physical mixture of ALA and Hf-MOL showed weakly additive phototoxicity with an IC_{50} value of 0.63 ± 0.09 μM (**Figure 4-5b**). As Hf-MOL and ALA/Hf-MOL show comparable cellular uptake and ROS generation (**Figure 4-5f**), we hypothesize that the synergistic PDT enhancement by ALA/Hf-MOL over Hf-MOL is attributed to improved ALA delivery and PpIX synthesis.

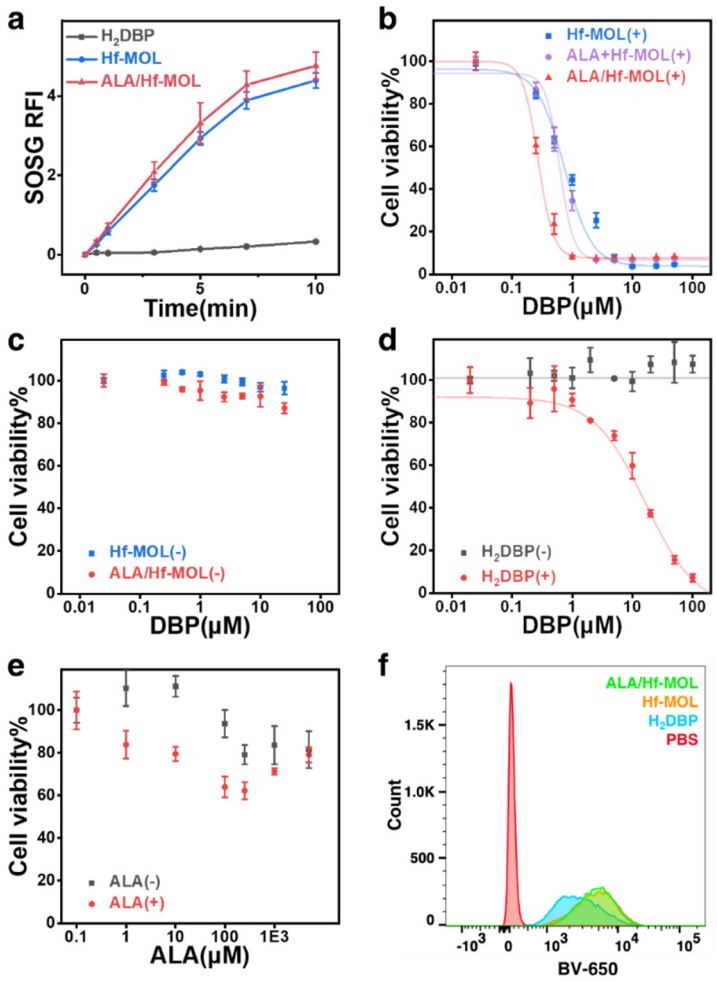

Figure 4-5. ROS Generation and *in vitro* cell killing. (a) SOSG assays showing comparable $^1O_2$ generation by Hf-MOL and ALA/Hf-MOL under 630 nm light irradiation (100 mW/cm^2). All data are shown as mean ± SD with *n*=3. (b) Cell viability assays of Hf-MOL, a physical mixture of ALA and Hf-MOL, and ALA/Hf-MOL in CT26 cells with a total light dose of 90 J/cm^2 at 630 nm (mean ± SD, *n*=3). Cell viability curves (mean ± SD) of (c) ALA/Hf-MOL and Hf-MOL without light irradiation [denoted (-)], and (d) H2DBP and (e) ALA with or without light irradiation. (f) Histograms showing DBP fluorescence intensity of H2DBP, Hf-MOL, and ALA/Hf-MOL-treated cells by flow cytometry.

4.2.4 ALA Delivery *In Vitro* and PpIX Accumulation in Mitochondria

We used LC-MS to quantify PpIX in cultured CT26 cells and subcutaneous CT26 tumors after different treatments (**Figure 4-6a**).[34] ALA/Hf-MOL showed significantly higher PpIX accumulation with 2.3-fold and 1.5-fold higher PpIX content than free ALA *in vitro* (**Figure 4-**

6b) and *in vivo* (**Figure 4-6c**), respectively. Flow cytometric analysis of mitochondria isolated from cultured CT26 cells showed that ALA/Hf-MOL treatment led to >4.3-fold PpIX accumulation than free ALA or PBS treatment (**Figure 4-6d**). These results confirm the improved ALA delivery and PpIX synthesis by ALA/Hf-MOL.

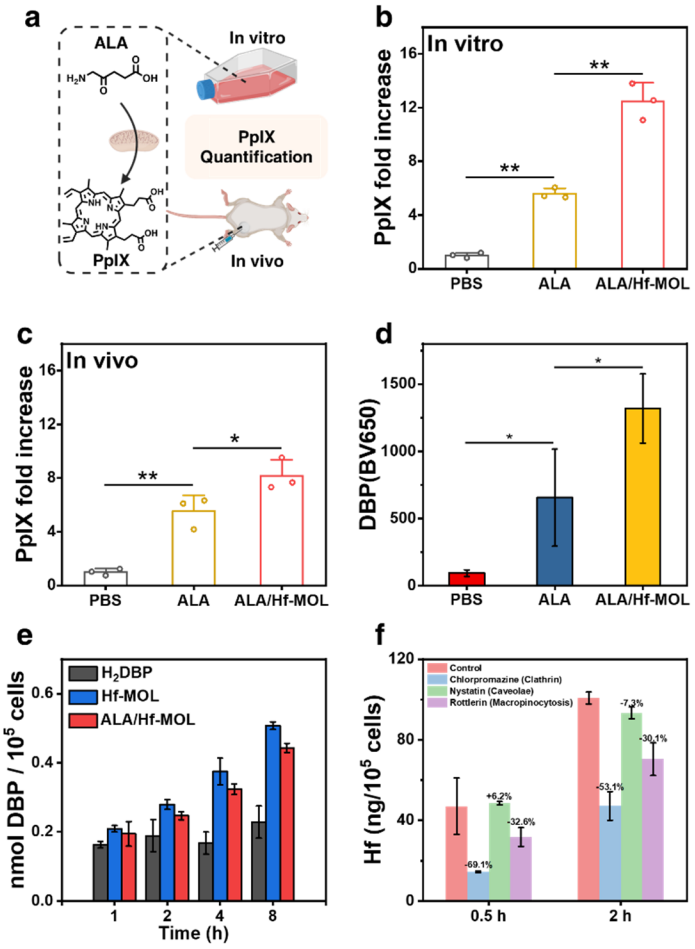

Figure 4-6. PpIX quantification and cellular uptake. (a) Schematic showing PpIX quantification. PpIX fold increase in (b) CT26 cells or in (c) CT26 tumor-bearing BALB/c mice after indicated treatments (mean + SD, *n*=3). (d) MFI (mean ± SD, *n*=3) of PpIX in isolated mitochondria. (e) Time-dependent cellular uptake (mean ± SD, *n*=3) of H_2DBP, Hf-MOL, and ALA/Hf-MOL quantified by UV-Vis. (f) Time-dependent endocytosis with inhibition (mean ± SD, *n*=3) by chlorpromazine, nystatin, and rottlerin.

4.2.5 Dual-Organelle Disruption by ALA/Hf-MOL

To study the endocytosis mechanism, 100 μM chlorpromazine, 270 μM nystatin, or 5 μM Rottlerin was added to CT26 cells and incubated for 30 minutes to inhibit clathrin, caveolae, or macropinocytosis-mediated endocytotic pathway, respectively.[35] The obvious inhibition by chlorpromazine and rottlerin indicates that Hf-MOL is uptaken into CT26 cells through the clathrin-dependent pathway and macropinocytosis and retained DBP in lysosomes (**Figure 4-6e,f**).

We next used CLSM to study the subcellular localization of ALA/Hf-MOL and to observe the dual-organelle targeting in real-time. ALA/Hf-MOL-treated CT26 cells showed smeared red signals (PpIX) in addition to distinct puncta (Hf-MOL), suggesting the conversion of ALA to PpIX and retention of Hf-MOL in lysosomes (**Figure 4-7**).

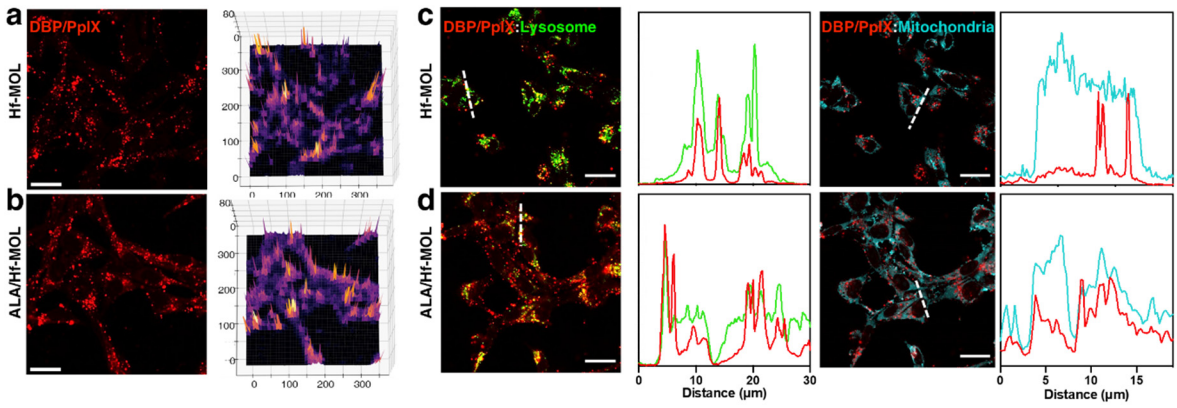

Figure 4-7. Colocalization analysis of PpIX and DBP with mitochondria and lysosomes. CLSM images showing red fluorescence puncta of (a) Hf-MOL and smeared red fluorescence in (b) ALA/Hf-MOL treated cells, indicating PpIX synthesis in cells. Intensity profiles of the white dashed lines in the CLSM images show the colocalization between Hf-MOL and lysosomes and colocalization between PpIX and mitochondria in (c) Hf-MOL and (d) ALA/Hf-MOL groups (H_2DBP or PpIX, red; lysosomes, green; mitochondria, cyan; scale bar = 10 μm).

We then co-stained CT26 cells with LysoTracker Green DND-26 and MitoSOX Superoxide Indicator Red to monitor the real-time status of lysosomes and mitochondria, respectively. Using the built-in 630 nm monochromatic laser in the confocal microscope, we performed *in situ* PDT

while recording real-time images of subcellular organelles. The fluorescence signals of lysosomes and mitochondria were retained in the cells treated with PBS(+) or ALA(+), indicating no cellular damage (**Figure 4-8a,b**). Hf-MOL(+) moderately compromised the integrity of lysosomes and mitochondria, but neither organelle reached more than 40% damage after 15 minutes of PDT (**Figure 4-8c**). In stark contrast, ALA/Hf-MOL(+) induced rapid depolarization of both lysosomes and mitochondria (**Figure 4-8d**), with fluorescence signals decreasing to <50% within 2 minutes of light exposure (**Figure 4-8e,f**).

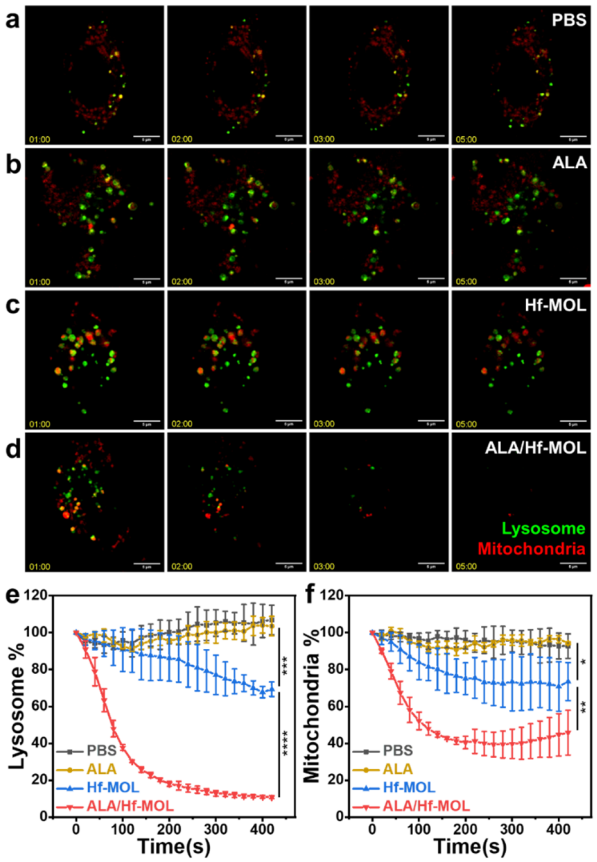

Figure 4-8. Live imaging of dual-organelle disruption in vitro. Real-time imaging of lysosomes (green) and mitochondria (red) in CT26 cells treated with (a) PBS(+), (b) ALA(+), (c) Hf-MOL(+), and (d) ALA/Hf-MOL(+). A dose of 1 μM DBP and a fluence of 100 mW/cm^2 laser at 630 nm were used. From left to right, the cells were irradiated for 1, 2, 3, and 5 minutes, respectively. All scale bars are 5 μm. Time-dependent retention (mean ± SD, n=3) of (e) lysosomal and (f) mitochondrial signals in different treatment groups.

4.2.6 Mitochondria and Lysosome Membrane Permeabilization

To investigate the effect of dual-organelle-targeted PDT on MMP and LMP, we stained mitochondria and lysosomes for viability markers and organelle contents.[36-39] ALA/Hf-MOL(+) caused the strongest depolarization of mitochondrial membrane potential as visualized by increased monomer signals in JC-1 assay (**Figure 4-9a**) and the higher cytochrome C release from mitochondria (**Figure 4-9b**). The reduced fluorescence of acridine orange (AO) in the Hf-MOL(+) and ALA/Hf-MOL(+) groups indicated the induction of LMP, suggesting the dysregulation of lysosome pH due to photodamage (**Figure 4-9c**). The release of cathepsin B from lysosomes was visualized as scattered fluorescence signals in the cytosol (**Figure 4-9d**). The ROS level in ALA/Hf-MOL(+)-treated cells was 2.3-fold higher than Hf-MOL(+) (**Figure 4-9e**), which further supported the photosensitization of the synthesized PpIX and the increased oxidative stress from enhanced MMP and LMP. Apoptotic cells were labeled by Annexin-V, and the plasma membrane permeabilization was stained with PI. CLSM and flow cytometry studies showed that ALA/Hf-MOL(+) treatment gave a higher Annexin-V^+/PI^+ population than Hf-MOL(+) treatment (**Figure 4-9f**). ALA/Hf-MOL(+) also upregulated CRT on cell surfaces for enhanced immunogenic cell death (**Figure 4-9g**). Taken together, ALA/Hf-MOL(+) synergistically disrupts lysosomes and mitochondria to enhance cell death, thus providing a novel platform for dual-organelle-targeted PDT.

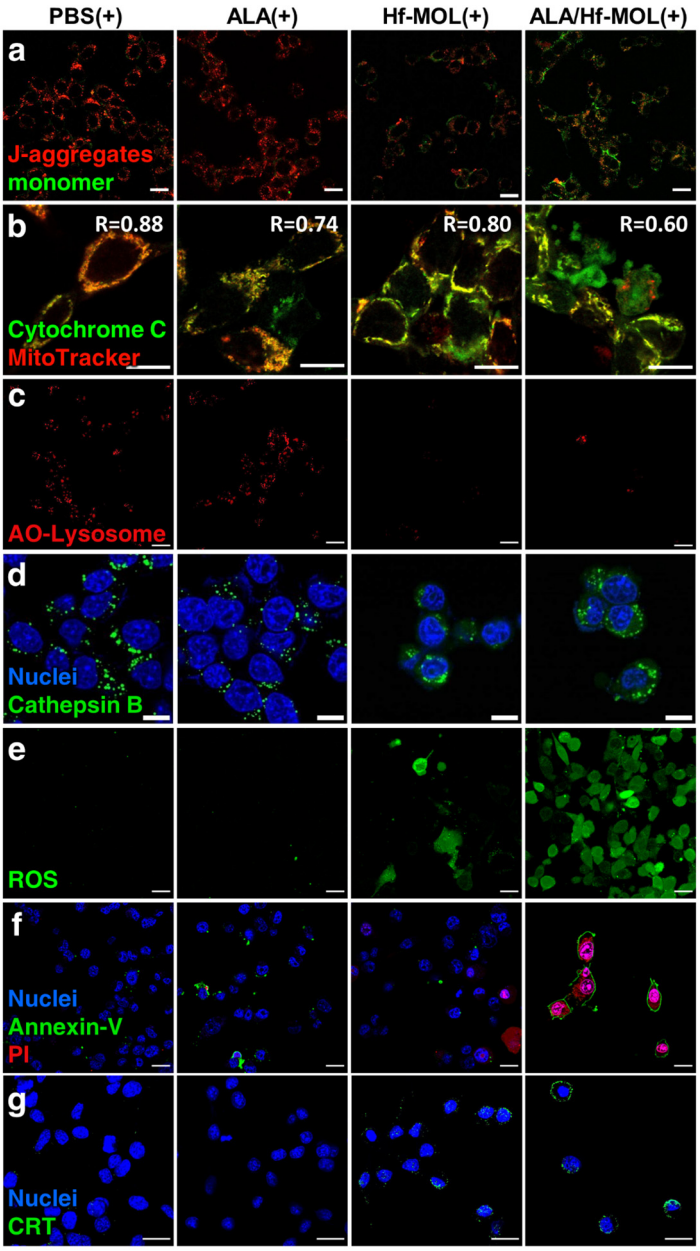

Figure 4-9. LMP, MMP, and ICD observed by CLSM. (a) Mitochondrial potential depolarization by JC-1 assay. Red and green channels indicate J-aggregate and monomer forms of JC-1 molecules, respectively. b) Cytochrome C (green) release from mitochondria. c) LMP visualized by AO assay. d) Cathepsin B (green) release from lysosomes by CV-Cathepsin-B assay. e) DCF-DA assay showing total ROS (green) generation. f) Apoptosis assay by Annexin-V (green) and PI (red) staining. Nuclei were visualized by Hoechst 33342 (blue). The different treatments are shown at the top. A dose of 5 μM DBP and a light dose of 60 J/cm^2 at 630 nm were used in CT26 cells. All scale bars are 20 μm.

4.2.7 *In Vivo* Antitumor Efficacy

The *in vivo* antitumor efficacy was then evaluated in subcutaneous CT26 tumor-bearing BALB/c mice. Compared to PBS(+) control group, ALA(-), Hf-MOL(-), and ALA/Hf-MOL(-) groups showed negligible antitumor efficacy with tumor growth inhibition (TGI) values of <2% (**Table 4-1, Figure 4-10a-d**). ALA(+) moderately inhibited tumor growth with a TGI value of 54.1%. ALA/Hf-MOL(+) significantly improved tumor regression with a TGI value of 99.2%, which was higher than the TGI value of 89.6% for Hf-MOL(+) (**Figure 4-10a,b**). ALA/Hf-MOL(+) was also significantly more effective than a physical mixture of ALA and MOL plus light irradiation (TGI = 84.8%, **Figure 4-10e**).

Table 4-1. TGI values of CT26-bearing BALB/c mice at day 20.

Treatment	TGI(CT26)
ALA(+)	0.541
Hf-MOL(+)	0.896
ALA/Hf-MOL(+)	0.992
ALA(-)	-0.0939
Hf-MOL(-)	-0.152
ALA/Hf-MOL(-)	0.0151
ALA+Hf-MOL(-)	0.0204
ALA+Hf-MOL(+)	0.848

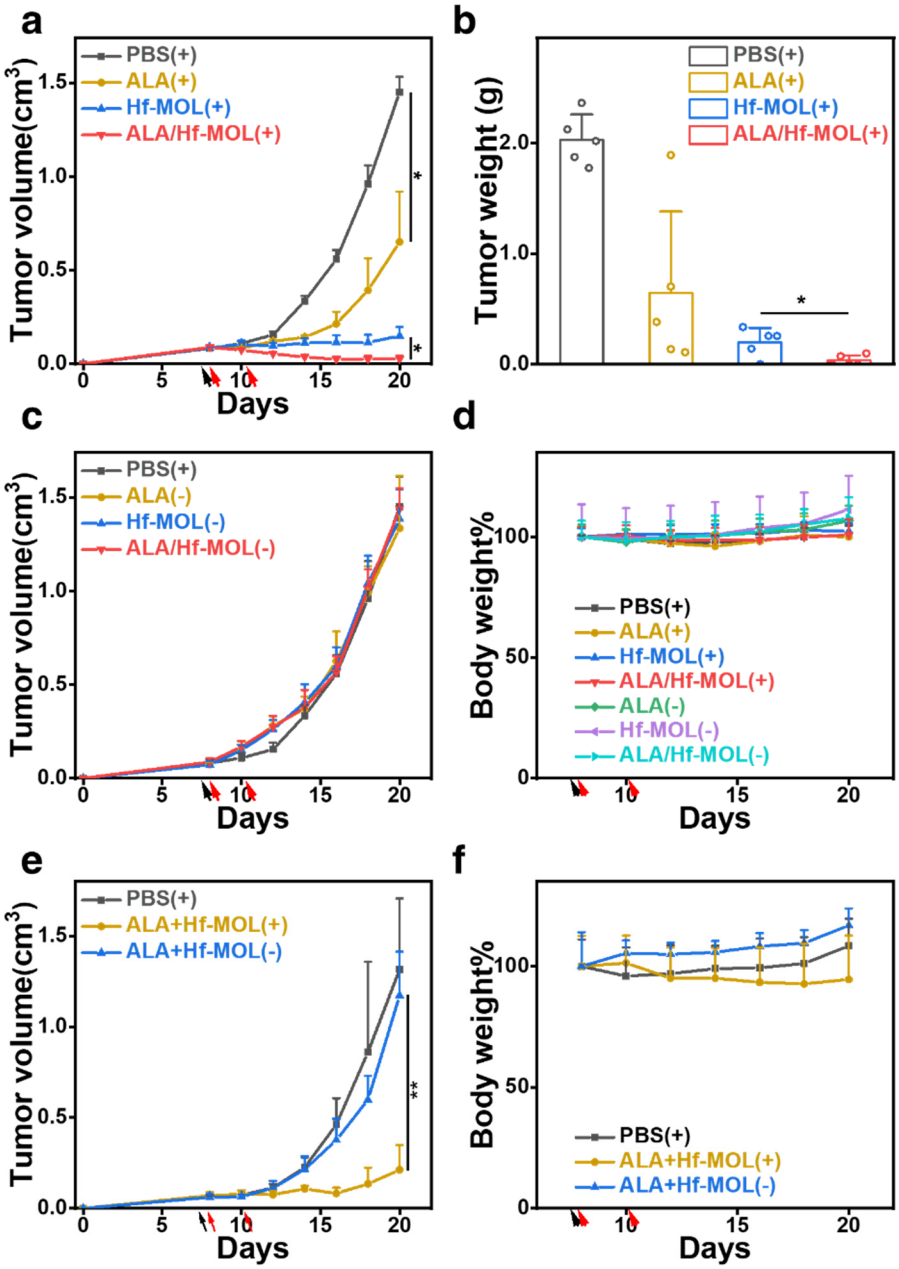

Figure 4-10. Antitumor efficacy. (a) Tumor growth curves and (b) tumor weights of CT26 tumor-bearing BALB/c mice (n=5) after PDT treatment with PBS(-), ALA(+), Hf-MOL(+), or ALA/Hf-MOL(+) (black and red arrows refer to particle administration and light irradiation of 90 J/cm^2 at 630 nm, respectively). (c) CT26 tumor volume curves and (d) body weight plots of CT26-bearing BALB/c mice without light irradiation. (e) CT26 tumor volumes and (f) body weights of CT26-bearing BALB/c mice treated by a physical mixture of ALA and Hf-MOL with or without light irradiation. All data are shown as mean + SD with n=5. *, $p < 0.05$; **, $p < 0.01$; ***, $p < 0.001$.

Hf-MOL(+) eradicated tumors in only 20% of mice, while ALA/Hf-MOL(+) eradicated tumors in 60% of mice. These treatments had minimal impact on mouse health (**Figure 4-10f, Figure 4-11a**). The effective cancer cell killing was also corroborated by TUNEL staining; ALA/Hf-MOL(+) showed more DNA fragments than Hf-MOL(+) and other control groups (**Figure 4-11b,c**).

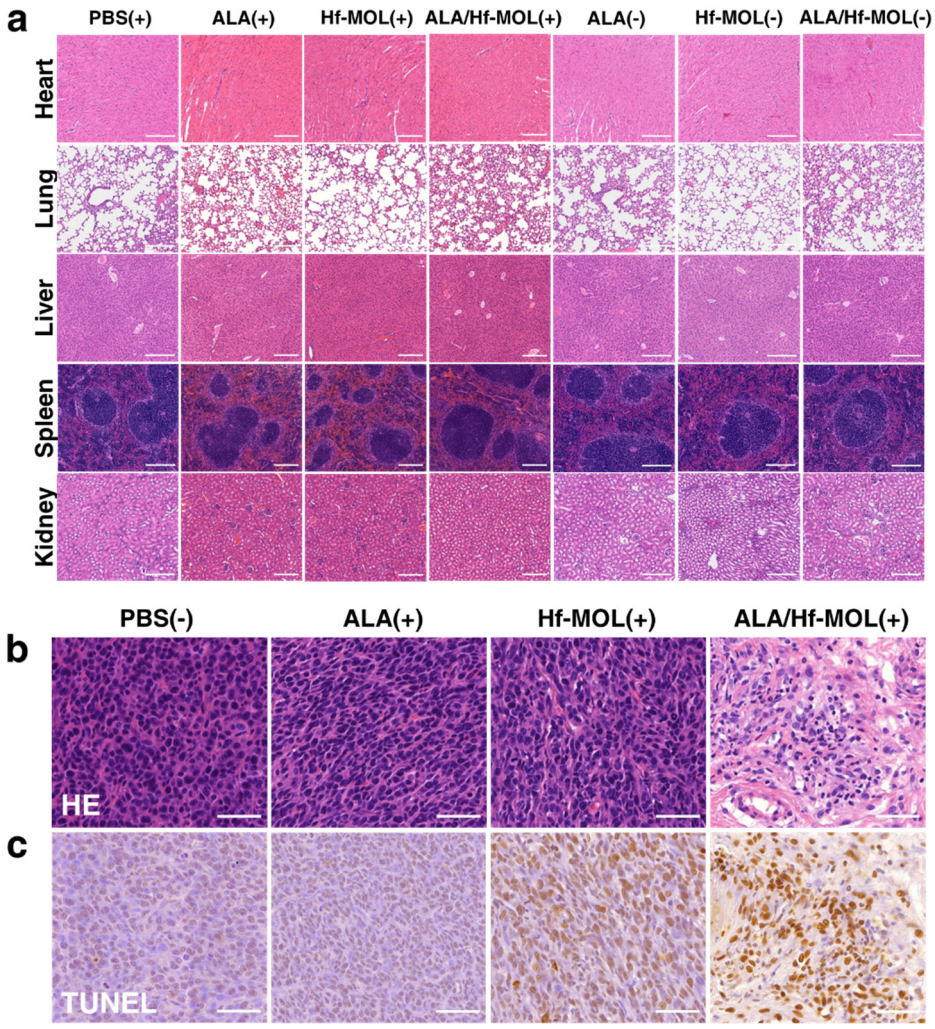

Figure 4-11. Histological staining. (a) H&E staining of hearts, lungs, livers, spleens, and kidneys from CT26 tumor-bearing BALB/c mice in different treatment groups (scale bar = 200 μm). Representative images of (b) H&E staining and (c) TUNEL staining of excised CT26 tumors (Scale bars = 100 μm).

4.2.8 *In Vivo* Dual-Organelle Targeting

We excised the tumors immediately after PDT treatment and stained viable tumor cells with functional lysosome and mitochondria markers to verify the dual-organelle disruption. Compared to ALA(+), ALA/Hf-MOL(+) showed 5.5-fold and 1.9-fold decreases in viable mitochondria and lysosomes, respectively (**Figure 4-12**).

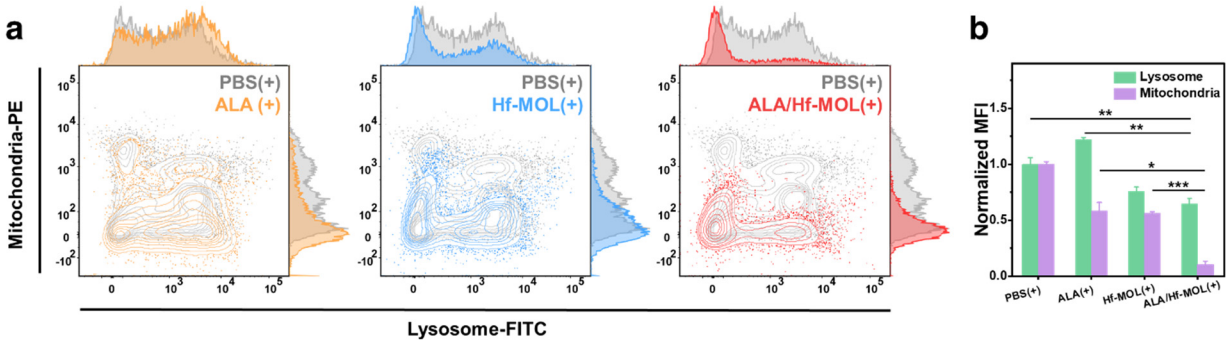

Figure 4-12. Viable lysosomes and mitochondria in tumors. (a) Representative contour plots with adjunct histograms showing functional staining of both lysosome (LysoTracker Green DND-26 in FITC channel, x-axis) and mitochondria (MitoSOX Superoxide Indicator Red in PE channel, y-axis) of viable CT26 tumor cells. (b) Normalized MFI of lysosomal and mitochondrial staining of viable CT26 tumor cells showing significant dual-organelle damage induced by ALA/Hf-MOL(+) *in vivo* (n=3).

4.3 Conclusions

In this Chapter, we have designed a dual-organelle-targeted nanophotosensitizer by conjugating ALA to the SBUs of Hf-MOL. ALA/Hf-MOL enhanced ALA delivery and PpIX synthesis in mitochondria while retaining the photosensitizing Hf-MOL in lysosomes. Dual-organelle disruption induced synergistic PDT enhancement for superb anticancer efficacy *in vitro* and *in vivo*. Thus, MOLs provide a unique molecular nanomaterial platform to develop dual-organelle-targeted cancer therapy.

4.4 Methods

Synthesis and characterization of Hf-MOL and ALA/Hf-MOL. H_2DBP and Hf-MOL were synthesized as previously reported.[5] Trifluoroacetic acid (TFA) modification of Hf-MOL was conducted according to previous reports.[40] Briefly, a Hf-MOL suspension in ethanol was washed sequentially with anhydrous acetonitrile and toluene. The Hf-MOL suspension was degassed with N_2, and 5 mL of Hf-MOL in toluene (DBP concentration = 1 mM) was added and then treated with 20-fold TFA-TMS over PA. The reaction was stirred at room temperature for 16 hours. The Hf-MOL was then centrifuged and washed with acetonitrile and ethanol sequentially. The replacement of PA by TFA was demonstrated by ^{1}H-NMR and ^{19}F-NMR spectroscopy. To prepare ALA/Hf-MOL, 1 mL TFA-modified Hf-MOL was dispersed in DMF at a DBP concentration of 1 mM, and 10 mg of ALA was added to the suspension under stirring overnight. The resulting ALA/Hf-MOL was then collected by centrifugation, washed with ethanol, and stored in ethanol in a 4 ºC refrigerator. For NMR analysis, 1 mg of the sample was dried in a vacuum overnight and dispersed in a mixture of 500 μL DMSO-D_6 and 50 μL of D_3PO_4. 50 μL of D_2O was then added to the mixture, vortexed, and measured by NMR. For ζ-potential measurement, Hf-MOL and ALA/Hf-MOL were redispersed in deionized water at a DBP concentration of 5 μM. 1 mL of the sample was added to the DTS1060 cell and measured on a Malvern Zetasizer Nano ZS instrument.

Release profiles of ALA/Hf-MOL. Stock solutions of 100 ppb - 20 ppm ALA standards were freshly prepared. The mobile phase A consisted of 100% water with 0.1%TFA, and the mobile phase B consisted of 100% MeOH with 0.1% TFA. The eluent was held at 90% A and 10% B for 3 minutes. The flow rate was 0.2 mL/min, and the injection volume was 20 μL. For release profiles, ALA/Hf-MOL was freshly prepared and redispersed in 1× PBS, 0.1× PBS, pH=4, pH=5.5, or

pH=7.4 solutions (100 μL/tube) in 1.5 mL Eppendorf tubes (3 replicates for each time point), respectively. The EP tubes were transferred to a 37 °C incubator. The supernatants (80 μL/tube) were collected at 0 h, 0.5 h, 1 h, 4 h, 8 h, 24 h, and 48 h by centrifugation at 14,000 rpm and directly subjected to LC-MS quantification. The release profiles were fitted by the Hill function in OriginLab software. The stability of ALA in 1× PBS and 0.1× PBS was also tested, showing no obvious ALA degradation during incubation. $[ALA+H]^+$ (m/z = 132.06).

Singlet oxygen generation. SOSG assay was used to measure time-dependent $^1O_2$ generation of H_2DBP, Hf-MOL, and ALA/Hf-MOL upon 630 nm LED irradiation. H_2DBP, Hf-MOL, and ALA/Hf-MOL suspensions were prepared in water with the same DBP concentration of 5 μM. To 2 mL of each of these suspensions, 5 μL of SOSG stock solution (5 mM in MeOH) was added to give a final SOSG concentration of 12.5 μM. The mixed solution was irradiated by an LED light (630 nm, 100 mW/cm^2) for 0, 0.5, 1, 3, 5, 7, and 10 minutes, and the fluorescence intensity was immediately measured with a Synergy HTX plate reader (excitation 485 nm / emission 520 nm).

Cell viability assay. The cytotoxicity of H_2DBP, ALA, Hf-MOL, and ALA/Hf-MOL was evaluated in CT26 cells by CellTiter 96 AQ_{ueous} One Solution Cell Proliferation Assay (Promega, USA). The cells were seeded in 96-well plates at a density of 1,000 cells/well and cultured overnight. H_2DBP, Hf-MOL, or ALA/Hf-MOL was added at an equivalent DBP concentration of 0, 0.025, 0.25, 0.5, 1, 2.5, 5, 10, 25, 50, and 100 μM and incubated for 6 hours (n = 3). For the ALA control, the concentration gradient was 0.1, 1, 10, 100, 250, 1,000, and 5,000 μM. The plates were then irradiated with a 630 nm LED (150 mW/cm^2, 10 minutes, 90 J/cm^2 as the total dose). The cells were further incubated for 48 hours, and the cell viability was determined by MTS assay. IC_{50} values of all treatment groups were fitted with the dose-response curves in Origin Lab software. (IC_{50} H_2DBP(+)=16.73 μM)

Cellular uptake. CT26 cells were seeded in 6-well plates at a density of 2×10^5/well and incubated overnight. H_2DBP, Hf-MOL, or ALA/Hf-MOL was added at an equivalent DBP dose of 5 μM (n = 3). The cells were incubated at 37 ℃ for 1, 2, 4, and 8 hours. At each time point, the medium was aspirated, and the cells were washed with PBS three times, trypsinized, and collected by centrifugation at 1,800 rpm for 3 minutes. The cell pellets were digested with 1 mL of DMSO with 10% H_3PO_4 in 1.5 mL Eppendorf tubes for 48 hours with vigorous vortexing and sonication every 12 hours. The DBP concentration was determined by UV-Vis absorbance at 409 nm (ε=341 $mM^{-1} \cdot cm^{-1}$). The cellular uptake of Hf-MOL and ALA/Hf-MOL was also confirmed by flow cytometry after 8-hour incubation of CT26 cells with H_2DBP, Hf-MOL, or ALA/Hf-MOL. The fluorescence intensity of DBP was measured using the BV650 channel (ex. 405 nm / em. 645 nm).

PpIX quantification. PpIX synthesis and accumulation were evaluated in CT26 cells. The cells were seeded in 75 cm^2 cell culture flasks followed by overnight incubation (n = 3). ALA or ALA/Hf-MOL was added to the culture media at an equivalent ALA dose of 14 μM (DBP concentration = 20 μM). All groups were supplemented with an iron chelator, 3-hydroxy-1,2-dimethyl-4(1H)-pyridone, at a concentration of 1 mM to allow PpIX accumulation. After 20-hour incubation, the cells were washed with PBS twice, trypsinized, and counted by a hemocytometer. PpIX extraction from cell pellets was performed according to a literature report.[34] The cells were homogenized in 200 μL of ethyl acetate and acetic acid (v/v = 4:1) by sonication for 5 minutes and centrifuged at 3,000 g for 30 minutes at 4 ºC. The supernatants were collected and treated with 50 μL 5% HCl to extract PpIX. The extraction was repeated twice. The aqueous fractions were combined and subjected to LC-MS quantification. The standard curves of PpIX were prepared by serial dilution in 5% HCl with a linear range from 50 ppb to 20 ppm. The mobile phase A consisted of 100% water with 0.1%TFA, and the mobile phase B consisted of 100% acetonitrile with 0.1%

TFA. The gradient started with 0% B in 1 minute and then increased to 70% B in 7 minutes. The gradient was held at 70% B for 4 minutes and then decreased to 0% B in 1 minute. The total run time was 15 minutes with an injection volume of 15 μL. $[PpIX+H]^+$ (m/z = 563.26). To quantify PpIX synthesis in tumors, a subcutaneous CT26 tumor model was established in BALB/c mice by inoculating 2×10^6 cells/mouse subcutaneously. At day 7, the mice with tumor volumes around 75 mm^3 were randomized to 3 groups (n = 3). PBS, ALA, or ALA/Hf-MOL was *i.t.* injected with an equivalent ALA dose of 0.14 μmol (DBP dose 0.2 μmol). Twenty-four hours later, the mice were euthanized, and the tumors were harvested and homogenized by probe sonication (500 W, 20 kHz) for 2 minutes in a 500 μL solution of ethyl acetate and acetic acid (v/v = 4:1). PpIX was extracted as described above and subjected to LC-MS quantification.

Mitochondrial PpIX assay by flow cytometry. 2×10^5 cells/mL of CT26 cells were seeded in 6-well plates in 2 mL of culture medium and cultured overnight. ALA/Hf-MOL and ALA were added at an ALA concentration of 3.5 μM in the medium and incubated for 24 hours. 100 nM MitoTracker Red was supplemented to the medium and incubated at 37 ºC for 15 minutes. The cells were washed with PBS, exchanged to fresh medium, and incubated for another 15 minutes. The mitochondria were isolated by the mitochondria isolation kit according to the manufacturer's manual (Thermo Fisher Scientific, USA). The isolated fraction was analyzed by flow cytometry, and the mitochondria were gated as the PE^+ population.

Colocalization study by CLSM. CT26 cells were seeded in 6-well plates with coverslips at a density of 10^5 cells/mL and cultured overnight. ALA/Hf-MOL or Hf-MOL was added at a DBP concentration of 5 μM in the medium, together with 200 nM LysoTracker Green DND-26 (ex/em 504/511 nm, Thermo Fisher Scientific, USA) and incubated for 24 hours. Due to the weak fluorescence of PpIX and fluorescence interference from Hf-MOL (ex/em 630/650 nm), the

concentration of ALA was increased to 1 mM for the CLSM study. The cells were washed with PBS twice and stained with 100 nM MitoTracker Orange CMTMROS (ex/em 554/576 nm, Thermo Fisher Scientific, USA) at 37 ºC for 30 minutes. The cells were washed with PBS and exchanged to a warm medium for another 15 minutes. The cells were then fixed with 4% PFA at room temperature for 10 minutes, washed with PBS twice, and observed on a Leica Stellaris 8 microscope.

Dual-organelle disruption by live imaging. CT26 cells were seeded at a density of 5×10^4 cells/mL in 35 mm glass bottom dishes with 2 mL RPMI medium and cultured overnight. After incubation with ALA/Hf-MOL, the cells were washed with PBS three times and stained with 500 nM LysoTracker™ Green DND-26 and 2000 nM MitoSOX Superoxide Indicator Red (ex/em 396/610 nm, Thermo Fisher Scientific, USA) in serum-free RMPI-1640 medium for 45 min at 37 ℃. The cells were rinsed once with PBS and exchanged into warm RPMI-1640 medium with 10% FBS for 15 min at 37 ℃. The cells were then washed with PBS twice and exchanged into phenol red-free RPMI-1640 medium for live imaging. The laser at 630 nm from Leica Stellaris 8 confocal microscope was used as an *in situ* excitation source for PpIX or DBP in Hf-MOL. The laser power was calibrated by a photometer and set at 100 mW/cm^2. The cells were imaged in the sequence mode with continuous 630 nm laser irradiation at room temperature (n=3).

Mitochondrial membrane potential depolarization. The depolarization of mitochondrial membrane potential after PDT treatment was evaluated in CT26 cells by JC-1 assay (Monomer: ex/em 514/529 nm; Aggregate: ex/em 514/590 nm; Abcam). Inside 35 mm glass bottom dishes, CT26 cells were seeded at a density of 5×10^4 cells/mL with 2 mL RPMI medium and cultured overnight. H_2DBP, ALA, Hf-MOL, or ALA/Hf-MOL was added at a DBP concentration of 5 μM (3.5 μM ALA) and further incubated for 24 hours. The cells were washed with PBS twice and

exchanged with fresh RPMI medium. The cells were then irradiated with a 630 nm LED (100 $mW \cdot cm^{-2}$) for 10 min, exchanged to a warm medium with 10 μM JC-1, and further incubated for 30 minutes. The JC-1-containing medium was removed and exchanged for a warm fresh medium. The cells were incubated for 5 additional minutes and observed under a Leica Stellaris 8 microscope.

Cytochrome c release. CT26 cells were seeded in two 6-well plates at a density of 1×10^5 cells/mL with a coverslip in each well and cultured overnight. The cells were treated with H_2DBP, ALA, Hf-MOL, or ALA/Hf-MOL at a DBP concentration of 5 μM (3.5 μM ALA) and further incubated for 24 hours. Then one of the plates was irradiated with a 630 nm LED (100 $mW \cdot cm^2$) for 10 min. The cells in both plates were washed with PBS to remove excess ligands or MOL, exchanged with warm fresh medium, and further incubated for another 6 hours. The cells were exchanged with a warm medium containing 100 nM MitoTracker Red CMXROS (Thermo Fisher Scientific, USA) and were incubated for 15 minutes at 37 ºC, and then the medium was exchanged with fresh warm medium, and the cells were further incubated for 5 minutes. The cells were washed with PBS twice and fixed with 4% PFA in PBS (pH=7.0) for 10 minutes at room temperature. The cells were then washed with PBS, blocked, and permeabilized by 3% BSA + 0.3% Triton-X in PBS at room temperature for 1 hour. After blocking, the cells were incubated with FITC-conjugated cytochrome c antibody (ex/em 494/520 nm, Thermo Fisher Scientific, USA) 1:150 in 1% BSA + 0.3% Triton-X in PBS at 4 ºC overnight. The cells were washed with PBS, mounted on glass slides with ProLong Glass Antifade Mountant (Invitrogen), and cured overnight before CLSM imaging on a Leica Stellaris 8 microscope. The Pearson's coefficients R and scatter plots were generated by the Colocalization Finder plugin in ImageJ.

LMP and cathepsin B release. Lysosome membrane permeabilization was evaluated in CT26 cells. The cells were seeded in two 6-well plates at a density of 5×10^4 cells/mL with 2 mL RPMI medium and cultured overnight. The cells were treated with H_2DBP, ALA, Hf-MOL, or ALA/Hf-MOL and further incubated for 24 hours. Then one of the plates was irradiated with a 630 nm LED (100 mW·cm^2) for 10 min. The cells were washed with PBS and exchanged with warm fresh medium containing 5 μM acridine orange (AO) and further incubated for 30 minutes at 37 ºC. The cells were washed with PBS, exchanged to a warm phenol-red-free medium, and immediately visualized under a Leica Stellaris 8 microscope. For cathepsin B release, the cells were seeded and treated similarly. After PDT, the cells were treated with CV-$(RR)_2$ reagent as provided in the CV-Cathepsin B detection kit (ex/em 550/620 nm, Enzo Biochem) and incubated for 1 hour at 37 ºC. The cells were washed with PBS twice and exchanged to a warm medium for direct observation by a Leica Stellaris 8 microscope.

***In vitro* ROS generation.** For flow cytometry analysis, CT26 cells were seeded at a density of 1×10^5 cells/ml with 2 mL medium on two 6-well plates and cultured overnight. After incubation with ALA/Hf-MOL, 20 μM DCF-DA (Invitrogen) was added to the medium for 1-hour incubation. Then one plate was irradiated with a 630 nm LED (100 mW·cm^{-2}) for 15 minutes. The cells were washed with PBS, detached, and analyzed by flow cytometry. For CLSM, inside 35 mm glass bottom dishes, CT26 cells were seeded at a density of 5×10^4 cells/mL with 2 mL medium and cultured overnight. The cells were treated the same way as flow cytometry, except the light irradiation time was 10 minutes. The cells were washed with PBS three times, exchanged with warm phenol-red-free RPMI-1640 medium, and mounted for CLSM immediately using a Leica Stellaris 8 microscope.

Apoptotic cell death. For flow cytometry analysis, in two 6-well plates, CT26 cells were seeded at a density of 2×10^5 cells/ml with medium and cultured overnight. The cells on both plates were treated with H_2DBP, ALA, Hf-MOL, or ALA/Hf-MOL and further incubated for 24 hours. Then the plates were irradiated with a 630 nm LED (100 $mW\cdot cm^{-2}$) for 15 minutes. The cells in both plates were washed with PBS, exchanged to a warm fresh medium, and further incubated overnight. The cells were then scraped off and stained with Alexa Fluor 488 Annexin V/dead cell apoptosis kit (Thermo Fisher Scientific, USA) following the vendor's manual for flow cytometry analysis. For CLSM analysis, CT26 cells were seeded at a density of 5×10^4 cells/well with a coverslip in each well and cultured overnight. Then the treatment and staining were the same with flow cytometry except for a counterstain step of Hoechst-33342 3 μg/mL for 5 minutes at room temperature and fixation by 2% PFA (in 1 × Ca^{2+} containing binding buffer). The coverslips were washed with PBS, mounted on glass slides with ProLong Glass Antifade Mountant, and cured overnight at room temperature. The cells were then observed by a Leica Stellaris 8 microscope.

CRT expression. For flow cytometry analysis, CT26 cells were seeded in two 6-well plates at a density of 1×10^5 cells/mL with 2 mL medium and cultured overnight. The cells were treated with H_2DBP, ALA, Hf-MOL, or ALA/Hf-MOL and further incubated for 24 hours. Then one of the plates was irradiated with a 630 nm LED (100 $mW\cdot cm^{-2}$) for 15 minutes. The cells in both plates were washed with PBS and exchanged with warm fresh medium, and further incubated overnight. The cells were washed with PBS and scraped off. The cells were stained with anti-Calreticulin Alexa Fluor 488 (NOVUS) (1:150 dilution in PBS solution) on ice for 30 minutes, washed with PBS once, and resuspended in PBS solution for flow cytometry analysis. For CLSM analysis, the PDT treatment procedure was the same with flow cytometry, except CT26 cells were seeded with a coverslip in each well with a cell density diluted to 5×10^4 cells/mL. The light

irradiation time was also decreased to 10 minutes. The cells were fixed with -20 ºC methanol for 5 minutes, washed with PBS twice, and then stained with anti-Calreticulin Alexa Fluor 488 (NOVUS) (1:100 dilution in 1% BSA PBS solution) at room temperature for 30 minutes. The cells were washed with PBS and counterstained with Hoechst (3 μg/mL) for 5 minutes at room temperature. The coverslips were mounted on glass slides with ProLong Glass Antifade Mountant and cured overnight for confocal imaging under a Leica Stellaris 8 microscope.

***In vivo* anti-cancer efficacy.** To evaluate *in vivo* PDT efficacy of Hf-MOL and ALA/Hf-MOL, a subcutaneous CT26 model was established in BALB/c mice by inoculating 2×10^6 cells/mouse subcutaneously. At day 7, the mice with tumor volumes around 75 mm^3 were randomized for PDT treatment. PBS, ALA, Hf-MOL, or ALA/Hf-MOL was *i.t.* injected with an equivalent DBP dose of 0.2 μmol (ALA dose 0.14 μmol) (n = 5). Twenty hours later, the mice were anesthetized with 2.5% (V/V) isoflurane/O_2 and covered by a black cloth. The tumor area was exposed and irradiated with a 630 nm LED(150 mW/cm^2, 10 minutes, the CT26 model received a second dose of 90 J/cm^2 on day 10). Tumor sizes were measured with an electronic caliper (tumor volume = length×$width^2$/2), and body weight was monitored with an electronic scale. At day 20 for the subcutaneous CT26 model, the mice were euthanized, and the tumors were weighed and sectioned for H&E and TUNEL staining. Major organs were sectioned for H&E staining to evaluate general toxicity.

TUNEL assay. Tumor tissues were fixed in 4% PFA (freshly prepared and pH=7.1) for 1 day and 70% ethanol for 1 day. Tissues were embedded in paraffin, sectioned, and stained for TUNEL assay by the Human Tissue Resource Center at the University of Chicago. The slides were then sealed and scanned on a CRi Panoramic SCAN 40x whole slide scanner by Integrated Light

Microscopy Core at the University of Chicago. The images were viewed and analyzed by QuPath-0.2.3 software.[41]

In vivo dual-organelle disruption analyzed by flow cytometry. The subcutaneous CT26 model was established and treated as described in S6.1. Right after the PDT procedure, the tumor was excised and digested with collagenase I (0.5 mg/mL) and DNase (0.05 mg/mL) in RPMI medium at 37 ℃ for 45 minutes. The reaction was quenched by FBS containing RPMI, and the tumors were ground through a 40 μm cell strainer to obtain single-cell suspensions. The cells were then stained with Viability Dye eFluor 506 (1:1000, eBioscience, USA), 1 μM LysoTracker Green DND-26, and 5 μM MitoSOX Superoxide Indicator Red in serum-free RPMI medium at 37 ℃ for 60 minutes. The cells were then suspended in RPMI with 10% FBS for another 15 minutes, washed with PBS once, and then suspended in PBS for flow cytometry analysis.

4.5 Reference

(1) Xu, Z.; Luo, T.; Lin, W., Nanoscale Metal–Organic Layers for Biomedical Applications. *Acc. Mater. Res.* **2021,** *2* (10), 944-953.

(2) Song, Y.; Wang, L.; Xie, Z., Metal–Organic Frameworks for Photodynamic Therapy: Emerging Synergistic Cancer Therapy. *Biotechnol. J.* **2021,** *16* (2), 1900382.

(3) Banerjee, S.; Lollar, C. T.; Xiao, Z.; Fang, Y.; Zhou, H.-C., Biomedical Integration of Metal-Organic Frameworks. *Trends Chem.* **2020,** *2* (5), 467-479.

(4) Lan, G.; Quan, Y.; Wang, M.; Nash, G. T.; You, E.; Song, Y.; Veroneau, S. S.; Jiang, X.; Lin, W., Metal–Organic Layers as Multifunctional Two-Dimensional Nanomaterials for Enhanced Photoredox Catalysis. *J. Am. Chem. Soc.* **2019,** *141* (40), 15767-15772.

(5) Luo, T.; Fan, Y.; Mao, J.; Yuan, E.; You, E.; Xu, Z.; Lin, W., Dimensional Reduction Enhances Photodynamic Therapy of Metal–Organic Nanophotosensitizers. *J. Am. Chem. Soc.* **2022,** *144* (12), 5241-5246.

(6) Agostinis, P.; Berg, K.; Cengel, K. A.; Foster, T. H.; Girotti, A. W.; Gollnick, S. O.; Hahn, S. M.; Hamblin, M. R.; Juzeniene, A.; Kessel, D.; Korbelik, M.; Moan, J.; Mroz, P.; Nowis, D.; Piette, J.; Wilson, B. C.; Golab, J., Photodynamic therapy of cancer: An update. *CA. Cancer J. Clin.* **2011,** *61* (4), 250-281.

(7) Sokolov, V. S.; Batishchev, O. V.; Akimov, S. A.; Galimzyanov, T. R.; Konstantinova, A. N.; Malingriaux, E.; Gorbunova, Y. G.; Knyazev, D. G.; Pohl, P., Residence time of singlet oxygen in membranes. *Sci. Rep.* **2018,** *8* (1), 14000.

(8) Chen, Y.; Gao, P.; Wu, T.; Pan, W.; Li, N.; Tang, B., Organelle-localized radiosensitizers. *Chem. Commun.* **2020,** *56* (73), 10621-10630.

(9) Yang, M.; Yang, T.; Mao, C., Enhancement of Photodynamic Cancer Therapy by Physical and Chemical Factors. *Angew. Chem. Int. Ed.* **2019,** *58* (40), 14066-14080.

(10) Wang, R.; Li, X.; Yoon, J., Organelle-Targeted Photosensitizers for Precision Photodynamic Therapy. *ACS Appl. Mater. Interfaces* **2021,** *13* (17), 19543-19571.

(11) Li, X.; Lovell, J. F.; Yoon, J.; Chen, X., Clinical development and potential of photothermal and photodynamic therapies for cancer. *Nat. Rev. Clin. Oncol.* **2020,** *17* (11), 657-674.

(12) Saad, M. A.; Hasan, T., Spotlight on Photoactivatable Liposomes beyond Drug Delivery: An Enabler of Multitargeting of Molecular Pathways. *Bioconjug. Chem.* **2022,** *33* (11), 2041-2064.

(13) Chang, Y.; Li, X.; Zhang, L.; Xia, L.; Liu, X.; Li, C.; Zhang, Y.; Tu, L.; Xue, B.; Zhao, H.; Zhang, H.; Kong, X., Precise Photodynamic Therapy of Cancer via Subcellular Dynamic Tracing of Dual-loaded Upconversion Nanophotosensitizers. *Sci. Rep.* **2017,** *7* (1), 45633.

(14) Gomes-da-Silva, L. C.; Zhao, L.; Bezu, L.; Zhou, H.; Sauvat, A.; Liu, P.; Durand, S.; Leduc, M.; Souquere, S.; Loos, F.; Mondragón, L.; Sveinbjørnsson, B.; Rekdal, Ø.; Boncompain, G.; Perez, F.; Arnaut, L. G.; Kepp, O.; Kroemer, G., Photodynamic therapy with redaporfin targets the endoplasmic reticulum and Golgi apparatus. *EMBO J.* **2018,** *37* (13), e98354.

(15) Li, C.; Zhang, W.; Liu, S.; Hu, X.; Xie, Z., Mitochondria-Targeting Organic Nanoparticles for Enhanced Photodynamic/Photothermal Therapy. *ACS Appl. Mater. Interfaces* **2020,** *12* (27), 30077-30084.

(16) Sai, D. L.; Lee, J.; Nguyen, D. L.; Kim, Y.-P., Tailoring photosensitive ROS for advanced photodynamic therapy. *Exp. Mol. Med.* **2021,** *53* (4), 495-504.

(17) Castano, A. P.; Mroz, P.; Hamblin, M. R., Photodynamic therapy and anti-tumour immunity. *Nat. Rev. Cancer* **2006,** *6* (7), 535-545.

(18) Kessel, D., Subcellular Targeting as a Determinant of the Efficacy of Photodynamic Therapy. *Photochem. Photobiol.* **2017,** *93* (2), 609-612.

(19) Liu, Z.; Zou, H.; Zhao, Z.; Zhang, P.; Shan, G.-G.; Kwok, R. T. K.; Lam, J. W. Y.; Zheng, L.; Tang, B. Z., Tuning Organelle Specificity and Photodynamic Therapy Efficiency by Molecular Function Design. *ACS Nano* **2019,** *13* (10), 11283-11293.

(20) Stummer, W.; Pichlmeier, U.; Meinel, T.; Wiestler, O. D.; Zanella, F.; Reulen, H.-J., Fluorescence-guided surgery with 5-aminolevulinic acid for resection of malignant glioma: a randomised controlled multicentre phase III trial. *Lancet Oncol.* **2006,** *7* (5), 392-401.

(21) Jansen, M. H. E.; Kessels, J. P. H. M.; Nelemans, P. J.; Kouloubis, N.; Arits, A. H. M. M.; van Pelt, H. P. A.; Quaedvlieg, P. J. F.; Essers, B. A. B.; Steijlen, P. M.; Kelleners-Smeets, N. W. J.; Mosterd, K., Randomized Trial of Four Treatment Approaches for Actinic Keratosis. *N. Engl. J. Med.* **2019,** *380* (10), 935-946.

(22) van Solinge, T. S.; Nieland, L.; Chiocca, E. A.; Broekman, M. L. D., Advances in local therapy for glioblastoma — taking the fight to the tumour. *Nat. Rev. Neurol.* **2022,** *18* (4), 221-236.

(23) Liu, Y.; Liu, C.-Z.; Wang, Z.-K.; Zhou, W.; Wang, H.; Zhang, Y.-C.; Zhang, D.-W.; Ma, D.; Li, Z.-T., Supramolecular organic frameworks improve the safety of clinically used porphyrin photodynamic agents and maintain their antitumor efficacy. *Biomater.* **2022,** *284*, 121467.

(24) Vettore, L.; Westbrook, R. L.; Tennant, D. A., New aspects of amino acid metabolism in cancer. *Br. J. Cancer* **2020,** *122* (2), 150-156.

(25) McNicholas, K.; MacGregor, M. N.; Gleadle, J. M., In order for the light to shine so brightly, the darkness must be present—why do cancers fluoresce with 5-aminolaevulinic acid? *Br. J. Cancer* **2019,** *121* (8), 631-639.

(26) Ding, H.; Sumer, B. D.; Kessinger, C. W.; Dong, Y.; Huang, G.; Boothman, D. A.; Gao, J., Nanoscopic micelle delivery improves the photophysical properties and efficacy of photodynamic therapy of protoporphyrin IX. *J. Control. Release* **2011,** *151* (3), 271-277.

(27) McCarron, P. A.; Donnelly, R. F.; Andrews, G. P.; Woolfson, A. D., Stability of 5-aminolevulinic acid in novel non-aqueous gel and patch-type systems intended for topical application. *J. Pharm. Sci.* **2005,** *94* (8), 1756-1771.

(28) Penido, M. G. M. G.; Alon, U. S., Phosphate homeostasis and its role in bone health. *Pediatr. Nephrol.* **2012,** *27* (11), 2039-2048.

(29) Bowen, J. W.; Levinson, C., Phosphate concentration and transport in Ehrlich ascites tumor cells: Effect of sodium. *J. Cell. Physiol.* **1982,** *110* (2), 149-154.

(30) Knochel, J. P.; Haller, R.; Ferguson, E., Selective Phosphorus Deficiency in the Hyperalimented Hypophosphatemic Dog and Phosphorylation Potentials in the Muscle Cell. In *Phosphate and Minerals in Health and Disease*, Massry, S. G.; Ritz, E.; Jahn, H., Eds. Springer US: Boston, MA, 1980; pp 323-334.

(31) Chazot, G.; Lemoine, S.; Kocevar, G.; Kalbacher, E.; Sappey-Marinier, D.; Rouvière, O.; Juillard, L., Intracellular Phosphate and ATP Depletion Measured by Magnetic Resonance Spectroscopy in Patients Receiving Maintenance Hemodialysis. *J. Am. Soc. Nephrol.* **2021,** *32* (1), 229-237.

(32) Auesukaree, C.; Homma, T.; Tochio, H.; Shirakawa, M.; Kaneko, Y.; Harashima, S., Intracellular Phosphate Serves as a Signal for the Regulation of the PHO Pathway in Saccharomyces cerevisiae*. *J. Biol. Chem.* **2004,** *279* (17), 17289-17294.

(33) Luo, T.; Nash, G. T.; Jiang, X.; Feng, X.; Mao, J.; Liu, J.; Juloori, A.; Pearson, A. T.; Lin, W., A 2D Nanoradiosensitizer Enhances Radiotherapy and Delivers STING Agonists to Potentiate Cancer Immunotherapy. *Adv. Mater.* **2022,** *34* (39), 2110588.

(34) Perotti, C.; Fukuda, H.; DiVenosa, G.; MacRobert, A. J.; Batlle, A.; Casas, A., Porphyrin synthesis from ALA derivatives for photodynamic therapy. In vitro and in vivo studies. *Br. J. Cancer* **2004,** *90* (8), 1660-1665.

(35) Orellana-Tavra, C.; Mercado, S. A.; Fairen-Jimenez, D., Endocytosis Mechanism of Nano Metal-Organic Frameworks for Drug Delivery. *Adv. Healthc. Mater.* **2016,** *5* (17), 2261-2270.

(36) Ow, Y.-L. P.; Green, D. R.; Hao, Z.; Mak, T. W., Cytochrome c: functions beyond respiration. *Nat. Rev. Mol. Cell Biol.* **2008,** *9* (7), 532-542.

(37) Tait, S. W. G.; Green, D. R., Mitochondria and cell death: outer membrane permeabilization and beyond. *Nat. Rev. Mol. Cell Biol.* **2010,** *11* (9), 621-632.

(38) Erdal, H.; Berndtsson, M.; Castro, J.; Brunk, U.; Shoshan, M. C.; Linder, S., Induction of lysosomal membrane permeabilization by compounds that activate p53-independent apoptosis. *Proc. Natl. Acad. Sci. U.S.A.* **2005,** *102* (1), 192-197.

(39) Oberle, C.; Huai, J.; Reinheckel, T.; Tacke, M.; Rassner, M.; Ekert, P. G.; Buellesbach, J.; Borner, C., Lysosomal membrane permeabilization and cathepsin release is a Bax/Bak-dependent, amplifying event of apoptosis in fibroblasts and monocytes. *Cell Death Differ.* **2010,** *17* (7), 1167-1178.

(40) Ni, K.; Luo, T.; Culbert, A.; Kaufmann, M.; Jiang, X.; Lin, W., Nanoscale Metal–Organic Framework Co-delivers TLR-7 Agonists and Anti-CD47 Antibodies to Modulate Macrophages and Orchestrate Cancer Immunotherapy. *J. Am. Chem. Soc.* **2020,** *142* (29), 12579-12584.

(41) Bankhead, P.; Loughrey, M. B.; Fernández, J. A.; Dombrowski, Y.; McArt, D. G.; Dunne, P. D.; McQuaid, S.; Gray, R. T.; Murray, L. J.; Coleman, H. G.; James, J. A.; Salto-Tellez, M.; Hamilton, P. W., QuPath: Open source software for digital pathology image analysis. *Sci. Rep.* **2017,** *7* (1), 16878.

Chapter 5. Phosphate Coordination to Metal-Organic Layer Secondary Building Units Prolongs Drug Retention for Synergistic Chemoradiotherapy

5.1 Introduction

Traditional chemotherapy targets fast-proliferating tumor cells using cytotoxic drugs,[1-2] but most chemotherapeutics have narrow therapeutic indices because of their nonspecific distribution to normal organs.[3-4] Localized chemotherapy has been developed to reduce systemic side effects,[5] which has proven effective for some tumors, including bladder and liver cancer.[6-8] However, localized chemotherapy is limited by poor retention of small molecule drugs in tumors.[9-10] Maintaining intratumoral drugs above therapeutic concentrations over a period of time is crucial to achieving optimal treatment outcomes.

RT is another widely used cancer treatment that utilizes ionizing radiation to kill malignant cells.[11-14] Despite extensive research on radiosensitization over the past century, non-toxic radiosensitizers have not been approved by the FDA for cancer treatment.[15] Some chemotherapeutics are used in combination with RT to enhance antitumor effects,[16-19] but these chemoradiotherapy regimens exacerbate the toxicities of both modalities, leading to debilitating side effects in cancer patients.[20-23] Thus, there is a need for novel strategies to simultaneously control the release of chemotherapeutics in tumors and enhance the antitumor activity of RT.

MOFs consisting of high-Z-metal-based SBUs and photosensitizing ligands have been demonstrated as efficient and non-toxic radiosensitizers via a unique RT-RDT process.[24-28] We have recently shown that dimensional reduction of 3-D MOFs to 2-D MOLs further improves the PDT and RT-RDT efficiency by enhancing the diffusion of reactive oxygen species and energy-transfer efficiency.[29-32] Furthermore, 2-D MOLs possess more accessible binding sites than 3-D

MOFs, allowing for facile conjugation of therapeutic molecules via post-synthetic functionalization.[33-36]

Antimetabolite chemotherapeutics such as gemcitabine and 5-fluorouracil are converted to their active triphosphates to exert antitumor effects, with the conversion to their monophosphates as the rate-limiting step.[37-38] As a result, gemcitabine monophosphate (GMP) is much more potent than gemcitabine but is quickly cleared from tumors due to its hydrophilicity. We hypothesized that GMP could be loaded on MOL SBUs to slowly release it in tumors and enhance the RT effects.[35-36] In this Chapter, we report the conjugation of GMP to the SBUs of a 2-D MOL comprising Hf_{12}-SBUs and Ir-based photosensitizing ligands for synergistic chemoradiotherapy.

5.2 Results and Discussions

5.2.1 Synthesis of Phosphate-Conjugated MOLs

We first synthesized the 2-D MOL via a solvothermal reaction between $HfCl_4$ and $Ir(DBB)[dF(CF_3)ppy]^{2+}$ [DBB= 4,4'-di(4-benzoato)-2,2'-bipyridine; $dF(CF_3)ppy$= 2-(2,4-difluorophenyl)-5-(trifluoromethyl)pyridine] in DMF as previously reported.[30] GMP was loaded onto the MOL by stirring a mixture of GMP and MOL in ethanol/water at one GMP per Hf_{12}-SBU at room temperature for 15 minutes, followed by washing with water to afford GMP/MOL (**Figure 5-1a**). Two control samples, DPPA/MOL and PPA/MOL, were similarly prepared with diphenylphosphinic acid (DPPA) and phenylphosphonic acid (PPA) instead of GMP to study the interaction between phosphates and SBUs. ^{1}H- and ^{31}P-NMR signals of GMP, DPPA, and PPA in D_2O disappeared after conjugation to the MOL (**Figure 5-1b-g**) due to decreases in tumbling rates upon coordination to Hf_{12} SBUs.[39-40]

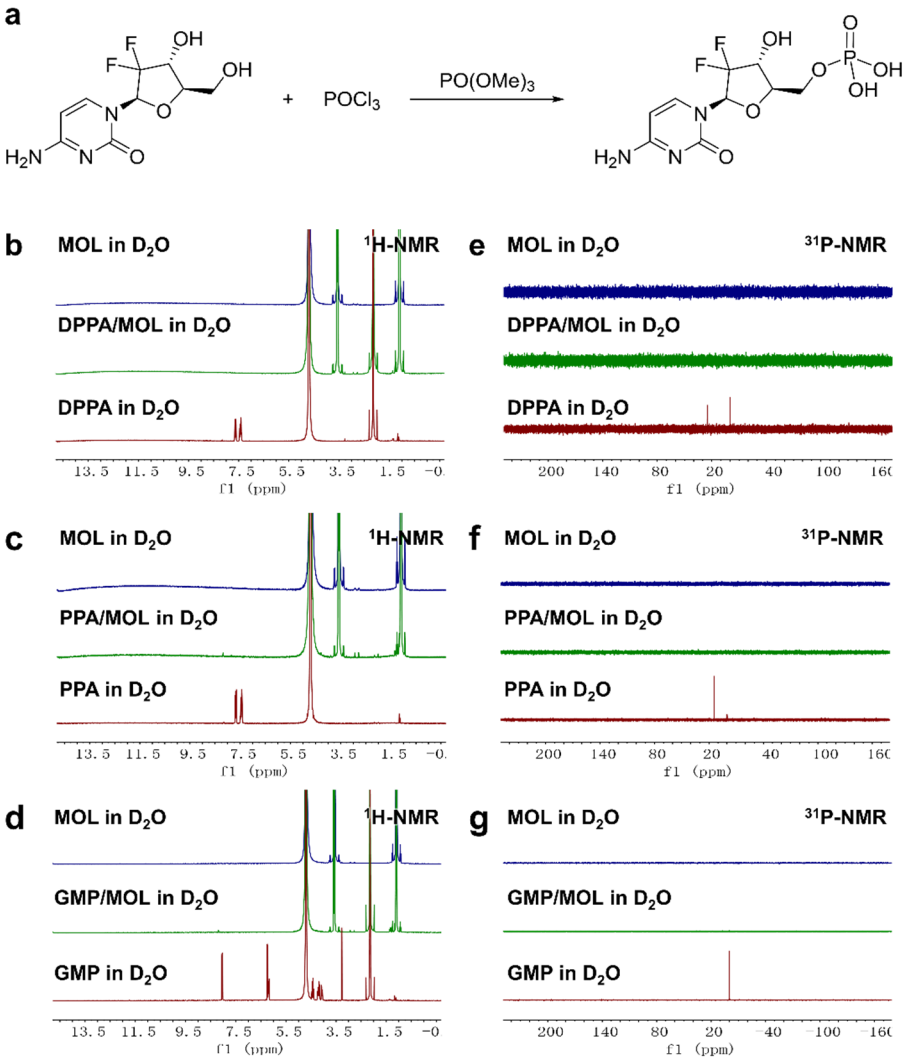

Figure 5-1. Synthesis of GMP and characterization of phosphate conjugated MOLs. (a) Synthetic route for GMP. (b-d) ^{1}H-NMR of (b) DPPA and DPPA/MOL, (c) PPA and PPA/MOL, and (d) GMP and GMP/MOL in D_2O. (e-g) ^{31}P-NMR of (e) DPPA and DPPA/MOL, (f) PPA and PPA/MOL, and (g) GMP and GMP/MOL in D_2O.

5.2.2 Characterization of Phosphate Conjugated MOLs

TEM showed unchanged nanosheet morphology upon conjugating GMP, DPPA, and PPA to the MOL (**Figure 5-2a-c**). AFM revealed the monolayer structure of all MOLs but slight increases in thickness from 1.8 nm for the MOL to 1.8, 1.9, and 2.3 nm, respectively, for PPA/MOL, GMP/MOL, and DPPA/MOL. The increases in heights are consistent with increasing sizes of PPA,

GMP, and DPPA and support their coordination with Hf_{12}-SBUs (**Figure 5-2d-f**). All MOLs exhibited the same crystalline structure with identical PXRD patterns (**Figure 5-2g**) and similar hydrodynamic sizes with average diameters ranging from 225 nm to 265 nm (**Figure 5-2h**).

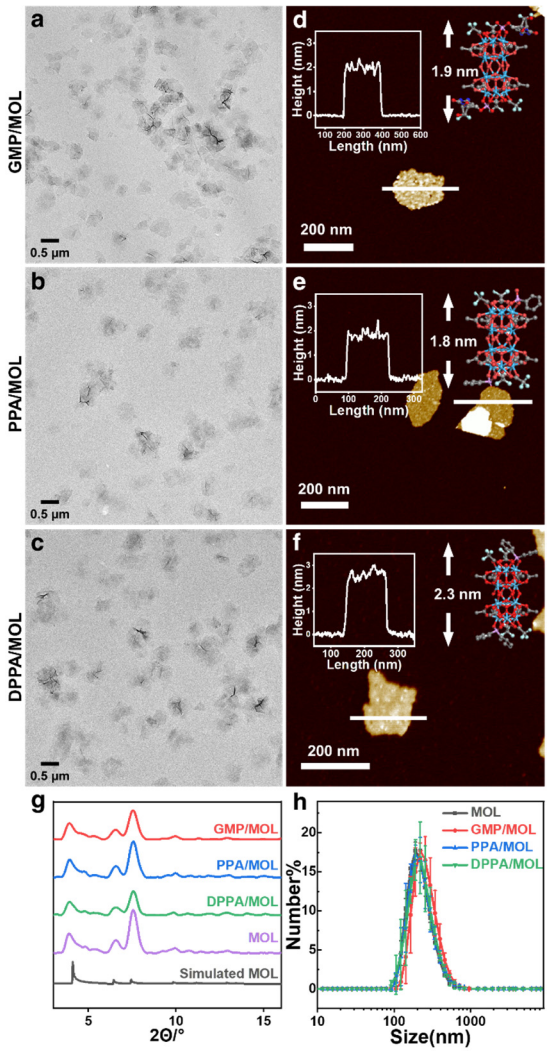

Figure 5-2. Characterization of phosphate conjugated MOLs. (a-c) TEM images of (a) GMP/MOL, (b) PPA/MOL, (c) DPPA/MOL. (d-f) AFM images of (d) GMP/MOL, (e) PPA/MOL, (f) DPPA/MOL. (g) PXRD patterns of MOLs and the simulated pattern for the bare MOL. (h) Number-averaged sizes of MOLs in water.

5.2.3 Coordination and Binding Affinity

Solid-state ^{31}P-NMR spectroscopy showed broadening and upfield shifts of DPPA, PPA, and GMP signals upon conjugation to the MOL (**Figure 5-3a,b**), which supported their coordination

with Hf_{12}-SBUs.[41-42] DFT revealed decreases in free energy changes following the order of GMP (ΔG=-42.4 kcal·mol^{-1}), PPA (ΔG=-28.3 kcal·mol^{-1}), and DPPA (ΔG=-22.8 kcal·mol^{-1}) in their substitution for TFA groups on Hf_{12}-SBUs, indicating the strongest binding between GMP and Hf_{12} SBU (**Figure 5-3c**). Isothermal titration calorimetry (ITC) measurements showed that GMP possessed a 1.8 times higher association constant (Ka) than PPA (**Figure 5-3d**). DPPA did not show an obvious exotherm during titration. At stoichiometric ratios relative to capping TFA groups, DPPA and PPA showed higher loading efficiencies than GMP, likely due to the spatial hindrance of GMP (**Figure 5-4**).

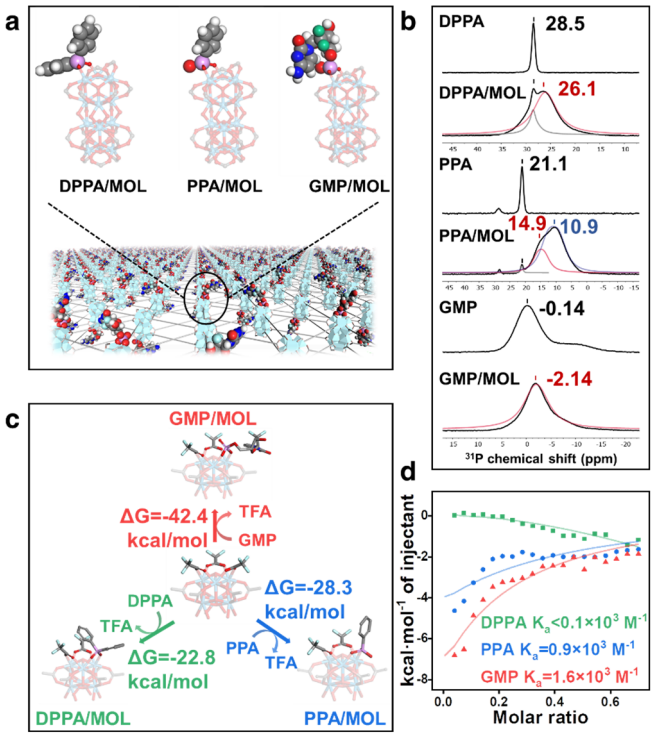

Figure 5-3. Phosphate coordination onto SBUs. (a) Schematic showing coordination between DPPA, PPA, or GMP and the MOL (ligands were simplified as grey sticks for clarity; white=H; grey=C; red=O; blue=N; green=F; pink=P; cyan=Hf). (b) Solid-state ^{31}P NMR spectra of DPPA, PPA, GMP, and their MOL conjugates. (c) Free energy changes of TFA substitution by DPPA, PPA, or GMP from DFT calculations. (d) ITC results showing binding affinity between the MOL and DPPA, PPA, or GMP.

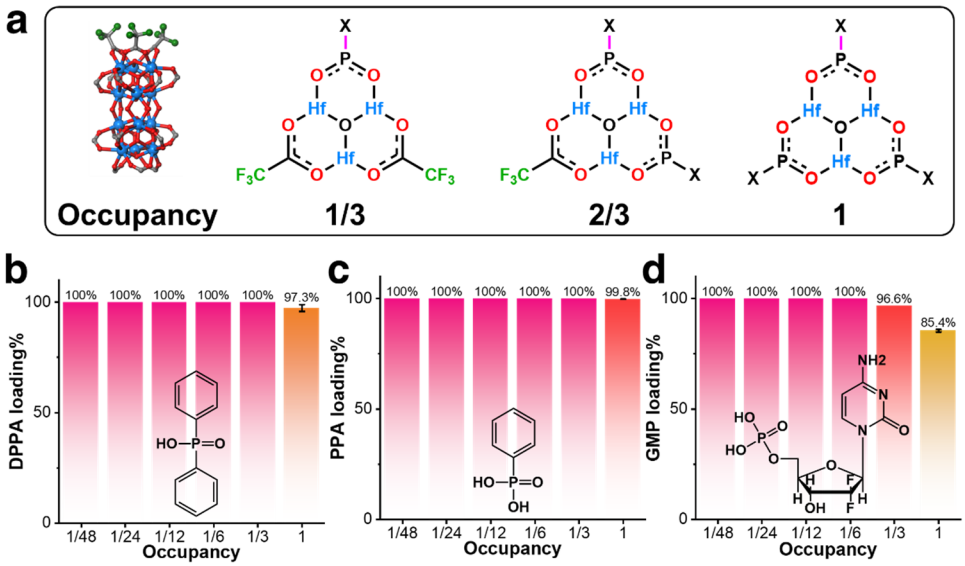

Figure 5-4. Loading capacity of MOLs. (a) Schematic showing loading occupancies of DPPA, PPA, or GMP onto SBUs. (b-d) Loading percentages of (b) DPPA, (c) PPA, and (d) GMP from occupancy of 1/48 to 1 (n=3).

5.2.4 Release Profiles

We hypothesized that the coordinated GMP, DPPA, and PPA on Hf_{12}-SBUs could be released by high concentrations of phosphate ions under certain physiological conditions. The release profiles of DPPA/MOL, PPA/MOL, and GMP/MOL were studied by LC-MS in 0.1× PBS (1.18 mM phosphate) and 1× PBS (11.8 mM phosphate), which mimic extracellular and intracellular phosphate concentration, respectively (**Figure 5-5a**).[43-47] At higher occupancy, GMP, DPPA, and PPA were more readily released from their MOL conjugates whereas 10-fold phosphate concentrations increased their release by 1.6-fold (**Figure 5-5e-g**). The release rate followed the order of DPPA>PPA>GMP, which correlated with the binding affinity trend from DFT and ITC studies (**Figure 5-3, Figure 5-6**). These results suggest the ability to slowly release small molecule drugs from their MOL conjugates at an elevated phosphate concentration intracellularly.[35, 48]

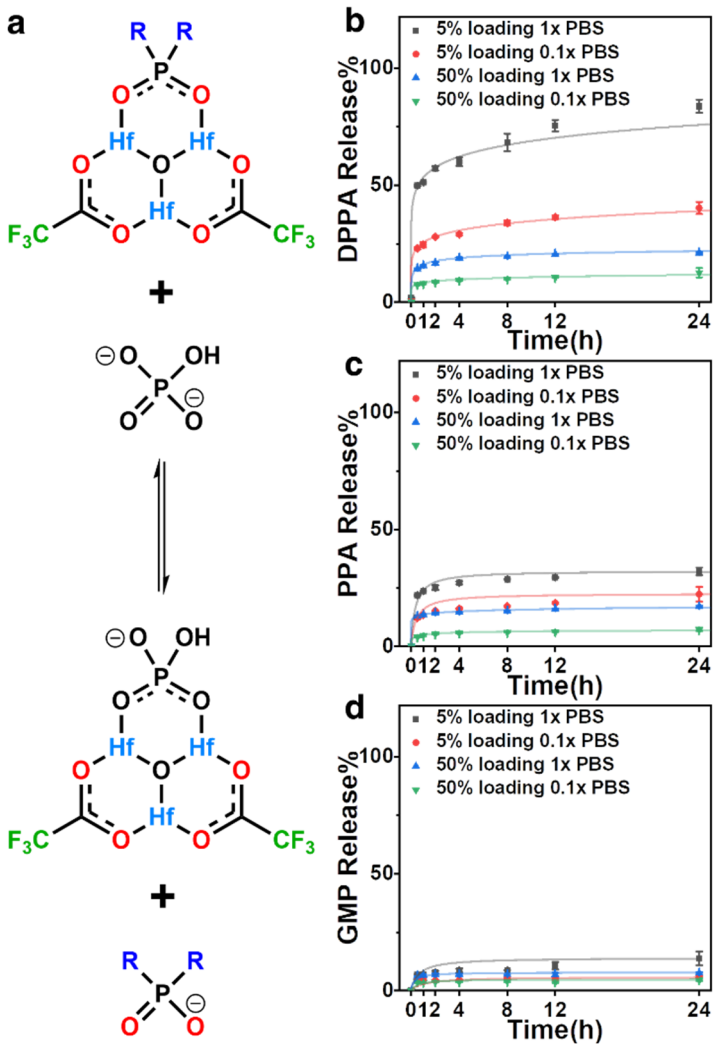

Figure 5-5. Release profiles of DPPA, PPA, and GMP. (a) Schematic showing phosphate-dependent release. (b-d) Release percentages of (b) DPPA, (c) PPA, and (d) GMP from the MOL with 5% or 50% of drug loading in 0.1× PBS or 1× PBS, respectively (n=3).

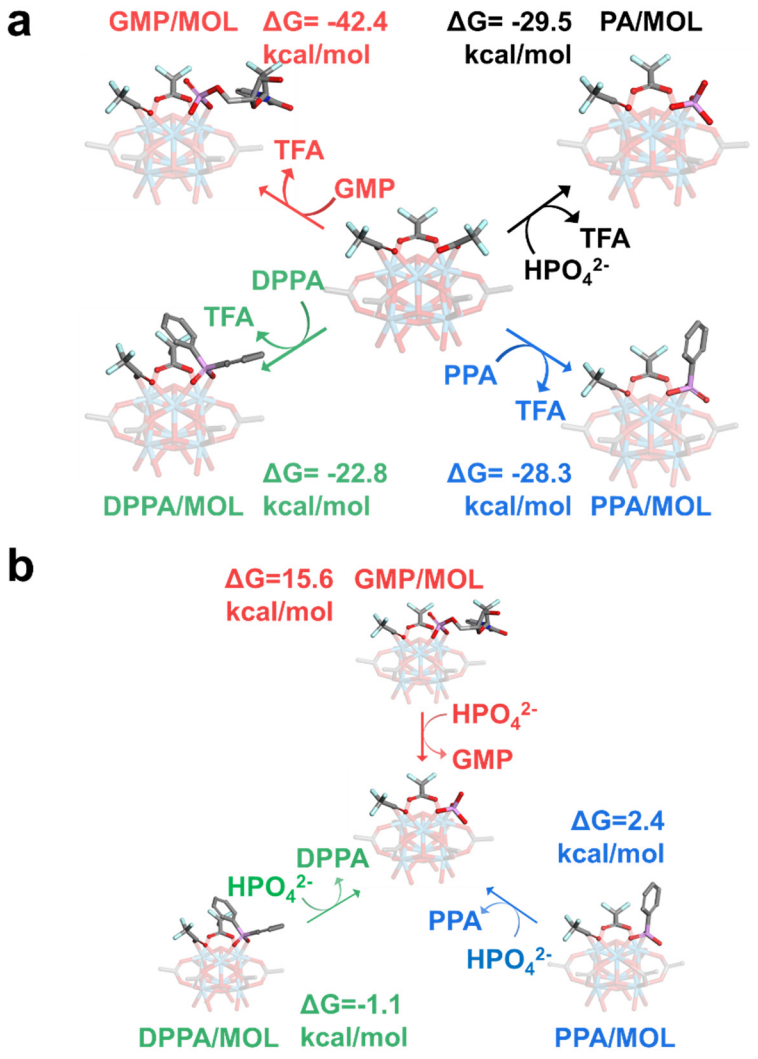

Figure 5-6. DFT calculations showing free energy changes of phosphate replacing TFA and releasing of phosphate from SBUs. (a) Free energy changes of substitution reactions of TFA on SBUs by inorganic phosphate anions, GMP, PPA, and DPPA. (b) Free energy changes of substitution reactions of GMP, PPA, and GMP on SBUs by inorganic phosphate anions.

5.2.5 *In Vitro* Radiosensitization by GMP/MOL

Based on these findings, we tested if GMP/MOL could slowly release GMP for enhanced anticancer efficacy. CT26 cells exhibited similar uptake of GMP and GMP/MOL over 12 hours (**Figure 5-7a**). GMP/MOL showed higher cytotoxicity than GMP with 1.87-fold and 1.91-fold lower IC_{50} than free GMP in CT26 (**Figure 5-7b**) and MC38 (**Figure 5-7c**) cells, respectively. The

enhanced cytotoxicity of GMP/MOL is likely due to the increased cellular availability of GMP via endocytosis of GMP/MOL followed by the phosphate-triggered release of GMP from GMP/MOL.

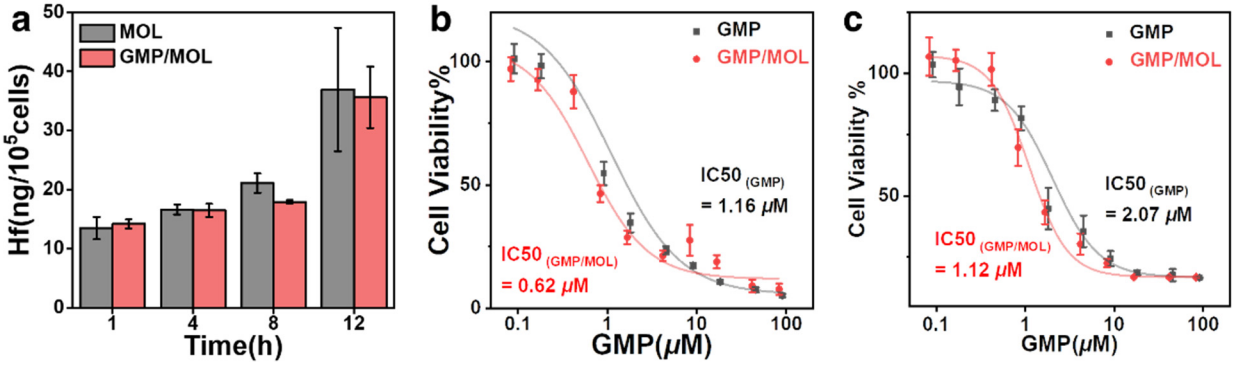

Figure 5-7. Cellular uptake and IC_{50} of GMP/MOL. (a) Time-dependent uptake of MOL and GMP/MOL by CT26 cells (n=3). (b,c) Viability of (b) CT26 cells and (c) MC38 cells after incubation with free GMP or GMP/MOL for 48 hours (n=3).

The radiosensitizing effects of the MOL and GMP/MOL were evaluated by growth rate (GR) inhibition assays and immunofluorescence staining of phosphorylated histone H2A.X (γ-H2AX) in CT26 cells at a GMP concentration of 1.67 μM and a Hf concentration of 20 μM. Compared to radiation alone [PBS(+)], MOL plus X-ray [MOL(+)] treatment showed a steeper X-ray-dose-dependent toxicity with a growth inhibition factor at 10% growth rate ($GIF_{10\%}$) of 1.27 due to the reported RT-RDT effect (**Figure 5-8a-f**).[24, 35, 49] GMP and GMP/MOL had lower starting GR at 0 Gy due to their cytotoxicity against proliferating cancer cells. GMP/MOL(+) outperformed GMP(+) with a $GIF_{10\%}$ of 2.69, which was calculated relative to the GR curve of GMP (**Figure 5-8e**). γ-H2AX staining of CT26 nuclei showed that GMP/MOL(+) treatment caused the highest DNA double-strand breaks (DSB), which was 3.66-fold and 2.16-fold higher than MOL(+) and GMP(+) groups, respectively (**Figure 5-8g,h**).

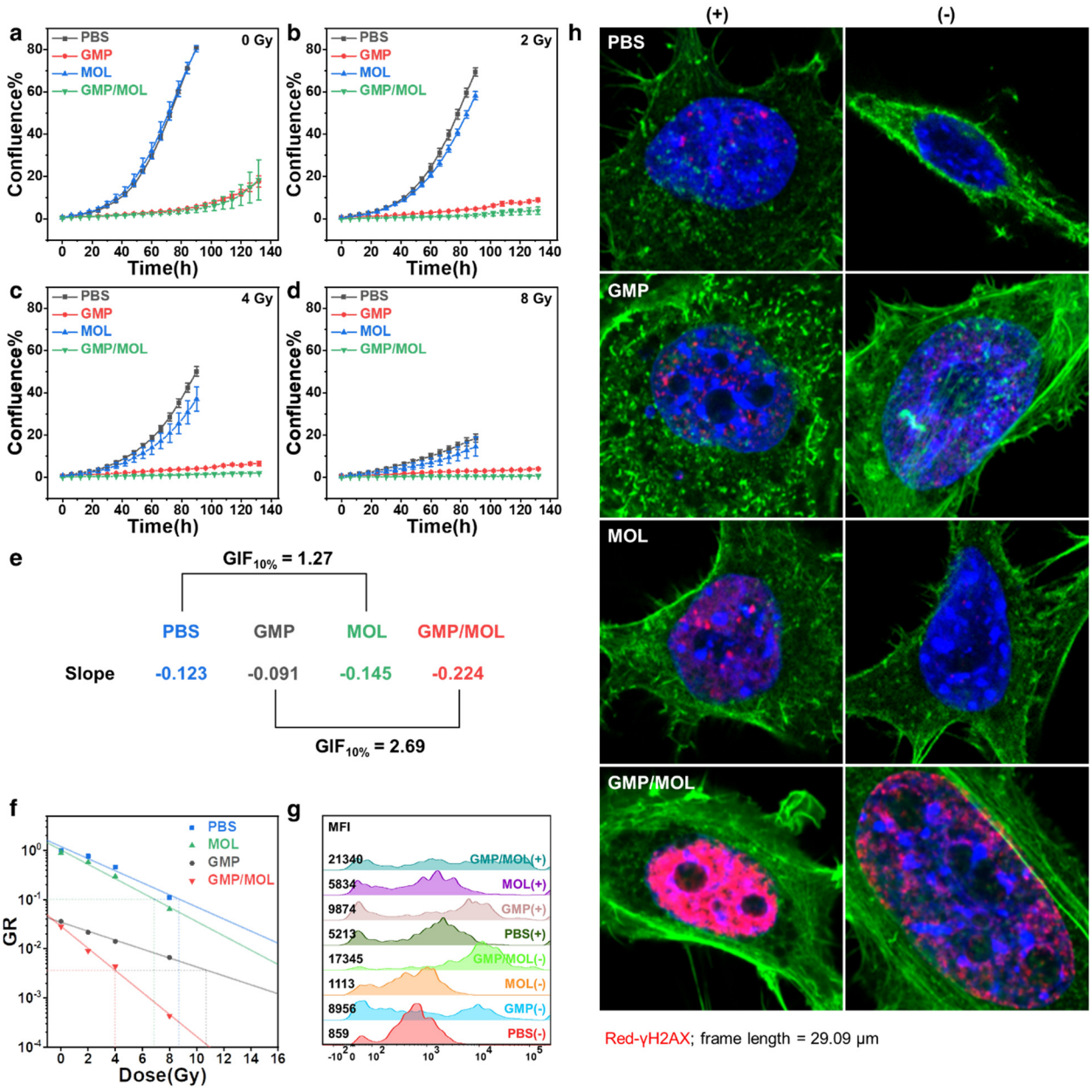

Figure 5-8. Radiosensitization effect of GMP/MOL. (a-d) Time-dependent confluence curves of cells irradiated by (a) 0 Gy, (b) 2 Gy, (c) 4 Gy, and (d) 8 Gy. (e) Relative $GIF_{10\%}$ values of PBS to MOL and GMP to GMP/MOL. (f) GR assays showing radioenhancement of MOL, GMP, or GMP/MOL in CT26 cells (n=3). (g) Fluorescence histograms showing DNA DSBs quantified with γ-H2AX staining by flow cytometry. (h) Representative CLSM images of DNA damage after different treatments. Nuclei were blued by Hoechst 33342. Cytoskeletons were green by Phalloidin. DNA damage was red by γ-H2AX. Frame length = 29.09 μm.

5.2.6 Retention of GMP/MOL in Tumors

We then investigated if GMP/MOL could retain GMP in subcutaneous CT26 tumors by LC-MS quantification of GMP and ICP-MS analysis of Hf. After *i.t.* injection, GMP was mostly (>88%) cleared from the tumors within 20 minutes and fell below the detection limit in 6 hours (**Figure 5-9a**). In contrast, GMP/MOL retained GMP with a 24.7-fold higher tumor area under the curve (AUC) than free GMP. Approximately 5% GMP was retained in tumors 4 days post *i.t.* injection (**Figure 5-9a**). As this time frame covered all RT fractions, we expected significant synergy between the slowly released GMP and fractionated RT. We further showed that GMP release was not caused by the disintegration of the MOL as >60% of the MOL was retained in the tumors 4 days post *i.t.* injection (**Figure 5-9b**). Steady and low plasma concentrations of GMP and Hf supported the slow release of GMP from GMP/MOL and intratumoral retention of the MOL (**Figure 5-9c,d**). These results show that GMP/MOL is retained in tumors to slowly release GMP and can act as a drug reservoir for antitumor applications.

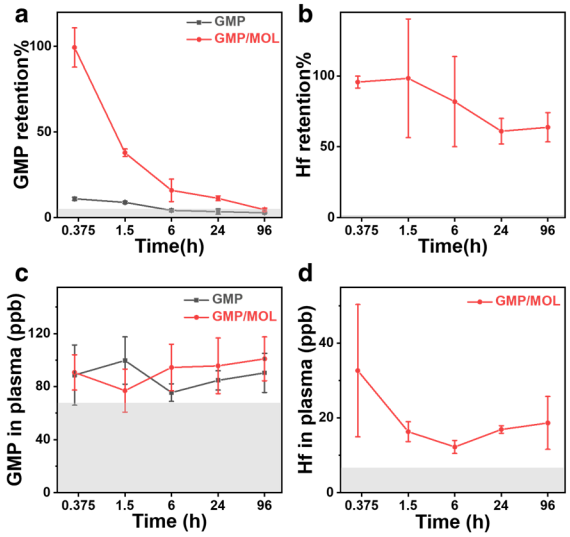

Figure 5-9. Intratumoral retention and plasma PK of GMP/MOL. (a,b) Tumor retention of (a) GMP (31.4 μg/mouse) and (b) Hf (1 μmol/mouse) after *i.t.* injection of free GMP or GMP/MOL into subcutaneous CT26 tumors. (c) GMP and (d) Hf concentrations in plasma after *i.t.* injection of GMP or GMP/MOL. (n=3; The grey area indicates the detection limit)

5.2.7 In Vivo Antitumor Efficacy

The antitumor efficacy of GMP/MOL(+) was evaluated in CT26 tumor-bearing BALB/c mice. The mice were *i.t.* injected with saline, GMP, MOL, or GMP/MOL and then irradiated with 2 Gy X-rays per fraction for 3 consecutive days (**Figure 5-10**).

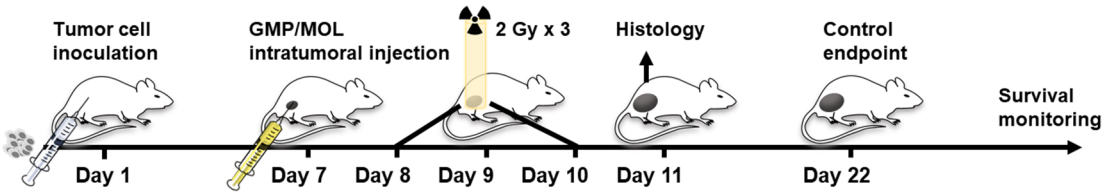

Figure 5-10. Treatment schedules for efficacy, histology, and survival studies in CT26-bearing BALB/c mice.

GMP/MOL(-) moderately inhibited tumor growth by chemotherapeutic effects with a tumor growth inhibition index (TGI) of 0.50. The radiotherapeutic effects of PBS(+) also moderately inhibited tumor growth with a TGI of 0.59. GMP(+) and MOL(+) enhanced RT with TGIs of 0.75 and 0.77, respectively. GMP/MOL(+) synergized the chemotherapeutic effects of slowly released GMP and enhanced RT by the MOL to regress tumors with a TGI of 0.98 (**Figure 5-11 and Table 5-1**).

Table 5-1. TGI values of CT26-bearing BALB/c mice at day 22.

Treatment	TGI(CT26)
PBS(+)	0.59
GMP(+)	0.75
MOL(+)	0.77
GMP/MOL(-)	0.50
GMP/MOL(+)	0.98

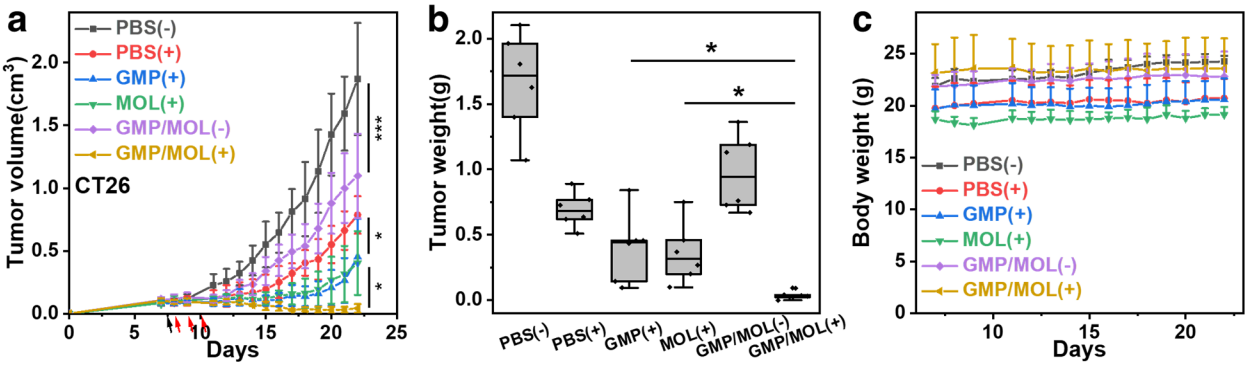

Figure 5-11. Antitumor efficacy and body weight. (a) Tumor volumes, (b) excised tumor weights, and (c) body weights of CT26 tumor-bearing BALB/c mice after different treatments (n=6, the black arrow indicates *i.t.* injection, and the red arrow indicates X-ray irradiation of 2 Gy for 3 fractions).

Half of GMP/MOL(+)-treated mice were tumor-free on Day 90 post-treatment, while all mice in GMP(+) and MOL(+) groups reached euthanization limit by Day 42 and Day 44, respectively (**Figure 5-12 and Table 5-2**). No apparent body weight loss and organ toxicities were observed during the study (**Figure 5-11 and Figure 5-13**).

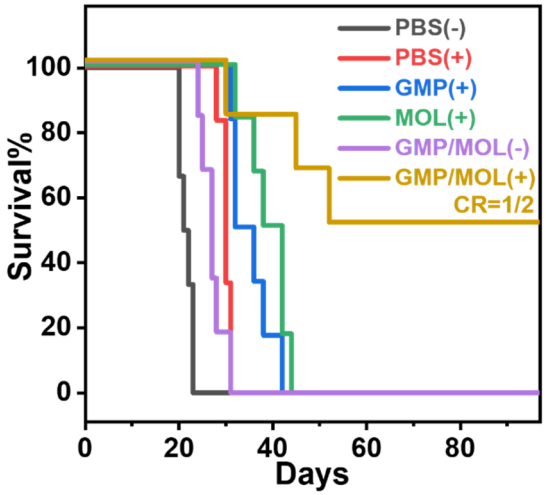

Figure 5-12. Survival of mice in different treatment groups after tumor inoculation.

Table 5-2. Median survival of CT26-bearing BALB/c mice.

Treatment	Median
PBS(-)	21.5 d
PBS(+)	29.5 d
GMP(+)	36.5 d
MOL(+)	38.0 d
GMP/MOL(-)	27.5 d
GMP/MOL(+)	N/A

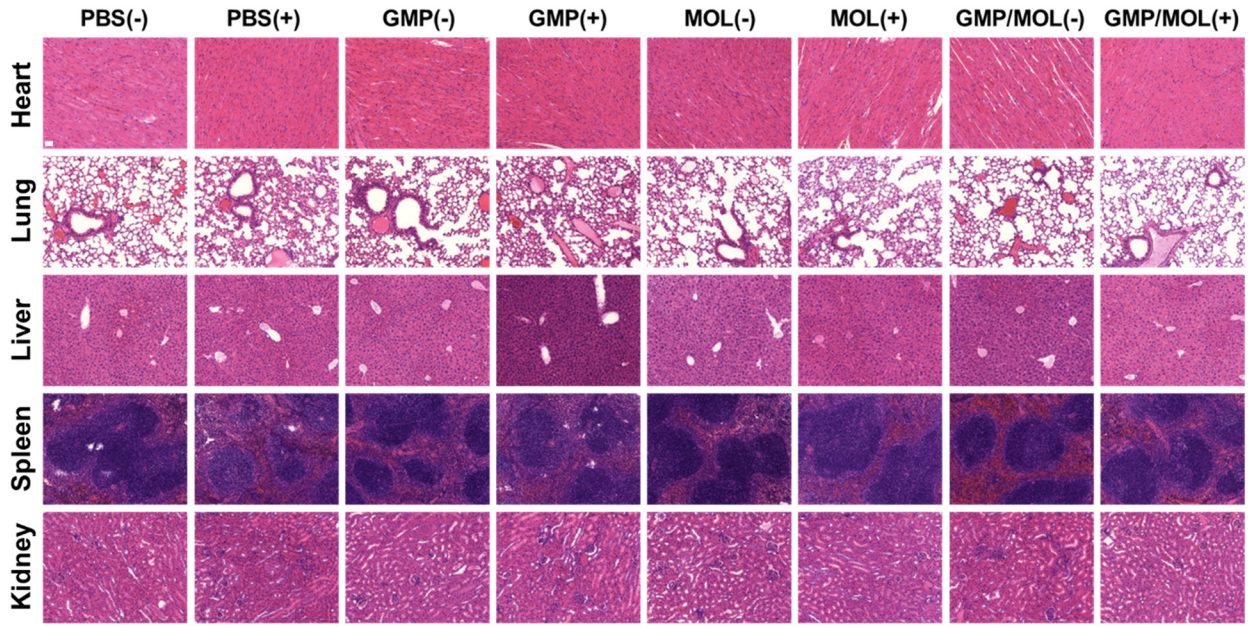

Figure 5-13. H&E staining of major organs of CT26-bearing BALB/c mice.

Immunohistochemistry (IHC) staining of CT26 tumors was performed 24 hours after the last X-ray irradiation to quantify DNA DSBs and the proliferation and apoptosis of cancer cells. While both PBS(+) and GMP(+) increased γ-H2AX-positive cells to 61.4% and 68.0% from 15.6% for PBS(-), MOL(+) and GMP/MOL(+) further increased γ-H2AX-positive cells to 77.5% and 80.5% (**Figure 5-14**).

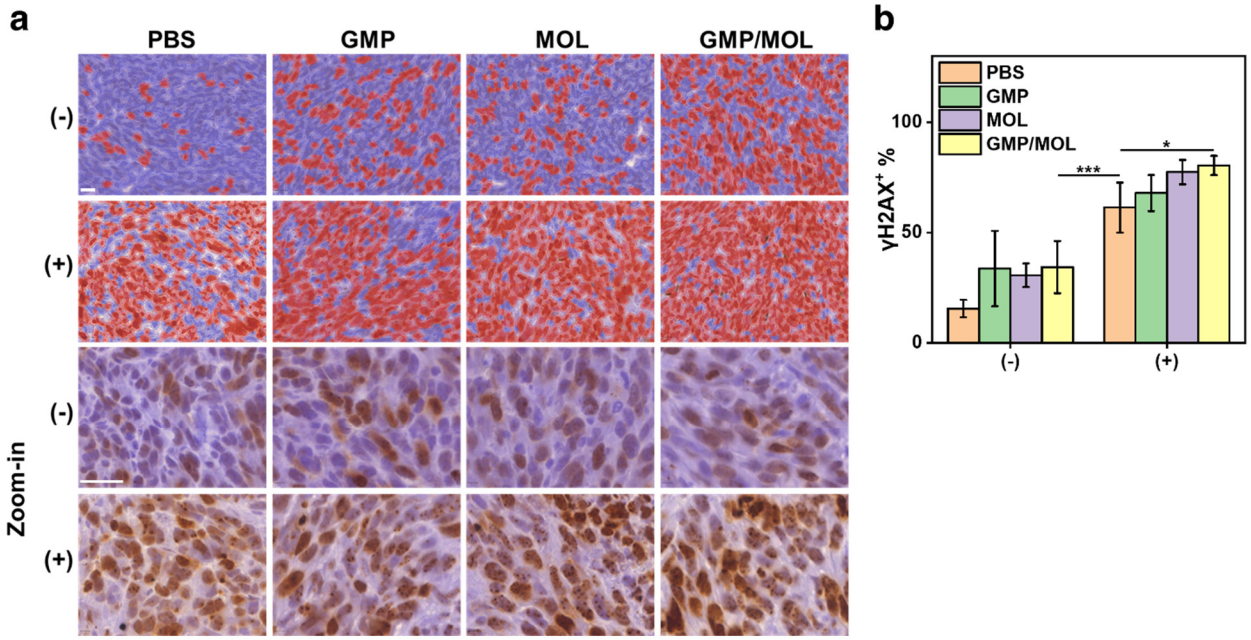

Figure 5-14. γ-H2AX IHC staining. (a) Representative images with positive cell detection of γ-H2AX staining in CT26 tumors treated by PBS, GMP, MOL, and GMP/MOL with or without RT, respectively. The zoom-in figures show the γ-H2AX foci after different treatments. (Scale bar = 20 μm; the DAB-positive cells were marked with red masks, and the negative cells were marked with blue masks). (b) Quantification of positive cell percentages in IHC staining of γ-H2AX for evaluation of DNA damage (n = 6). *p<0.05, **p<0.01, ***p<0.001, ****p<0.0001.

GMP/MOL(+) significantly suppressed tumor proliferation with the percentage of Ki67-positive tumor cells 10.6-fold and 16.5-fold lower than GMP(+) and PBS(+) groups, respectively (**Figure 5-15a,b**). TUNEL revealed that GMP/MOL(+) induced 3.4-fold and 3.5-fold stronger tumor apoptosis than GMP(+) and PBS(+), respectively (**Figure 5-15c,d**). These results strongly support synergistic chemoradiotherapy by slowly releasing GMP from GMP/MOL and enhancing RT by the MOL.

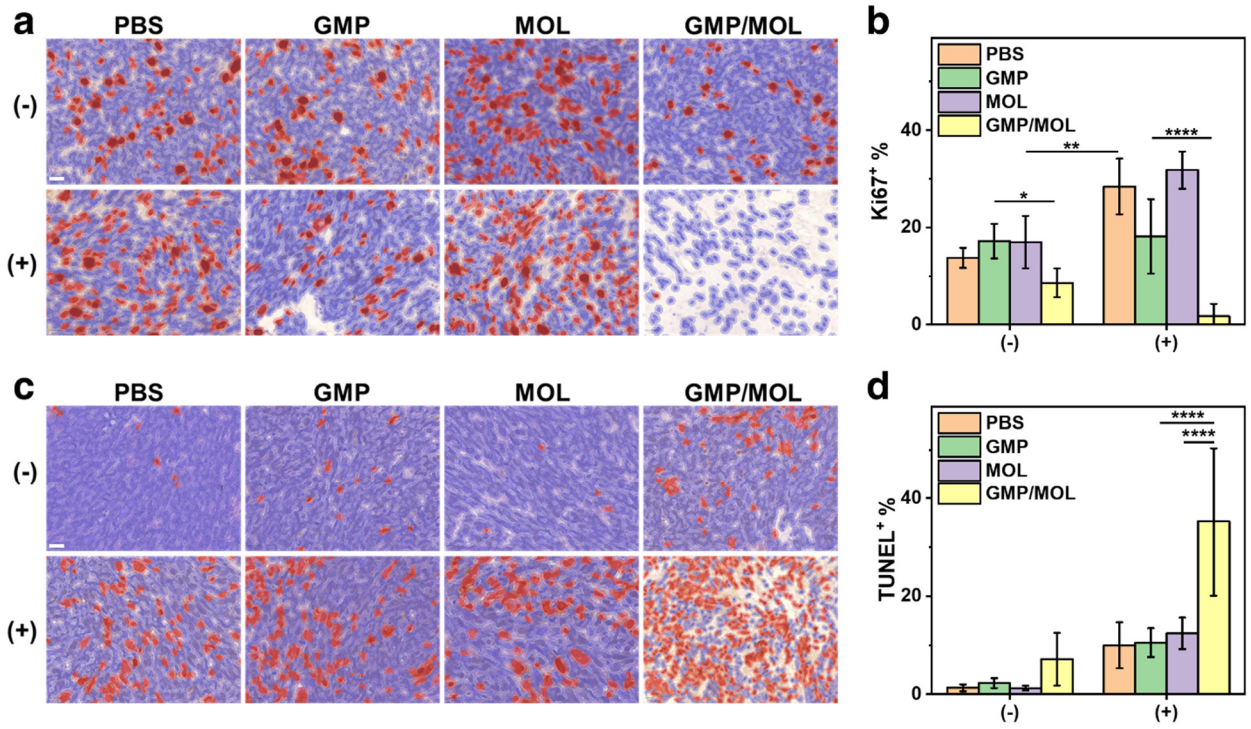

Figure 5-15. Ki67 and TUNEL IHC staining. (a) Representative images with (b) positive cell detection of Ki67 staining in CT26 tumors after indicated treatments. (c) Representative images with (d) positive cell detection of TUNEL staining in CT26 tumors after indicated treatments. (Scale bar = 20 μm; the DAB-positive cells were marked with red masks, and the negative cells were marked with blue masks)

5.3 Conclusions

In this Chapter, we used a 2-D MOL comprising Hf_{12}-SBUs and Ir-based photosensitizing ligands to deliver GMP and enhance radiotherapy. DFT calculations, ITC measurements, phosphate-dependent release, and intratumoral pharmacokinetics studies demonstrated that strong coordination between GMP and Hf_{12}-SBUs prolonged its intratumor retention and triggered its slow release in tumors through a phosphate concentration increase inside cells. Upon low-dose X-ray irradiation, the intrinsic radioenhancement by the MOL synergized with the enhanced chemotherapeutic effect of locally released GMP to significantly inhibit tumor growth with

complete tumor eradication in 50% of mice. This work establishes a new treatment paradigm for combining radiotherapy and chemotherapy with a single nanoparticle.

5.4 Methods

Synthesis and characterization of GMP. 1.58 g of gemcitabine (6 mmol, 1 eq) was added portion-wise to a solution of $POCl_3$ (60 mmol, 10 eq) in 40.0 mL of $PO(OMe)_3$ for 10 minutes in an ice-water bath. The reaction mixture was stirred for 5 minutes at 5 °C followed by 2 hours at room temperature. The mixture was carefully added to a mixture of deionized water (140 mL) and Et_2O (300 mL) while chilling in an ice-water bath. The aqueous layer was collected and washed with extra Et_2O (2 × 200 mL), and the pH was adjusted to 7 using concentrated NH_4OH while keeping the mixture chilled. The aqueous layer was then washed with more Et_2O (200 mL) and concentrated at a temperature lower than 30 °C to obtain a white slurry, which was stirred with MeOH (250 mL) at room temperature for 4 hours, filtered, and then concentrated to a slurry. Absolute EtOH (800 mL) was added to this slurry, stirred for another 4 hours, and filtered, and the resulting solid was dispersed and stirred in 400 mL of EtOH for 2 hours. The crude product was then dried and ground into a powder, which was recrystallized from MeOH to yield GMP as an ammonium salt (white solid, 1.8 g, 79.5%).^{1}H-NMR (400 MHz, D_2O) δ 8.13 (d, J = 8.0 Hz, 1H), 6.32 (d, J = 8.0 Hz, 1H), 6.30 – 6.23 (m, 1H), 4.59 – 4.46 (m, 1H), 4.28 (m, 2H), 4.15 (m, 1H). HRMS: m/z=344.0440 (expected 344.0460 for $[M+H]^+$).

Synthesis and characterization of MOL, DPPA/MOL, PPA/MOL, and GMP/MOL. $Ir(DBB)[dF)CF_3)ppy]^2$ and Hf_{12}-Ir MOL were synthesized according to the literature reports.[34-35, 50] For Hf_{12}-Ir MOL, 500 μL of $HfCl_4$ solution [2.0 mg/mL in DMF], 500 μL of H_2DBB-Ir-F solution (4.0 mg/mL in DMF), 2 μL of TFA, and 5 μL of water were added to a 1-dram glass vial.

The mixture was sonicated and heated in an 80 °C oven for 24 h. The yellow suspension was collected by centrifugation and washed with DMF and ethanol. The final product Hf_{12}-Ir MOL was dispersed in ethanol for storage. To prepare DPPA/MOL and PPA/MOL, the Hf_{12}-Ir MOL was dispersed in ethanol at an equivalent Hf concentration of 2 mM, and an equivalent volume of DPPA and PPA solution (0.33 mM in ethanol) was added to the MOL suspension. The mixture was vortexed for 15-35 minutes to afford the conjugated MOL. To prepare GMP/MOL, 0.17 mM GMP was dissolved in water and then added to Hf_{12}-Ir and vortexed as above.

400 μL of bare MOL or conjugated MOL solution was centrifuged and dried under vacuum and then digested in a solution of 400 μL D_6-DMSO, 50 μL D_2O, and 50 μL D_3PO_4 by sonication for 10 minutes. The mixture was then analyzed by ^{1}H-NMR and ^{31}P-NMR. After digestion of three conjugated MOLs in D_3PO_4/ D_6-DMSO, the peaks of the three organophosphorus molecules reappeared in ^{1}H-NMR and ^{31}P-NMR spectra because the structure of MOLs is disrupted, allowing the release of organophosphorus molecules.

Isothermal titration calorimetry. The interaction between GMP, DPPA, or PPA, and MOL was measured and analyzed by ITC on a MicroCal iTC_{200} system (Malvern Instruments) equipped with reference and sample cells (V = 400 μL). All titrations were carried out using a 40 μL syringe at 298.15 K with a stirring rate of 250 rpm. 900 μM MOL (based on SBU) water solution was titrated with 3 mM DPPA, PPA, or GMP water solution. The first injection of 0.4 μL was followed by 20 injections of 2 μL at intervals of 150 s. The same GMP, DPPA, or PPA samples were used to titrate H_2O to subtract background noise. Data analysis was performed using the MicroCal iTC_{200} software, and all data were fitted to an independent single-site model.

Loading capacity. The loading capacity of MOLs was tested by gradually increasing the ratio of DPPA, PPA, or GMP to MOL. Considering that both sides of MOL could conjugate molecules,

the occupancy of SBU was defined as 1 when six molecules were coordinated with one SBU (three on each side). When the occupancy of MOL was ≤1/3, all three model compounds afforded complete loading. DPPA and PPA exhibited a >97% loading efficiency when reaching the maximal occupancy of 1. In comparison, GMP showed a loading of 85% when the occupancy was equal to 1, indicating that spatial hindrance might negatively impact the loading efficiency.

DFT calculations. DFT calculations were performed with Gaussian 16 software, Revision A.03.[51] To reduce the computational cost, we used the Hf_6 cluster as a substitute for the Hf_{12} cluster and acetates to replace DBB-Ir linkers. Both approximations do not affect the binding interaction between the organophosphorus molecules and the SBUs. The structures of HPO_4^{2-}, Hf_6-SBU, GMP, PPA, DPPA, and the conjugates were fully optimized using the B3LYP-D3(BJ) functional.[52-53] The 6-31G(d) basis set was used for C, H, O, N, P, and F, and the SDD basis set was used for Hf. The single-point energy calculation was based on the Def2TZVP basis set to ensure accuracy, and the corresponding thermal correction calculation was based on the 6-31G(d) basis set. The solvation effect (in H_2O) was calculated using the SMD solvation model.[54]

Loading efficiency and release profiles. LC-MS quantification of DPPA, PPA, and GMP was achieved by an Agilent 6540 Q-Tof system with Agilent ZORBAX Extend-C18 Column (2.1 mm × 50 mm, 3.5 μm). Mobile phase A (0.1% TFA in water [v/v]) and mobile phase B (0.1% TFA in acetonitrile [v/v]) were operated with a fixed elution at a flow rate of 0.5 mL/min as 5% B for 5 min. The column temperature and sample temperature were both room temperature. The injection volume was 5 μL. For loading efficiency, different ratios of DPPA, PPA, or GMP were mixed with MOL as described in S2.2. The mixture was centrifuged at 14,000 rpm for 15 minutes, and the supernatant was directly subjected to LC-MS to quantify the concentrations of unconjugated molecules. For release profiles, DPPA/MOL, PPA/MOL, or GMP/MOL was freshly

prepared and redispersed in 1× PBS or 0.1× PBS (200 μL/tube) in 1.5 mL Eppendorf tubes (n = 3), respectively. The EP tubes were transferred to a 37 °C incubator. The supernatants (100 μL/tube) were collected at 0 h, 0.5 h, 1 h, 2h, 4 h, 8 h, and 24 h by centrifugation at 14,000 rpm and directly subjected to LC-MS quantification. The release profiles were fitted by the Hill function in OriginLab software.

Cellular uptake. CT26 cells were seeded in 6-well plates at a density of 2 × 10^5/well and incubated overnight. MOL or GMP/MOL was added at an equivalent Hf dose of 20 μM (n = 3). The cells were incubated at 37 ℃ for 1, 4, 8, and 12 hours. At each time point, the medium was aspirated, and the cells were washed with PBS three times, trypsinized, and collected by centrifugation at 1,800 rpm for 3 minutes. The cell pellets were digested with 1 mL of concentrated HNO_3 with 1% HF in 1.5 mL Eppendorf tubes for 48 hours. The Hf concentration was determined by ICP-MS after dilution.

Cell viability assay. The cytotoxicity of GMP and GMP/MOL was evaluated in CT26 cells by CellTiter 96 AQ_{ueous} One Solution Cell Proliferation Assay (MTS assay, Promega, USA). The cells were seeded in 96-well plates at a density of 1,500 cells/well and cultured overnight. GMP or GMP/MOL was added at an equivalent GMP concentration of 0, 0.02, 0.2, 0.5, 1, 2, 5, 10, 20, 50, and 100 μM and incubated for 6 hours (n = 3). The cells were further incubated for 2 days, and the cell viability was determined by MTS assay. IC_{50} values of all treatment groups were fitted with the dose-response curves in Origin Lab software.

Growth rate inhibition assay. 1×10^5 cells/mL of CT26 cells were seeded in 6-well plates with or without coverslip in 2 mL of culture medium and cultured overnight for CLSM or flow cytometry, respectively. GMP or GMP/MOL was added at a GMP concentration of 1.67 μM and incubated for 8 hours. The cells were irradiated by 2 Gy X-ray and immediately trypsinized to

afford single-cell suspensions. The cells were then counted, diluted to 1000~2000 cells/mL, and reseeded in 24-well plates. The plates were put in IncuCyte S3 live imaging system and continuously observed by a 10× objective in phase contrast mode. The phase contrast images were collected and analyzed with IncuCyte 2021A software to obtain a time-dependent confluence in each well (25 tiles per well, triplicates for each treatment group). The first derivative was calculated based on a time-dependent growth curve to give a growth rate (k_t). The time point where the k of the control group (PBS, 0 Gy) reached a maximum (t_{max}) was selected as the time to define the growth rate inhibition index (GRI). The GRI in the radiosensitization experiment was defined using the equation below[55]:

$$GRI(D, t_{max}) = 2^{k(D,t_{\max})/k(0)} - 1$$

Where D was the radiation dose and $k(0)$ was the growth rate of the control group at t_{max}. GRI data could be fitted linearly with GRI in log scale:

$$\log\left[GRI(D)\right] = \alpha D + \beta$$

Then the relative growth inhibition factor at $GRI = 10\%$ ($GIF_{10\%}$) was defined based on the fitting curve of $GRI(D)$ to quantify the radiosensitizing effects:

$$GIF_{10\%} = \frac{D_{treatment\ A}}{D_{treatment\ B}}$$

γ-H2AX immunofluorescence staining. 1×10^5 cells/mL of CT26 cells were seeded in 6-well plates with or without coverslip in 2 mL of culture medium and cultured overnight for CLSM or flow cytometry, respectively. The cells were treated the same way as GR assays and incubated for another 24 hours. For CLSM, the cells were fixed with 4% paraformaldehyde (pH = 7.2) at room temperature for 20 minutes. The cells were washed with PBS, blocked, and permeabilized by 5% FBS + 0.3% Triton-X in PBS at room temperature for 1 hour. After blocking, the cells were incubated with primary antibodies in 1% BSA + 0.3% Triton-X in PBS at 4°C overnight (phospho-

histone H2A.X (Ser139) (20E3) rabbit mAb #9718, 1:400). The cells were then washed by PBS and incubated with secondary antibodies in 1% BSA + 0.3% Triton-X in PBS at room temperature for 1 hour (anti-rabbit IgG (H+L), F(ab')2 fragment (Alexa Fluor® 647 conjugate) #4414, 1:1000). After staining, cells were washed by PBS and further incubated with 1:500 Acti-stain™ 488 and 1:3000 Hoechst 33342 in PBS for 30 minutes. After washing with PBS, the coverslips were mounted on glass slides with ProLong™ glass antifade mountant, cured at room temperature overnight, sealed by nail polish, and observed on a Leica Stellaris 8 confocal microscope. The images were processed and analyzed by Fiji ImageJ (NIH). For flow cytometry, the cells were collected as single-cell suspensions, fixed, blocked, and permeabilized in the same way as above, but stained only with primary and secondary antibodies. The cells were finally suspended in 0.5% BSA in PBS for flow cytometry analysis.

Intratumoral retention and PK of GMP/MOL. To evaluate intratumoral retention and PK of GMP/MOL, a subcutaneous CT26 model was established in BALB/c mice by inoculating 2×10^6 cells/mouse subcutaneously. At day 7, GMP or GMP/MOL was *i.t.* injected with an equivalent Hf dose of 1 μmol (GMP dose 1/12 μmol) (n = 3). Three control mice without treatment served as control to calculate the detection limit and the recovery rate of the GMP extraction method. At each time point, the mice were anesthetized, and the blood was drawn by retro-orbital bleeding. The tumors were excised and kept on ice, and the mice were euthanized. The whole blood was immediately centrifuged at 2,000 g for 15 minutes, and the clear top layer was collected as plasma. For LC-MS of GMP, samples were diluted 5-fold by PBS (40 μL + 160 μL) and centrifuged by Centrifree centrifugal filters (Merck, Millipore) to obtain LC-MS samples (Swinging bucket, 1,000 g, room temperature, 20 minutes). For ICP-MS of Hf, 20 μL of plasma samples were diluted into 1 mL concentrated HNO_3 in 15 mL ep tubes and heated in a 60 ^oC oven for 2 hours. The samples

were digested overnight, filtered, and diluted 35-fold with MilliQ water before ICP-MS. Meanwhile, the tumors were excised and immersed in 15 mL ep tubes filled with 2 mL 5% H_3PO_4 (on ice). The tumor tissues were then homogenized with a probe sonicator (500 W, 20 kHz) with 30% power for 1 minute on ice. The mixture was centrifuged at 2,000 g for 15 minutes to remove all the solid residues, and 500 μL of supernatants were collected. For LC-MS of GMP, the tumor lysis was first diluted 5-fold by PBS and transferred 200 μL of supernatant into Centrifree centrifugal filters (Merck, Millipore) to obtain LC-MS samples (Swinging bucket, 1,000 g, room temperature, 20 minutes). For ICP-MS of Hf, 100 μL of tumor lysis was transferred into 1 mL concentrated HNO_3 and processed the same way as plasma samples for ICP-MS.

In vivo anti-cancer efficacy. To evaluate in vivo chemoradiotherapy efficacy of GMP/MOL, a subcutaneous CT26 model was established in BALB/c mice by inoculating 2×10^6 cells/mouse subcutaneously. At day 7, the mice with tumor volumes around 75 mm^3 were randomized for treatment. PBS, GMP, MOL, or GMP/MOL was *i.t.* injected with an equivalent Hf dose of 1 μmol (GMP dose 1/12 μmol) (n = 6). Eight hours later, the mice were anesthetized with 2.5% (V/V) isoflurane/O_2 and irradiated by 2 Gy X-ray. Tumor sizes were measured with an electronic caliper (tumor volume = length×$width^2$/2), and body weight was monitored with an electronic scale. On day 22, the mice were euthanized, and the tumors were excised and weighed. Major organs were sectioned for H&E staining to evaluate general toxicity.

IHC staining and analysis. One day after the last X-ray irradiation on day 11, the mice were euthanized, and the tumors were excised. Tumor tissues were fixed in 4% PFA for 1 day and 70% ethanol for 1 day. Tissues were embedded in paraffin, sectioned, and stained for γ-H2AX, Ki67, and TUNEL by the Human Tissue Resource Center at the University of Chicago.[28] The slides were sealed and scanned on a CRi Panoramic SCAN 40x whole slide scanner by Integrated Light

Microscopy Core at the University of Chicago. The images were viewed and analyzed by QuPath-0.4.2 software.[56]

5.5 References

(1) Chabner, B. A.; Roberts, T. G., Chemotherapy and the war on cancer. *Nat. Rev. Cancer* **2005,** *5* (1), 65-72.

(2) DeVita, V. T., Jr.; Chu, E., A History of Cancer Chemotherapy. *Cancer Res.* **2008,** *68* (21), 8643-8653.

(3) Vogelzang, N. J., Continuous infusion chemotherapy: a critical review. *J. Clin. Oncol.* **1984,** *2* (11), 1289-1304.

(4) Decosterd, L. A.; Widmer, N.; Zaman, K.; Cardoso, E.; Buclin, T.; Csajka, C., Therapeutic drug monitoring of targeted anticancer therapy. *Biomark. Med.* **2015,** *9* (9), 887-893.

(5) Wolinsky, J. B.; Colson, Y. L.; Grinstaff, M. W., Local drug delivery strategies for cancer treatment: Gels, nanoparticles, polymeric films, rods, and wafers. *J. Control. Release* **2012,** *159* (1), 14-26.

(6) Morales, A.; Eidinger, D.; Bruce, A. W., Intracavitary Bacillus Calmette-Guerin in the treatment of superficial bladder tumors. *J. Urol.* **1976,** *116* (2), 180-3.

(7) Walter, K. A.; Tamargo, R. J.; Olivi, A.; Burger, P. C.; Brem, H., Intratumoral chemotherapy. *Neurosurgery* **1995,** *37* (6), 1128-45.

(8) Haroun, R. I.; Brem, H., Local drug delivery. *Curr. Opin. Oncol.* **2000,** *12* (3), 187-93.

(9) Goldberg, E. P.; Hadba, A. R.; Almond, B. A.; Marotta, J. S., Intratumoral cancer chemotherapy and immunotherapy: opportunities for nonsystemic preoperative drug delivery. *J. Pharm. Pharmacol.* **2002,** *54* (2), 159-180.

(10) Chua, C. Y. X.; Ho, J.; Demaria, S.; Ferrari, M.; Grattoni, A., Emerging Technologies for Local Cancer Treatment. *Adv. Ther.* **2020,** *3* (9), 2000027.

(11) Spiotto, M.; Fu, Y.-X.; Weichselbaum, R. R., The intersection of radiotherapy and immunotherapy: Mechanisms and clinical implications. *Sci. Immunol.* **2016,** *1* (3), eaag1266-eaag1266.

(12) Weichselbaum, R. R.; Liang, H.; Deng, L.; Fu, Y.-X., Radiotherapy and immunotherapy: a beneficial liaison? *Nat. Rev. Clin. Oncol.* **2017,** *14* (6), 365-379.

(13) Petroni, G.; Cantley, L. C.; Santambrogio, L.; Formenti, S. C.; Galluzzi, L., Radiotherapy as a tool to elicit clinically actionable signalling pathways in cancer. *Nat. Rev. Clin. Oncol.* **2022,** *19* (2), 114-131.

(14) Price, J. M.; Prabhakaran, A.; West, C. M. L., Predicting tumour radiosensitivity to deliver precision radiotherapy. *Nat. Rev. Clin. Oncol.* **2023,** *20* (2), 83-98.

(15) Begg, A. C.; Stewart, F. A.; Vens, C., Strategies to improve radiotherapy with targeted drugs. *Nat. Rev. Cancer* **2011,** *11* (4), 239-253.

(16) Seiwert, T. Y.; Salama, J. K.; Vokes, E. E., The concurrent chemoradiation paradigm—general principles. *Nat. Clin. Pract. Oncol.* **2007,** *4* (2), 86-100.

(17) Kleinberg, L.; Gibson, M. K.; Forastiere, A. A., Chemoradiotherapy for localized esophageal cancer: regimen selection and molecular mechanisms of radiosensitization. *Nat. Clin. Pract. Oncol.* **2007,** *4* (5), 282-294.

(18) Weichselbaum, R. R.; Ishwaran, H.; Yoon, T.; Nuyten, D. S. A.; Baker, S. W.; Khodarev, N.; Su, A. W.; Shaikh, A. Y.; Roach, P.; Kreike, B.; Roizman, B.; Bergh, J.; Pawitan, Y.; van de Vijver, M. J.; Minn, A. J., An interferon-related gene signature for DNA damage resistance is a predictive marker for chemotherapy and radiation for breast cancer. *Proc. Natl. Acad. Sci. U.S.A.* **2008,** *105* (47), 18490-18495.

(19) Kono, K.; Mimura, K.; Kiessling, R., Immunogenic tumor cell death induced by chemoradiotherapy: molecular mechanisms and a clinical translation. *Cell Death Dis.* **2013,** *4* (6), e688-e688.

(20) Seiwert, T. Y.; Salama, J. K.; Vokes, E. E., The chemoradiation paradigm in head and neck cancer. *Nat. Clin. Pract. Oncol.* **2007,** *4* (3), 156-171.

(21) Wang, Y. H.; Yao, N.; Wei, K. K.; Jiang, L.; Hanif, S.; Wang, Z. X.; Pei, C. X., The efficacy and safety of probiotics for prevention of chemoradiotherapy-induced diarrhea in people with abdominal and pelvic cancer: a systematic review and meta-analysis. *Eur. J. Clin. Nutr.* **2016,** *70* (11), 1246-1253.

(22) De Ruysscher, D.; Niedermann, G.; Burnet, N. G.; Siva, S.; Lee, A. W. M.; Hegi-Johnson, F., Radiotherapy toxicity. *Nat. Rev. Dis. Primers* **2019,** *5* (1), 13.

(23) Mangesius, J.; Minasch, D.; Fink, K.; Nevinny-Stickel, M.; Lukas, P.; Ganswindt, U.; Seppi, T., Systematic risk analysis of radiation pneumonitis in breast cancer: role of cotreatment with chemo-, endocrine, and targeted therapy. *Strahlenther. Onkol.* **2023,** *199* (1), 67-77.

(24) Lu, K.; He, C.; Guo, N.; Chan, C.; Ni, K.; Lan, G.; Tang, H.; Pelizzari, C.; Fu, Y.-X.; Spiotto, M. T.; Weichselbaum, R. R.; Lin, W., Low-dose X-ray radiotherapy–radiodynamic therapy via nanoscale metal–organic frameworks enhances checkpoint blockade immunotherapy. *Nat. Biomed. Eng.* **2018,** *2* (8), 600-610.

(25) Huang, Z.; Wang, Y.; Yao, D.; Wu, J.; Hu, Y.; Yuan, A., Nanoscale coordination polymers induce immunogenic cell death by amplifying radiation therapy mediated oxidative stress. *Nat. Commun.* **2021,** *12* (1), 145.

(26) Hao, F.; Yan, Z.-Y.; Yan, X.-P., Recent Advances in Research on the Effect of Physicochemical Properties on the Cytotoxicity of Metal–Organic Frameworks. *Small Sci.* **2022,** *2* (9), 2200044.

(27) Ni, K.; Lan, G.; Lin, W., Nanoscale Metal–Organic Frameworks Generate Reactive Oxygen Species for Cancer Therapy. *ACS Cent. Sci.* **2020,** *6* (6), 861-868.

(28) Xu, Z.; Ni, K.; Mao, J.; Luo, T.; Lin, W., Monte Carlo Simulations Reveal New Design Principles for Efficient Nanoradiosensitizers Based on Nanoscale Metal–Organic Frameworks. *Adv. Mater.* **2021,** *33* (40), 2104249.

(29) Cao, L.; Lin, Z.; Shi, W.; Wang, Z.; Zhang, C.; Hu, X.; Wang, C.; Lin, W., Exciton Migration and Amplified Quenching on Two-Dimensional Metal–Organic Layers. *J. Am. Chem. Soc.* **2017,** *139* (20), 7020-7029.

(30) Lan, G.; Ni, K.; Veroneau, S. S.; Song, Y.; Lin, W., Nanoscale Metal–Organic Layers for Radiotherapy–Radiodynamic Therapy. *J. Am. Chem. Soc.* **2018,** *140* (49), 16971-16975.

(31) Lan, G.; Quan, Y.; Wang, M.; Nash, G. T.; You, E.; Song, Y.; Veroneau, S. S.; Jiang, X.; Lin, W., Metal–Organic Layers as Multifunctional Two-Dimensional Nanomaterials for Enhanced Photoredox Catalysis. *J. Am. Chem. Soc.* **2019,** *141* (40), 15767-15772.

(32) Luo, T.; Fan, Y.; Mao, J.; Yuan, E.; You, E.; Xu, Z.; Lin, W., Dimensional Reduction Enhances Photodynamic Therapy of Metal–Organic Nanophotosensitizers. *J. Am. Chem. Soc.* **2022,** *144* (12), 5241-5246.

(33) Shi, W.; Cao, L.; Zhang, H.; Zhou, X.; An, B.; Lin, Z.; Dai, R.; Li, J.; Wang, C.; Lin, W., Surface Modification of Two-Dimensional Metal–Organic Layers Creates Biomimetic Catalytic Microenvironments for Selective Oxidation. *Angew. Chem. Int. Ed.* **2017,** *56* (33), 9704-9709.

(34) Quan, Y.; Lan, G.; Fan, Y.; Shi, W.; You, E.; Lin, W., Metal–Organic Layers for Synergistic Lewis Acid and Photoredox Catalysis. *J. Am. Chem. Soc.* **2020,** *142* (4), 1746-1751.

(35) Luo, T.; Nash, G. T.; Jiang, X.; Feng, X.; Mao, J.; Liu, J.; Juloori, A.; Pearson, A. T.; Lin, W., A 2D Nanoradiosensitizer Enhances Radiotherapy and Delivers STING Agonists to Potentiate Cancer Immunotherapy. *Adv. Mater.* **2022,** *34* (39), 2110588.

(36) Luo, T.; Fan, Y.; Mao, J.; Jiang, X.; Albano, L.; Yuan, E.; Germanas, T.; Lin, W., Metal-Organic Layer Delivers 5-Aminolevulinic Acid and Porphyrin for Dual-Organelle-Targeted Photodynamic Therapy. *Angew. Chem. Int. Ed.* **2023**, e202301910.

(37) Longley, D. B.; Harkin, D. P.; Johnston, P. G., 5-Fluorouracil: mechanisms of action and clinical strategies. *Nat. Rev. Cancer* **2003,** *3* (5), 330-338.

(38) Mullen, N. J.; Singh, P. K., Nucleotide metabolism: a pan-cancer metabolic dependency. *Nat. Rev. Cancer* **2023**.

(39) Reif, B.; Ashbrook, S. E.; Emsley, L.; Hong, M., Solid-state NMR spectroscopy. *Nat. Rev. Methods Primers* **2021,** *1* (1), 2.

(40) Foster, M. P.; McElroy, C. A.; Amero, C. D., Solution NMR of Large Molecules and Assemblies. *Biochemistry* **2007,** *46* (2), 331-340.

(41) Kohli, P.; Blanchard, G. J., Probing Interfaces and Surface Reactions of Zirconium Phosphate/Phosphonate Multilayers Using 31P NMR Spectrometry. *Langmuir* **2000,** *16* (2), 695-701.

(42) Wang, Z.; Fu, Y.; Kang, Z.; Liu, X.; Chen, N.; Wang, Q.; Tu, Y.; Wang, L.; Song, S.; Ling, D.; Song, H.; Kong, X.; Fan, C., Organelle-Specific Triggered Release of Immunostimulatory Oligonucleotides from Intrinsically Coordinated DNA–Metal–Organic Frameworks with Soluble Exoskeleton. *J. Am. Chem. Soc.* **2017,** *139* (44), 15784-15791.

(43) Knochel, J. P.; Haller, R.; Ferguson, E., Selective Phosphorus Deficiency in the Hyperalimented Hypophosphatemic Dog and Phosphorylation Potentials in the Muscle Cell. In *Phosphate and Minerals in Health and Disease*, Massry, S. G.; Ritz, E.; Jahn, H., Eds. Springer US: Boston, MA, 1980; pp 323-334.

(44) Bowen, J. W.; Levinson, C., Phosphate concentration and transport in Ehrlich ascites tumor cells: Effect of sodium. *J. Cell. Physiol.* **1982,** *110* (2), 149-154.

(45) Auesukaree, C.; Homma, T.; Tochio, H.; Shirakawa, M.; Kaneko, Y.; Harashima, S., Intracellular Phosphate Serves as a Signal for the Regulation of the PHO Pathway in Saccharomyces cerevisiae. *J. Biol. Chem.* **2004,** *279* (17), 17289-17294.

(46) Goretti Pinedo, M.; Alon, U. S., Erratum to: Phosphate homeostasis and its role in bone health. *Pediatr. Nephrol.* **2017,** *32* (10), 1999-1999.

(47) Chazot, G.; Lemoine, S.; Kocevar, G.; Kalbacher, E.; Sappey-Marinier, D.; Rouvière, O.; Juillard, L., Intracellular Phosphate and ATP Depletion Measured by Magnetic Resonance Spectroscopy in Patients Receiving Maintenance Hemodialysis. *J. Am. Soc. Nephrol.* **2021,** *32* (1), 229-237.

(48) Nash, G. T.; Luo, T.; Lan, G.; Ni, K.; Kaufmann, M.; Lin, W., Nanoscale Metal–Organic Layer Isolates Phthalocyanines for Efficient Mitochondria-Targeted Photodynamic Therapy. *J. Am. Chem. Soc.* **2021,** *143* (5), 2194-2199.

(49) Xu, Z.; Luo, T.; Lin, W., Nanoscale Metal–Organic Layers for Biomedical Applications. *Acc. Mater. Res.* **2021,** *2* (10), 944-953.

(50) Zhu, Y.-Y.; Lan, G.; Fan, Y.; Veroneau, S. S.; Song, Y.; Micheroni, D.; Lin, W., Merging Photoredox and Organometallic Catalysts in a Metal–Organic Framework Significantly Boosts Photocatalytic Activities. *Angew. Chem. Int. Ed.* **2018,** *57* (43), 14090-14094.

(51) Frisch, M. J.; Trucks, G. W.; Schlegel, H. B.; Scuseria, G. E.; Robb, M. A.; Cheeseman, J. R.; Scalmani, G.; Barone, V.; Petersson, G. A.; Nakatsuji, H.; Li, X.; Caricato, M.; Marenich, A. V.; Bloino, J.; Janesko, B. G.; Gomperts, R.; Mennucci, B.; Hratchian, H. P.; Ortiz, J. V.; Izmaylov, A. F.; Sonnenberg, J. L.; Williams; Ding, F.; Lipparini, F.; Egidi, F.; Goings, J.; Peng, B.; Petrone, A.; Henderson, T.; Ranasinghe, D.; Zakrzewski, V. G.; Gao, J.; Rega, N.; Zheng, G.; Liang, W.; Hada, M.; Ehara, M.; Toyota, K.; Fukuda, R.; Hasegawa, J.; Ishida, M.; Nakajima, T.; Honda, Y.; Kitao, O.; Nakai, H.; Vreven, T.; Throssell, K.; Montgomery Jr., J. A.; Peralta, J. E.; Ogliaro, F.; Bearpark, M. J.; Heyd, J. J.; Brothers, E. N.; Kudin, K. N.; Staroverov, V. N.; Keith, T. A.; Kobayashi, R.; Normand, J.; Raghavachari, K.; Rendell, A. P.; Burant, J. C.; Iyengar, S. S.; Tomasi, J.; Cossi, M.; Millam, J. M.; Klene, M.; Adamo, C.; Cammi, R.; Ochterski, J. W.; Martin, R. L.; Morokuma, K.; Farkas, O.; Foresman, J. B.; Fox, D. J. *Gaussian 16 Rev. C.01*, Wallingford, CT, 2016.

(52) Becke, A. D., Density-functional exchange-energy approximation with correct asymptotic behavior. *Phys. Rev. A* **1988,** *38* (6), 3098-3100.

(53) Lee, C.; Yang, W.; Parr, R. G., Development of the Colle-Salvetti correlation-energy formula into a functional of the electron density. *Phys. Rev. B* **1988,** *37* (2), 785-789.

(54) Marenich, A. V.; Cramer, C. J.; Truhlar, D. G., Universal Solvation Model Based on Solute Electron Density and on a Continuum Model of the Solvent Defined by the Bulk Dielectric Constant and Atomic Surface Tensions. *J. Phys. Chem. B* **2009,** *113* (18), 6378-6396.

(55) Hafner, M.; Niepel, M.; Chung, M.; Sorger, P. K., Growth rate inhibition metrics correct for confounders in measuring sensitivity to cancer drugs. *Nat. Meth.* **2016,** *13* (6), 521-527.

(56) Bankhead, P.; Loughrey, M. B.; Fernández, J. A.; Dombrowski, Y.; McArt, D. G.; Dunne, P. D.; McQuaid, S.; Gray, R. T.; Murray, L. J.; Coleman, H. G.; James, J. A.; Salto-Tellez, M.; Hamilton, P. W., QuPath: Open source software for digital pathology image analysis. *Sci. Rep.* **2017,** *7* (1), 16878.

Chapter 6. A 2-D Nanoradiosensitizer Enhances Radiotherapy and Delivers STING Agonists to Potentiate Cancer Immunotherapy

6.1 Introduction

Immunotherapies such as immune checkpoint blockade (ICB) and adoptive T-cell transfer have revolutionized the treatment of some cancers.[1-2] Besides pharmacologic activation of the adaptive immune system, innate immune modulators such as agonists of STING and TLRs have also been explored as potential immunotherapies.[3-5] As an endogenous STING agonist in mammalian cells,[6-7] 2',3'-cyclic guanosine monophosphate–adenosine monophosphate (cGAMP) along with its derivatives has been extensively studied in preclinical models and clinical trials.[8-9] Despite strong preclinical antitumor effects, cGAMP and other STING agonists have shown modest efficacy as monotherapies or in combination with ICB in clinical trials, likely due to poor pharmacokinetics, insufficient tumor antigen presentation, and asynchronous immune activation.[8, 10-11] Novel platforms are needed to efficiently deliver STING agonists and combine them with other treatment modalities for enhanced immunotherapeutic effects.[12-13]

RT utilizes ionizing radiation to damage tumor cells and is used to treat approximately 50% of all cancer patients during their disease courses.[14] In addition to direct cell killing, recent evidence has indicated that RT can modulate the tumor microenvironment (TME) and cause multifaceted immune outcomes, including the release of immunostimulatory factors and infiltration of immunosuppressive cells.[15] As a result, a large number of clinical investigations have been launched to test RT and ICB combinations on different tumors.[16] However, RT has provided moderate clinical benefits to anti-PD-1 antibodies in randomized and controlled phase 2 clinical trials.[17-21] These preliminary clinical readouts suggest that ICB alone may not be sufficient

for overcoming immunosuppression in irradiated tumors. Increasing RT efficiency, enhancing antigen presentation, and bridging innate and adaptive immune systems are potential approaches to improve the synergy between RT and ICB. Innovative treatment regimens are required to synergize RT and immunotherapy for optimal therapeutic outcomes.

In this Chapter, we report a 2-D nanoplatform based on a MOL to integrate RT and immunotherapy for improved local tumor regression and systemic antitumor effect when combined with ICB. The 2-D MOL maximally expanded the surface area to achieve potent radiosensitization via a unique RT-RDT process and provide anchoring sites to conjugate cGAMP molecules for STING activation.[22] cGAMP/MOL sustained the release of cGAMP in tumors via a phosphate concentration gradient to elicit stronger STING activation than free cGAMP. The synergistic action of RT-RDT and STING agonists effectively regressed local tumors and activated the tumor immune environment on two murine colon cancer models. Further combination of cGAMP/MOL plus X-ray irradiation with an anti-PD-L1 antibody showed improved distant tumor control and abscopal effect on a bilateral tumor model, thus extending the scope of cGAMP/MOL treatment from local synergy to systemic anti-cancer immune response.

6.2 Results and Discussions

6.2.1 Hf_{12}-Ir MOL Enhances Radiotherapy and Induces Immunogenic Cell Death

Hf_{12}-Ir MOL was synthesized by a solvothermal reaction between $HfCl_4$ and H_2DBB-Ir-F in DMF with TFA as modulators.[23] The MOL is composed of periodically arranged Hf_{12} secondary SBUs and DBB-Ir photosensitizer (Ir-PS) ligands (**Figure 6-1**).

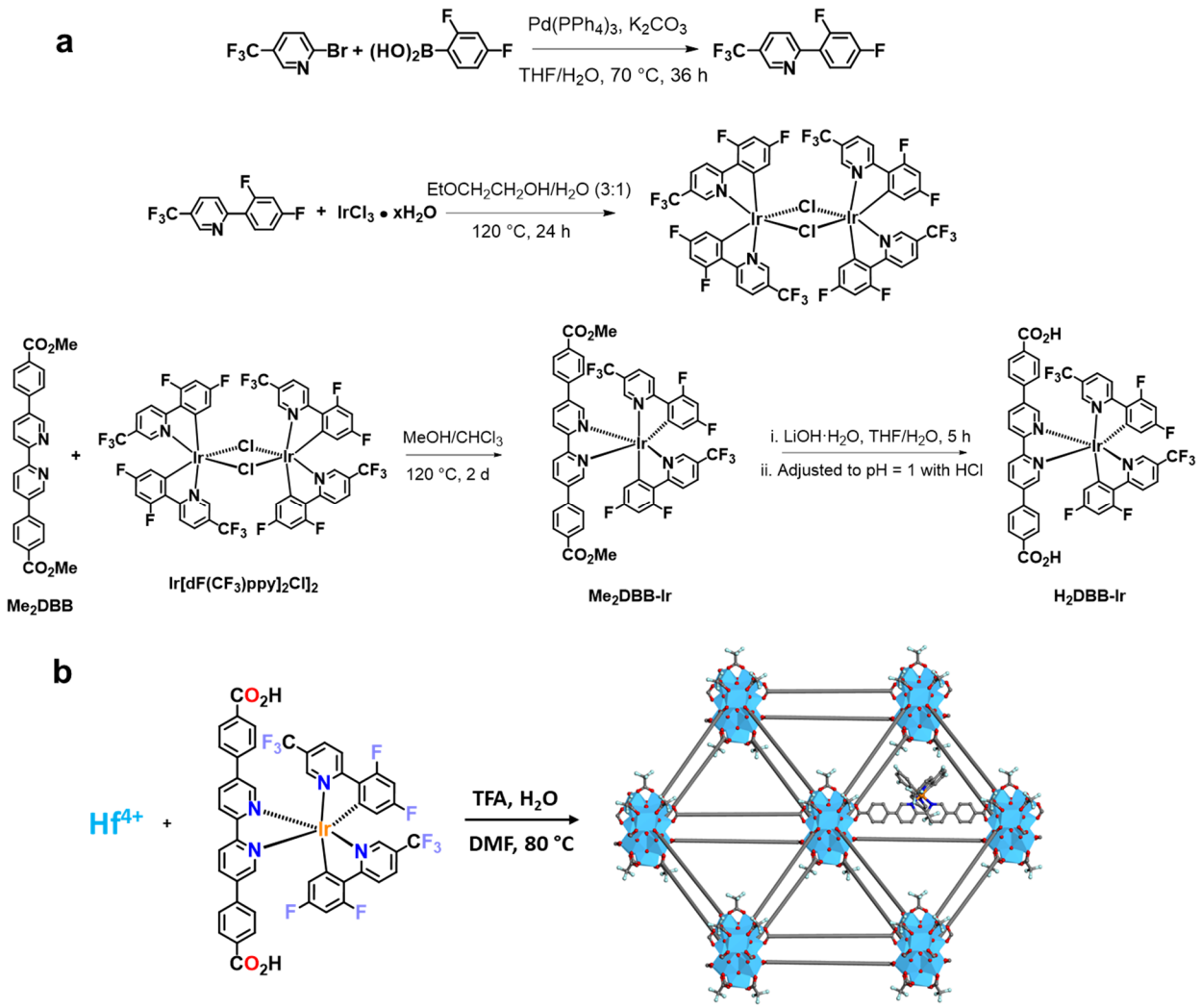

Figure 6-1. Synthetic routes of (a) Ir(DBB)[dF(CF$_3$)ppy]$_2^+$ ligand and (b) Hf$_{12}$-Ir MOL. Hf atoms are shown as blue polyhedron units. Oxygen, carbon, nitrogen, fluoride, and iridium are shown as red, gray, navy blue, pale green, and orange spheres, respectively. To simplify, only one ligand is shown, and the rest are shown as grey sticks. All hydrogen atoms were omitted for clarity.

TEM (**Figure 6-2a**) and AFM (**Figure 6-2b**) imaging indicated a single-layer crystalline nanosheet morphology of the MOL, whereas PXRD studies confirmed the crystalline **kgd** lattice topology of the MOL (**Figure 6-2c**). The MOL was well dispersed and stable in saline (**Figure 6-2d**), exhibiting a highly positive surface charge with a ζ-potential of 40.4 ± 1.2 mV (**Figure 6-2e**). The MOL showed rapid and efficient cellular uptake as quantified by ICP-MS (**Figure 6-2f**).

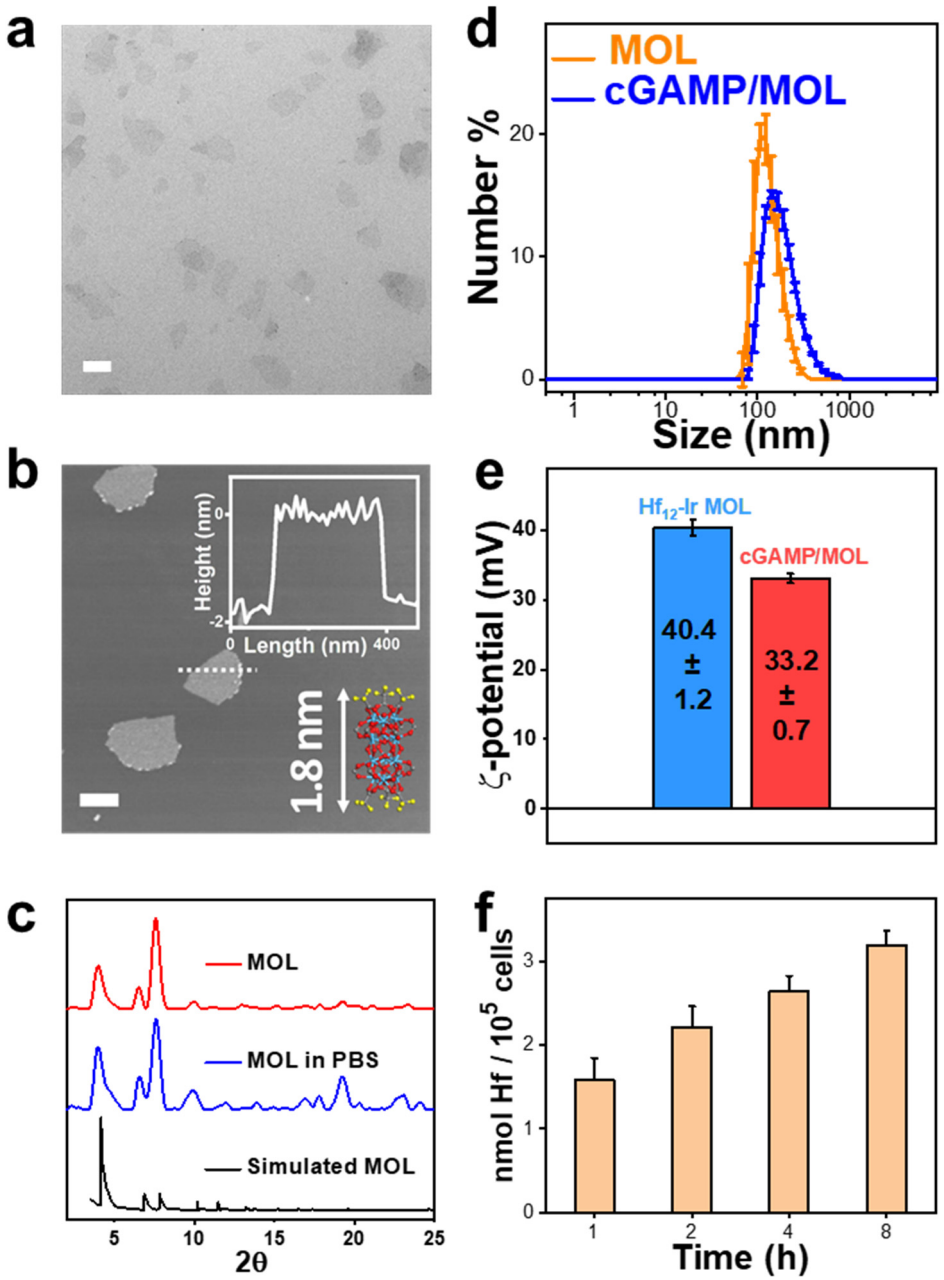

Figure 6-2. MOL characterization. (a) TEM image showing a nanosheet morphology of the MOL (scale bar = 200 nm). (b) AFM image and height profile (inset) showing a monolayer morphology of the MOL. The height of the simulated Hf_{12} SBU structure is 1.8 nm, which matches well with AFM height profile (scale bar = 200 nm). (c) PXRD patterns of as-synthesized MOL, the MOL soaked in PBS for 24 hours, and simulated MOL structure. (d) Size distribution of Hf_{12}-Ir MOL and cGAMP/MOL by DLS. (e) Surface ζ potentials of Hf_{12}-Ir MOL and cGAMP/MOL. (f) Time-dependent cellular uptake of Hf_{12}-Ir MOL by MC38 cells by ICP-MS

Upon X-ray irradiation, the MOL efficiently generated ROS via the RT-RDT process in test tubes (**Figure 6-3a**) and *in vitro* (**Figure 6-3b**) on murine colon cancer MC38 cells.

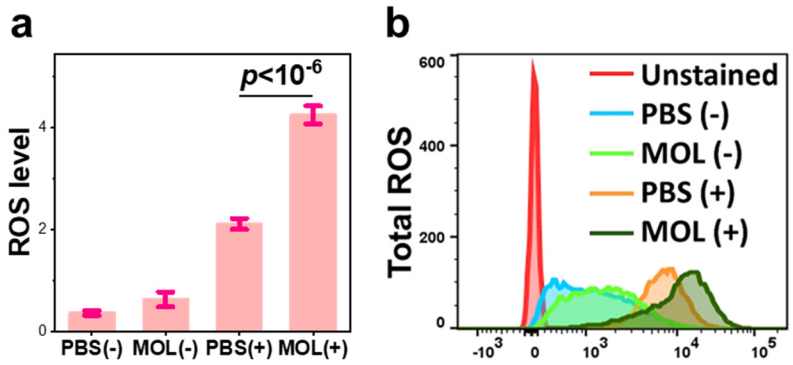

Figure 6-3. ROS generation. (a) ROS generation of the MOL in test tube upon 2 Gy X-ray irradiation (n = 6). (b) DCF-DA assay showing *in vitro* ROS generation in CT26 cells by flow cytometry (FITC channel).

The radiosensitizing efficiency was further investigated *in vitro* by a growth rate inhibition assay via live cell imaging, which shows improved sensitivity over traditional clonogenic assay (**Figure 6-4**).[24-25]

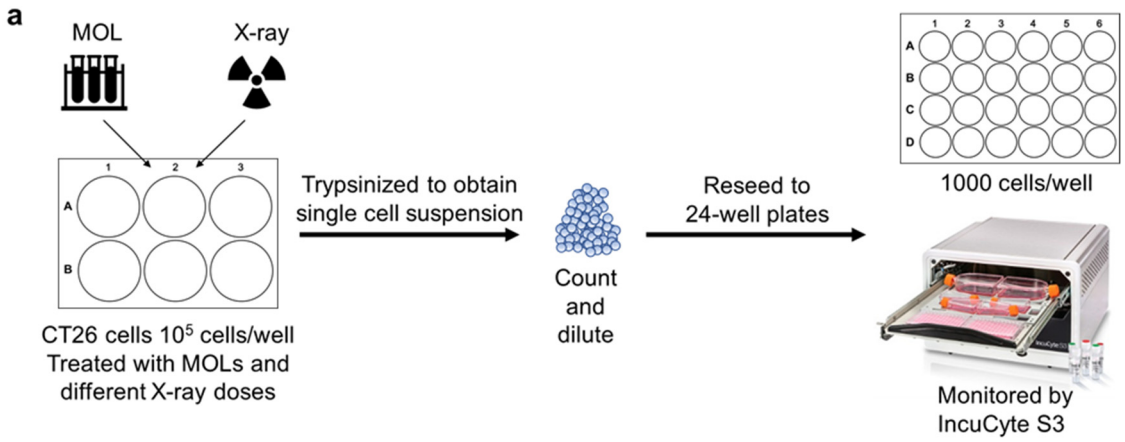

Figure 6-4. Schematic showing the workflow of growth rate inhibition assay. The cells were reseeded in 24-well plates after different treatments in a low cell density. The plates were put in an IncuCyte S3 live-cell analysis system (www.essenbioscience.com) to observe real-time cell density.

After X-ray treatment, MC38 and CT26 colon cancer cell lines were observed and analyzed by IncuCyte S3 to provide real-time cell proliferation. The GRI and GIF were calculated based on time-dependent confluence of MC38 and CT26 cells. The MOL sensitized the cell lines to X-ray irradiation with $GIF_{10\%}$ values of 1.68 and 1.26 for CT26 and MC38 cells, respectively, but showed minimal dark toxicity on both cell lines (**Figure 6-5 and Table 6-1**).

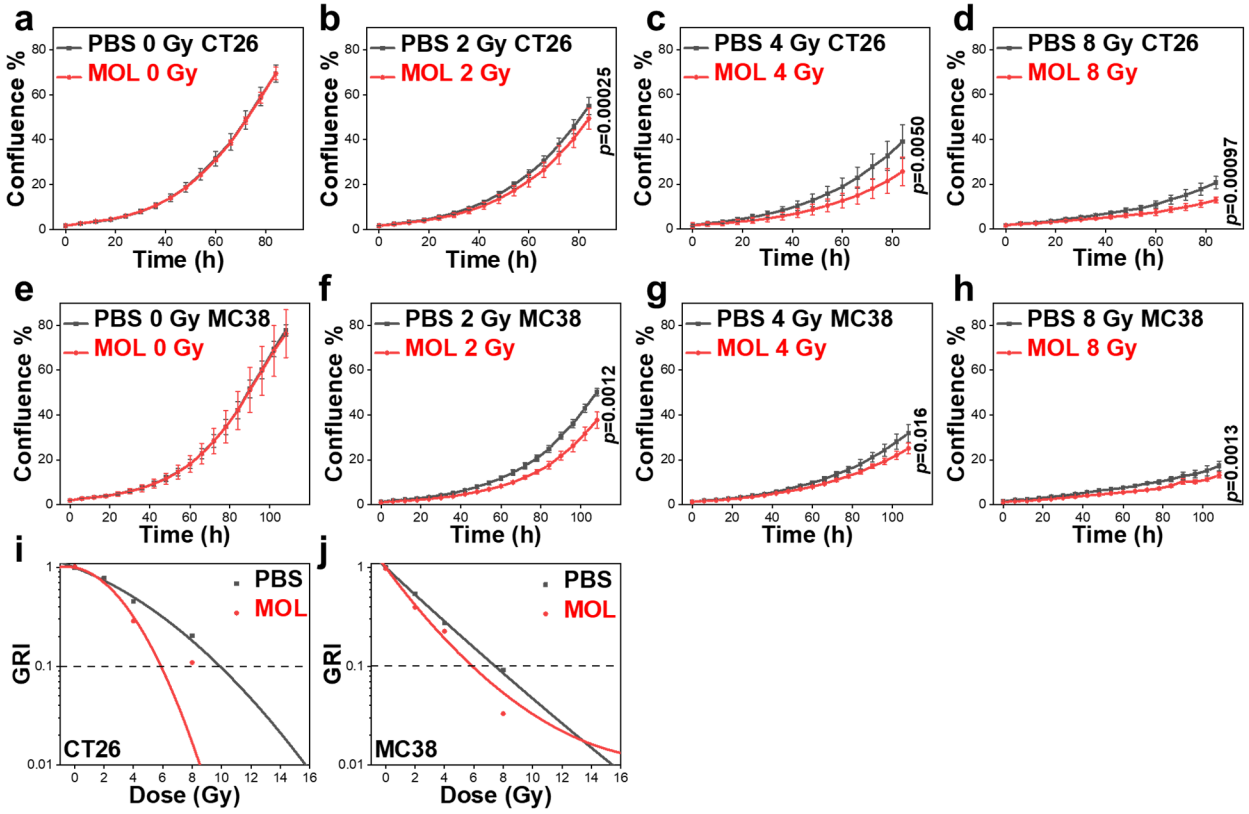

Figure 6-5. GR assay for evaluation of radiosensitization by MOL. (a-d) The real-time confluence of CT26 cells upon X-ray irradiation from (a) 0, (b) 2 Gy, (c) 4 Gy to (d) 8 Gy in GR assay (paired-sample *t*-test, n=6). (e-h) The real-time confluence of MC38 cells upon X-ray irradiation from (a) 0, (b) 2 Gy, (c) 4 Gy to (d) 8 Gy in GR assay (paired-sample *t*-test, n=6). (i,j) Dose fitting curve for GRI of (i) CT26 and (j) MC38.

Table 6-1. GRI, fitting parameters of the linear-quadratic model, and GIF of GR assays.

Cell Line		CT26		MC38	
	Treatment	**PBS**	**MOL**	**PBS**	**MOL**
GRI	**0 Gy**	1.000	1.021	1.000	0.978
	2 Gy	0.781	0.722	0.540	0.396
	4 Gy	0.455	0.288	0.273	0.226
	8 Gy	0.203	0.109	0.091	0.069
Fitting Parameters	**α**	0.131	0.0635	0.319	0.460
	β	0.0103	0.0559	-0.00133	-0.0119
	α/β	12.7	1.14	-240	-38.7
$GIF_{10\%}$		1.68		1.26	

Upregulation of γ-H2AX in the MOL group was visualized by 3-D reconstructed CLSM (**Figure 6-6a**) and quantified by western blot (**Figure 6-6b**). MOL-mediated RT-RDT enhanced DNA DSBs by more than 1.5-fold.[26-27]

In addition to enhancing radiotherapeutic effects through RT-RDT, Hf_{12}-Ir MOL also induced ROS-mediated ICD of cancer cells to expose danger-associated molecular patterns (DAMPs) and tumor-associated antigens (TAAs).[28] The MOL plus X-ray group [denoted MOL(+)], increased the translocation of CRT on the cell membrane by 1.6-fold over the PBS(+) group (**Figure 6-6c,d**), indicating stronger ICD of cancer cells.[29] The upregulation of surface phosphatidylserine with surrounding apoptotic bodies (**Figure 6-6e**) suggested enhanced apoptosis of cancer cells after MOL-mediated RT-RDT.[30]

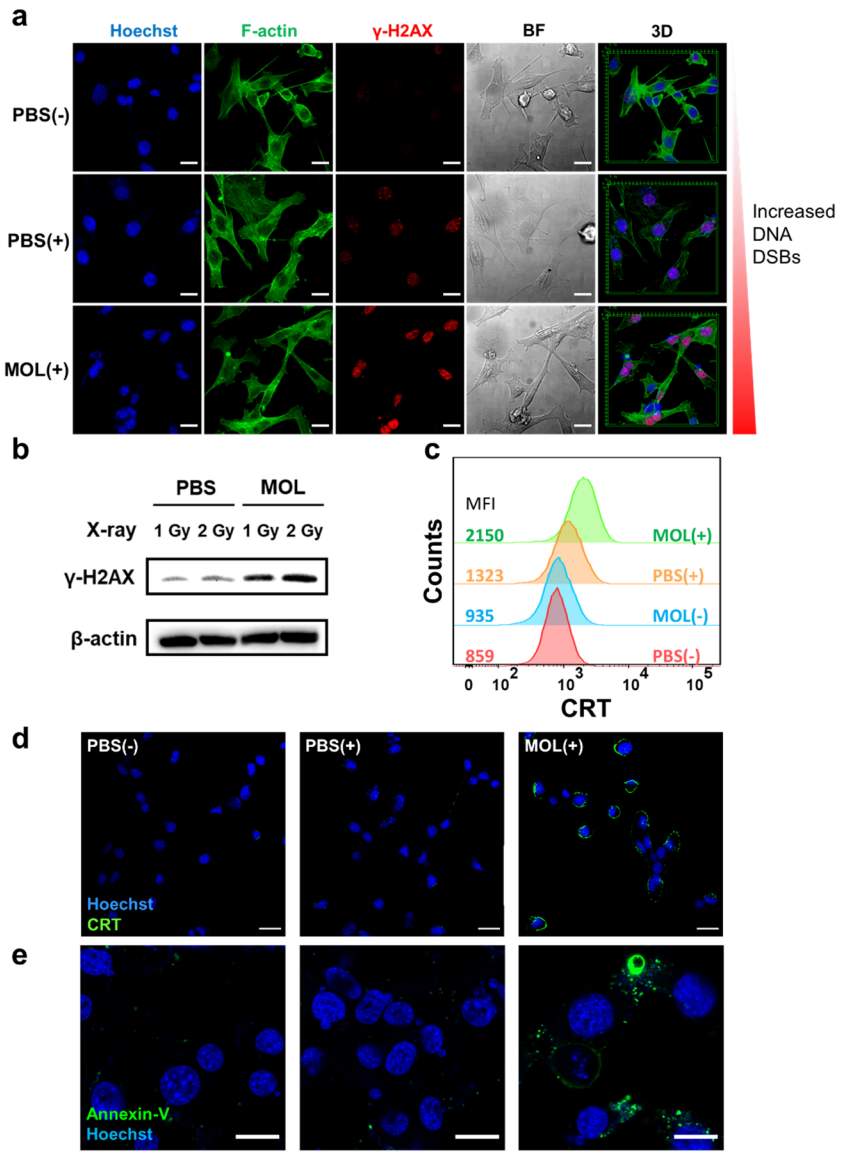

Figure 6-6. DNA damage and ICD induced by MOL. (a) CLSM images showing DNA DSBs 24 hours after 2 Gy X-ray irradiation of MC38 cells. Hoechst (blue), F-actin (green), γ-H2AX (red), and BF (grey) channels were shown in Z-stack mode scale bar = 20 μm. In the reconstructed 3-D images, the scale bars were shown in the green boxes, and each grid equals 5 μm. (b) Nuclear DSBs quantified by western blot 24 hours after irradiation of MC38 cells with 2 Gy X-ray. (c) CRT expression by flow cytometry 24 hours after irradiation of MC38 cells with 2 Gy X-ray. MFI values are shown in the figure, and MOL(+) elicited the strongest CRT upregulation. (d) CLSM imaging showing surface CRT translocation of MC38 cells induced by MOL-enabled RT-RDT (scale bar = 20 μm). (e) Apoptosis marker phosphatidylserine stained by Annexin-V and visualized by CLSM on MC38 cells 24 hours after 2 Gy X-ray irradiation (scale bar = 10 μm).

Furthermore, the cell viability of MOL-treated MC38, CT26, Raw264.7, and bone marrow-derived dendritic cells (BMDC) and macrophages (BMDM) from C57BL/6 mice was tested by MTS assay. No obvious toxicity was found for these cell lineages at an equivalent Hf concentration of up to 50 μM (**Figure 6-7**). BMDC and BMDM were also resistant to X-ray irradiation of 4 Gy, which indicates that their cell viability and immune functions may not be adversely impacted by RT-RDT of MOL (**Figure 6-7c**). These results confirm the MOL as a biocompatible and potent nanoradiosensitizer *in vitro*.

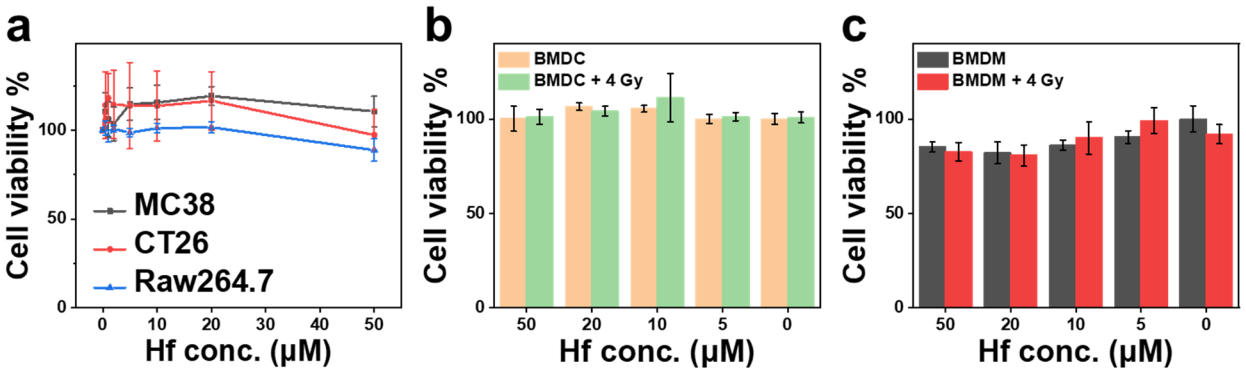

Figure 6-7. Toxicity of MOL. MTS assays showing the minimal dark toxicity of MOL in (a) MC38, CT26, Raw264.7, (b) BMDC, and (c) BMDM at a Hf concentration up to 50 uM.

6.2.2 Hf_{12}-Ir MOL Efficiently Delivers and Releases cGAMP

Hf_{12}-Ir MOL has exchangeable sites on Hf_{12} SBUs for further functionalization.[31] The weakly-bound TFA capping groups on the Hf_{12} SBUs can be substituted by other small molecules with strongly-binding carboxyl groups or phosphate groups.[23] We hypothesized that phosphate groups on cGAMP could bind to Hf_{12} SBUs by replacing TFA groups to afford cGAMP/MOL (**Figure 6-8a,b**). Conjugation of cGAMP to the MOL is expected to enhance intracellular delivery of cGAMP and protect cGAMP from enzymatic degradation. We first performed DFT calculations to profile the free energy change of the substitution reaction. Substitution of TFA by cGAMP on a Zr_{12} SBU yielded a ΔG of -6. 86 kcal/mol, indicating favorable interactions between the phosphate groups

and SBUs **(Figure 6-8a,b)**. We then determined the binding affinity between cGAMP and Hf_{12}-Ir MOL by ITC. The association constant K of cGAMP ($K_{cGAMP} = 5.3 \times 10^3\ M^{-1}$) was 2.5-fold higher than that of acetate ($K_{Ac} = 2.1 \times 10^3\ M^{-1}$) (**Figure 6-8c**). Consistent with these results, cGAMP was readily conjugated to the MOL by simply mixing the two components at a 0.66 wt% cGAMP loading in water at room temperature. The loading efficiency of cGAMP was 99.2% by LC-MS, and the nanoconjugate was stable in water after incubation at 37 ℃ for 48 hours.

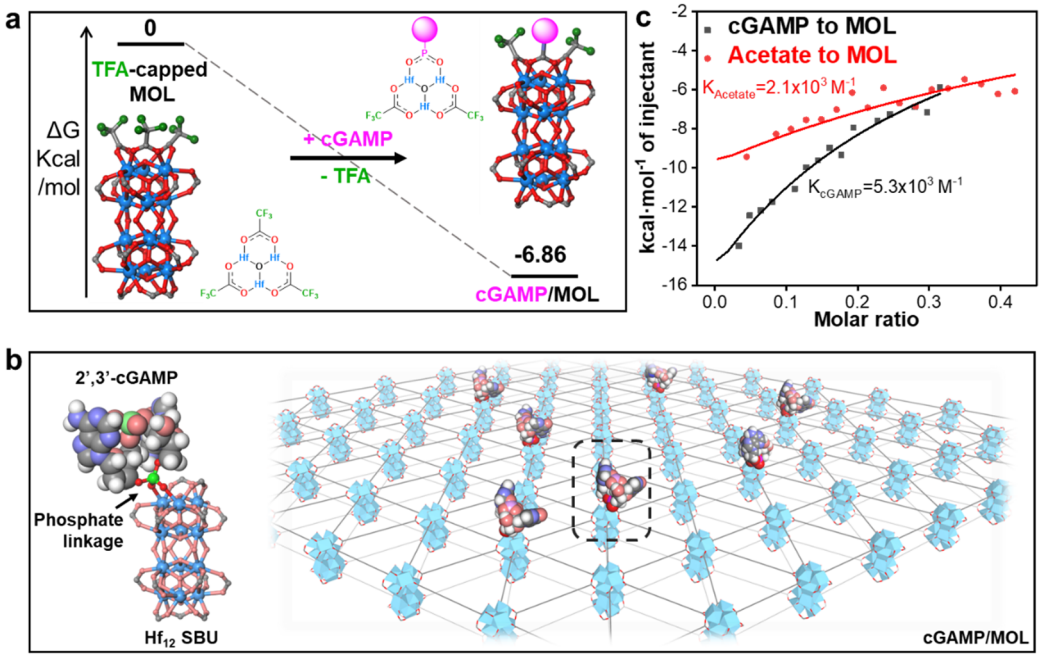

Figure 6-8. Coordination and binding between cGAMP and MOL. (a) Free energy profiles of substitution of TFA on the SBU by cGAMP by DFT calculations. (b) Schematic showing coordination between cGAMP and Hf_{12} SBU. The cGAMP (except the phosphate linkage) is shown in a space-filling model. The phosphate linkages are shown using a ball-stick model. (c) ITC analysis of binding affinity between the MOL and cGAMP.

AFM, TEM, and PXRD showed no obvious change in morphology and crystallinity of the MOL after cGAMP loading (**Figure 6-9 and Figure 6-2c**). Dynamic light scattering (DLS) measurement showed that the size of the MOL slightly increased from 173.9 ± 5.5 nm to 190.1 ± 4.3 nm after cGAMP loading (**Figure 6-2d**), whereas the ζ-potential of cGAMP/MOL slightly

decreased from 40.4 mV to 33.2 mV due to the conjugation of negatively charged cGAMP molecules (**Figure 6-2e**).

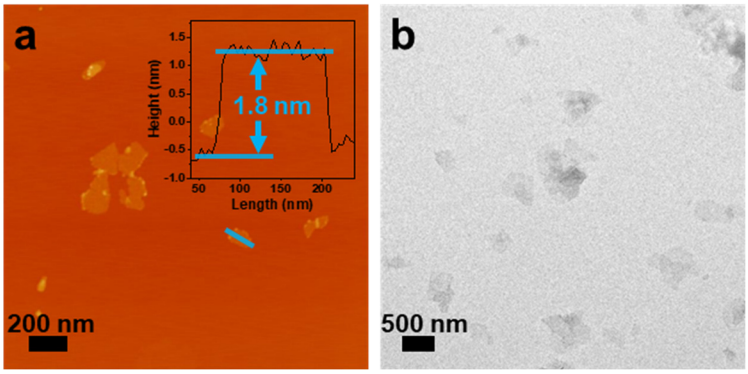

Figure 6-9. AFM and TEM characterization of cGAMP/MOL. (a) AFM (with height profiles in the insets) and (b) TEM images of cGAMP/MOL.

We investigated release profiles of cGAMP/MOL under different physiological conditions by LC-MS. cGAMP/MOL was dispersed in 0.1× PBS (1.18 mM phosphate), 1× PBS (11.8 mM phosphate), and FBS (~1 mM phosphate) at 37 ℃ to mimic interstitial, intracellular, and serum environments, respectively.[32-33] Incubation of cGAMP/MOL in 1× PBS resulted in burst release of 73.4% cGAMP within 4 hours, likely due to the rapid replacement of cGAMP by phosphate ions (**Figure 6-10a**). Incubation of cGAMP/MOL in 0.1× PBS and FBS released cGAMP slowly, resulting in the release of 56.6% and 44.5% cGAMP in 48 hours, respectively (**Figure 6-10a**). These results indicate that cGAMP can be released from cGAMP/MOL via an intracellular/extracellular phosphate gradient: cGAMP is retained on the MOL in the extracellular space with low phosphate concentration but can be rapidly released from the MOL inside the cells with high phosphate concentration (**Figure 6-10b**).[34]

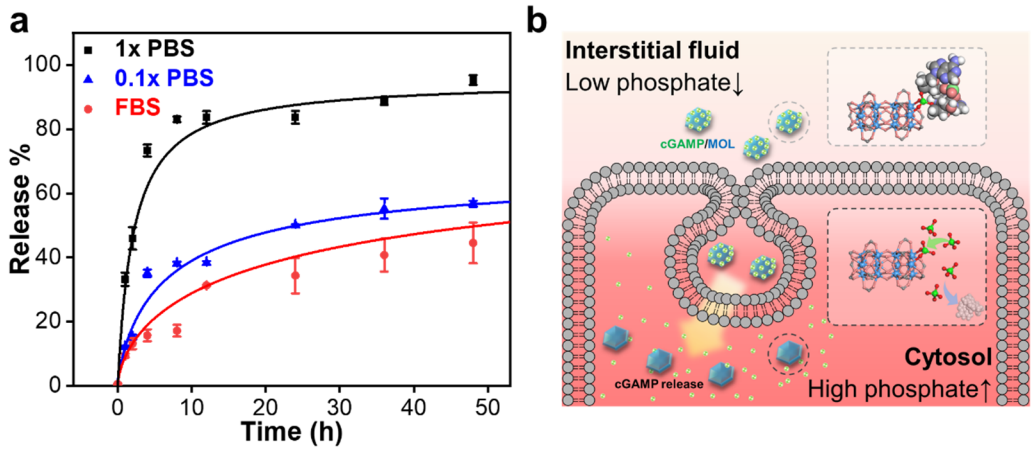

Figure 6-10. Phosphate-dependent release. (a) Release profiles of cGAMP/MOL in 1× PBS, 0.1× PBS, and FBS at 37 ℃, n = 3. (b) Schematic showing cellular uptake of cGAMP/MOL and controlled release of cGAMP inside cells via the intra- and extra-cellular phosphate concentration difference. The blue hexagonal sheet represents the MOL, and the green sphere represents cGAMP.

The cellular uptake and retention of cGAMP by cGAMP/MOL were studied using Cyanine5-labelled cGAMP (cGAMP-Cy5). 3-D reconstructed CLSM imaging showed rapid uptake of both free cGAMP-Cy5 and cGAMP-Cy5/MOL by MC38 and Raw264.7 cells in 8 hours (**Figure 6-11a,b**). However, the signals of free cGAMP-Cy5 gradually decreased upon further incubation and mostly disappeared after 24 hours (**Figure 6-11a,b**). In contrast, significant cGAMP-Cy5 signals were retained in both cell lines after incubation with cGAMP-Cy5/MOL for 24 hours (**Figure 6-11a,b**). We further investigated cGAMP retention in subcutaneous MC38 tumors by In Vivo Imaging Systems (IVIS). After *i.t.* injection, the fluorescence of free cGAMP-Cy5 decreased rapidly and reached <0.5% of the initial value within 24 hours (**Figure 6-11c,d**). In contrast, the fluorescence of cGAMP-Cy5/MOL slowly decreased to 23.9% and 8.1% of the initial value in 24 and 96 hours, respectively. These values were 54- and 106-fold higher than those of free cGAMP-Cy5 at the same time points (**Figure 6-11c,d**). These results show that conjugation of cGAMP to

the MOL affords higher cellular uptake of cGAMP *in vitro* and longer intratumoral retention of cGAMP *in vivo*.

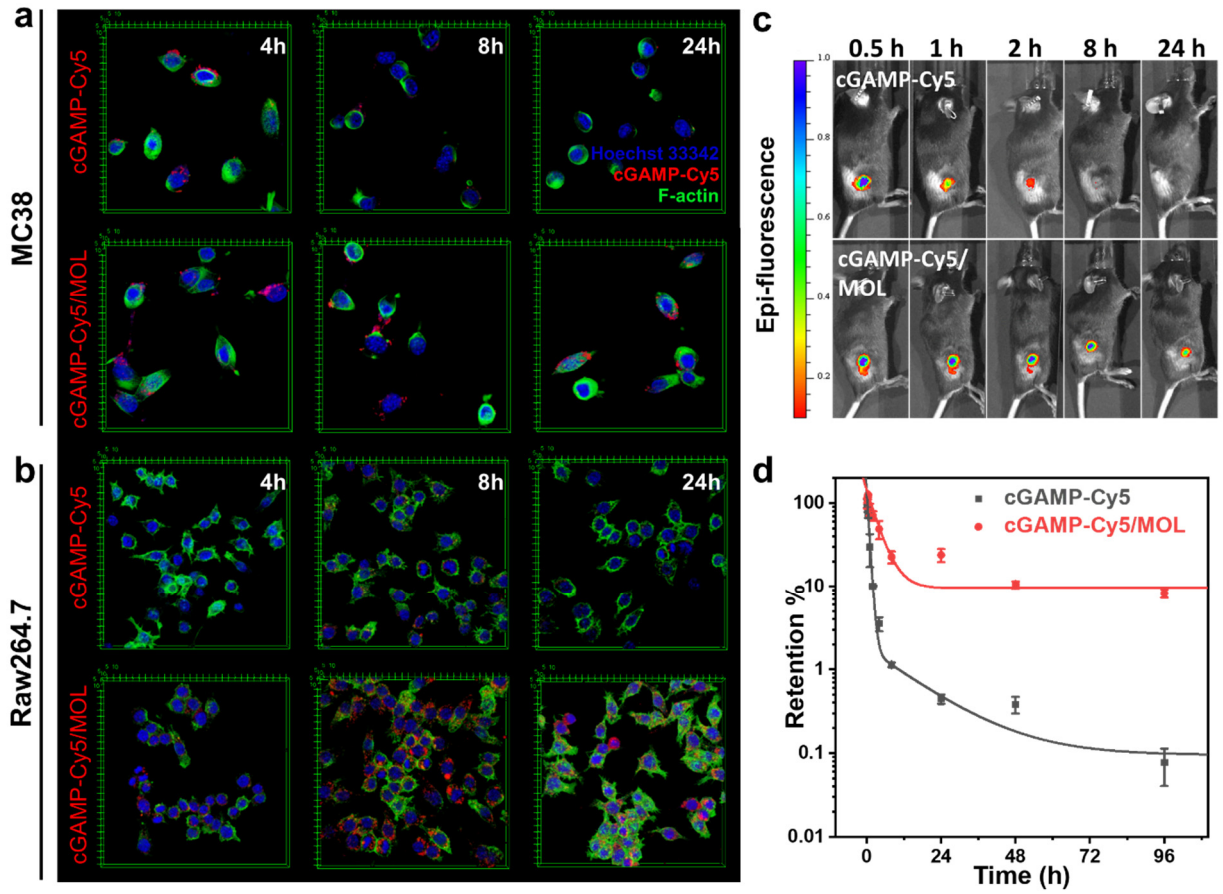

Figure 6-11. Delivery of cGAMP *in vitro* and *in vivo*. (a,b) Reconstructed 3-D CLSM images showing uptake of free Cy5-labeled cGAMP or cGAMP-Cy5/MOL after incubation of (a) MC38 and (b) Raw264.7cells for 4 hours, 8 hours, and 24 hours. (c) IVIS images showing enhanced intratumoral retention of Cy5-cGAMP/MOL over free Cy5-cGAMP (1 μg per mouse). (d) Percentages of cGAMP-Cy5 retention in MC38 tumors at different time points post *i.t.* injection as quantified by epi-fluorescence with IVIS (n = 3).

6.2.3 cGAMP/MOL Elicits Robust and Sustained STING Activation

We first determined if cGAMP/MOL could induce strong STING activation using THP-1 cells with incorporated IFN-stimulated gene as reporter cells.[3] While free cGAMP showed a half-maximal effective concentration (EC_{50}) of 665 nM ± 1 nM for interferon regulatory factor (IRF)

response, cGAMP/MOL exhibited a 6.5-fold lower EC_{50} of 103 nM ± 1 nM, showing cGAMP/MOL as a more potent STING agonist (**Figure 6-12a**). We also examined the phosphorylation of STING (p-STING) and IRF-3 (p-IRF-3) in Raw264.7 cells as measures of downstream signals of STING activation. Western blot showed that cGAMP/MOL upregulated 2-fold more p-STING at 4 hours and 3-fold more p-IRF-3 at 8 hours than free cGAMP (**Figure 6-12b and Figure 6-13c**).

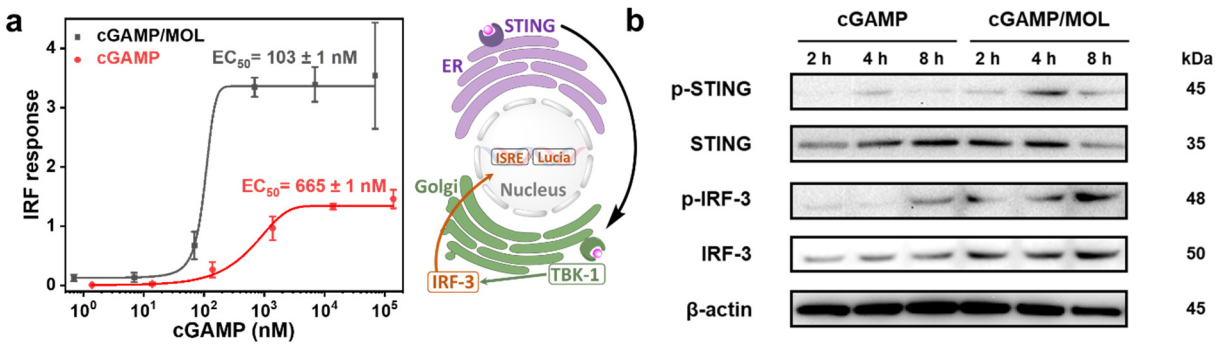

Figure 6-12. Quantification of STING activation. (a) IRF responses on THP-1 reporter cells (THP1-Dual™ KO-MyD cells) stimulated by free cGAMP and cGAMP/MOL. cGAMP/MOL exhibited a 6.5-fold lower EC_{50} than free cGAMP. The scheme on the right shows the STING-TBK-IRF-ISRE-Lucia pathway to generate luminescence signals in THP-1 reporter cells. TBK, TANK-binding kinase. ISRE, interferon-stimulated response element. Lucia, Lucia luciferase reporter gene system. (b) Western blot analysis showing enhanced STING activation with stronger p-STING and p-IRF-3 signals in Raw264.7 cells by cGAMP/MOL over cGAMP at different time points.

BMDCs from C57BL/6 mice were next used as an *ex vivo* indicator for STING activation. Upon stimulation by free cGAMP, phosphorylation of STING occurred in 2 hours but quickly disappeared in 4 hours (**Figure 6-13a**), likely due to low cellular uptake and fast enzymatic degradation.[35-36] In contrast, cGAMP/MOL elicited a sustained and strong STING phosphorylation with a p-STING signal increasing steadily over a period of 8 hours and 4 times higher p-STING signal than that of free cGAMP 8 hours post-treatment (**Figure 6-13a,b**).

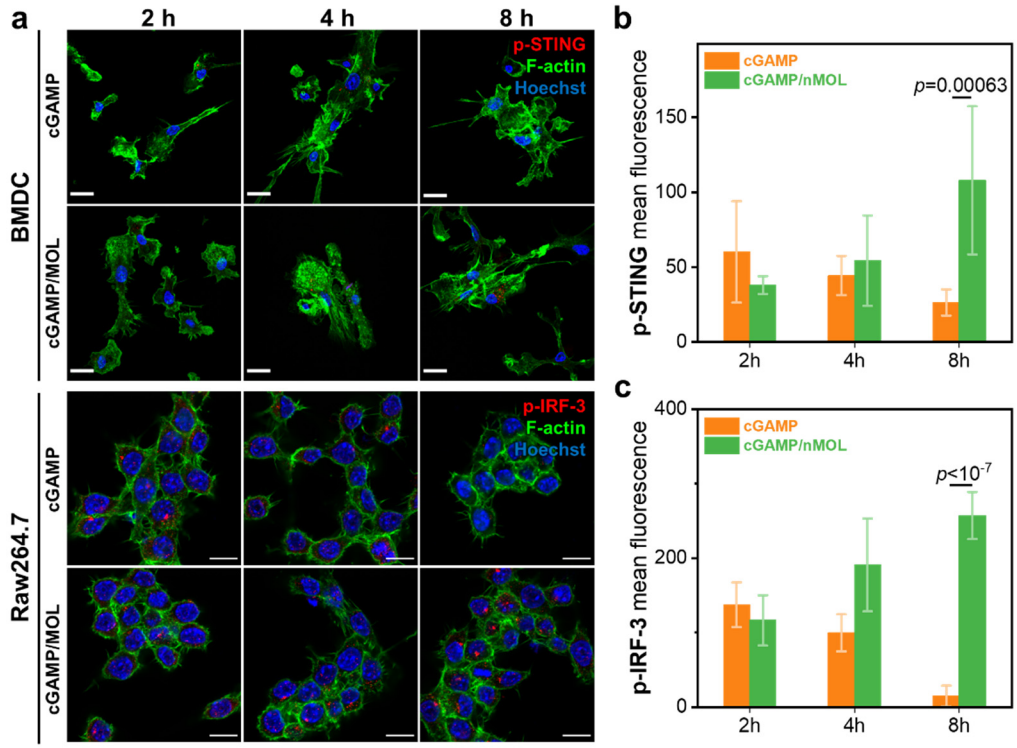

Figure 6-13. Visualization of STING activation by CLSM. (a) Representative CLSM images showing time-dependent expression of p-STING (top) and p-IRF-3 (bottom) in BMDCs and Raw264.7 cells treated with cGAMP or cGAMP/MOL. For BMDC, scale bar = 20 μm. For Raw264.7, scale bar = 10 μm. (b,c) MFI of (b) p-STING and (c) p-IRF-3 in CLSM images quantified by ImageJ (n = 6, ANOVA with Tukey test).

We further showed that cGAMP/MOL(+) enhanced phagocytosis and secretion of inflammatory cytokines along the STING-IFN axis.[4] BMDCs or BMDMs were co-incubated with MC38 cells that had been treated with cGAMP/MOL and 2 Gy X-ray to observe phagocytosis. Live cell imaging and CLSM studies showed that cGAMP/MOL(+) treatment induced apoptosis of MC38 cells and enhanced phagocytosis by BMDCs (**Figure 6-14a**). The time-dependent confluence results showed that cGAMP/MOL(+) significantly inhibited MC38 proliferation when co-incubated with BMDCs or BMDMs (**Figure 6-14b**).

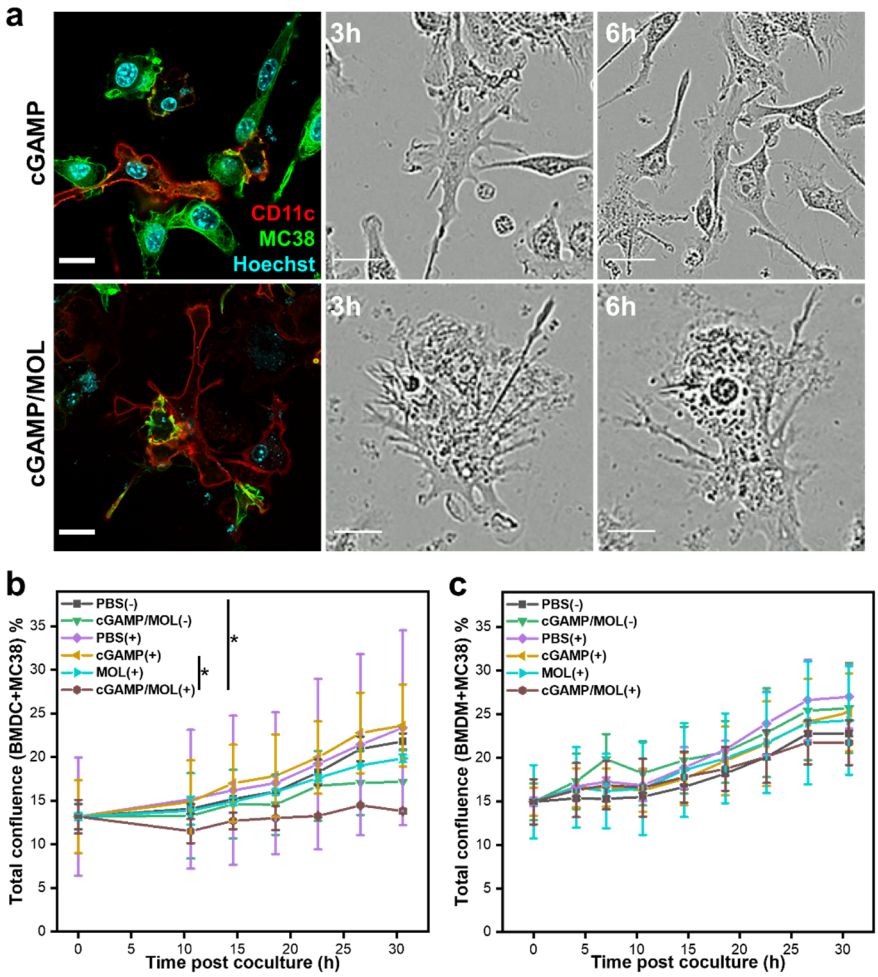

Figure 6-14. Stimulation of phagocytosis. (a) CLSM (colored) and live cell (black and white) images showing phagocytosis of cGAMP/MOL(+) treated MC38 cells (green) by BMDCs (red). All scale bars are 20 μm. (b,c) The total confluence of (b) BMDC+MC38 and (c) BMDM+MC38 in different treatment groups observed by live cell imaging. (+) and (-) denotes with and without 2 Gy X-ray irradiation, respectively (n = 8, ANOVA with Tukey test).

Furthermore, cGAMP/MOL(+) treatment induced the secretion of type-I IFNs and inflammatory cytokines in immune cells. After cGAMP/MOL(+) treatment, Raw264.7 and BMDMs showed a rapid release of IFN-β for up to 24 hours (**Figure 6-15a**) while BMDCs continuously secreted IFN-β for 72 hours (**Figure 6-15d**). Free cGAMP had negligible effects, likely due to low cellular uptake and fast degradation by pyrophosphatase and phosphodiesterase.[35-37] Upon cGAMP/MOL(+) treatment, Raw264.7 and BMDCs showed

enhanced secretion of interleukin 6 (IL-6) (**Figure 6-15c,f**) while Raw264.7 and BMDMs showed enhanced secretion of tumor necrosis factor α (TNF-α) (**Figure 6-15b,e**). 2 Gy X-ray treatment increased the secretion of these cytokines without impacting normal cellular functions. Taken together, cGAMP/MOL(+) elicited stronger and more durable activation of STING and secretion of inflammatory cytokines over cGAMP(+).

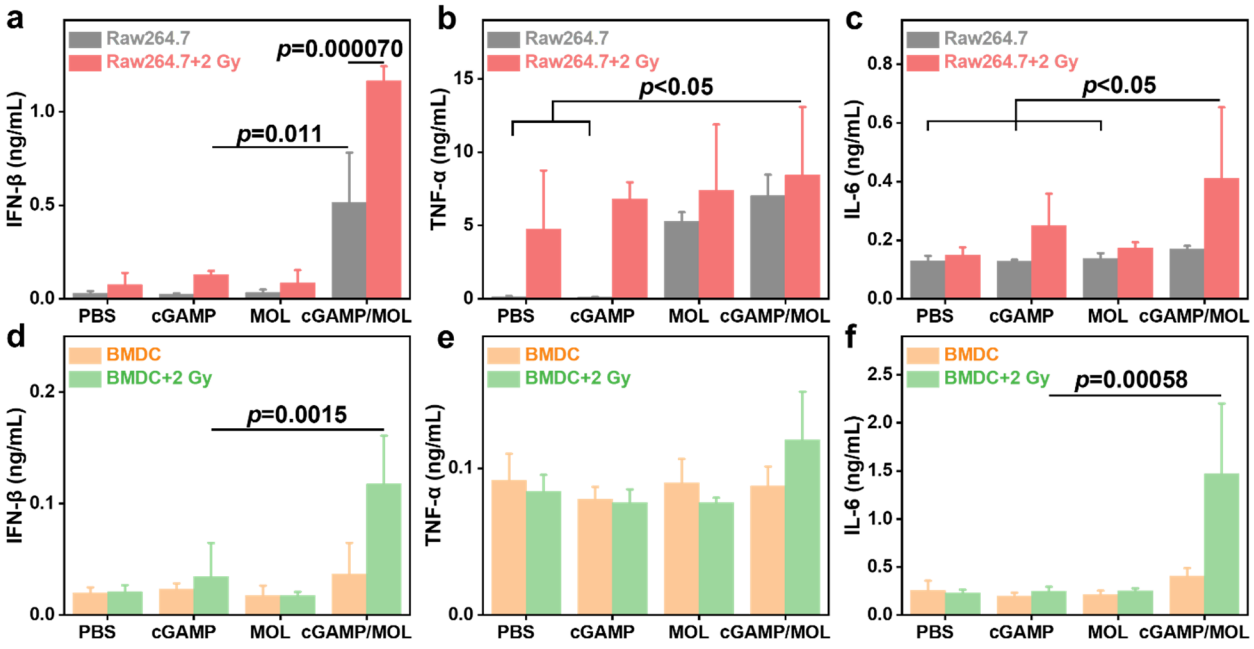

Figure 6-15. Cytokine secretion in vitro. (a-c) Secretion levels of (a) IFN-β (24 hours post-treatment), (b) TNF-α (72 hours post-treatment), (c) IL-6 (72 hours post-treatment) by cGAMP/MOL(+) treated Raw264.7 cells tested with enzyme-linked immunosorbent assays (ELISA). ANOVA with Tukey test, n = 6. (d-f) Secretion levels of (d) IFN-β (72 hours post-treatment), (e) TNF-α (72 hours post-treatment), (f) IL-6 by cGAMP/MOL(+) treated BMDCs tested with ELISA (72 hours post-treatment). ANOVA with Tukey test, n = 6.

6.2.4 cGAMP/MOL Elicits Potent Antitumor Effects and Activates the TME.

We evaluated the antitumor activity of cGAMP/MOL(+) in CT26-bearing BALB/c mice and MC38-bearing C57BL/6 mice. The mice were *i.t.* injected with cGAMP/MOL at a dose of 2 μg cGAMP and 0.5 μmol MOL or other controls, and their tumor areas were irradiated with 2 Gy X-ray/fraction on 6 consecutive days (**Figure 6-16a**). At a dose of 2 μg/mouse, cGAMP alone had

little effect on tumor growth with TGI (**Table 6-2**) of 6% and 20% for MC38 and CT26 tumors, respectively. Compared to PBS(+), cGAMP(+) moderately slowed tumor growth with TGI values of 64.7% and 88.0% for MC38 and CT26 tumors, respectively. MOL(-) or cGAMP/MOL(-) treatment had a modest TGI value of 6.1% or 26.2% in the CT26-bearing BALB/c model. As an efficient 2-D nanoradiosensitizer, MOL(+) significantly slowed tumor growth with TGI values of 83.9% and 97.6% for MC38 and CT26 tumors, respectively. cGAMP/MOL(+) treatment synergized the effects of RT-RDT and STING activation to lead to superb antitumor efficacy with TGI values of 96.4% and 99.7% for CT26 and MC38 tumors, respectively (**Figure 6-16b,c**). Importantly, 4 out of 6 CT26 tumor-bearing mice in the cGAMP/MOL(+) group were completely cured. The tumor-free BALB/c mice were challenged with CT26 cells on day 33 to examine the immune memory effect of cGAMP/MOL(+) as an "*in situ* cancer vaccine".[38] The CT26 tumors grew rapidly on naïve mice but not on the cured BALB/c mice on day 60 (**Figure 6-16d**). Superb antitumor efficacies, steady body weights (**Figure 6-16e,f**), and minimal abnormalities in major organs (**Figure 6-17**) of treated mice indicated that cGAMP/MOL was a biocompatible and integrated nanoplatform for synergistic radiosensitization and STING activation.

Table 6-2. TGI values of different treatment groups in CT26 and MC38 models.

Treatment	$TGI_{(MC38)}$	$TGI_{(CT26)}$
PBS(+)	0.60	0.79
cGAMP(-)	0.06	0.20
cGAMP(+)	0.65	0.88
MOL(-)	N/A	0.06
MOL(+)	0.84	0.98
cGAMP/MOL(-)	N/A	0.26
cGAMP/MOL(+)	0.96	1.00

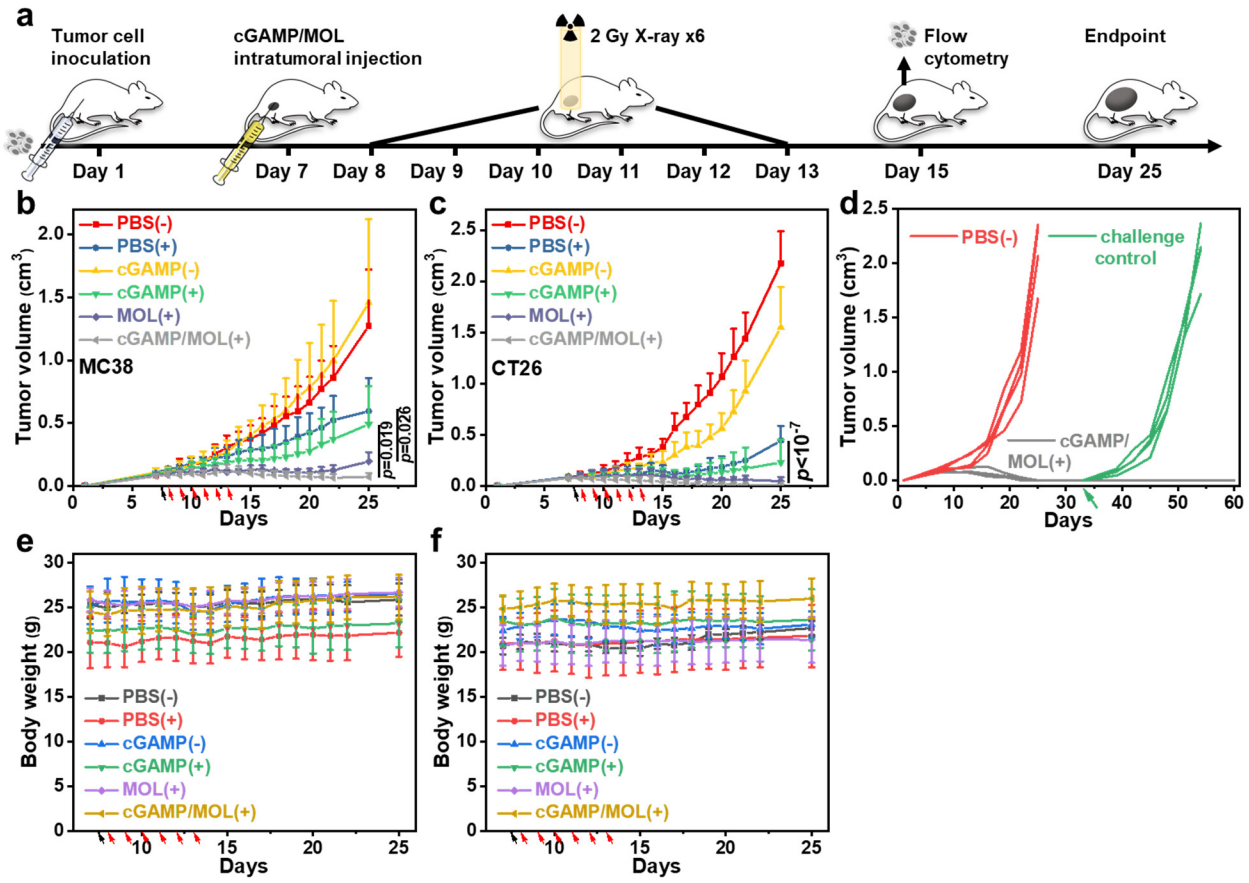

Figure 6-16. Antitumor efficacy. (a) Tumor inoculation and treatment schedules. All controls or particles were *i.t.* injected, and 2 Gy X-ray per fraction was given on 6 consecutive days starting on day 7 post tumor inoculation. Two days after the last X-ray treatment, one batch of mice were sacrificed for immune profiling experiments. (b,c) Tumor growth curves of subcutaneous (b) MC38-bearing C57BL/6 and (c) CT26-bearing BALB/c mouse models (ANOVA with Tukey test, $n = 6$). The black arrow indicates *i.t.* injection, and the red arrows indicate X-ray irradiation. (d) Individual tumor growth curves of tumor challenge experiment on cured BALB/c mice by cGAMP/MOL(+).

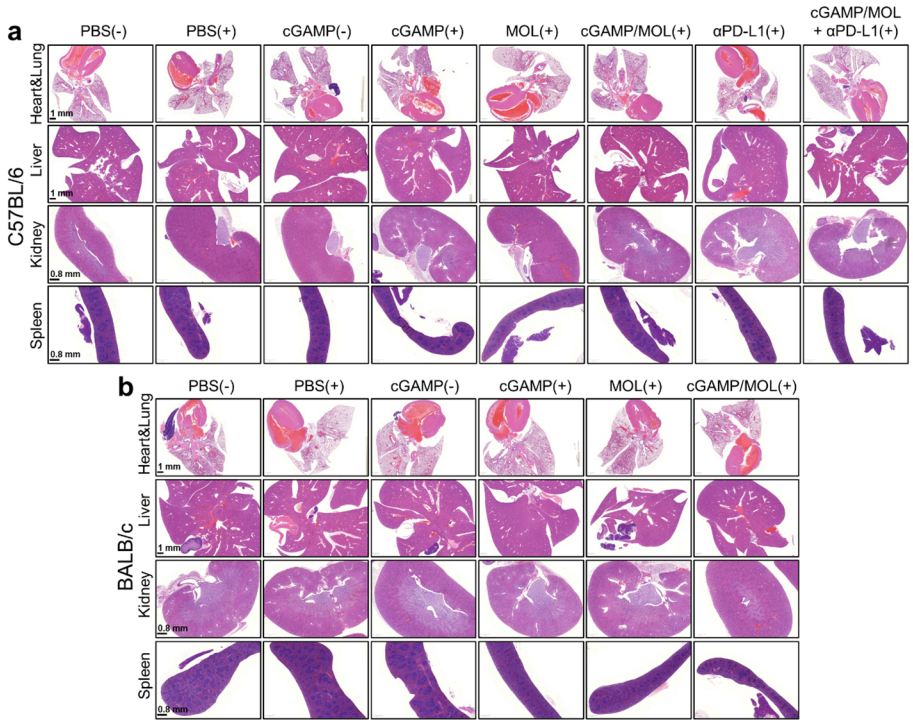

Figure 6-17. H&E staining of major organs from (a) MC38-bearing C57BL/6 mice and (b) CT26-bearing BALB/c mice in all treatment groups.

To investigate the tumor immune microenvironment, we profiled leukocytes in tumors and tumor-draining lymph nodes (TDLNs) 2 days after the last X-ray irradiation by flow cytometry. The total intratumoral infiltrating $CD45^+$ leukocytes were similar among all groups, but cGAMP(+), MOL(+), and cGAMP/MOL(+) accumulated more $CD45^+$ leukocytes in TDLNs (**Figure 6-18a**). $Gr\text{-}1^+$ $F4/80^{med}$ myeloid cells, including granulocytes and myeloid-derived suppressor cells (MDSCs), accumulated in MOL(+) and cGAMP/MOL(+) treated tumors (**Figure 6-18b**), which is consistent with previous observations on nMOF and other nanoparticles.[39] cGAMP/MOL(+) caused infiltration of $F4/80^{high}$ macrophages and $CD11c^+$ $MHCII^+$ DCs in tumors (**Figure 6-18c,d**), where no obvious polarization of macrophages was found between pro-inflammatory M1 ($F4/80^{high}$ $CD86^+$) macrophages and anti-inflammatory M2 ($F4/80^{high}$ $CD206^+$) macrophages (**Figure 6-18e**). In lymph nodes, however, the treatment induced an obvious polarization of macrophages to an anti-inflammatory M2 state with a lower M1/M2 ratio, and

together with a higher percentage of CD8α$^+$ DCs for the possible cross-priming process (**Figure 6-18g**). These observations demonstrated that the synergistic treatment enhanced inflammatory responses, including antigen uptake in tumors and higher antigen presentation in TDLNs.[40-41] Compared to PBS(-) control, cGAMP(+), MOL(+), and cGAMP/MOL(+) increased T cell population in tumors and TDLNs (**Figure 6-18f**), indicating an early T-cell inflamed TME induced by these treatments. Furthermore, cGAMP/MOL(+) significantly increased the population of CD4$^+$ T cells and CD8α$^+$ T cells in TDLNs (**Figure 6-18h,i**), suggesting an enhanced antigen presentation to T cells for adaptive antitumor immunity.

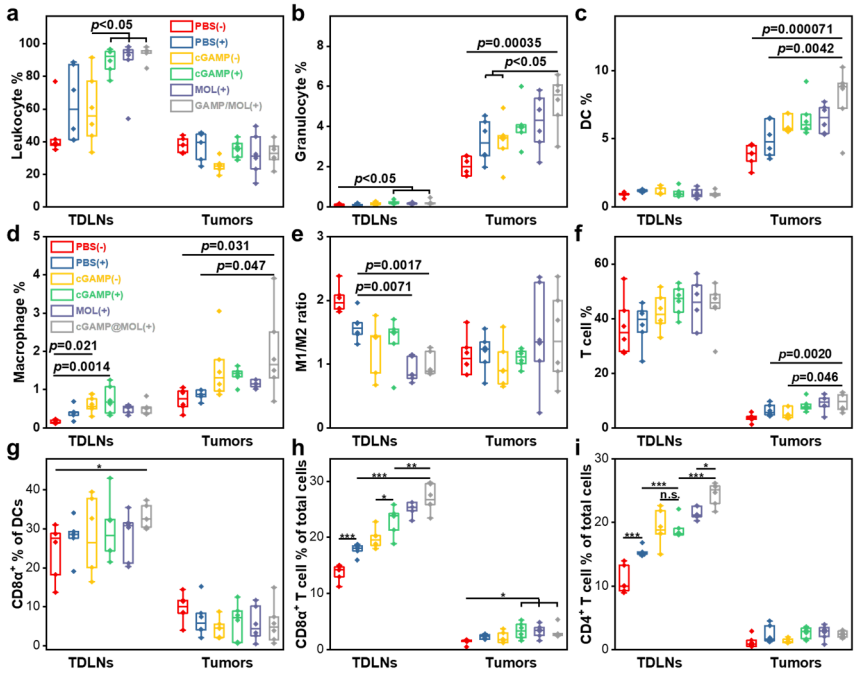

Figure 6-18. Immune cell infiltration in tumors and TDLNs on day 15 (2 days after the last dose of X-ray) quantified by fluorescence-activated cell sorting (FACS). The subpopulations were defined as: (a) Leukocytes as CD45$^+$; (b) Granulocytes/MDSC as CD45$^+$ CD11b$^+$ GR-1$^+$ F4/80^{med}; (c) Dendritic cells as CD45$^+$ CD11b$^+$ CD11c$^+$ MHCII$^+$; (d) Macrophages as CD45$^+$ CD11b$^+$ GR-1$^-$ F4/80^{high}; (e) M1 macrophages as CD45$^+$ CD11b$^+$ GR-1$^-$ F4/80^{high} CD86$^+$ and M2 macrophages as CD45$^+$ CD11b$^+$ GR-1$^-$ F4/80^{high} CD206$^+$; (f) T cells as CD45$^+$ CD3e$^+$; (g) CD8$^+$ DCs as CD45$^+$ CD11b$^+$ CD11c$^+$ MHCII$^+$ CD8$^+$; (h) Cytotoxic T cells as CD45$^+$ CD3e$^+$ CD8$^+$; (i) helper T cells as CD45$^+$ CD3e$^+$ CD4$^+$. ANOVA with Tukey test, n = 6.

6.2.5 cGAMP/MOL Plus αPD-L1 Elicits Systemic Immune Responses

We established a bilateral MC38 model on C57BL/6 mice to evaluate systemic antitumor immunity with cGAMP/MOL(+) plus anti-PD-L1 (αPD-L1) antibody. X-ray radiation slightly inhibited the growth of primary and distant tumors with TGI values of 38.8% and 13.7%, respectively (**Table 6-3**). The αPD-L1(+) treatment enhanced local tumor control with a TGI of 62.6% but failed to control the distant tumor with a TGI value of 6.0%. cGAMP/MOL(+) exhibited excellent control of primary tumor growth with a TGI of 82.1% but had a modest impact on distant tumors with a TGI of 26.8%. cGAMP/MOL(-) plus αPD-L1 treatment showed minimal control of both primary and distant tumors with TGI values of <22%. Combination treatment of cGAMP/MOL(+) plus αPD-L1 showed strong growth inhibition of both primary and distant tumors with TGI values of 94.7% and 70.6%, respectively (**Figure 6-19a,b**).

To investigate the mechanism of systemic immune responses, we performed IFN-γ enzyme-linked immunospot (ELISpot) assay for splenocytes and lymphocyte profiling for both primary and distant tumors. The cGAMP/MOL(+) group showed significantly more spot-forming cells (SFC) than the PBS(+) group, and the combination of cGAMP/MOL(+) with αPD-L1 further enhanced the adaptive immunity to afford more IFN-γ-generating splenocytes (**Figure 6-19c**).

Table 6-3. TGI values of different treatment groups in the bilateral MC38 model.

Treatment	$TGI_{(primary)}$	$TGI_{(distant)}$
PBS(+)	0.39	0.14
αPD-L1(+)	0.63	-0.26
cGAMP/MOL(+)	0.82	0.27
cGAMP/MOL(-)+αPD-L1	0.21	0.21
cGAMP/MOL(+)+αPD-L1	0.95	0.71

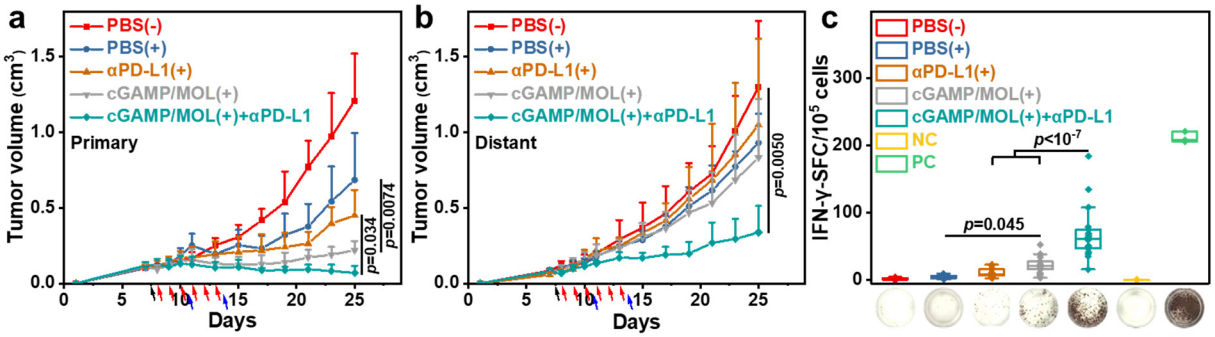

Figure 6-19. Abscopal effect. (a,b) Tumor growth curves of (a) treated primary tumors and (b) untreated distant tumors in the bilateral subcutaneous MC38 bearing C57BL/6 mouse model (ANOVA with Tukey test, $n = 6$). The black arrow indicates *i.t.* injection, the red arrows indicate X-ray irradiation, and the blue arrows indicate intraperitoneal injection of αPD-L1 (75 μg). (c) ELISpot assay detecting MC38 tumor-specific IFN-γ secreting splenocytes (NC, negative control with no stimulants; PC, positive control stimulated by anti-CD3e and anti-CD28 antibodies). Images of representative wells are shown under the corresponding bar (ANOVA with Tukey test, 6 replicates with $n = 3$).

Both cGAMP/MOL(+) and cGAMP/MOL(+)+αPD-L1 treatments enhanced infiltration of mature DCs and $XCR1^+$ DCs in primary and distant tumors (**Figure 6-20**), which indicates an enhanced process of antigen presentation systemically. The total T cell infiltration and percentages of $CD8^+$, $CD4^+$, and effector T cells increased in the primary tumors for cGAMP/MOL(+) and cGAMP/MOL(+) plus αPD-L1 groups (**Figure 6-21a-d**). In distant tumors, the cGAMP/MOL(+) plus αPD-L1 group showed more T-cell inflamed TME than other treatment groups (**Figure 6-21a-d**). The cGAMP/MOL(+) plus αPD-L1 group also showed enhanced infiltration of NK, NKT, and memory T cells in both primary and distant tumors (**Figure 6-21e-f**).

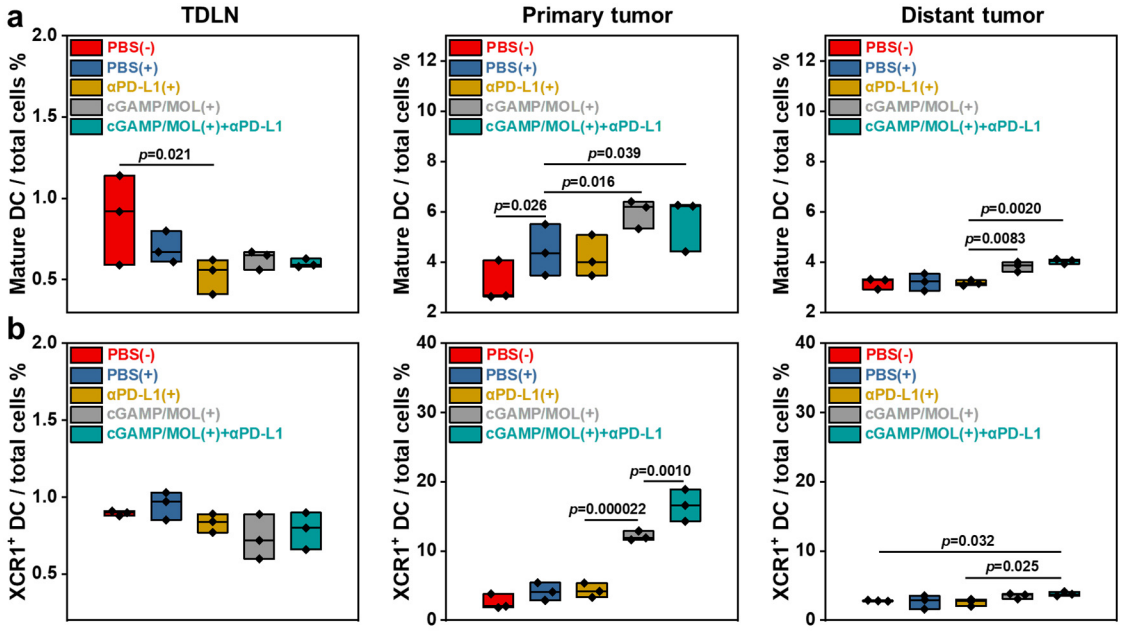

Figure 6-20. Percentages of (a) mature DC and (b) XCR1$^+$ DC among total cells in TDLNs, primary tumors, and distant tumors, respectively. (n = 3, ANOVA with Tukey test).

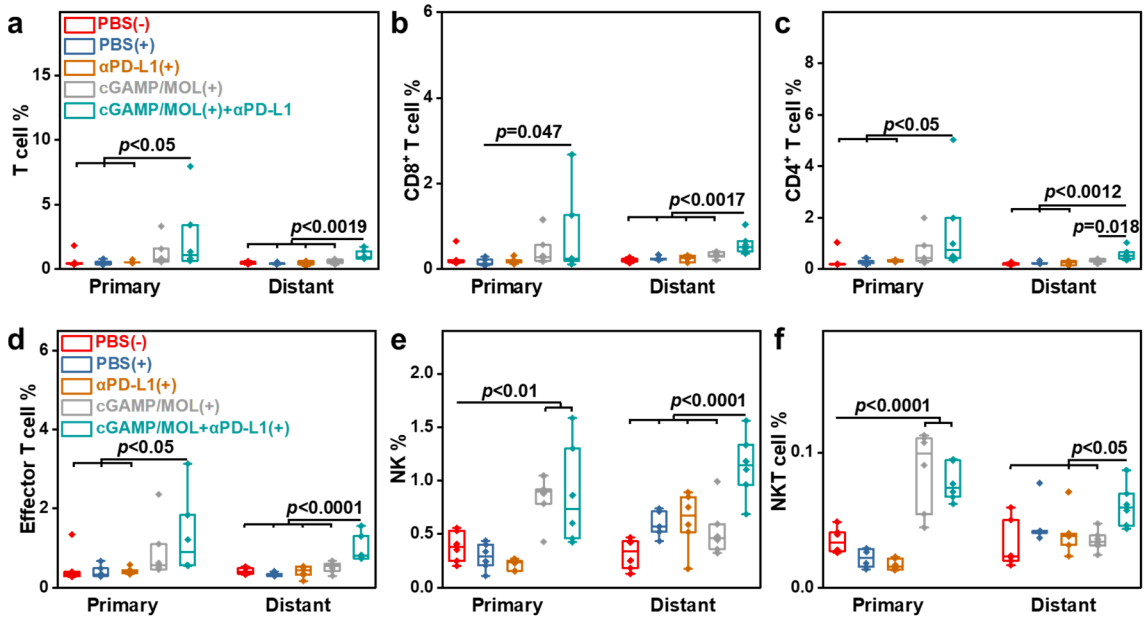

Figure 6-21. Immune cell infiltration into primary and distant tumors on day 25 (12 days after the last dose of X-ray) quantified by flow cytometry. T cell subpopulations are defined as: (a) Total T cells as CD45$^+$ CD3e$^+$; (b) CD8$^+$ T cells as CD45$^+$ CD3e$^+$ CD8$^+$; (c) CD4$^+$ cells as CD45$^+$ CD3e$^+$ CD4$^+$; (d) Effector T cells as CD45$^+$ CD3e$^+$ CD44$^+$ CD62L$^-$; (e) NK cells as CD45$^+$ CD3e$^-$ NK1.1$^+$; (f) NKT cells as CD45$^+$ CD3e$^+$ NK1.1$^+$ (ANOVA with Tukey test, n = 6).

Interestingly, cGAMP/MOL(+) treatment suppressed local immunosuppressive regulatory T cells more than 8-fold compared to PBS(+) or αPD-L1(+), and significantly downregulated transformation growth factor β (TGF-β) in tumor matrices and TDLNs (**Figure 6-22**). In combination with αPD-L1, cGAMP/MOL(+) significantly reduced the regulatory T cell population in distant tumors (**Figure 6-22**). Altogether, these results indicate that the synergistic treatment induces an inflammatory TME and active adaptive immune responses.

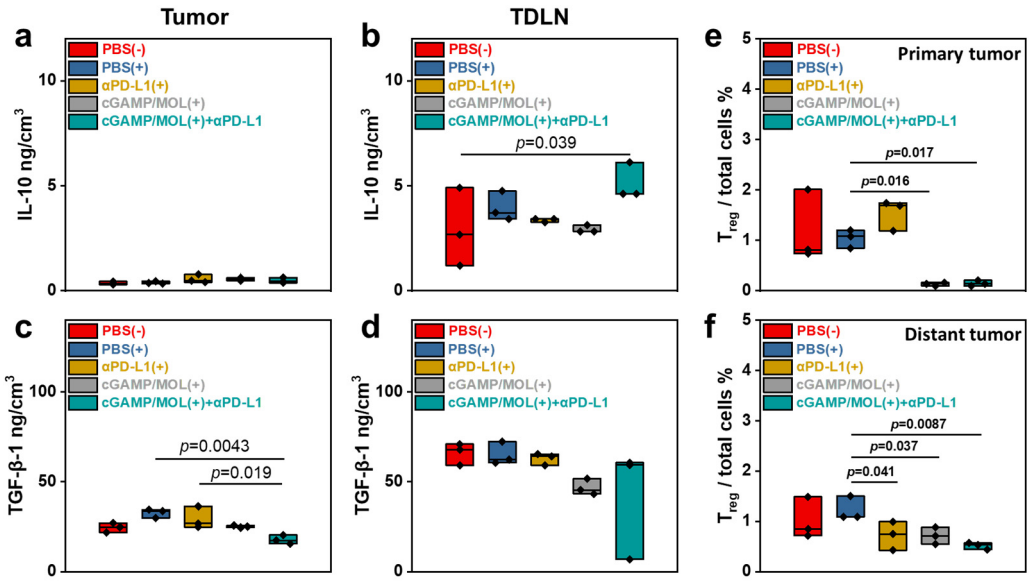

Figure 6-22. Immunosuppressive cytokines and T cells. (a,b) IL-10 concentration in (a) tumors and (b) TDLNs. (c,d) TGF-β-1 concentration in (c) tumors and (d) TDLNs. (e,f) Percentages of regulatory T cells among total cells in (e) primary tumors and (f) distant tumors. n = 3, ANOVA with Tukey test.

Combining PD-L1 blockade reversed immunosuppression to enhance immune cell infiltration and antitumor responses. Whole tumor IHC staining of ionized calcium binding adaptor molecule 1 (IBA-1) and CD3 marker revealed spatial distribution of both innate and adaptive immune cells and enhanced immune infiltration in the cGAMP/MOL(+) group (**Figure 6-23**).[42] The combination of cGAMP/MOL(+) with αPD-L1 further increased T cell infiltration without

impacting the innate (IBA-1$^+$) and myeloid (CD11b$^+$) cell populations. These findings were corroborated by flow cytometric analysis (**Figure 6-23**).

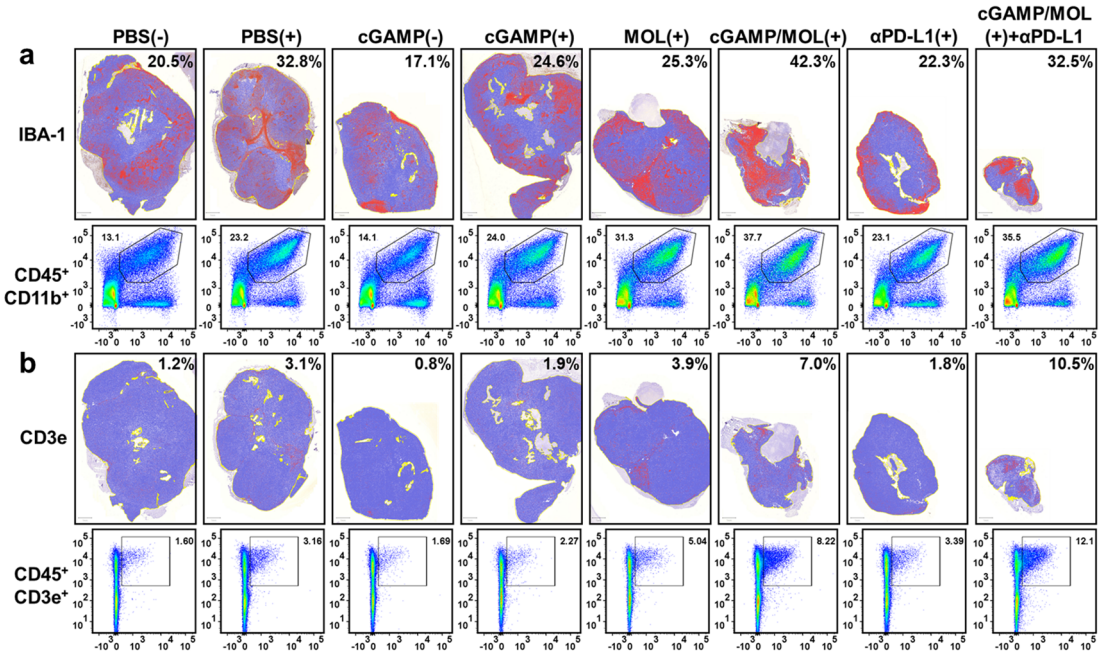

Figure 6-23. Spatial distribution of immune cells by IHC staining. (a,b) Immunohistochemistry (top) and flow cytometry (bottom) analysis of (a) pan-macrophage cells and (b) T cells in whole tumors. In IHC, pan-macrophage cells were stained by IBA-1 antibody, and T cells were stained by CD3e antibody. The diaminobenzidine (DAB) negative cells were marked in blue, and the positive cells were in red. The regions of analysis were marked with yellow borders. Skin, fat and necrotic tissues were excluded from the analysis. In flow cytometry, pan-macrophage cells were roughly defined as CD45$^+$ CD11b$^+$ myeloid cells, and T cells were defined as CD45$^+$ CD3e$^+$ subpopulation. The X-axis represents CD11b and CD3e fluorescence in (a) and (b), respectively. The Y-axis represents the CD45 signal. The positive percentages are shown in each individual figure/gate. All scale bars are 1 mm.

Fluorescence staining of cryo-sectioned slides revealed downregulation of PD-L1 (**Figure 6-24**) in cancer tissues and higher CD8$^+$ and CD4$^+$ T cell infiltration in the cGAMP/MOL(+) plus αPD-L1 group.

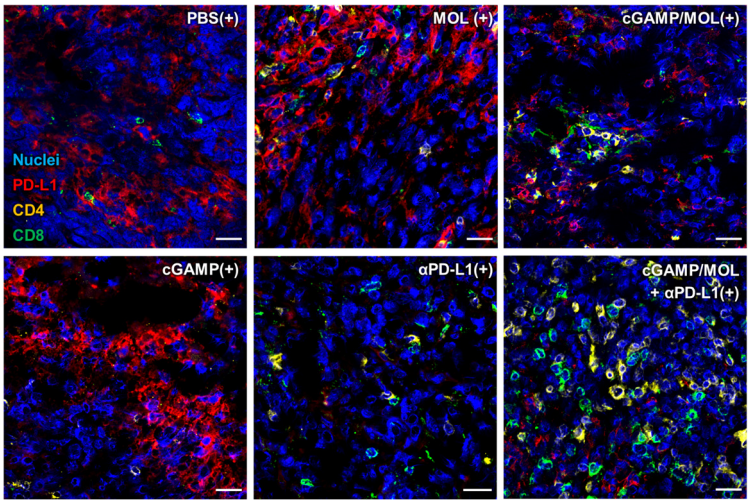

Figure 6-24. Representative immunofluorescence staining of PD-L1 (red), CD4 (orange), and CD8 (green) from cryo-sectioned slides of subcutaneous tumors in different treatment groups (scale bar = 20 μm).

6.2.6 Discussion

Radiosensitizers reduce the radiation dose by enhancing the cancer-killing effect of RT and hence alleviate radiotoxicity in patients.[43-44] High-Z nanoparticles such as hafnium oxide nanoparticles and nanoscale metal-organic frameworks are emerging radiosensitizers in clinical testings.[22, 45-46] Heavy metals in these nanoparticles increase radiation energy deposition to generate more ROS for enhanced DNA damage.[47-49] As radiosensitizing effects correlate to the surface areas of the nanoparticles, 2-D MOL particles maximally increase the surface area for enhanced radiosensitization and ROS diffusion.[31] The linking of high-Z secondary building units with photosensitizing ligands in crystalline MOL particles further enabled RT-RDT to not only generate multiple ROS for stronger cancer cell killing but also induce ICD to release TAAs and DAMPs.[22, 38] In addition, the high density of exchange sites on the MOL allows the delivery of cGAMP for TME activation to enhance the antitumor efficacy of MOL-mediated RT-RDT.

Direct *i.t.* injection of free cyclic dinucleotide-type STING agonists such as ADU-S100 resulted in fast systemic absorption and clearance and modest efficacy in the clinic.[11]

Nanotechnology has been used to deliver immunotherapeutics and improve drug retention and efficacy.[50-55] MOFs and MOLs have been applied to load small molecules or macromolecules by pore loading or surface modification.[31, 56-57] By coordinatively binding cGAMP to SBUs on the MOL, cGAMP/MOL increased the intracellular uptake and intratumoral retention of cGAMP by more than an order of magnitude. cGAMP/MOL also enabled the controlled release of cGAMP inside immune cells by taking advantage of the large difference in intracellular and extracellular phosphate concentrations. The synergistic effects between MOL-enabled RT-RDT and STING activation achieved potent immune activation and significant tumor regression at a low cGAMP dose of 2 μg per mouse. Thus, MOL provides an integrated nanoplatform for radiotherapy and STING activation and can be extended to the delivery of other immunotherapeutics with non-ideal pharmacokinetic behavior and high systemic toxicity.

6.3 Conclusions

cGAMP/MOL functions as a nanocarrier for STING agonists and a potent radiosensitizer in the tumor matrix (**Figure 6-25**). On the one hand, the improved uptake and retention of cGAMP by the MOL in immune cells enhance the maturation and activation of local APCs, which stimulates the release of inflammatory cytokines and type I-IFNs to enhance local innate and adaptive immune responses and induces the infiltration of immune cells to create a “hot” tumor immune environment. On the other hand, the 2-D MOL provides potent radiosensitization to strongly inhibit the proliferation of cancer cells and to induce ICD for the release of TAAs and DAMPs via the unique RT-RDT process. cGAMP/MOL thus enhances antigen uptake by APC and presentation to T cells, leading to local tumor regression. Further combination of cGAMP/MOL with αPD-L1 reverses immune suppression by cancer cells to reinvigorate T cells

for cancer cell recognition and destruction, effectively bridging innate and adaptive immune systems for systemic antitumor effects. The robust antitumor immune activation and immune memory effect make cGAMP/MOL a potential X-ray activatable cancer vaccine. As a new multifunctional nanomaterial, 2-D MOLs present a great platform for the development of novel nanoradiosensitizers and for integrating multiple treatment regimens, including RT and immunotherapy, to afford unique combination nanotherapeutics for clinical translation.

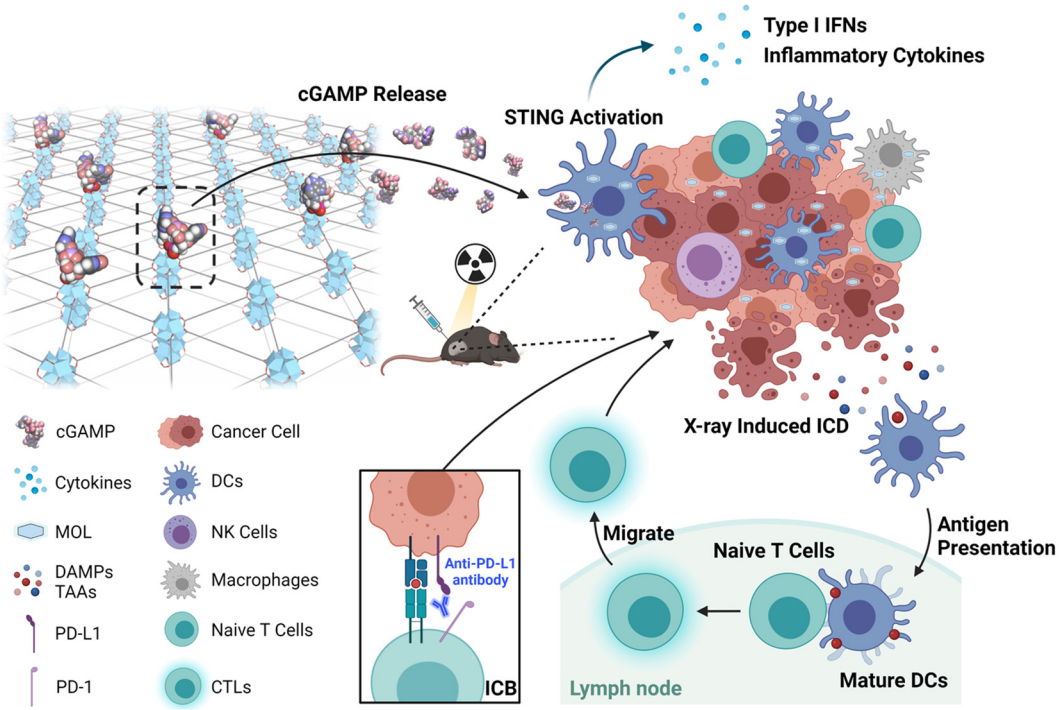

Figure 6-25. Mechanistic summary of synergistic radiosensitization and immune activation by cGAMP/MOL. The MOL not only acts as a powerful radiosensitizer but also functions as an ideal nanoplatform to deliver cGAMP for activating the host immune system. MOL-mediated RT-RDT induces strong ICD to release TAAs and DAMPs, whereas controlled release of cGAMP from cGAMP/MOL elicits potent and sustained STING activation of APCs, including macrophages and DCs. Activated APCs secrete type-I IFN and inflammatory cytokines for subsequent recruitment and stimulation of infiltrating leukocytes. Meanwhile, DAMPs and TAAs are uptaken and processed by homing APCs for further maturation and antigen presentation to T cells in lymph nodes. ICB by αPD-L1 reverses immune suppression to enhance antitumor immunity by cytotoxic lymphocytes (CTLs).

6.4 Methods

Synthesis and characterizations of cGAMP/MOL. Hf_{12}-Ir MOL was synthesized according to a previous literature report.[23] Briefly, to a 1-dram glass vial, 500 μL of $HfCl_4$ solution (2.0 mg/mL in DMF), 500 μL of H_2DBB-Ir-F solution (4.0 mg/mL in DMF), 2 μL of TFA, and 5 μL of water were added. The mixture was sonicated and heated in an 80 °C oven for 1 day. The yellow suspension was collected by centrifugation and washed with DMF and ethanol. The final product Hf_{12}-Ir MOL was dispersed in ethanol for characterization and storage.

To prepare cGAMP/MOL, the Hf_{12}-Ir MOL was dispersed in 100 μL nuclease-free water at an equivalent Hf concentration of 2 mM, and 1 μg 2'3'-cGAMP was added to the MOL suspension. The mixture was vortexed every 5 minutes 3 times to afford cGAMP/MOL. The concentrations of Hf were detected by an Agilent 7700x ICP-MS and analyzed using an ICP-MS Mass Hunter version 4.6 C.01.06. Samples were digested in concentrated HNO_3 (trace metal grade) with 1% HF acid solution for 2 days and then diluted in a final concentration of 2% HNO_3 matrix. ^{159}Tb was used as internal standards against 10-point standard curves over the range from 0 ppb to 500 ppb. The crystallinities of both nanoparticles were examined by PXRD on a Bruker D8 Venture diffractometer using a Cu Kα radiation source (λ = 1.54178 Å). The sizes and ζ-potentials were measured by a Malvern Nano Series ZetaSizer. The morphologies were observed by TEM on a TECNAI Spirit TEM and AFM on a Bruker V/Multimode 8 instrument.

cGAMP loading efficiency and release profiles of cGAMP/MOL. The concentration of cGAMP was quantified by LC-MS on an Agilent 6540 Q-Tof MS-MS with 1290 UHPLC (5 μm Agilent C_{18} reverse phase column). The standard curve of cGAMP was prepared by dissolving lyophilized cGAMP powder in nuclease-free water to afford 1000 ppm stock solution. The

gradient dilutions were prepared, and the linear range was between 50 ppb and 20 ppm. The elution of the LC-MS was set as: 0-5 min, 95% H_2O + 5% MeOH. The flow rate was 0.5 mL/min with an injection volume of 20 μL. To determine the loading efficiency of cGAMP on Hf_{12}-Ir MOL, GAMP/MOL was freshly prepared as the above procedure, but the supernatant was collected afterward by 14,000 g centrifugation. The cGAMP concentration in the supernatant was directly quantified by LC-MS, n = 3. As for release profiles, cGAMP/MOL was freshly prepared and redispersed in the same volume of 1× PBS, 0.1× PBS, and FBS (100 μL/tube) in 1.5 mL Eppendorf tubes (3 replicates for each time point), respectively. The ep tubes were transferred onto a 37 °C heat block, and the supernatants (80 μL/tube) were collected at 0 h, 1 h, 2 h, 4 h, 8 h, 12 h, 24 h, 36 h, and 48 h by centrifugation at 14000 g. The supernatants in 1× PBS and 0.1× PBS groups were directly analyzed by LC-MS. The supernatants in the FBS group were mixed with 320 μL methanol per tube, sonicated for 1 minute to afford white precipitates, centrifuged again at 14000 g, and the supernatants were then analyzed by LC-MS. The release percentages were fitted by the Hill function in Origin Lab software.

X-ray irradiation. For test tube and *in vitro* experiments, an RT250 orthovoltage X-ray machine model (Philips, USA) with a fixed setting at 250 kVp, 15 mA, and a built-in 1 mm Cu filter was used. The X-ray dose rate of RT250 was 0.02564 Gy/second. For irradiating animals *in vivo*, an X-RAD 225 image-guided biological irradiator (Precision X-ray Inc., USA) was used with voltage at 225 kVp, current at 13 mA, 0.3 mm Cu filter, and 15 mm collimator. The X-ray dose rate of X-RAD 225 was 0.04167 Gy/second. The X-ray dosimetry was corrected by an ionization chamber before use.

Hydroxyl radical generation by APF assay. PBS and 50 μM Hf_{12}-Ir MOL were added to a 96-well plate with 100 μL volume per well. Then 100 μL 20 μM APF (ThermoFisher Scientific,

USA) aqueous solution was added to each well, and half of the plate was irradiated with 4 Gy X-ray. Then the fluorescence (em. 520/20 nm) was read immediately by a Synergy HTX plate reader with a fixed green light filter (ex. 485/20 nm), $n = 6$.

Total ROS detection *in vitro* by DCF-DA assay. Total ROS generation *in vitro* was measured by DCF-DA assay kit (ThermoFisher Scientific, USA). Briefly, MC38 cells were seeded in a 6-well plate and cultured overnight. The cells were treated with Hf_{12}-Ir MOL at an equivalent Hf concentration of 50 μM for 8 hours. The cells were washed with PBS twice and exchanged with 10 μM DCF-DA in prewarmed DMEM medium. The cells were incubated in a 37°C incubator for 45 minutes and then irradiated with 4 Gy X-ray. The cells were then washed with PBS and detached by cell scraper (Fisher Scientific) in FACS buffer (0.5% BSA, 2 mM EDTA, and 0.05% NaN_3 containing PBS). The single-cell suspension was analyzed by an LSR Fortessa 4-15 (BD Biosciences) flow cytometer at the FITC channel.

Growth rate inhibition assay by IncuCyte S3. GR assay is an improved version of the clonogenic assay with less deviation in the number of initial cell seeding and more details about time-dependent cell proliferation status, which gave a more accurate result of radiosensitization of nanoparticles. CT26 or MC38 cells were first seeded in 6-well plates at a density of 2×10^5 cells/well and cultured overnight. The cells were incubated with PBS or Hf_{12}-Ir MOL at an equivalent Hf concentration of 50 μM for 8 hours and then irradiated with 0, 2, 4, or 8 Gy X-ray. The cells were washed by PBS twice and then trypsinized to afford single-cell suspensions. The cells were counted, diluted to 1000 cells/mL, and reseeded in 24-well plates. The plates were put in an IncuCyte S3 live-cell analysis system (Essen BioScience) and continuously observed by a 10× objective in phase contrast mode for up to 5 days, with a 6-hour interval. The phase contrast images were collected and analyzed by IncuCyte 2020B software to obtain time-dependent

confluence in each well (25 tiles per well, 6 replicates for each treatment group). The first derivative was calculated based on a time-dependent growth curve to give the growth rate (k_t). The time point where the k of the control group (PBS, 0 Gy) reached the maximum (t_{max}) was selected as the time for the definition of GRI.[24] The GRI in radiosensitization experiment with fixed concentration of nanoparticles is defined as the equation below:

$$GRI(D, t_{max}) = 2^{k(D,t_{\max})/k(0)} - 1$$

Where D is the X-ray dose, and $k(0)$ is the growth rate of the control group at t_{max}. GRI for X-ray-treated cells always falls in the range of 0~1, which means partial proliferation inhibition. $GRI = 0$ means complete cytostasis, and $GRI = 1$ means the cells are growing without inhibition or the same as the control group. GRI data was found to be able to be fitted with a linear-quadratic model like the surviving fraction in colony formation assay:[25]

$$GRI(D) = e^{(-\alpha D - \beta D^2)}$$

Where α and β are fitting parameters. Then the growth inhibition factor at $GRI = x\%$ ($GIF_{x\%}$) was defined based on the fitting curve of $GRI(D)$ as the equation shown below:

$$GIF_{x\%} = \frac{D_{PBS}}{D_{MOL}}$$

Where D_{PBS} and D_{MOL} are the X-ray doses required to produce the same effect of $x\%$ GRI. In this manuscript, $GRI = 10\%$ was used for $GIF_{10\%}$ to quantify the radiosensitizing effect of Hf_{12}-Ir MOL.

Cell viability assay. The dark toxicity of MOL on various cell lines was determined by MTS assay. MC38 and CT26 cells were seeded in 96-well plates at a density of 1500 cells, and Raw264.7, BMDC, and BMM cells were seeded at a density of 5000 cells. Different concentrations of MOL were added, and 48 hours later, 10% v/v of MTS reagent (CellTiter 96®

AQueous One Solution Cell Proliferation Assay, Promega) was added to each well. 1-1.5 hours later, the absorbance at 490 nm was read by a Synergy HTX plate reader to calculate cell viability.

DFT calculations. DFT calculations were performed with Gaussian 16 software, Revision A.03[55]. The structures of Zr_{12} SBU, cGAMP, and the conjugates in solution-phase were fully optimized by using the B3LYP-D3(BJ) functional.[58-59] The 6-31G+(d) basis set was used for C, H, O, N, P, and F. SDD basis set was used for Zr. The solvation effect (in H_2O) during optimization was accounted by using the IEFPCM solvation model. The single-point energy calculation was based on Def2TZVP basis set to ensure accuracy, and the corresponding thermal correction calculation was based on the 6-31G+(d) basis set. The solvation effect (in H_2O) was accounted by using the SMD solvation model.

Western blot. All antibodies used in western blot experiments were purchased from Cell Signaling Technology. All buffers, assays, and XCell SureLock™ Mini-Cell were from ThermoFisher Scientific. The mini trans-blot electrophoretic transfer cell was from Bio-Rad, and the FluorChem R system was from ProteinSimple. Cells were lysed by RIPA buffer with protease and phosphatase inhibitor cocktail following the manufacturer's specification. The proteins in the supernatant were collected by centrifugation at 14000 g, and the concentrations were measured and normalized by BCA assay. The proteins were denatured and reduced by NuPAGE™ LDS sample buffer with 50 mM DTT, and then heated to 70 °C for 10 min. 10 to 20 μg of samples were loaded on NuPAGE™ 4 to 12%, Bis-Tris gel for electrophoresis on a XCell SureLock™ Mini-Cell (200V, 35-50 minutes), and electrotransfer to PVDF membrane (200 mA, 90 min) on a mini trans-blot electrophoretic transfer cell. The membrane was blocked by TBST with 5% non-fat dry milk at room temperature for 1 hour and incubated with primary antibody solution in TBST with 5% BSA at 4°C overnight (Phospho-histone H2A.X (Ser139) (20E3) rabbit mAb #9718, 1:2000;

phospho-STING (Ser365) (D8F4W) rabbit mAb #7297, 1:1000; phospho-IRF-3 (Ser396) (D6O1M) rabbit mAb #29047, 1:1000; STING (D1V5L) Rabbit mAb (Rodent Preferred) #50494, 1:1000; IRF-3 (D83B9) rabbit mAb #4302 1:1000; β-Actin (8H10D10) mouse mAb #3700, 1:2000). The membrane was washed with TBST and incubated with secondary antibody with HRP conjugate in TBST with 5% BSA at room temperature for 1 hour (anti-rabbit IgG, HRP-linked antibody #7074, 1:2000-5000; anti-mouse IgG, HRP-linked antibody #7076, 1:5000). The membrane was again washed with TBST and Pierce™ ECL western blotting substrate was added. The chemiluminescence was then recorded by a FluorChem R system.

Immunofluorescence microscopy. All antibodies used in immunofluorescence experiments were purchased from Cell Signaling Technology except anti-mouse CD11c-PE/Cy5.5 from Invitrogen and Calreticulin Antibody (1G6A7) [Alexa Fluor® 488] from NOVUS. Acti-stain™ 488 was purchased from Cytoskeleton, Inc. Hoechst 33342 and ProLong™ glass antifade mountant were purchased from ThermoFisher Scientific. The cells were seeded in 6-well plates with a coverslip at the bottom of each well. The cells were treated with different conditions and fixed by 4% PFA (pH = 7.2) at room temperature for 20 minutes. For general intracellular staining, the cells were washed with PBS, blocked, and permeabilized by 5% FBS + 0.3% Triton-X in PBS at room temperature for 1 hour. After blocking, the cells were incubated with primary antibodies in 1% BSA + 0.3% Triton-X in PBS at 4°C overnight (phospho-histone H2A.X (Ser139) (20E3) rabbit mAb #9718, 1:400; phospho-STING (Ser365) (D1C4T) rabbit mAb #62912, 1:200; phospho-STING (Ser366) (D8K6H) rabbit mAb #40818, 1:200). The cells were then washed by PBS and incubated with secondary antibodies in 1% BSA + 0.3% Triton-X in PBS at room temperature for 1 hour (anti-rabbit IgG (H+L), F(ab')2 fragment (Alexa Fluor® 647 conjugate) #4414, 1:1000). For staining of surface markers, the cells were blocked by PBS with 5% FBS and

stained with the dye-conjugate antibody 1:100 in PBS with 1% BSA. For staining of CRT surface translocation, the cells were fixed in -20°C methanol for 5 minutes and incubated with anti-CRT-AlexaFluor488 in 1% BSA at 4°C overnight. After staining, cells were washed with PBS and further incubated with 1:500 Acti-stain™ 488 and 1:3000 Hoechst 33342 in PBS for 30 min if needed. After washing with PBS, the coverslips were mounted on glass slides with ProLong™ glass antifade mountant, cured at room temperature overnight, sealed by nail polish, and observed on a Leica SP8 confocal microscope. The Z-stack images were reconstructed into 3-D images by 3-D viewer plugin in Fiji ImageJ.

Isothermal titration calorimetry. The interaction between cGAMP and Hf_{12}-Ir MOL was measured and analyzed on a MicroCal iTC_{200} system (Malvern Instruments) equipped with reference and sample cells (V = 400 μL). All titrations were carried out using a 40 μL syringe at 298.15 K with a stirring rate of 250 rpm. 71 μM Hf_{12}-Ir MOL water solution was titrated with 300 μM cGAMP water solution or 300 μM NH_4Ac. The first injection of 0.4 μL was followed by 20 injections of 2 μL at intervals of 150 s. A water sample was used to titrate MOL to subtract background noise. Data analysis was performed using the MicroCal iTC_{200} software, and all data were fitted to an independent single-site model.

STING activation *in vitro* and *ex vivo*. THP1-Dual™ KO-MyD88 reporter cells were used to quantify STING activation of free cGAMP and cGAMP/MOL *in vitro*. The cells were seeded in 96-well plates at a density of 10^5 cells/mL (n = 6), and up to 10 μM cGAMP and cGAMP/MOL were added and incubated for 24 hours. The stimulation of the IRF pathway was quantified by QUANTI-Luc (InvivoGen) assay on a Synergy HTX plate reader according to the vendor's protocol. The phosphorylated STING was also stained and visualized for THP-1 (#40818), Raw264.7, and BMDCs (#62912). The cytokines secreted in the medium were quantified by

LumiKine™ Xpress mIFN-β 2.0 (InvivoGen), TNFα mouse ELISA kit, and IL-6 mouse ELISA kit (Invitrogen) according to the manufacturer's specification.

Phagocytosis. In collagen-coated 24-well plates, BMDCs or BMDMs (1 mL RPMI-1640 full medium, 10000 cells/well) were seeded and incubated at 37 °C. 6 hours later, MC38 cells (1 mL RPMI-1640 full medium, 5000 cells/well) were added together with cGAMP (0.2 μg/mL), Hf_{12}-Ir MOL (20 μM Hf), or cGAMP/MOL (0.2 μg/mL cGAMP with 20 μM Hf). 4 hours later, the plates were irradiated with 2 Gy X-ray and immediately put in an IncuCyte S3 live-cell analysis system and continuously observed by a 20× objective in phase contrast mode for 32 hours. The phase contrast images were collected and analyzed by IncuCyte 2020B software to obtain time-dependent confluence in each well (4 tiles per well, 2 replicates for each treatment group).

***In vivo* antitumor efficacy.** The antitumor efficacy of cGAMP/MOL was evaluated on subcutaneous CT26-bearing BALB/c and MC38-bearing C57BL/6 mouse models. For the single tumor model, 2×10^6 CT26 cells or MC38 cells were subcutaneously injected into the right flanks of BALB/c or C57BL/6 mice, respectively (both $n = 6$). When the tumors reached 75-100 mm^3, 20 μL of Hf_{12}-Ir MOL (0.5 μmol Hf), cGAMP/MOL (2 μg/0.5 μmol Hf), cGAMP (2 μg), or PBS was *i.t.* injected into the mice. After 8 hours, the mice were anesthetized with 2.5 % (v/v) isoflurane/oxygen, and the tumors were irradiated with 2 Gy X-ray/fraction for 6 consecutive days. The tumor volumes, body weights, and health conditions of the mice were closely monitored, and the mice were euthanized according to experimental requirements (for immune cell profiling, the mice were euthanized 2 days or 12 days after the last dose of X-ray) or when the control groups (PBS without radiation) reached the protocol limit.

Abscopal effect. For the bilateral MC38 tumor model, 2×10^6 MC38 cells were subcutaneously injected into the right flank, and 1×10^6 MC38 cells were injected into the left

flank of C57BL/6 mice (n = 6). When the primary tumors (right) reached 100-125 mm^3, the primary tumors were injected with 20 μL of cGAMP/MOL (2 μg/0.5 μmol Hf) or PBS. The mice received the same procedure of X-ray treatment on the primary tumors. The mice in αPD-L1 or cGAMP/MOL+ αPD-L1 group were intraperitoneally injected with 2 × 75 μg/mouse αPD-L1 antibody on day 3 and day 6 after the first X-ray treatment.

***In vivo* imaging system analysis.** The subcutaneous MC38-bearing C57BL/6 mouse model was established by the procedure above. When tumors reached ~150 mm^3, 20 μL of cGAMP-Cy5/MOL (2 μg/0.5 μmol Hf) or free cGAMP-Cy5 (2 μg) was *i.t.* injected into the mice. The mice were anesthetized with 2% (v/v) isoflurane/oxygen and imaged by an IVIS Spectrum 200 (Xenogen, USA, ex. 640 nm/em. 680 nm) at 10 minutes, 20 minutes, 30 minutes, 1 hour, 2 hours, 4 hours, 8 hours, 24 hours, 48 hours and 96 hours after injection. The images were processed and analyzed by Living Image® 4.7.2 software (PerkinElmer). The fluorescence signals were fitted by a two-phase exponential association equation in Origin Lab software.

Tumor challenge studies. 35 days after the first CT26 inoculation, the tumor-free BALB/c mice treated by cGAMP/MOL(+) were inoculated again with 2 × 10^6 CT26 cells subcutaneously. Control mice were inoculated simultaneously and monitored until reaching the protocol limit. All mice were euthanized after day 65.

Immune cell profiling. MC38 tumor-bearing C57BL/6 mice (n = 6) received treatment with nanoparticles and X-ray, and the tumors and TDLNs were harvested on day 15 or day 25 for immune cell profiling by flow cytometry. The tumors and TDLNs were digested by 600 μL of RPMI-1640 + 10% FBS + 1 mg/mL collagenase I (Gibco) + 250 μg/mL collagenase IV (Gibco)+ 50 μg/mL DNase I (Sigma-Aldrich) cocktail at 37 °C for 45 minutes. The digests were neutralized with 4.4 mL complete RPMI-1640 medium, and gently ground and filtered through sterile cell

strainers (40 μm, Corning) to obtain single-cell suspensions (~10^7 cells/mL). The cell pellets were collected by centrifugation with 300 g for 10 minutes at 4 °C. The supernatants were collected for cytokine testing. For live staining, the red blood cells were lysed by ACK buffer (ThermoFisher Scientific, 2 mL per sample), and the remaining cells were washed by ice-cold FACS buffer and stained first with LIVE/DEAD™ fixable yellow dead cell stain kit (ThermoFisher Scientific, 1:1000). The cells were then washed with FACS buffer, blocked by anti-CD16/32 antibody (clone 93, 1:100) at 4 °C for 15 minutes, and stained with the fluorochrome-conjugated rat anti-mouse antibodies 1:200 (1:500 for CD45-BV421) at 4 °C for 45 minutes. For intracellular staining of regulatory T cells, the cells were fixed with 4% paraformaldehyde (pH = 7.2) at room temperature for 10 minutes, centrifuged and washed twice with FACS buffer, then incubated with BD Perm/Wash™ Buffer at room temperature for 15 minutes, blocked by anti-CD16/32 antibody (clone 93, 1:100) at 4 °C for 15 minutes, and stained with the fluorochrome-conjugated rat anti-mouse antibodies 1:200 (1:500 for CD45-BV421) at 4 °C for 45 minutes. The antibodies, conjugated dyes, and clone numbers were listed as followed: CD45-BV421 (30-F11), CD11b-FITC (M1/70), NK1.1-PE/Dazzole594 (PK130), F4/80-PerCP/Cy5.5 (BM8), Gr-1-PE (RB6-8C5), CD86-APC (GL1), CD206-PE/Cy7 (C068C2), CD11c-PE/Cy5.5 (N418), MHCII-PE (M5/114.15.2), CD3Ɛ-PE/eFluor610 (145-2C11), CD3Ɛ-PE/Cy7 (145-2C11), CD4-APC/H7 (GK1.5), CD8α-PerCP/eFluor710 (53-6.7), B220-APC (RA3-6B2), CD44-PE (IM7), CD62L-FITC (MEL-14), XCR1-APC/Cy7 (ZET), CD80-PE-Cy7 (B7-1), CD25-FITC (PC61.5.3), Foxp3-APC (FJK-16s). CD45-BV421 was from BD Bioscience. CD206-PE/Cy7, NK1.1-PE/Dazzole594, CD3Ɛ-PE/Cy7, and XCR1-APC/Cy7 were from BioLegend. Others were from eBioscience. The cells were finally washed and resuspended in FACS buffer and analyzed on an LSR Fortessa 4-15 flow cytometer.

Immunohistochemistry analysis. For the formalin-fixed-paraffin-embedded (FFPE) samples, the tumors and major organs were harvested from the treated mice, washed with PBS, fixed with 10% neutral buffer for 72 hours, and 70% ethanol for 24 hours. The tissues were processed, embedded in paraffin, sectioned, and stained (H&E, IBA-1, CD3e) by Human Tissue Resource Center at the University of Chicago. Briefly, the slides were deparaffinized and rehydrated through xylenes and serial dilutions of ethanol to distilled water. Then the slides were treated with an antigen retrieval buffer (S1699, DAKO for CD3e; S2367, DAKO for IBA-1) and heated in a steamer over 97°C for 20 minutes). After washing, the slides were incubated with primary antibodies (anti-CD3, Abcam (ab5690), 1:100; anti-IBA-1, Cell Signaling (E4O4W), 1:600) at room temperature for 1 hour in a wet chamber. The slides were washed with TBS, then CD3 and IBA-1 slides were incubated with biotinylated anti-rabbit IgG (1:200, BA-1000, Vector Laboratories) and anti-rabbit-polymer (Bond Polymer refine Detection, Leica Biosystems, DS9800) for 30 minutes at room temperature, respectively. The antigen-antibody binding was detected by Elite kit (PK-6100, Vector Laboratories) and DAB (DAKO, K3468) system. Tissue sections were then immersed in hematoxylin for counterstaining and covered with cover glasses. The slides were scanned on a CRi Pannoramic SCAN 40x whole slide scanner by Integrated Light Microscopy Core at the University of Chicago. The images were analyzed by QuPath-0.2.3 software.[60] For the frozen slides, the tumors were harvested and frozen with OCT compound (Fisher Healthcare) at -80 °C. The blocks were sectioned, fixed with 75% acetone + 25% ethanol at -20 °C for 10 minutes, washed with TBST to remove OCT, blocked by 5% FBS in PBS, incubated with CD4-PE (GK1.5) antibody (eBioscience, 1:100), CD8-FITC (54-6.7) antibody (eBioscience, 1:100), PD-L1-APC (10F.9G2) antibody (BioLegend, 1:200) at a 4 °C wet chamber overnight, and observed by a Leica SP8 confocal microscope.

IFN-γ ELISPOT assay. A Multiscreen HTS-IP plate (Millipore Sigma) was activated by 70% ethanol, washed with PBS, coated with anti-mouse IFN-γ capture antibody (BD Biosciences) at 37 °C for 8 hours, and blocked with sterile 1% BSA in PBS at room temperature for 2 hours. The spleens were harvested from the treated bilateral MC38 tumor-bearing C57BL/6 mice and were then gently ground and filtered through sterile cell strainers to afford single-cell suspensions. Red blood cells were then lysed by sterile ACK buffer (Corning), and splenocytes were counted and seeded in the plate at a density of 2×10^5 cells/well in RPMI-1640 full medium (6 mice in each treatment group and each mouse with 3 replicates). MC38 tumor-associated KSPWFTTL (KSP) peptide was added to each well at a concentration of 10 μg/mL except for negative control wells. The splenocytes in positive control wells were directly stimulated with anti-mouse CD3Ɛ (145-2C11) and anti-mouse CD28 (37.51) antibodies (eBioscience, 1:1000). The splenocytes were incubated at 37 °C for 48 hours and culture media were discarded. The plates were then washed and incubated with a biotinylated anti-IFN-γ detection antibody, streptavidin-HRP conjugate, and AEC substrate following the manufacturer's specification (BD Biosciences). The plate was air-dried and analyzed by a CTL ImmunoSpot® S6 Analyzer.

6.5 References

(1) Byun, D. J.; Wolchok, J. D.; Rosenberg, L. M.; Girotra, M., Cancer immunotherapy — immune checkpoint blockade and associated endocrinopathies. *Nat. Rev. Endocrinol.* **2017,** *13* (4), 195-207.

(2) Majzner, R. G.; Mackall, C. L., Clinical lessons learned from the first leg of the CAR T cell journey. *Nat. Med.* **2019,** *25* (9), 1341-1355.

(3) Corrales, L.; Matson, V.; Flood, B.; Spranger, S.; Gajewski, T. F., Innate immune signaling and regulation in cancer immunotherapy. *Cell Res.* **2017,** *27* (1), 96-108.

(4) Demaria, O.; Cornen, S.; Daëron, M.; Morel, Y.; Medzhitov, R.; Vivier, E., Harnessing innate immunity in cancer therapy. *Nature* **2019,** *574* (7776), 45-56.

(5) Zhu, Y.; An, X.; Zhang, X.; Qiao, Y.; Zheng, T.; Li, X., STING: a master regulator in the cancer-immunity cycle. *Mol. Cancer* **2019,** *18* (1), 152.

(6) Sun, L.; Wu, J.; Du, F.; Chen, X.; Chen, Z. J., Cyclic GMP-AMP Synthase Is a Cytosolic DNA Sensor That Activates the Type I Interferon Pathway. *Science* **2013,** *339* (6121), 786-791.

(7) Wu, J.; Sun, L.; Chen, X.; Du, F.; Shi, H.; Chen, C.; Chen, Z. J., Cyclic GMP-AMP Is an Endogenous Second Messenger in Innate Immune Signaling by Cytosolic DNA. *Science* **2013,** *339* (6121), 826-830.

(8) Motedayen Aval, L.; Pease, J. E.; Sharma, R.; Pinato, D. J., Challenges and Opportunities in the Clinical Development of STING Agonists for Cancer Immunotherapy. *J. Clin. Med.* **2020,** *9* (10), 3323.

(9) Liang, H.; Deng, L.; Hou, Y.; Meng, X.; Huang, X.; Rao, E.; Zheng, W.; Mauceri, H.; Mack, M.; Xu, M.; Fu, Y.-X.; Weichselbaum, R. R., Host STING-dependent MDSC mobilization drives extrinsic radiation resistance. *Nat. Commun.* **2017,** *8* (1), 1736.

(10) Harrington, K. J.; Brody, J.; Ingham, M.; Strauss, J.; Cemerski, S.; Wang, M.; Tse, A.; Khilnani, A.; Marabelle, A.; Golan, T., LBA15 - Preliminary results of the first-in-human (FIH) study of MK-1454, an agonist of stimulator of interferon genes (STING), as monotherapy or in combination with pembrolizumab (pembro) in patients with advanced solid tumors or lymphomas. *Ann. Oncol.* **2018,** *29*, viii712.

(11) Meric-Bernstam, F.; Sandhu, S. K.; Hamid, O.; Spreafico, A.; Kasper, S.; Dummer, R.; Shimizu, T.; Steeghs, N.; Lewis, N.; Talluto, C. C.; Dolan, S.; Bean, A.; Brown, R.; Trujillo, D.; Nair, N.; Luke, J. J., Phase Ib study of MIW815 (ADU-S100) in combination with spartalizumab (PDR001) in patients (pts) with advanced/metastatic solid tumors or lymphomas. *J. Clin. Oncol.* **2019,** *37* (15_suppl), 2507-2507.

(12) Nam, J.; Son, S.; Park, K. S.; Zou, W.; Shea, L. D.; Moon, J. J., Cancer nanomedicine for combination cancer immunotherapy. *Nat. Rev. Mater.* **2019,** *4* (6), 398-414.

(13) Li, S.; Luo, M.; Wang, Z.; Feng, Q.; Wilhelm, J.; Wang, X.; Li, W.; Wang, J.; Cholka, A.; Fu, Y.-x.; Sumer, B. D.; Yu, H.; Gao, J., Prolonged activation of innate immune pathways by a polyvalent STING agonist. *Nat. Biomed. Eng.* **2021,** *5* (5), 455-466.

(14) Begg, A. C.; Stewart, F. A.; Vens, C., Strategies to improve radiotherapy with targeted drugs. *Nat. Rev. Cancer* **2011,** *11* (4), 239-253.

(15) Weichselbaum, R. R.; Liang, H.; Deng, L.; Fu, Y.-X., Radiotherapy and immunotherapy: a beneficial liaison? *Nat. Rev. Clin. Oncol.* **2017,** *14* (6), 365-379.

(16) Kang, J.; Demaria, S.; Formenti, S., Current clinical trials testing the combination of immunotherapy with radiotherapy. *J. ImmunoTher. Cancer.* **2016,** *4* (1), 51.

(17) Theelen, W. S. M. E.; Peulen, H. M. U.; Lalezari, F.; van der Noort, V.; de Vries, J. F.; Aerts, J. G. J. V.; Dumoulin, D. W.; Bahce, I.; Niemeijer, A.-L. N.; de Langen, A. J.; Monkhorst, K.;

Baas, P., Effect of Pembrolizumab After Stereotactic Body Radiotherapy vs Pembrolizumab Alone on Tumor Response in Patients With Advanced Non–Small Cell Lung Cancer: Results of the PEMBRO-RT Phase 2 Randomized Clinical Trial. *JAMA Oncol.* **2019,** *5* (9), 1276-1282.

(18) Kok, M.; Voorwerk, L.; Horlings, H.; Sikorska, K.; Vijver, K. v. d.; Slagter, M.; Warren, S.; Ong, S.; Wiersma, T.; Russell, N.; Lalezari, F.; Maaker, M. d.; Kemper, I.; Mandjes, I. A.; Chalabi, M.; Sonke, G. S.; Salgado, R.; Linn, S. C.; Schumacher, T.; Blank, C. U., Adaptive phase II randomized trial of nivolumab after induction treatment in triple negative breast cancer (TONIC trial): Final response data stage I and first translational data. *J. Clin. Oncol.* **2018,** *36* (15_suppl), 1012-1012.

(19) Sampson, J. H.; Omuro, A. M. P.; Preusser, M.; Lim, M.; Butowski, N. A.; Cloughesy, T. F.; Strauss, L. C.; Latek, R. R.; Paliwal, P.; Weller, M.; Reardon, D. A., A randomized, phase 3, open-label study of nivolumab versus temozolomide (TMZ) in combination with radiotherapy (RT) in adult patients (pts) with newly diagnosed, O-6-methylguanine DNA methyltransferase (MGMT)-unmethylated glioblastoma (GBM): CheckMate-498. *J. Clin. Oncol.* **2016,** *34* (15_suppl), TPS2079-TPS2079.

(20) Manukian, G.; Bar-Ad, V.; Lu, B.; Argiris, A.; Johnson, J. M., Combining Radiation and Immune Checkpoint Blockade in the Treatment of Head and Neck Squamous Cell Carcinoma. *Front. Oncol.* **2019,** *9* (122).

(21) Qian, J. M.; Schoenfeld, J. D., Radiotherapy and Immunotherapy for Head and Neck Cancer: Current Evidence and Challenges. *Front. Oncol.* **2021,** *10* (3307).

(22) Lu, K.; He, C.; Guo, N.; Chan, C.; Ni, K.; Lan, G.; Tang, H.; Pelizzari, C.; Fu, Y.-X.; Spiotto, M. T.; Weichselbaum, R. R.; Lin, W., Low-dose X-ray radiotherapy–radiodynamic therapy via nanoscale metal–organic frameworks enhances checkpoint blockade immunotherapy. *Nat. Biomed. Eng.* **2018,** *2* (8), 600-610.

(23) Quan, Y.; Lan, G.; Fan, Y.; Shi, W.; You, E.; Lin, W., Metal–Organic Layers for Synergistic Lewis Acid and Photoredox Catalysis. *J. Am. Chem. Soc.* **2020,** *142* (4), 1746-1751.

(24) Hafner, M.; Niepel, M.; Chung, M.; Sorger, P. K., Growth rate inhibition metrics correct for confounders in measuring sensitivity to cancer drugs. *Nat. Meth.* **2016,** *13* (6), 521-527.

(25) Franken, N. A. P.; Rodermond, H. M.; Stap, J.; Haveman, J.; van Bree, C., Clonogenic assay of cells in vitro. *Nat. Protoc.* **2006,** *1* (5), 2315-2319.

(26) Xiao, A.; Li, H.; Shechter, D.; Ahn, S. H.; Fabrizio, L. A.; Erdjument-Bromage, H.; Ishibe-Murakami, S.; Wang, B.; Tempst, P.; Hofmann, K.; Patel, D. J.; Elledge, S. J.; Allis, C. D., WSTF regulates the H2A.X DNA damage response via a novel tyrosine kinase activity. *Nature* **2009,** *457* (7225), 57-62.

(27) Ni, K.; Lan, G.; Chan, C.; Quigley, B.; Lu, K.; Aung, T.; Guo, N.; La Riviere, P.; Weichselbaum, R. R.; Lin, W., Nanoscale metal-organic frameworks enhance radiotherapy to potentiate checkpoint blockade immunotherapy. *Nat. Commun.* **2018,** *9* (1), 2351.

(28) Krysko, D. V.; Garg, A. D.; Kaczmarek, A.; Krysko, O.; Agostinis, P.; Vandenabeele, P., Immunogenic cell death and DAMPs in cancer therapy. *Nat. Rev. Cancer* **2012,** *12* (12), 860-875.

(29) Obeid, M.; Tesniere, A.; Ghiringhelli, F.; Fimia, G. M.; Apetoh, L.; Perfettini, J.-L.; Castedo, M.; Mignot, G.; Panaretakis, T.; Casares, N.; Métivier, D.; Larochette, N.; van Endert, P.; Ciccosanti, F.; Piacentini, M.; Zitvogel, L.; Kroemer, G., Calreticulin exposure dictates the immunogenicity of cancer cell death. *Nat. Med.* **2007,** *13* (1), 54-61.

(30) Reutelingsperger, C. P. M.; van Heerde, W. L., Annexin V, the regulator of phosphatidylserine-catalyzed inflammation and coagulation during apoptosis. *Cell. Mol. Life Sci.* **1997,** *53* (6), 527-532.

(31) Xu, Z.; Luo, T.; Lin, W., Nanoscale Metal–Organic Layers for Biomedical Applications. *Acc. Mater. Res.* **2021,** *2* (10), 944-953.

(32) Bowen, J. W.; Levinson, C., Phosphate concentration and transport in Ehrlich ascites tumor cells: Effect of sodium. *J. Cell. Physiol.* **1982,** *110* (2), 149-154.

(33) Baker, S. B.; Worthley, L. I., The essentials of calcium, magnesium and phosphate metabolism: part I. Physiology. *Crit. Care Resusc.* **2002,** *4* (4), 301-6.

(34) Penido, M. G. M. G.; Alon, U. S., Phosphate homeostasis and its role in bone health. *Pediatr. Nephrol.* **2012,** *27* (11), 2039-2048.

(35) Kato, K.; Nishimasu, H.; Oikawa, D.; Hirano, S.; Hirano, H.; Kasuya, G.; Ishitani, R.; Tokunaga, F.; Nureki, O., Structural insights into cGAMP degradation by Ecto-nucleotide pyrophosphatase phosphodiesterase 1. *Nat. Commun.* **2018,** *9* (1), 4424.

(36) Carozza, J. A.; Böhnert, V.; Nguyen, K. C.; Skariah, G.; Shaw, K. E.; Brown, J. A.; Rafat, M.; von Eyben, R.; Graves, E. E.; Glenn, J. S.; Smith, M.; Li, L., Extracellular cGAMP is a cancer-cell-produced immunotransmitter involved in radiation-induced anticancer immunity. *Nat. Cancer* **2020,** *1* (2), 184-196.

(37) Carozza, J. A.; Brown, J. A.; Böhnert, V.; Fernandez, D.; AlSaif, Y.; Mardjuki, R. E.; Smith, M.; Li, L., Structure-Aided Development of Small-Molecule Inhibitors of ENPP1, the Extracellular Phosphodiesterase of the Immunotransmitter cGAMP. *Cell Chem. Biol.* **2020,** *27* (11), 1347-1358.e5.

(38) Ni, K.; Lan, G.; Guo, N.; Culbert, A.; Luo, T.; Wu, T.; Weichselbaum, R. R.; Lin, W., Nanoscale metal-organic frameworks for x-ray activated in situ cancer vaccination. *Sci. Adv.* **2020,** *6* (40), eabb5223.

(39) Guo, N.; Ni, K.; Luo, T.; Lan, G.; Arina, A.; Xu, Z.; Mao, J.; Weichselbaum, R. R.; Spiotto, M.; Lin, W., Reprogramming of Neutrophils as Non-canonical Antigen Presenting Cells by Radiotherapy–Radiodynamic Therapy to Facilitate Immune-Mediated Tumor Regression. *ACS Nano* **2021,** *15* (11), 17515-17527.

(40) Biswas, S. K.; Mantovani, A., Macrophage plasticity and interaction with lymphocyte subsets: cancer as a paradigm. *Nat. Immunol.* **2010,** *11* (10), 889-896.

(41) Schnorrer, P.; Behrens, G. M. N.; Wilson, N. S.; Pooley, J. L.; Smith, C. M.; El-Sukkari, D.; Davey, G.; Kupresanin, F.; Li, M.; Maraskovsky, E.; Belz, G. T.; Carbone, F. R.; Shortman, K.; Heath, W. R.; Villadangos, J. A., The dominant role of CD8+ dendritic cells in cross-presentation is not dictated by antigen capture. *Proc. Natl. Acad. Sci. U.S.A.* **2006,** *103* (28), 10729-10734.

(42) Korangath, P.; Barnett, J. D.; Sharma, A.; Henderson, E. T.; Stewart, J.; Yu, S.-H.; Kandala, S. K.; Yang, C.-T.; Caserto, J. S.; Hedayati, M.; Armstrong, T. D.; Jaffee, E.; Gruettner, C.; Zhou, X. C.; Fu, W.; Hu, C.; Sukumar, S.; Simons, B. W.; Ivkov, R., Nanoparticle interactions with immune cells dominate tumor retention and induce T cell mediated tumor suppression in models of breast cancer. *Sci. Adv.* **2020,** *6* (13), eaay1601.

(43) Wang, H.; Mu, X.; He, H.; Zhang, X.-D., Cancer Radiosensitizers. *Trends Pharmacol. Sci.* **2018,** *39* (1), 24-48.

(44) Gill, M. R.; Vallis, K. A., Transition metal compounds as cancer radiosensitizers. *Chem. Soc. Rev.* **2019,** *48* (2), 540-557.

(45) Bonvalot, S.; Rutkowski, P. L.; Thariat, J.; Carrère, S.; Ducassou, A.; Sunyach, M.-P.; Agoston, P.; Hong, A.; Mervoyer, A.; Rastrelli, M.; Moreno, V.; Li, R. K.; Tiangco, B.; Herraez, A. C.; Gronchi, A.; Mangel, L.; Sy-Ortin, T.; Hohenberger, P.; de Baère, T.; Le Cesne, A.; Helfre, S.; Saada-Bouzid, E.; Borkowska, A.; Anghel, R.; Co, A.; Gebhart, M.; Kantor, G.; Montero, A.; Loong, H. H.; Vergés, R.; Lapeire, L.; Dema, S.; Kacso, G.; Austen, L.; Moureau-Zabotto, L.; Servois, V.; Wardelmann, E.; Terrier, P.; Lazar, A. J.; Bovée, J. V. M. G.; Le Péchoux, C.; Papai, Z., NBTXR3, a first-in-class radioenhancer hafnium oxide nanoparticle, plus radiotherapy versus radiotherapy alone in patients with locally advanced soft-tissue sarcoma (Act.In.Sarc): a multicentre, phase 2–3, randomised, controlled trial. *Lancet Oncol.* **2019,** *20* (8), 1148-1159.

(46) Hu, Y.; Paris, S.; Barsoumian, H.; Abana, C. O.; He, K.; Wasley, M.; Younes, A. I.; Masrorpour, F.; Chen, D.; Yang, L.; Dunn, J. D.; Zhang, J.; Gandhi, S.; Nguyen, Q.-N.; Cortez, M. A.; Welsh, J., Radiation Therapy Enhanced by NBTXR3 Nanoparticles Overcomes Anti-PD1 Resistance and Evokes Abscopal Effects. *Int. J. Radiat. Oncol. Biol. Phys.* **2021,** *111* (3), 647-657.

(47) Xie, J.; Gong, L.; Zhu, S.; Yong, Y.; Gu, Z.; Zhao, Y., Emerging Strategies of Nanomaterial-Mediated Tumor Radiosensitization. *Adv. Mater.* **2019,** *31* (3), 1802244.

(48) Jiang, X.; Du, B.; Yu, M.; Jia, X.; Zheng, J., Surface-ligand effect on radiosensitization of ultrasmall luminescent gold nanoparticles. *J. Innov. Opt. Health Sci.* **2016,** *09* (04), 1642003.

(49) Bai, L.; Jiang, F.; Wang, R.; Lee, C.; Wang, H.; Zhang, W.; Jiang, W.; Li, D.; Ji, B.; Li, Z.; Gao, S.; Xie, J.; Ma, Q., Ultrathin gold nanowires to enhance radiation therapy. *J. Nanobiotechnol.* **2020,** *18* (1), 131.

(50) Poon, W.; Kingston, B. R.; Ouyang, B.; Ngo, W.; Chan, W. C. W., A framework for designing delivery systems. *Nat. Nanotechnol.* **2020,** *15* (10), 819-829.

(51) Ouyang, B.; Poon, W.; Zhang, Y.-N.; Lin, Z. P.; Kingston, B. R.; Tavares, A. J.; Zhang, Y.; Chen, J.; Valic, M. S.; Syed, A. M.; MacMillan, P.; Couture-Senécal, J.; Zheng, G.; Chan, W. C. W., The dose threshold for nanoparticle tumour delivery. *Nat. Mater.* **2020,** *19* (12), 1362-1371.

(52) Skakuj, K.; Teplensky, M. H.; Wang, S.; Dittmar, J. W.; Mirkin, C. A., Chemically Tuning the Antigen Release Kinetics from Spherical Nucleic Acids Maximizes Immune Stimulation. *ACS Cent. Sci.* **2021,** *7* (11), 1838-1846.

(53) Ghosh, P.; Han, G.; De, M.; Kim, C. K.; Rotello, V. M., Gold nanoparticles in delivery applications. *Adv. Drug Delivery Rev.* **2008,** *60* (11), 1307-1315.

(54) Verma, A.; Uzun, O.; Hu, Y.; Hu, Y.; Han, H.-S.; Watson, N.; Chen, S.; Irvine, D. J.; Stellacci, F., Surface-structure-regulated cell-membrane penetration by monolayer-protected nanoparticles. *Nat. Mater.* **2008,** *7* (7), 588-595.

(55) Moon, J. J.; Huang, B.; Irvine, D. J., Engineering Nano- and Microparticles to Tune Immunity. *Adv. Mater.* **2012,** *24* (28), 3724-3746.

(56) Wang, S.; Park, S. S.; Buru, C. T.; Lin, H.; Chen, P.-C.; Roth, E. W.; Farha, O. K.; Mirkin, C. A., Colloidal crystal engineering with metal–organic framework nanoparticles and DNA. *Nat. Commun.* **2020,** *11* (1), 2495.

(57) Nam, K. W.; Park, S. S.; dos Reis, R.; Dravid, V. P.; Kim, H.; Mirkin, C. A.; Stoddart, J. F., Conductive 2D metal-organic framework for high-performance cathodes in aqueous rechargeable zinc batteries. *Nat. Commun.* **2019,** *10* (1), 4948.

(58) Becke, A. D., Density-functional exchange-energy approximation with correct asymptotic behavior. *Phys. Rev. A* **1988,** *38* (6), 3098-3100.

(59) Lee, C.; Yang, W.; Parr, R. G., Development of the Colle-Salvetti correlation-energy formula into a functional of the electron density. *Phys. Rev. B* **1988,** *37* (2), 785-789.

(60) Bankhead, P.; Loughrey, M. B.; Fernández, J. A.; Dombrowski, Y.; McArt, D. G.; Dunne, P. D.; McQuaid, S.; Gray, R. T.; Murray, L. J.; Coleman, H. G.; James, J. A.; Salto-Tellez, M.; Hamilton, P. W., QuPath: Open source software for digital pathology image analysis. *Sci. Rep.* **2017,** *7* (1), 16878.

Chapter 7. STING Agonist-Conjugated Metal-Organic Framework Induces Artificial Leukocytoid Structures and Immune Hotspots for Systemic Antitumor Responses

7.1 Introduction

RT is one of the most widely used cancer treatments in both curative and palliative settings,[1] with approximately half of all cancer patients treated with RT during their disease courses. RT utilizes ionizing radiation to generate reactive radicals and damage DNA, thereby killing fast-proliferating cancer cells.[2] While RT successfully eliminates cancerous cells, it is also highly toxic to normal tissues. Thus, RT is limited by cumulative radiation dose and localized radiation to avoid excessive damage to normal tissues. As a result, RT is mostly applied in a local-regional setting and cannot target distant metastases.[3] Furthermore, recurrent and metastatic tumors can develop radioresistant phenotypes, making RT much less effective for these tumors.[4-5]

To improve its efficacy, RT has traditionally been combined with chemotherapy. However, the combination of RT and chemotherapy is also highly toxic to normal tissues, causing debilitating side effects to patients. In the past three decades, significant efforts have been devoted to the search for non-chemotherapy radiosensitizers to augment the efficacy of RT without causing serious adverse effects.[6-7] Of particular interest, high-Z nanoradiosensitizers are non-toxic and can enhance RT by absorbing more radiation energy.[8-9] They are administered *i.t.* to achieve a high local concentration for effective radiosensitization and cancer cell killing.[10-11]

Despite preclinical efficacy in enhancing RT-mediated cell killing, non-chemotherapy radiosensitizer has not been approved for clinical use by FDA.[12] This lack of clinical success has been attributed to the immunosuppressive properties of RT in the complex TME.[13] RT often

induces an immunosuppressive TME due to increased recruitment of MDSCs, upregulation of the nuclear factor kappa-light-chain-enhancer of activated B cells (NF-κβ), and exhaustion of lymphoid cells.[14-15] This immunosuppressive TME is less responsive to RT and prevents the patient's immune system from attacking tumor cells.

Given these limitations of existing radiosensitizers, we have identified nMOFs as efficient and non-toxic nanoradiosensitizers via a unique RT-RDT process.[11, 16] The high-Z-metal-based SBUs in MOFs efficiently absorb X-rays to enhance RT effects (primarily by enhancing hydroxyl radical generation), whereas the photosensitizing ligands in the MOFs are excited for the RDT process (via $^1O_2$ generation).[9, 17-18] MOF-mediated RT-RDT causes ICD of cancer cells to synergize with immune modulators and immune checkpoint inhibitors.[19-21] We have also combined MOFs and innate immune agonists for TME regulation, including neutrophil reprogramming, macrophage polarization, *in situ* generation of tumor vaccines, and activation of the innate immune system.[22-23] However, the detailed mechanisms of MOF-mediated TME regulation, including MOF distribution in tumors, immune regulation pathways, and long-term immune effects after RT-RDT treatment, remain unclear.

Herein, we report a highly effective nanoradiosensitizer, GA-MOF, by conjugating DBP-Hf MOF with a STING agonist, 2',3'-cyclic guanosine monophosphate–adenosine monophosphate (GA), for synergistic RT and immunotherapy. Coordination between GA and Hf_{12}-SBU prolonged GA retention in tumors and enhanced STING activation. GA-MOF showed low preclinical toxicity, and when combined with low-dose RT, demonstrated superb anticancer efficacy in colon cancer, pancreatic cancer, and head and neck cancer models. We determined the uptake of MOF particles by tumor cells and different immune populations, and revealed the formation of immune cell-rich nodules, termed artificial leukocytoid structures (ALS), in the tumors after *i.t.* injection

of GA-MOF. Low-dose RT turned these ALS into immunostimulatory hotspots in the tumors and facilitated antitumor immunity. Further combination of GA-MOF plus RT with ICB not only improved local cancer eradication, but also suppressed distant tumors via systemic immune activation.

7.2 Results and Discussions

7.2.1 MOF Enhances RT and Enables Sustained Release of GA

DBP-Hf MOF was synthesized via a solvothermal reaction between $HfCl_4$ and H_2DBP in DMF with AA as a modulator (**Figure 7-1a**).[24] DBP-Hf MOF consisted of Hf_{12} SBUs and photosensitizing DBP ligands for RT-RDT effects.[11]

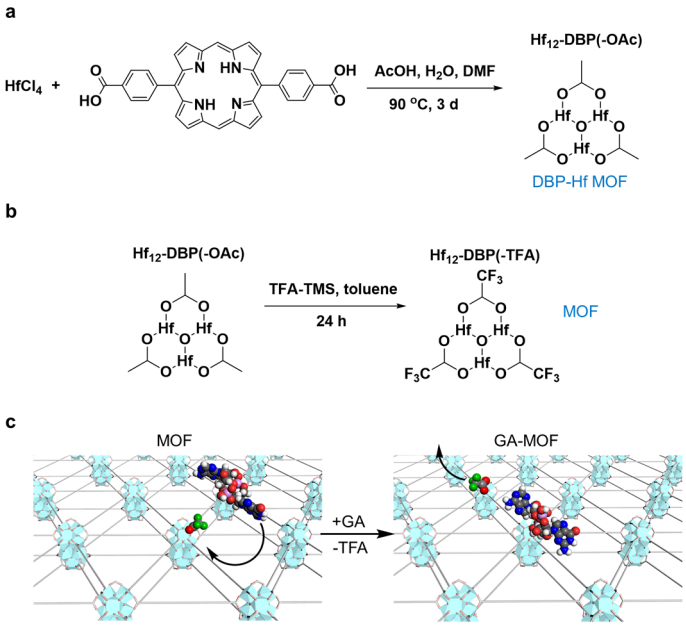

Figure 7-1. Synthesis of DBP-Hf, TFA-modified Hf-DBP, and GA-MOF. (a) Solvothermal synthesis of Hf-DBP nanoscale MOF. AcOH, acetic acid. (b) TFA replacement of acetate groups (OAc) on Hf_{12} SBUs by TFA-TMS in anhydrous toluene to afford TFA-modified MOF. (c) Substitution of TFA by phosphate groups of GA to afford GA-MOF. Cyan polyhedron, Hf; Grey stick, DBP ligand; Grey sphere, C. Green sphere, F; Blue sphere, N; Red sphere, O; Pink sphere; P. White sphere, H.

AA-capped DBP-Hf MOF was modified with TMS-TFA to afford TFA-capped DBP-Hf MOF (abbreviated as MOF in the following text) (**Figure 7-1b**).[19] This AA/TFA exchange created a dynamic surface for GA coordination[25] to afford GA-MOF by replacing the weakly bound TFA on Hf_{12}-SBUs with GA (**Figure 7-1c**). LC-MS analysis gave a GA loading of 0.74 wt% in GA-MOF, corresponding to 1 GA molecule per 14.9 Hf_{12}-SBUs. TEM revealed the same nanoplate morphology for MOF and GA-MOF (**Figure 7-2a,b**). PXRD showed that GA-MOF maintained the same crystalline **hcp** topology as MOF (**Figure 7-2c**). DLS revealed hydrodynamic sizes of 100.0 ± 2.2 and 133.3 ± 4.5 nm for MOF and GA-MOF, respectively (**Figure 7-2d**).

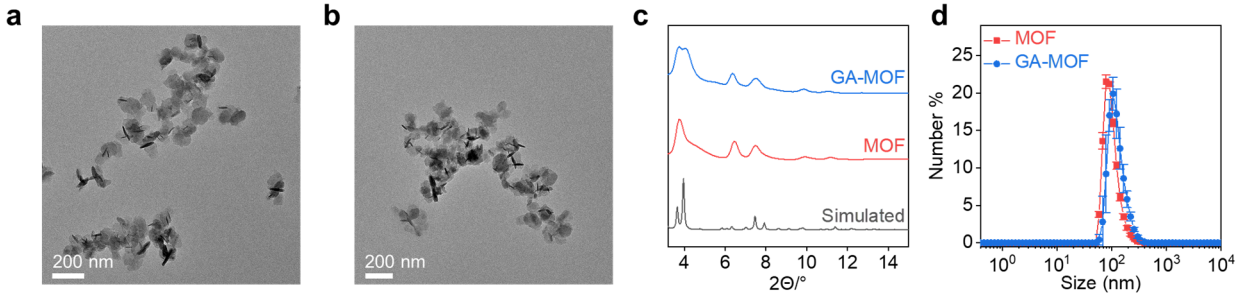

Figure 7-2. Morphology characterization of GA-MOF. (a,b) TEM images of (a) MOF and (b) GA-MOF (scale bar=200 nm). (c) PXRD patterns of simulated DBP-Hf, MOF, and GA-MOF. (d) Number-average sizes of MOF and GA-MOF by DLS in water.

RT enhancement by MOF was evaluated in four different cell lines, including murine colon cancer MC38 and CT26, pancreatic cancer Panc02, and head and neck cancer SCC7, by a GR assay.[26] The GIF values were calculated based on real-time growth rates of cancer cells with increasing doses of X-ray (**Table 7-1 and Table 7-2**). The cells treated by MOF without RT [denoted MOF(-)] showed minimal growth delay (**Figure 7-3**). With X-ray irradiation, MOF treatment [denoted MOF(+)] significantly reduced cell proliferating rates. The GIF values at the 10% GR level were 1.46, 1.17, 1.23, and 1.31 for MC38, CT26, Panc02, and SCC7, respectively. These results suggest that MOF is a biocompatible and efficient nanoradiosensitizer.

Table 7-1. GR and GIF of CT26 and SCC7 cells (*N*=3).

Cell Line		CT26		SCC7	
Treatment		PBS	MOF	PBS	MOF
GR	0	1.000	1.021	1.000	1.025
	2	0.764	0.714	0.669	0.396
	4	0.493	0.402	0.204	0.191
	8	0.204	0.159	0.0326	0.0100
GIF $_{10\%}$		1.17		1.31	

Table 7-2. GR and GIF of MC38 and Panc02 cells (*N*=3).

Cell Line		MC38		Panc02	
Treatment		PBS	MOF	PBS	MOF
GR	0	1.000	1.003	1.000	0.927
	2	0.615	0.440	0.838	0.601
	4	0.323	0.214	0.525	0.411
	8	0.0758	0.0245	0.156	0.112
GIF $_{10\%}$		1.17		1.46	

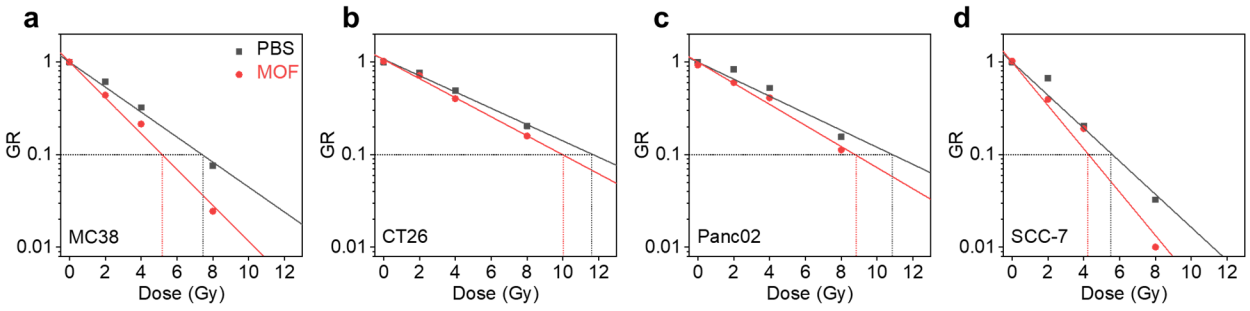

Figure 7-3. GR assays showing radiosensitization effects of MOF in (a) MC38, (b) CT26, (c) Panc02, and (d) SCC7 cell lines.

We recently showed that high inorganic phosphate concentrations inside cells could trigger the release of coordinated molecules from the SBUs.[21, 25] We used LC-MS to determine the release profiles of GA-MOF in 0.1× PBS (1.18 mM phosphate), 1× PBS (11.8 mM phosphate), and 10× PBS (118 mM phosphate) at 37 ℃ to mimic different physiological conditions.[27-28] Incubation of

GA-MOF in 0.1× PBS released <50% of GA in 6 days, while incubation in 1× PBS and 10× PBS released 80% and 92% of GA, respectively (**Figure 7-4a**). The binding strength between GA and MOF was quantified by ITC, affording an association constant (K_{GA}) of (1.50 ± 0.79) × 10^7 M^{-1} (**Figure 7-4b**). These findings suggest that GA can be released from Hf_{12}-SBUs by the intracellular/extracellular phosphate gradient (**Figure 7-4c**).[21, 25]

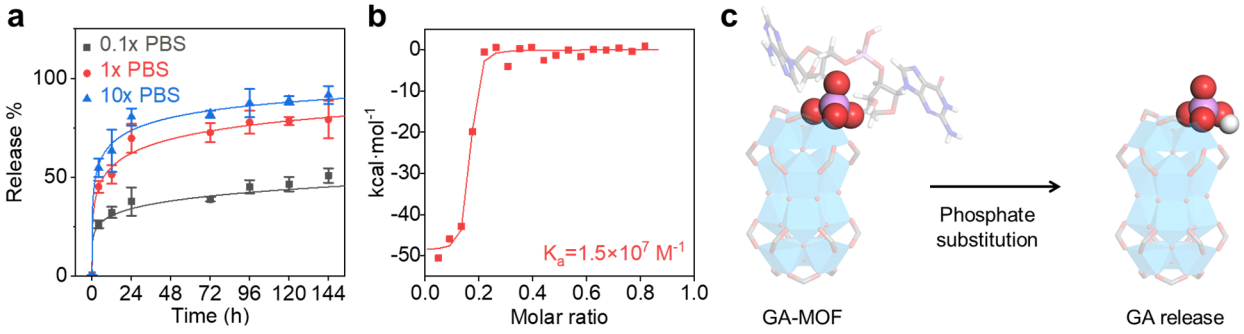

Figure 7-4. Release profiles and binding between GA and MOF. (a) Release percentages of GA from GA-MOF after incubation in 0.1× PBS, 1× PBS, and 10× PBS for 6 days. (b) Binding affinity between GA and MOF by ITC analysis. (c) Schematic showing coordination between GA and MOF and the replacement of GA by phosphate anions under physiological conditions. GA (except one phosphate) is shown in a stick model, and the phosphate is shown using a space-filling model. Cyan polyhedron, Hf; pink, P; Red, O; Blue, N; Grey, C; White, H.

7.2.2 GA-MOF Delivers GA and Elicits Robust STING Activation

The binding of GA to MOF did not affect the cellular uptake of MOF. MOF and GA-MOF showed similar Hf uptake in MC38, CT26, and SCC7 cells (**Figure 7-5a-c**) by ICP-MS. However, GA-MOF significantly enhanced GA uptake *in vitro*. We used cyanine5-conjugated GA (GA/Cy5) to track GA uptake by murine macrophage Raw264.7 cells by CLSM. GA/Cy5 showed rapid internalization of fluorescence signal in 2 hours, but the signal gradually decreased and almost completely disappeared in 24 hours (**Figure 7-5d**). In contrast, the intracellular fluorescence of GA/Cy5-MOF gradually increased and was 34.5-fold stronger than that of GA/Cy5 group at 24 hours (**Figure 7-5d**).

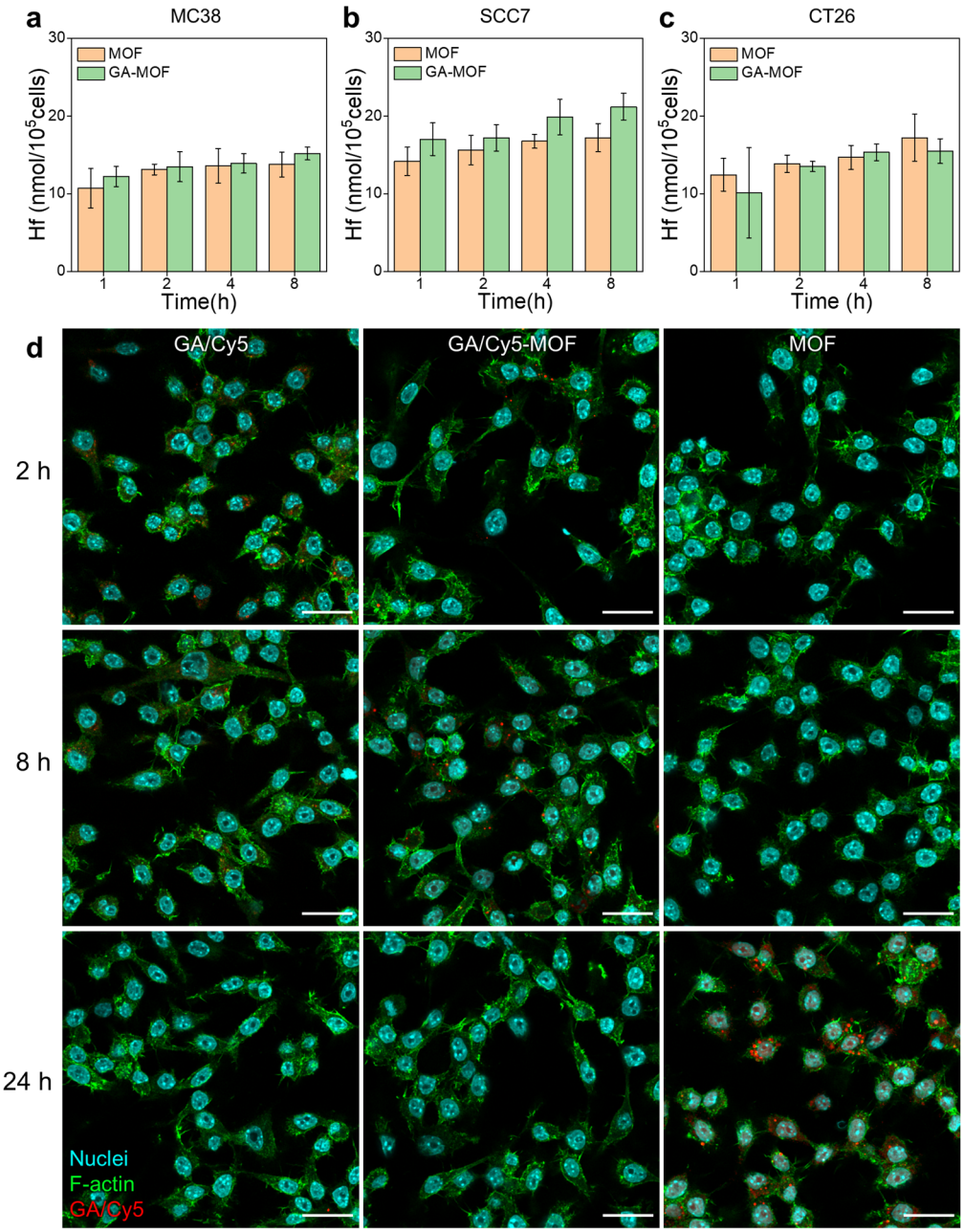

Figure 7-5. Cellular uptake and i*n vitro* trafficking of GA-MOF. (a-c) Cellular uptake of MOF and GA-MOF in (a) MC38, (b) SCC7, and (c) CT26 cells (*N*=3). (d) Representative CLSM images showing uptake of Cy5-labeled (red) GA or GA/Cy5-MOF after incubation with Raw264.7 cells for 2-8 hours. Cell nuclei are shown in cyan, and cytoskeletons are shown in green (scale bar = 10 μm).

STING activation was assessed using human monocyte THP-1 cells with a luciferase reporter gene linked to IFN-responsive elements.[29] After 24-hour incubation, GA-MOF showed an EC_{50} for the IRF response of 2.34 ± 1.44 μM, which was 3-fold lower than that of GA (EC_{50} = 6.98 ± 1.15 μM) (**Figure 7-6**). This result indicates that GA-MOF elicits stronger STING activation than GA.

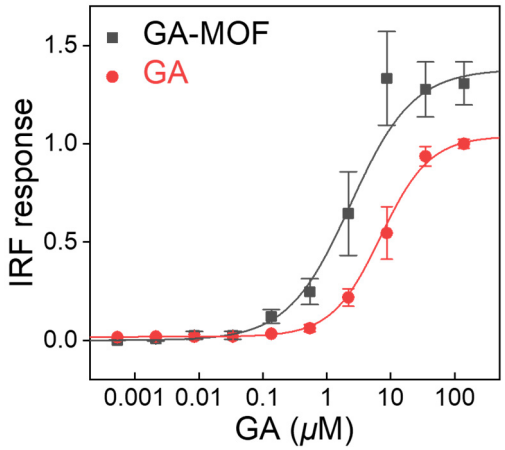

Figure 7-6. EC_{50} of STING activation by GA or GA-MOF. The STING activation was evaluated by its downstream IRF responses with QUANTI-Luc assay in THP-1 reporter cells (*N*=3).

STING activation was supported by the phosphorylation of STING by CLSM. BMDCs and BMDMs from C57BL/6 mice were incubated with GA or GA-MOF (0.27 μM GA / 50 μM Hf) for different lengths of time. GA treatment showed a peak signal of p-STING in BMDCs and BMDMs in 2 hours, while GA-MOF treatment showed sustained STING phosphorylation for up to 8 hours (**Figure 7-7**).

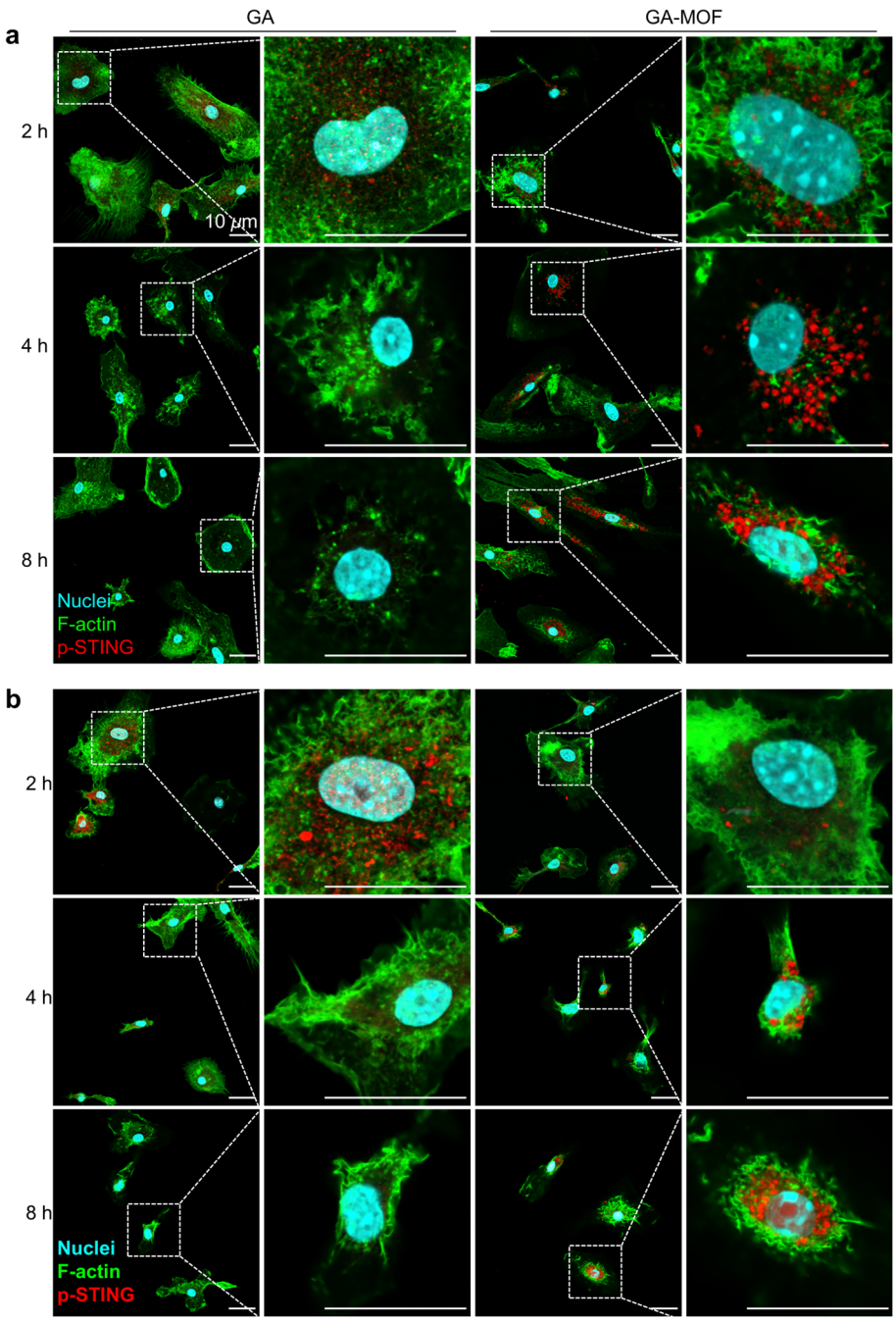

Figure 7-7. *In vitro* STING phosphorylation. Representative CLSM images showing time-dependent expression of p-STING (red) in (a) BMDCs and (b) BMDMs treated with GA or GA-MOF. Cell nuclei are shown in cyan, and cytoskeletons are shown in green (scale bar = 20 μm).

GA-MOF also showed stronger activation of IRF-3 (**Figure 7-8**) and improved phagocytosis capacity of innate immune cells (**Figure 7-9**).

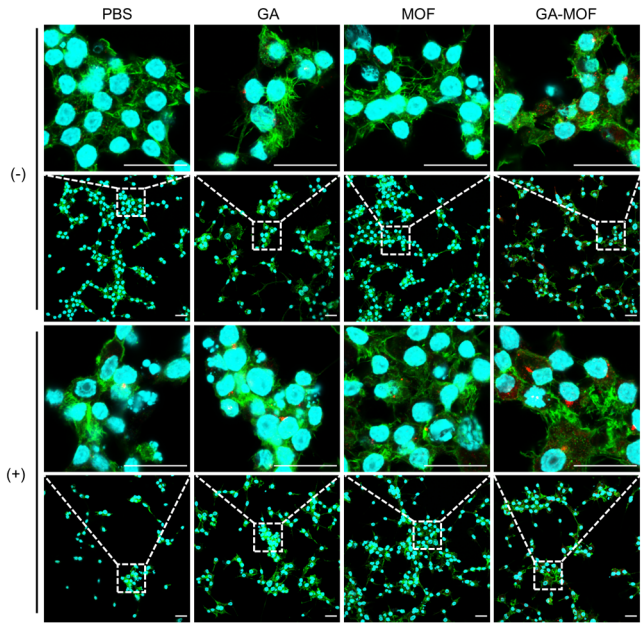

Figure 7-8. *In vitro* IRF phosphorylation. Representative CLSM images showing p-IRF-3 (red) upregulation in Raw264.7 cells treated with PBS, GA, MOF, or GA-MOF with (+) or without (-) 2 Gy X-ray irradiation. Cell nuclei are shown in cyan, and cytoskeletons are shown in green (scale bar = 10 μm).

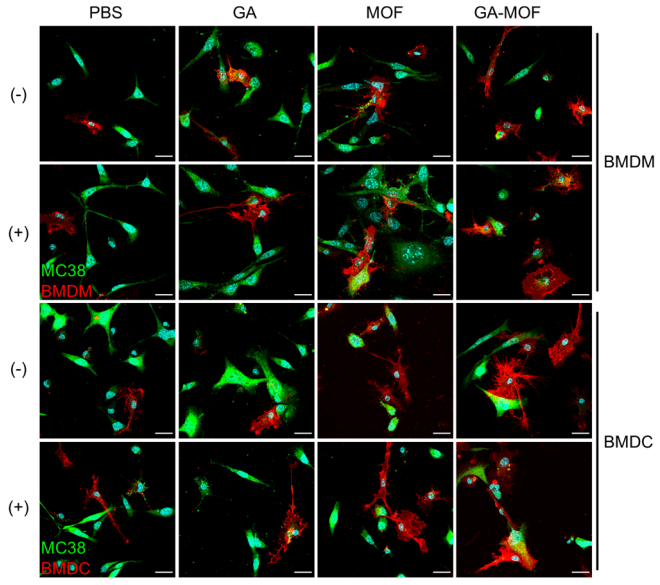

Figure 7-9. Phagocytosis stimulated by GA-MOF. Representative CLSM images showing CFSE-labeled MC38 cells (green) phagocytized by F4/80-labeled BMDMs (red) or CD11c-labeled BMDCs (red) after different treatments (scale bar = 20 μm). (+) denotes 2 Gy X-ray irradiation 4 hours post particle incubation. (-) denoted no irradiation treatment.

STING activation leads to the downstream secretion of type-I IFNs and proinflammatory cytokines.[30] GA-MOF treatment increased IFN-β secretion in BMDCs, BMDMs, and Raw264.7 cells over other groups, indicating stronger activation of the STING-IFN axis in immune cells (**Figure 7-10a,d**). Both GA-MOF(+) and GA-MOF(-) treated primary immune cells showed increased secretion of IL-6 and TNF-α (**Figure 7-10b,c,e,f**). GA-MOF(+) stimulated the secretion of IFN-β and TNF-α by Raw264.7 cells, but did not upregulate the secretion of immunosuppressive IL-10 and TGF-β (**Figure 7-11**). These results demonstrate that GA-MOF induces a more potent and sustained STING activation than GA, leading to enhanced secretion of immunostimulatory cytokines either with or without RT.

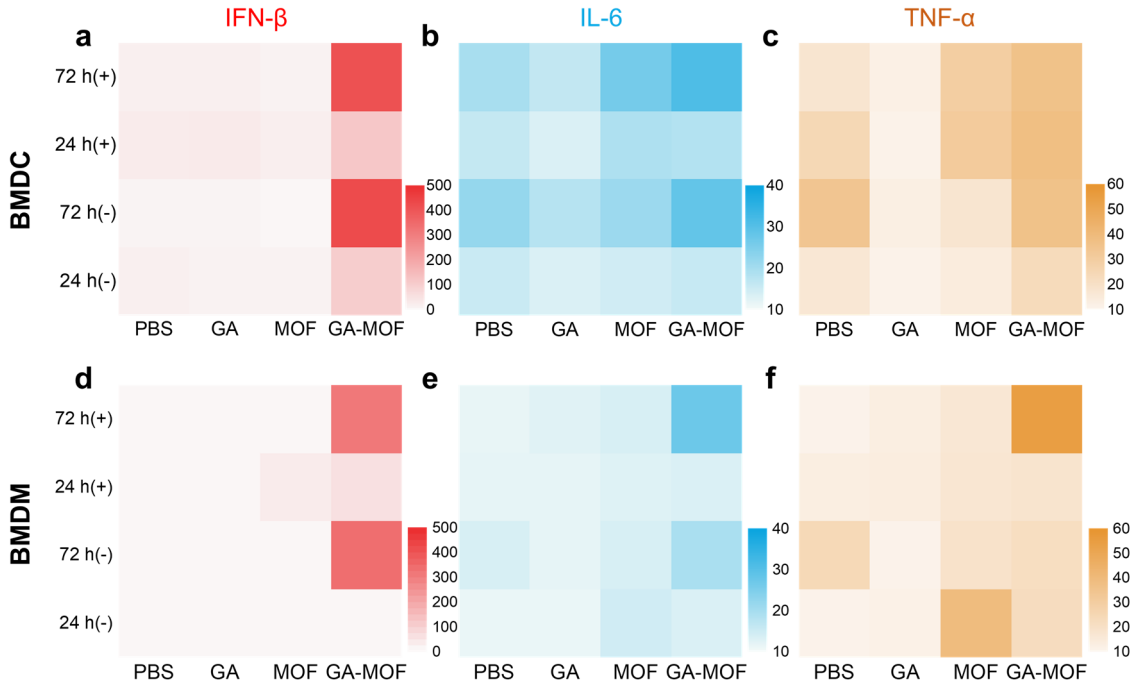

Figure 7-10. Cytokine secretion by BMDCs and BMDMs. (a-c) Heat maps showing secretion levels of (a) IFN-β, (b) IL-6, and (c) TNF-α by BMDCs after different treatments (*N*=3). (d-f) Heat maps showing secretion levels of (d) IFN-β, (e) IL-6, and (f) TNF-α by BMDMs after different treatments (*N*=3). In each figure, the concentration of the cytokine was given as pg/mL. (+) denotes 2 Gy RT 4 hours post incubation. (-) denotes no RT treatment. The x-axis showed treatment groups, and the y-axis showed incubation time and whether 2 Gy RT was given (+) or not (-).

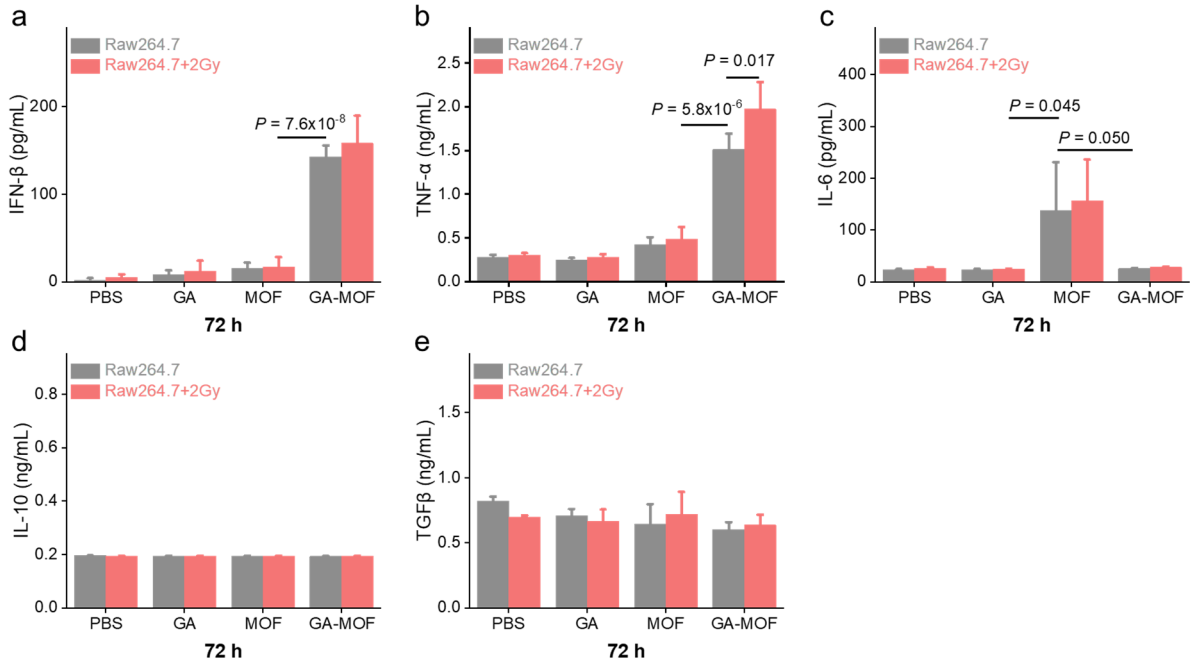

Figure 7-11. Cytokine secretion by Raw264.7 cells. Bar graphs showing secretion levels of (a) IFN-β, (b) IL-6, (c) TNF-α, (d) IL-10, and (e) TGF-β by Raw264.7 cells after different treatments with or without 2 Gy X-ray irradiation (N=3). The incubation time is listed under the y-axis.

Low-dose RT at 2 Gy did not affect IFN secretion, and immune cells were viable upon MOF(+) treatment (**Figure 7-12**).

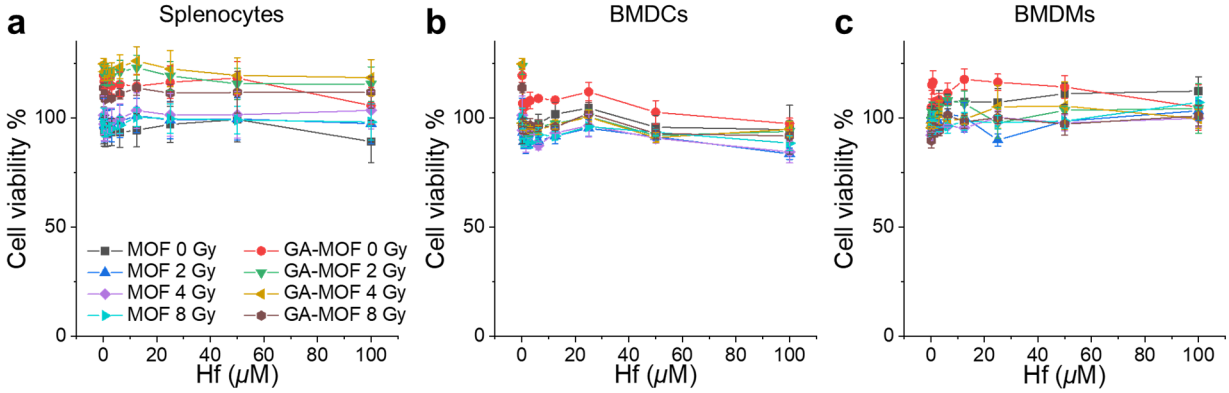

Figure 7-12. Cytotoxicity of MOF and GA-MOF on immune cells. Cell viabilities of (a) splenocytes, (b) BMDCs, and (c) BMDMs after MOF or GA-MOF incubation (up to an equivalent concentration of 100 μM Hf) for 3 days with 0, 2, 4, or 8 Gy X-ray irradiation by MTS assay.

7.2.3 GA-MOF Retains GA in Tumors and Induces Artificial Leukocytoid Structures

To assess the potential of GA-MOF as an immune agonist and a radiosensitizer, we evaluated the toxicity, PK, and tumor retention of GA-MOF in preclinical models. We injected PBS, GA, or GA-MOF at a GA or MOF dose of 1 or 100 mg/kg into the subcutaneous space of Sprague Dawley rats. The rats in all groups showed steady weights and had no health problems throughout the experiment (**Figure 7-13a**). Compared to GA, GA-MOF showed longer plasma retention of GA, as quantified by a competitive ELISA kit (**Figure 7-13b**). The AUC of GA-MOF in plasma was 1.48-fold higher than that of GA. We quantified the tumor retention of GA after *i.t.* injection of GA or GA-MOF into subcutaneous MC38 tumors in C57BL/6 mice. GA-MOF slowed the release of GA and retained 3-fold more GA in the tumors over a 7-day period (**Figure 7-13c**). These results demonstrate increased GA retention in tumors by GA-MOF.

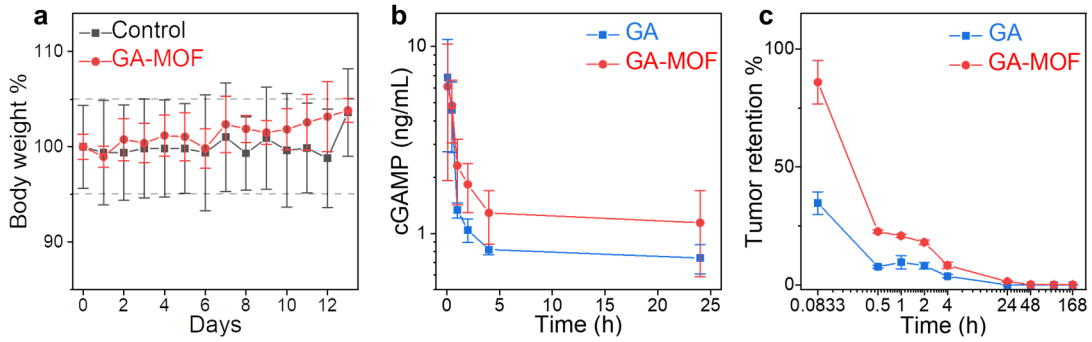

Figure 7-13. GA-MOF is nontoxic and prolongs GA retention. (a) Body weight curves of female rats after subcutaneous injection of PBS or GA-MOF at a GA dose of 1 mg/kg (*N*=3). The starting body weights of the rats were ~200 g. On day 7, the rats received a second subcutaneous injection on the opposite side. (b) Plasma GA concentrations of rats after subcutaneous injection of GA or GA-MOF at a GA dose of 1mg/kg (*N*=3). (c) Tumor retention percentages of GA after *i.t.* injection of GA or GA-MOF to MC38 tumor-bearing C57BL/6 mice at a GA dose of 1 mg/kg (*N*=3).

During preclinical evaluations of rats with subcutaneously injected GA-MOF, we observed the formation of dark subcutaneous nodules covered with fascias (**Figure 7-14a**). We observed similar nodules in MC38 tumors in C57BL/6 mice with *i.t.* injected GA-MOF. To characterize

these nodules, we first performed histological staining of the subcutaneous nodules in rats. Due to the dark red color of DBP, we could directly observe MOF by optical microscopy. H&E staining showed the presence of MOF (brown) in the centers and cells and connective tissues in the surrounding areas of the nodules (**Figure 7-14a**). IHC staining of IBA-1 and CD3 revealed that the majority of the cells in the nodules were innate immune cells, with some T cells at the nodule margins (**Figure 7-14b,c and Figure 7-15a**).

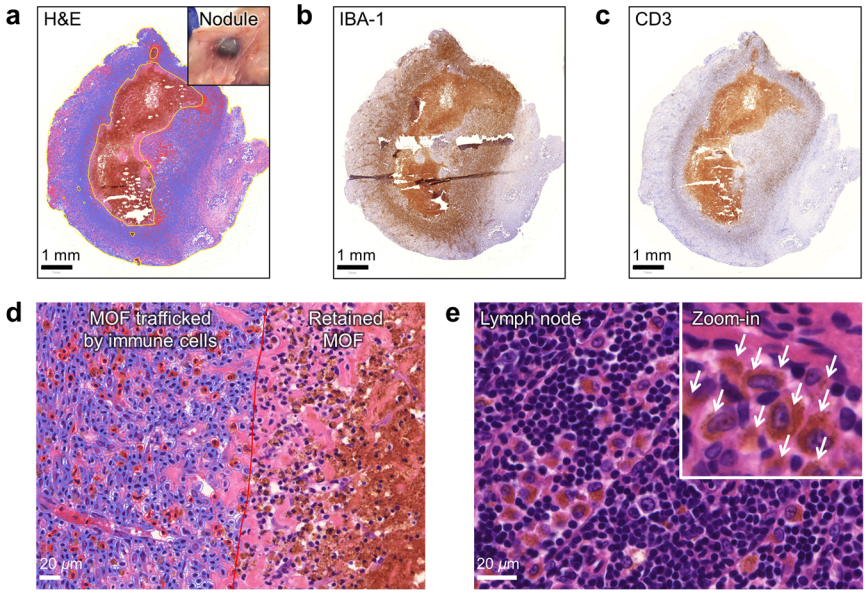

Figure 7-14. GA-MOF forms immune-cell-rich nodules. (a-c) Representative histological slides of the subcutaneous nodules excised from rats 14 days after injection. The slides were stained with (a) H&E, (b) IBA-1, and (c) CD3 for cell morphology, innate immune cells, and T cells, respectively. In the H&E-stained slides (a), the central part with dark brown colors circled by the yellow line corresponds to the retained MOF. Scale bars=1 mm. The zoomed-in view in (a) is the photo of the subcutaneous nodule. g, Enlarged H&E staining slides of the interface between the MOF part (right) and the cellular part (left) in the nodule. The red line shows an approximate border. Cells carrying MOF (MOF^+) are marked with red circles. Cells without MOF (MOF^-) are marked with blue circles. Scale bar=20 μm. h, H&E staining for the draining LN with a zoomed-in view near the lymphatic vessel (inset, MOF contents are marked by white arrows). Macrophages/monocytes carried GA-MOF back into draining LNs for clearance. Scale bar=20 μm.

We hypothesized that GA-MOF acted as a foreign object to attract immune cells into the injection site and activated the local immune system through STING activation.[31-33] Interestingly, we also found significantly less MOF and more cells in the nodules on day 14 (**Figure 7-15b**) than those on day 7 (**Figure 7-14a**), which suggests active and dynamic transport/clearance of MOF particles by immune cells.

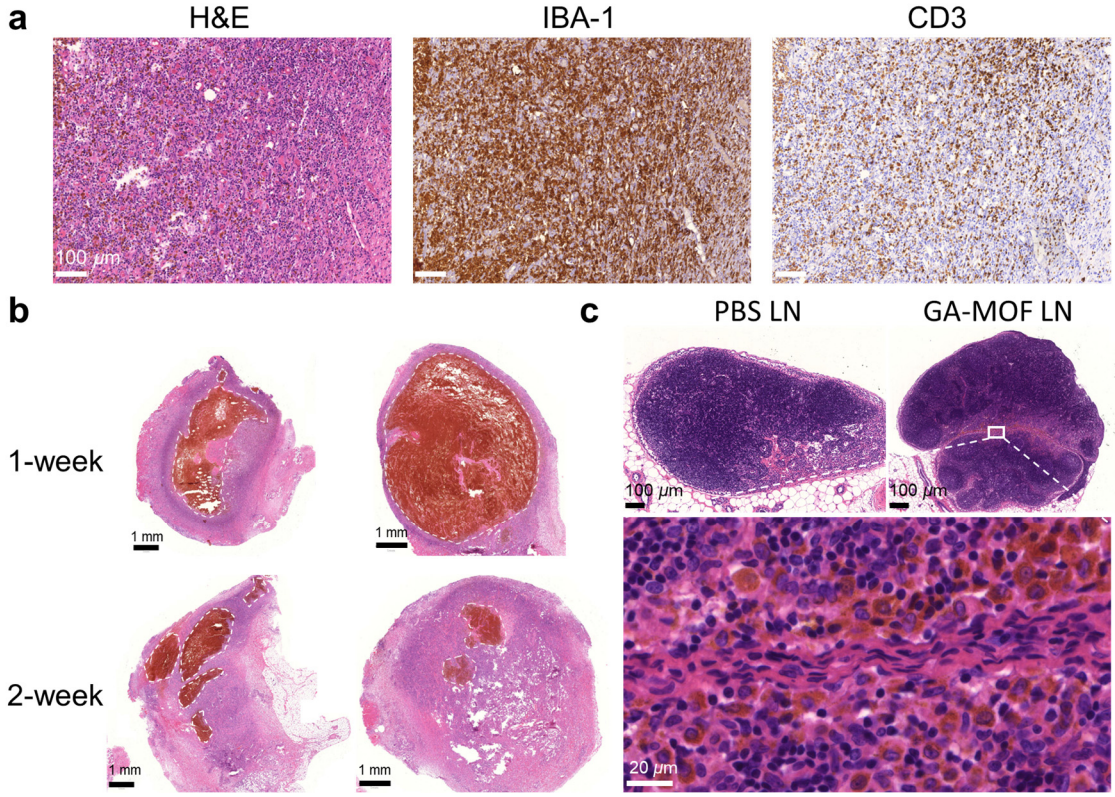

Figure 7-15. Histological staining of subcutaneous nodules. (a) H&E (left), IBA-1 (middle), and CD3 (right) staining showing the nodule morphology, infiltration of innate immune cells, and adaptive immune cells, respectively (scale bar = 100 μm). (b) H&E staining of the nodules one week (top) and two weeks (bottom) post injection (scale bar = 1 mm, MOF contents are circled with white dashed lines). (c) Draining LNs of PBS- and GA-MOF-treated rats (scale bar = 100 μm). The zoomed-in image for the GA-MOF group is shown at the bottom (scale bar = 20 μm).

In the H&E-stained slides of nodules, ~16.7% of cells in the nodules carried MOF. Most of these cells were macrophages or monocytes according to their morphologies (**Figure 7-14d,e**). In

the H&E-stained slides of draining LNs, we observed migrating macrophages/monocytes carrying MOF contents (**Figure 7-14e and Figure 7-15c**). We can depict the fate of GA-MOF after injection into subcutaneous space or tumors based on these observations. After injection, GA-MOF induces immune cell infiltration and triggers foreign body clearance mechanisms. Innate immune cells, including neutrophils, macrophages, and monocytes, form the nodules (ALS) surrounding the injected GA-MOF. The phagocytes carry GA-MOF back into the draining LNs for clearance and antigen presentation.[34] T cells are also known to be involved in this clearance and regenerative process.[35] GA may be released once GA-MOF is uptaken by these innate immune cells to activate their STING-related pathways, either in the nodules or in the draining LNs. However, it remains unclear if STING activation contributes to nodule formation.

7.2.4 RT Transforms Artificial Leukocytoid Structures into Immune Hotspots

Different from the subcutaneous space in rats, MOF after *i.t.* injection can access both tumor cells and immune cells. We performed flow cytometry staining to determine MOF uptake by different cell populations in MC38 tumor-bearing C57BL/6 mice. The fluorescence of DBP (BV711 channel) from MOF was used to differentiate MOF^- and MOF^+ cells in the tumor. One day after *i.t.* injection of MOF, 65.4% MOF^+ cells were non-immune cells ($CD45^-$), and 34.6% MOF^+ cells were leukocytes ($CD45^+$, **Figure 7-16a**). Approximately 97.9% MOF^+ leukocytes were myeloid cells ($MOF^+CD45^+CD11b^+$, **Figure 7-16b**), with 41.9% monocytes ($Ly6C^+$), 33.9% macrophages ($F4/80^+$), and 23.5% neutrophils ($Ly6G^+$) (**Figure 7-16c**). These results are consistent with the histological observations of subcutaneous nodules in rats (**Figure 7-14**).

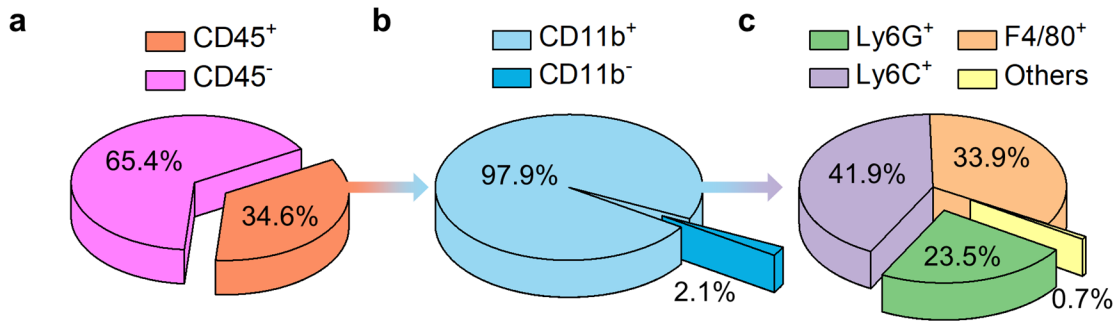

Figure 7-16. *In vivo* MOF uptake by tumor cells and immune cells. (a) Percentages of $CD45^+$ or $CD45^-$ populations in MOF^+ cells. (b) Percentages of $CD11b^+$ or $CD11b^-$ populations in MOF^+CD45^+ cells. (c) Percentages of $Ly6G^+$ or $Ly6C^+$ or $F4/80^+$ populations in $MOF^+CD45^+CD11b^+$ cells (N=5).

To understand the impact of RT on the nodules, we irradiated the injected tumors with 4 Gy X-ray for 3 daily fractions, excised the nodules from the tumors 14 days from the first RT, and performed flow cytometric staining. Both MOF and GA-MOF triggered nodule formation in the injected tumors (**Figure 7-17**).

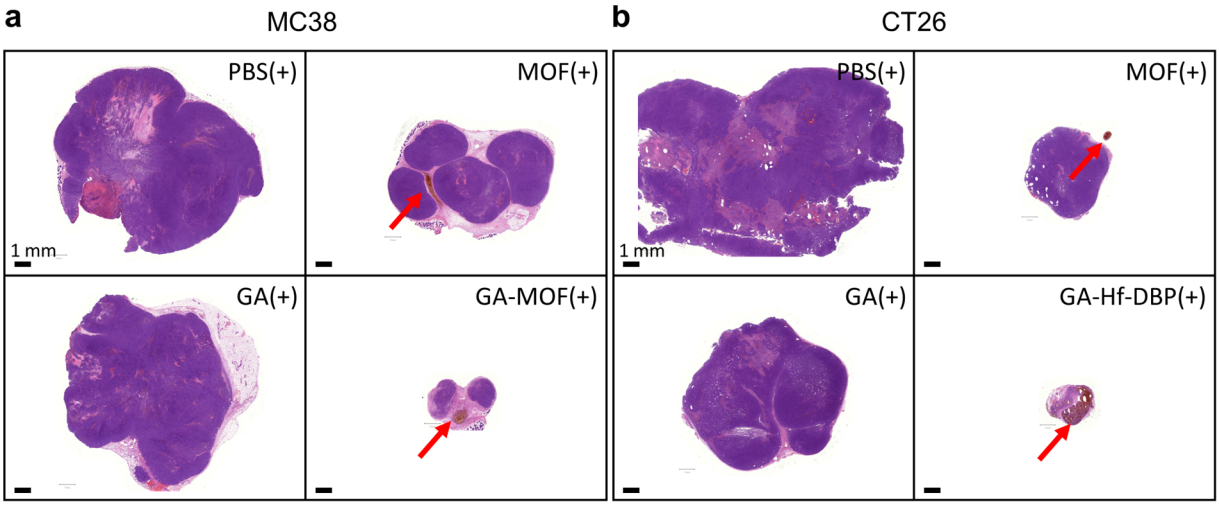

Figure 7-17. ALS formation in tumors. H&E staining of whole (a) MC38 and (b) CT26 tumors with the red arrows showing the location of ALS (scale bar = 1 mm).

These nodules were immunologically distinct from the tumors (**Figure 7-18a**). Compared to GA-MOF(-), MOF(-), and MOF(+), GA-MOF(+) resulted in smaller tumor sizes and a more inflammatory TME with significantly more infiltration of myeloid cells ($CD45^+CD11b^+$), helper

T cells($CD45^+CD3^+CD4^+$), effector T cells ($CD45^+CD3^+CD8^+CD44^+CD62L^-$), and central memory T cells ($CD45^+CD3^+CD8^+CD44^+CD62L^+$) and downregulation of regulatory T cells (T_{reg}, $CD45^+CD3^+CD4^+FOXP3^+CD25^+$) (**Figure 7-18a**). These results suggest that GA-MOF(+) produces immunologically "hot" nodules (immune hotspots) to suppress tumor growth.

IHC staining of GA-MOF(+)-treated tumors revealed similar nodule structures as the subcutaneous nodules in rats (**Figure 7-14a-c and Figure 7-18b**). The MOF center was surrounded by IBA-1^+ innate immune cells and $CD3^+$ T cells. Colonies of tumor cells were surrounded by a large number of immune cells, indicating an active and T-cell-dependent antitumor response. In contrast, MOF(+)-treated tumors did not exhibit immune infiltration near the nodules, with isolated MOF islands trapped in the tumor interstices (**Figure 7-17**). We also inoculated MC38 tumors in STING-knockout ($STING^{-/-}$) B6 mice, and *i.t.* or subcutaneously injected GA-MOF to observe nodule formation. Compared to wild-type (WT) mice, $STING^{-/-}$ mice showed little infiltration of lymphoid cells in both intratumoral and subcutaneous nodules (**Figure 7-19**). This result indicates that STING activation is required for the formation of immune hotspots in the tumors.

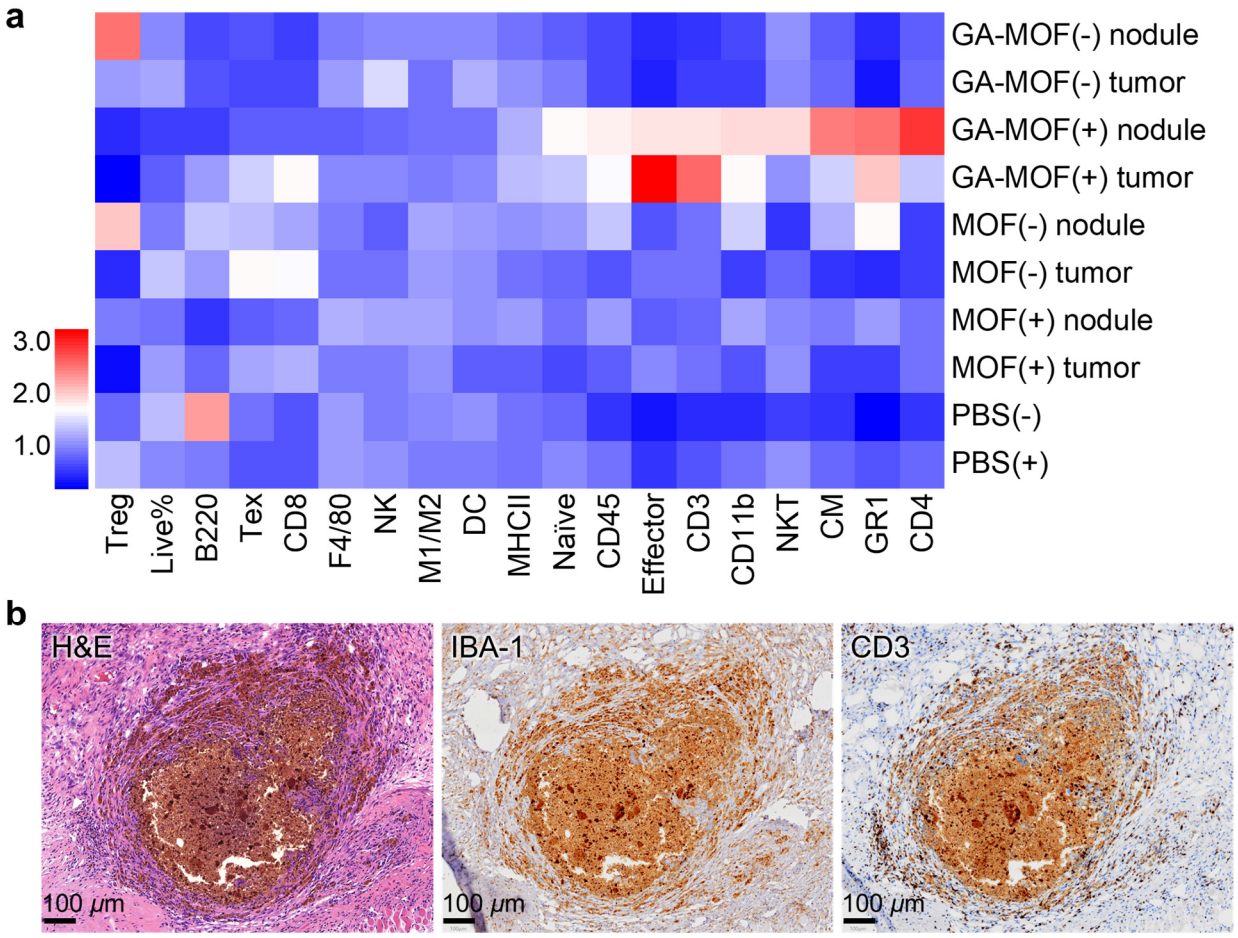

Figure 7-18. GA-MOF forms ALS and induces immune hotspots with RT. (a) Heatmaps showing immune profiles of tumors and nodules in different treatment groups quantified by flow cytometry (*N*=3). T_{reg}, regulatory T cells. Live%, percentages of live cells in total cells. B220, B cells. T_{ex}, exhausted T cells. CD8, cytotoxic T cells. F4/80, macrophages. NK, natural killer cells. M1/M2, the ratio of M1 macrophages to M2 macrophages. DC, dendritic cells. MHCII, $MHCII^{+}$ myeloid cells. Naïve, naïve T cells. CD45, leukocytes. Effector, T effector cells. CD3, T cells. CD11b, myeloid cells. NKT, natural killer T cells. CM, central memory T cells. GR1, granulocytes. CD4, helper T cells. The color scheme is displayed in a linear scale. (b) Histological slides of the intratumoral nodule induced by GA-MOF(+) excised from tumor-bearing mice 14 days after *i.t.* injection. The slides were stained with H&E (left, morphology), IBA-1 (middle, phagocytes), and CD3 (right, T cells). Scale bars=0.1 mm.

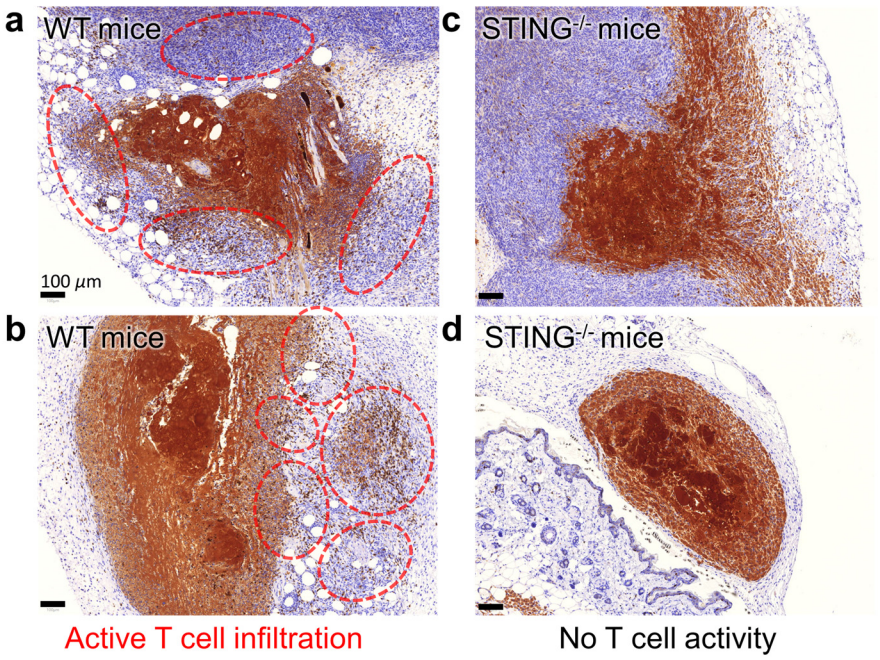

Figure 7-19. Histological observation of immune infiltration near ALS in STING$^{-/-}$ mice. (a-b) Active T cell infiltration around ALS observed in CD3 staining of MC38 tumors and subcutaneous nodule from WT B6 mice injected with GA-MOF. (b) Bare T cell infiltration around ALS in CD3 staining of MC38 tumors and subcutaneous nodules from STING$^{-/-}$ mice injected with GA-MOF (scale bar = 100 μm).

7.2.5 GA-MOF Elicits Antitumor Effects and Activates the TME

We evaluated the antitumor efficacy of GA-MOF in subcutaneous MC38, CT26, Panc02, and SCC7 models. Since different tumor models had different sensitivity to RT, we used 2 Gy by 3 fractions for CT26, 3 Gy by 3 fractions for Panc02 and SCC7, and 4 Gy by 3 fractions for MC38. GA(+) moderately slowed tumor growth with TGI values of 53-64% in the four tumor models. MOF(+) significantly slowed tumor growth with TGI values of 71-90%. The simple combination of GA and MOF(+) gave a TGI of 79% in the MC38 model (**Table 7-3**). In stark contrast, GA-MOF(+) treatment synergized RT-RDT effects and STING activation to greatly enhance antitumor efficacy with TGI values of 82-98% (**Figure 7-20a-d**). One out of 8 CT26 tumor-bearing mice and 5 out of 7 MC38 tumor-bearing mice were cured after GA-MOF(+) treatment. GA-MOF(-)

barely inhibited tumor growth. Superb antitumor efficacy and steady body weights (**Figure 7-20e-h**) of GA-MOF(+)-treated mice demonstrated GA-MOF as a biocompatible nanoradiosensitizer for synergistic radiosensitization and STING activation.

Table 7-3. TGI values of different treatment groups in four different subcutaneous murine cancer models.

Treatment	$TGI_{(MC38)}$	$TGI_{(CT26)}$	$TGI_{(Panc02)}$	$TGI_{(SCC7)}$
PBS(+)	0.61	0.58	0.61	0.50
GA(+)	0.64	0.64	0.53	0.61
MOF(+)	0.71	0.83	0.71	0.75
GA-MOF(+)	0.98	0.96	0.82	0.92
GA-MOF(-)	0.09	N/A		
GA+MOF(+)	0.79			

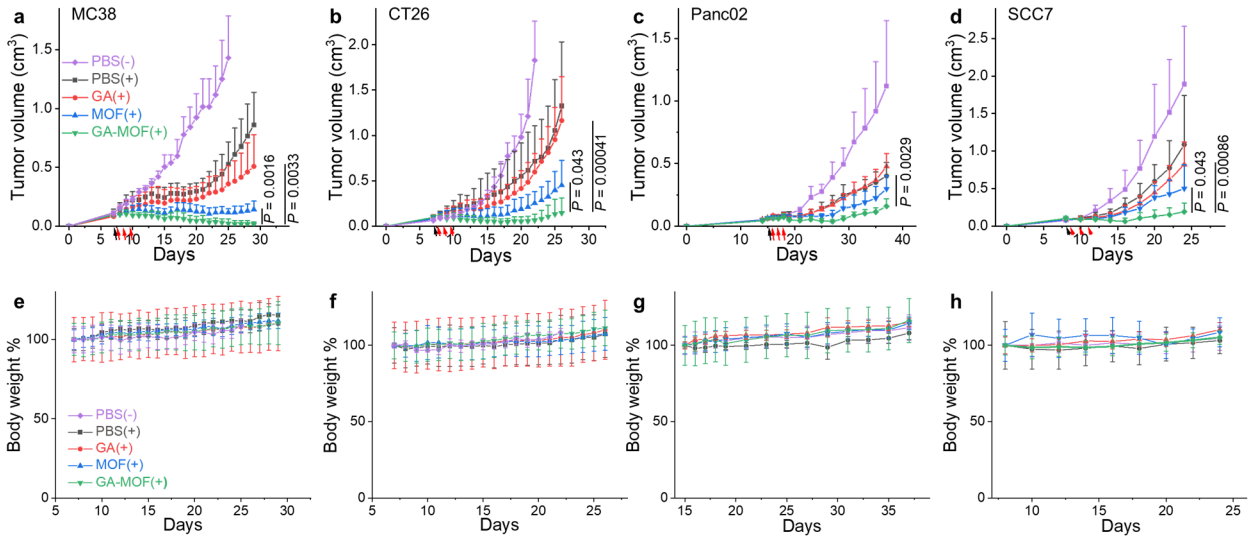

Figure 7-20. Antitumor efficacy and body weights after different treatments. (a-d) Growth curves of subcutaneous (a) MC38, (b) CT26, (c) Panc02, and (d) SCC7 tumors in different treatment groups (ANOVA with Tukey test, *N*=7 for MC38, *N*=8 for CT26, *N*=5 for Panc02, *N*=6 for SCC7). The black arrow indicates *i.t.* injection, and the red arrows indicate X-ray irradiation. (e-h) Body weight trends of MC38 tumor-bearing (e) C57BL/6, (f) CT26 tumor-bearing BALB/c, (g) Panc02 tumor-bearing C57BL/6, and (h) SCC7 tumor-bearing C3H mice in different treatment groups.

To reveal early changes in the TME, we quantified cytokines in tumor lysates and performed immune profiling of MC38 tumors by flow cytometry 3 days post-treatment (day 13). GA-MOF(+) induced significantly more secretion of IFN-β than GA(+) or PBS(+), but downregulated TGF-β in the tumors (**Figure 7-21**).

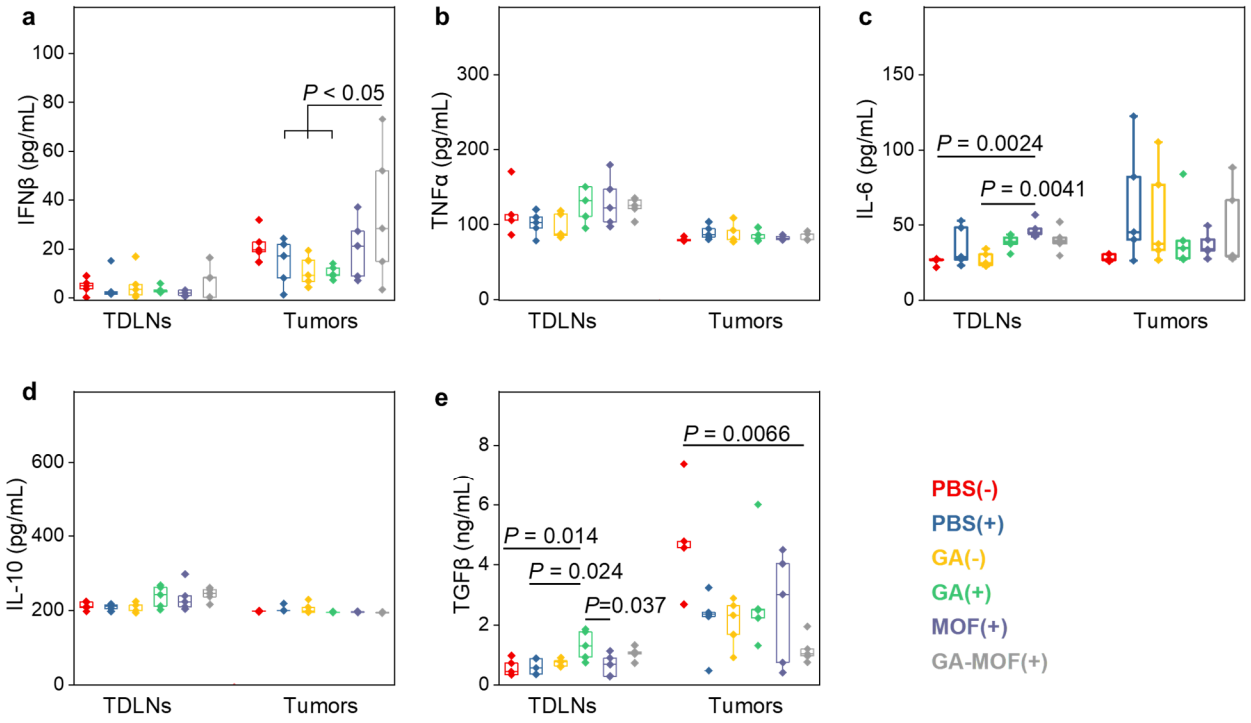

Figure 7-21. Intratumoral cytokine levels after different treatments. Intratumoral concentrations of (a) IFN-β, (b) TNF-α, (c) IL-6, (d) IL-10, and (e) TGFβ in the excised MC38 tumors 3 days after the last RT dose (*N*=5).

MOF(+)- and GA-MOF(+)-treated tumors showed >9-fold higher infiltration of DCs ($CD45^+CD11b^+CD11c^+$) than other groups (**Figure 7-22**), likely resulting from the enhanced DC differentiation from monocytes and upregulation of CD11c in granulocytes by RT-RDT.[11, 21-22] Furthermore, GA-MOF(+) induced 3.4-fold more DC infiltration than MOF(+). The upregulation of MHCII and CD45, together with the downregulation of naïve T-cell marker in the GA-MOF(+) group (**Figure 7-22**), indicated enhanced antigen presentation and T-cell maturation.

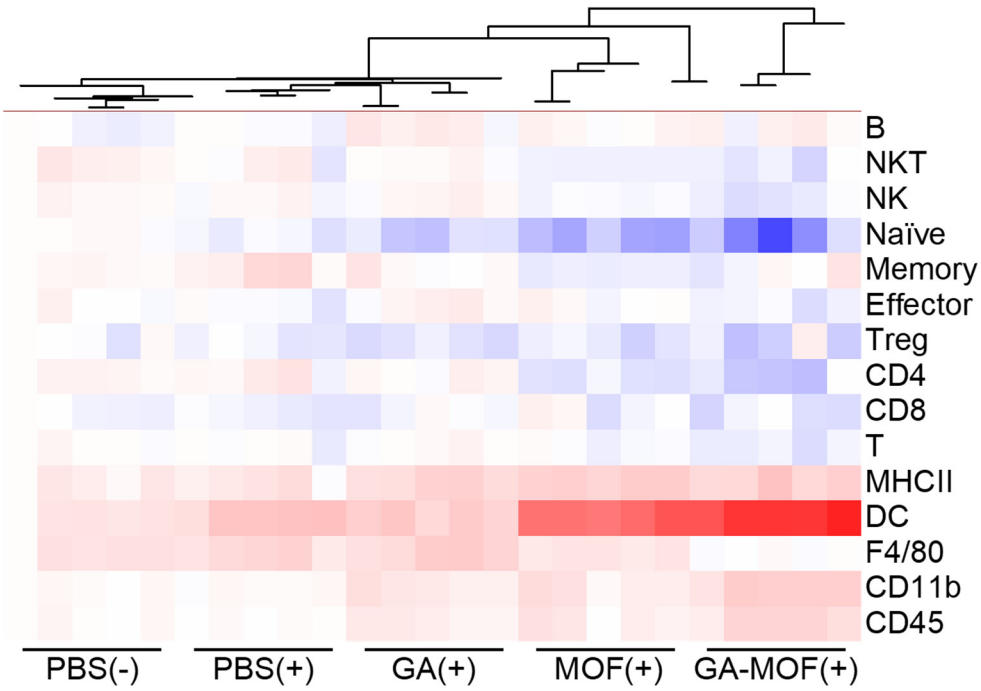

Figure 7-22. Immune profiling. Heat maps with dendrograms showing immune cell infiltration in tumors on day 13 (3 days after the last RT) quantified by flow cytometry (*N*=5). The color scheme shows $\log_{10}$ fold change. The hierarchical clustering was done by Origin Pro Software with HeatMapDendrogram plug-in.

To understand the synergistic effects of STING activation and RT-RDT effects on local tumor regression, we performed TME screening by extracting mRNA from SCC7 tumors for NanoString analysis. Gene Set Analysis (GSA) revealed that GA-MOF(+) showed higher scores for innate and adaptive immune responses than MOF(+) and GA-MOF(-) (**Figure 7-23**). In particular, GA-MOF(+) upregulated IFN, proinflammatory cytokines, phagocytosis-related transporter functions, antigen processing and presentation, DC and macrophage functions, and T/B cell functions.

Between MOF(+) and GA-MOF(+)-treated tumors, 51 genes passed the threshold of the nCounter PanCancer Immune Profiling Panel with ≥1.5-fold expression changes and adjacent *p* values (p_{adj}) less than 0.05 (**Figure 7-23**). Compared to MOF(+), GA-MOF(+) increased gene expression downstream of IFN, including radical S-adenosyl methionine domain-containing

protein 2 (*Rsad2*, 6.09-fold) and IFN-stimulated gene 20 (*Isg20*, 2.47-fold), and enhanced infiltration and migration of DCs (**Figure 7-23**), as demonstrated by upregulation of tyrosine-protein kinase *Lyn* (1.92-fold), solute carrier family 11-member 1 (*Slc11a1*, 2.91-fold), C-X-C chemokine receptor type 4 (*Cxcr4*, 3.88-fold), and C-C chemokine ligand 5 (*Ccl5*, 1.84-fold).[36-39] GA-MOF(+) treatment upregulated *Cd14* (3.42-fold), indicating enhanced differentiation of monocytes into DCs.[40] The expressions of cytokine/chemokine-related genes also showed significant changes. GA-MOF(+)-treated tumors upregulated TNF superfamilies, including *Tnfrsf13b*, *Tnfrsf1b*, *Tnfsf12*, and *Tnfaip3*, by >1.8-fold over MOF(+) group. Similar upregulation was observed in C-X-C chemokine ligand 1 (*Cxcl1*, 4.13-fold), *Ccl4* (13.06-fold), *Il1b* (6.72-fold), Pro-platelet basic protein (*Ppbp*, 6.97-fold), chemokine receptor-like 2 (*Ccrl2*, 8.63-fold), *Cxcl2* (12.84-fold), and *Ccl3* (10.61-fold). Inflammasome pathways were also activated with upregulation of *Nlrp3* (4.01-fold), *Il1b*, IL1 receptor type 2 (*Il1r2*, 6.42-fold), IL1 receptor-associated kinase 3 (*Irak3*, 3.87-fold), and nitric oxide synthase 2 (*Nos2*, 4.18-fold) in GA-MOF(+)-treated tumors. These changes in cytokines/chemokines reflected inflammatory responses of macrophages and active recruitment of leukocytes.[41] STING activation could reprogram tumor vasculature.[42-43] Angiogenesis-related genes were activated in GA-MOF(+)-treated tumors, including *Serpinb2* (9.78-fold), thrombomodulin (*Thbd*, 2.81-fold), and kinase insert domain receptor (*Kdr*, 2.90-fold). The complement system is essential for foreign body clearance and the removal of damaged cells in the innate immune system.[44] Upregulation of *Serping1* (2.74-fold) and complement component 3a receptor 1 (*C3ar1*, 2.24-fold) demonstrated dynamic regulation of the complement system, which might be related to cancer cell apoptosis, nodule formation, and MOF trafficking.

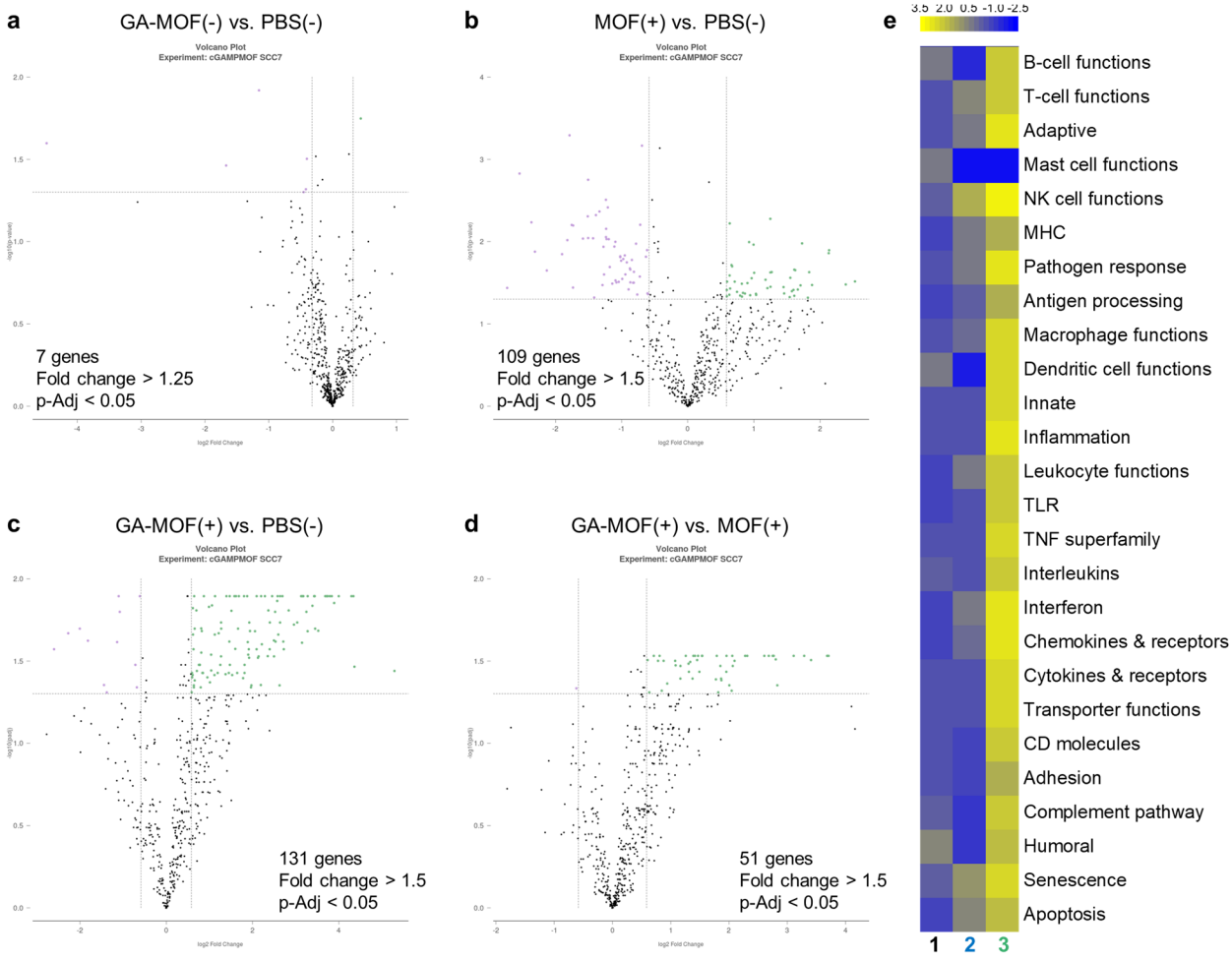

Figure 7-23. NanoString analysis. (a-d) Volcano plots showing genes passing the threshold for differential expressions (*N*=3) of (a) GA-MOF(-) vs. PBS(-), (b) MOF(+) vs. PBS(-), (c) GA-MOF(+) vs. PBS(-), and (d) GA-MOF(+) vs. MOF(+). Upregulation is shown in green dots, and downregulation is shown in purple dots. (e) NanoString GSA heatmap of directed global significance scores of 1: GA-MOF(-) vs. PBS(-), 2: MOF(+) vs. PBS(-), and 3: GA-MOF(+) vs. PBS(-) with the nCounter PanCancer Immune Profiling Panel (*N*=3). The scores quantify the degree to which a group of genes is either upregulated or downregulated in relation to the covariate. They were computed by taking the square root of the average signed squared t-statistic for the genes within the gene set. The t-statistics are obtained from the linear regression used in the analysis of differential expression.

7.2.6 GA-MOF plus αPD-L1 Elicits Robust Systemic Immune Responses

GA-MOF(+) treatment induces intratumoral immune hotspots and synergizes STING activation with RT-RDT for regression of local tumors and amelioration of the TME. Activated immune systems and improved antigen presentation provided excellent contexts for combination with ICB.[45] We established two bilateral tumor models to evaluate the antitumor efficacy and abscopal effects of GA-MOF(+) in combination with a monoclonal αPD-L1 antibody. We treated the primary tumors on the right flanks similarly to the single lateral model and left the distant tumors untreated. The tumor-bearing mice received intraperitoneal (*i.p.*) injections of αPD-L1 (**Figure 7-24**).

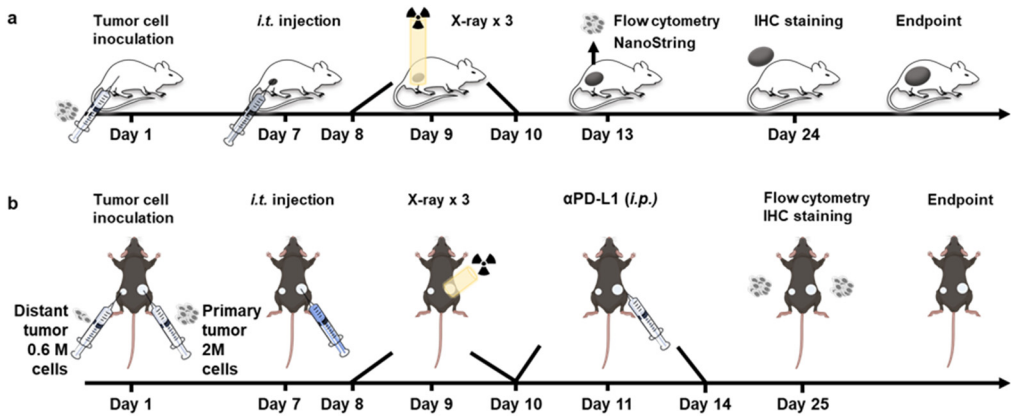

Figure 7-24. Treatment schedules for tumor-bearing mice. (a) The dosing schedule and analysis schedule for single subcutaneous tumor-bearing mice. (b) The treatment schedule for bilateral tumor-bearing mice.

In the bilateral CT26 model, PBS(+) or αPD-L1(+) moderately controlled local tumors with TGI values of <61% and had no effects on distant tumors (**Figure 7-25a,b and Table 7-4**). GA-MOF(+) exhibited excellent control of primary tumor growth with a TGI of 95% but had no effect on distant tumors. The addition of αPD-L1 to GA-MOF(+) not only enhanced local tumor regression to give a TGI of 98% but also controlled distant tumors with a TGI of 66%. The combination of GA(+) and αPD-L1 also moderately controlled both local and distant tumors with

TGI values of 75% and 41%, respectively. This result supports the role of ICB in activating cytotoxic T cells for systemic antitumor effects.

In the bilateral MC38 model, PBS(+) slightly inhibited the growth of primary and distant tumors with TGI values of 66% and 30%, respectively (**Figure 7-25c,d and Table 7-4**). The αPD-L1(+) treatment enhanced local tumor control with a TGI of 82% and moderately controlled distant tumors with a TGI of 47%. The addition of GA to αPD-L1(+) increased TGI values to 88% and 64% for local and distant tumors, respectively. GA-MOF(+) showed excellent regression of primary tumor growth with a TGI of 99% but had a modest impact on distant tumors with a TGI of 67%. Combination of GA-MOF(+) with αPD-L1 completely eradicated primary (100% TGI) and regressed distant tumors with a TGI of 93% and a 50% cure rate. The combination regimen did not show side effects in both models (**Figure 7-26**).

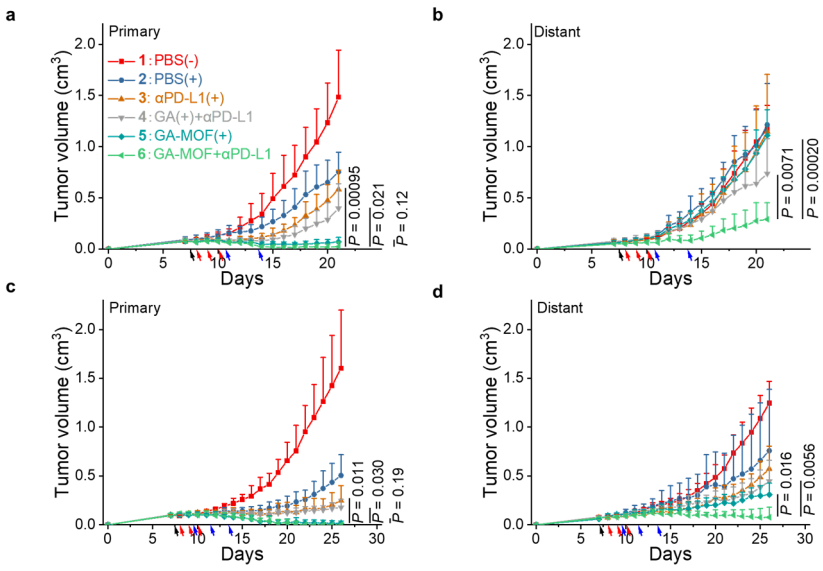

Figure 7-25. GA-MOF(+) plus αPD-L1 induces systemic antitumor immunity. (a) Primary tumor growth curves and (b) distant tumor growth curves of bilateral CT26 tumor-bearing BALB/c mice in different treatment groups (N=6). (c) Primary tumor growth curves and (d) distant tumor growth curves of bilateral MC38 tumor-bearing C57BL/6 mice in different treatment groups (N=6). The black arrow indicates particle injection; the red arrows indicate X-ray irradiation; the blue arrows indicate *i.p.* injection of αPD-L1.

Table 7-4. TGI values of different treatment groups in the CT26 and MC38 bilateral tumor models.

Cell Line	CT26		MC38	
Treatment	**$TGI_{(primary)}$**	**$TGI_{(distant)}$**	**$TGI_{(primary)}$**	**$TGI_{(distant)}$**
PBS(+)	0.56	-0.02	0.66	0.30
αPD-L1(+)	0.61	0.03	0.82	0.47
GA(+)+αPD-L1	0.75	0.41	0.88	0.64
GA-MOF(+)	0.95	-0.09	0.99	0.67
GA-	0.98	0.66	1	0.93

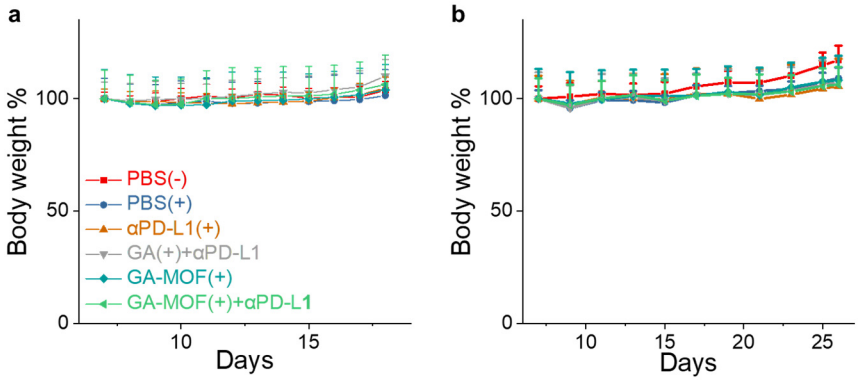

Figure 7-26. Body weight curves of bilateral tumor-bearing mice. Body weight % curves of (a) bilateral CT26 tumor-bearing BALB/c mice and (b) bilateral MC38 tumor-bearing C57BL/6 mice in different treatment groups (*N*= 6).

Flow cytometric profiling of immune cells at the late stage (day 25) showed that GA-MOF(+) enhanced *i.t.* infiltration of adaptive immune cells, particularly memory T cells, $CD8^+$ cytotoxic T cells, and NKT cells (**Figure 7-27a**). GA-MOF(+) plus αPD-L1 further enhanced systemic immune responses with increased effector T cells and memory T cells in the distant tumors (**Figure 7-27b**). The reduced T_{reg} populations in the primary and distant tumors of GA-MOF(+) and GA-MOF(+) plus αPD-L1 groups (**Figure 7-27b**) implied a more active T cell-dependent antitumor effect. Interestingly, the percentages of myeloid cells, including the $GR1^+$ population and macrophages, increased in the distant tumors of GA-MOF(+) and GA-MOF(+) plus αPD-L1

groups (**Figure 7-27b**). The enhanced infiltration of innate immune cells is consistent with the amelioration of immunosuppressive TMEs and active immune clearance of tumor cells.

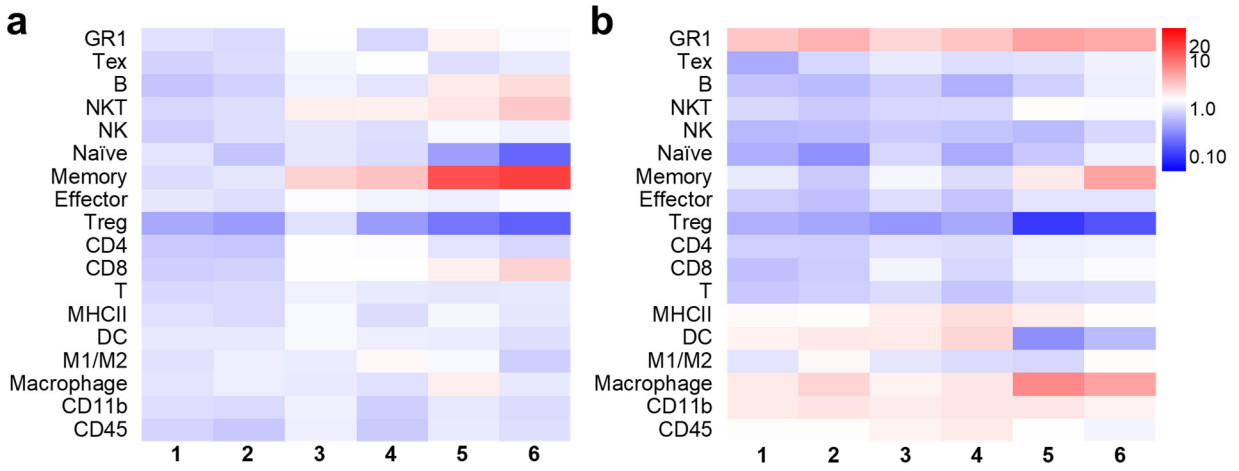

Figure 7-27. Immune profiling of bilateral tumors. Heat maps showing immune cell infiltration in (e) primary tumors and (f) distant tumors from bilateral MC38 tumor-bearing C57BL/6 mice on day 25, as quantified by flow cytometry (N=6). The color scheme is displayed in a $\log_{10}$ scale.

Analysis of IBA-1 and CD3 markers revealed spatial distributions of innate and adaptive immune cells in the primary and distant tumors. GA-MOF(+) plus αPD-L1 further increased T-cell infiltration without impacting the innate immune populations in distant MC38 tumors (**Figure 7-28a**). This result indicates that GA-MOF(+) plus αPD-L1 reverses immunosuppression to enhance immune cell infiltration and antitumor responses.

We also performed ELISpot assays to assess antigen-specific immune responses of T cells. Splenocytes were isolated from bilateral CT26-bearing BALB/c mice and bilateral MC38-bearing C57BL/6 mice and stimulated with tumor-specific peptide antigens AH1 (SPSYVYHQF) and KSP (KSPWFTTL), respectively. In both models, GA-MOF(+) plus αPD-L1 showed significantly more SFC than GA-MOF(+) or GA(+) plus αPD-L1, indicating enhanced adaptive immunity to produce more IFN-γ-generating splenocytes and stronger immune memory effects (**Figure 7-28b,c**). The enhanced recognition of tumor antigens correlated well with improved antigen presentation

(**Figure 7-23e**) and increased infiltration of memory T cells in the tumors after GA-MOF(+) plus αPD-L1 treatment (**Figure 7-27a,b**). These results show that the synergistic combination induces an inflammatory and T-cell infiltrated TME and activates systemic antitumor immune responses for abscopal effects.

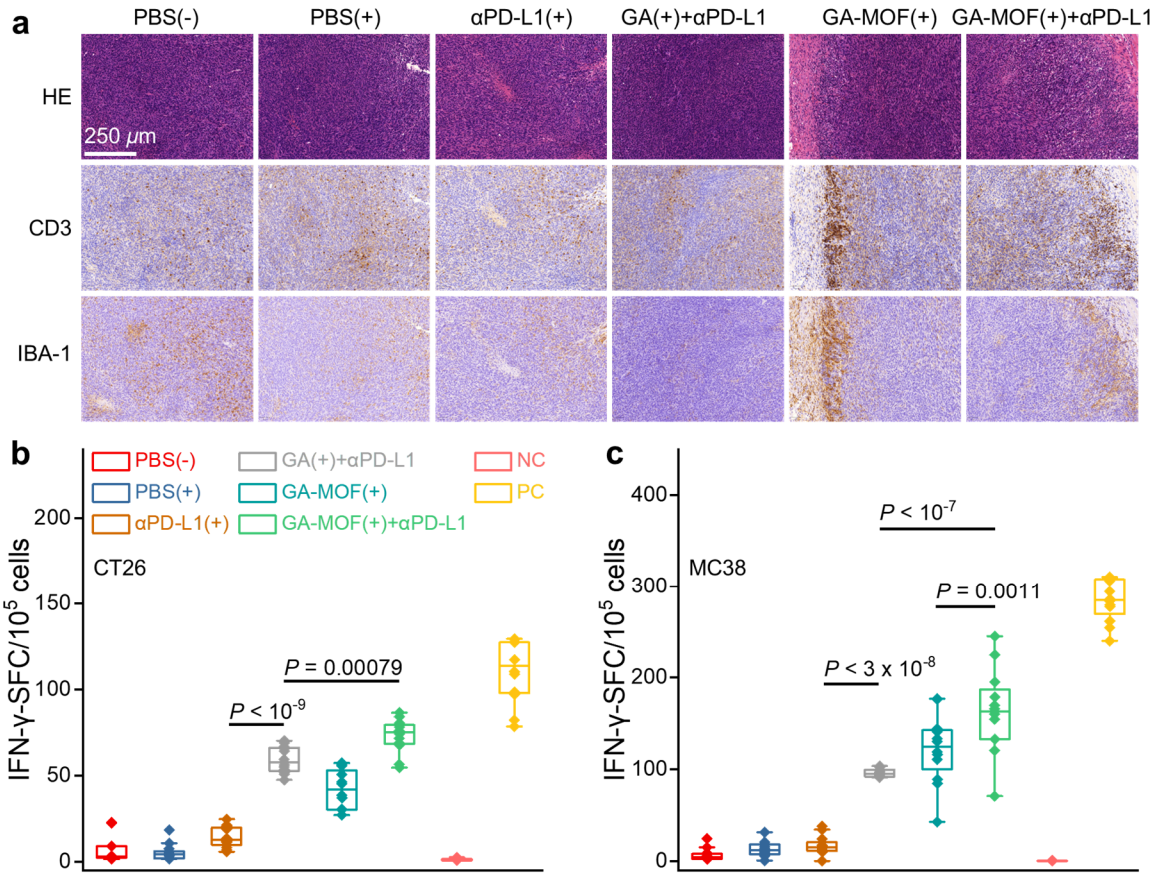

Figure 7-28. GA-MOF+αPD-L1 elicits tumor-specific immune responses at distant sites. (a) H&E staining (top) of viable cells and CD3 (middle) and IBA-1 (bottom) IHC staining of pan-macrophage cells and T cells, respectively, in distant MC38 tumors. Scale bar=250 μm. (b,c) ELISpot assays detecting (b) CT26 tumor-specific and (c) MC38 tumor-specific IFN-γ secreting splenocytes. The splenocytes from CT26-bearing BALB/c and MC38-bearing C57BL/6 mice were stimulated with AH1 and KSP, respectively. NC, negative control with no stimulants; PC, positive control stimulated by anti-CD3e and anti-CD28 antibodies; N=6.

7.2.7 Discussion

Although RT has been in clinical practice for over a century, non-toxic radiosensitizer has yet to be approved by the FDA.[46] Chemotherapeutics such as cisplatin, paclitaxel, and gemcitabine are used in combination with RT to enhance antitumor efficacy, but these chemoradiotherapy regimens cause debilitating adverse effects.[47-48] Oxygen mimetics and hypoxia-targeting reagents have been reported to enhance RT in preclinical models, but they failed to demonstrate clinical benefits in human patients.[6]

By absorbing more X-rays, high-Z particles increase ionizing events, generation of reactive radicals, and DNA damage by RT.[49] This mode of radiosensitization requires very high *i.t.* concentrations of high-Z particles to be effective, which cannot be achieved with existing systemic drug delivery.[50-53] As a result, the nanoradiosensitizers in clinical testing are administered by *i.t.* injection to achieve high local concentrations for cancer killing.[54] However, little is known about the trafficking and clearance of these particles and their induced immune effects.[55-59]

As a bifunctional particle, GA-MOF comprises MOF for radiosensitization and the endogenous STING agonist GA for STING activation. The STING pathway elicits antitumor functions such as type-I IFN-mediated T-cell dependent tumor eradication, modulation of the vasculature, and augmentation of adaptive immunity by developing tertiary lymphoid structures.[42, 60-61] In this work, we determined the uptake of MOF-based nanoradiosensitizers by different cell populations and their spatial-temporal distributions in tumors. One day post *i.t.* injection, 2/3 of MOF is uptaken by cancer cells, and the rest of MOF is uptaken by innate immune cells, including neutrophils, monocytes, and macrophages. MOF-mediated RT-RDT is non-toxic to terminally differentiated immune cells but significantly inhibits cancer cell proliferation. The MOF particle distribution in cancer cells ensures efficient radiosensitization for cancer cell killing, while MOF

uptake by immune cells provides an excellent avenue to deliver innate immune agonists. Indeed, GA-MOF prolongs GA retention in tumors to enhance STING activation of innate immune populations and facilitate antitumor immunity.

GA-MOF(+) induces intratumoral immune hotspots and efficiently inhibits tumor growth *in vivo*. We first observed nodule formation after subcutaneous injection and *i.t.* injection of GA-MOF to rats and mice, respectively. These nodules contained MOF in the center and innate and adaptive immune cells in the periphery, effectively forming a separated immune space from the rest of the tumor. These ALS are dominated by innate immune cells. Although both MOF and GA-MOF can trigger nodule formation in the tumors, only GA-MOF(+) results in an immunologically "hot" TME with immunostimulatory signatures. The immune hotspots in the tumors disrupt the immunosuppressive TME to elicit antitumor immunity. GA-MOF(+) treatment suppresses tumor growth in four tumor models, including immunologically "cold" Panc02 pancreatic cancer and SCC7 head and neck cancer models. Thus, GA-MOF(+) creates immune hotspots to turn "cold" TME "hot" for enhanced anticancer effects.

Figure 7-29 summarizes our hypothesis for immune hotspot formation and its role in antitumor immunity. As a foreign object, MOF triggers the complement pathway and attracts immune cells. Adsorption of albumin and other interstitial proteins on the MOF surface triggers immune cell recognition and infiltration.[55] Significant upregulation of complement-related genes, chemokines, and adhesion molecules causes active and continuous recruitment of leukocytes into MOF-treated tumors, leading to the formation of ALS. Upon low-dose X-rays, MOF(+) induces ICD of cancer cells and generates autologous tumor-specific antigens *in situ*.[23, 45] The released GA from GA-MOF induces robust and sustained STING activation and facilitates DC infiltration, antigen processing, and antigen presentation.

By inducing ALS formation, GA-MOF not only serves as a nanoradiosensitizer to kill cancer cells and expose tumor-specific antigens *in situ*, but also acts as an exogenous nano-adjuvant to induce immune cell infiltration and enhance antigen presentation.[62] STING activation can also induce vascular disruption and reprogram the tumor protective mechanisms that otherwise inhibit immune cell infiltration. Most importantly, sustained STING activation results in STING-IFN-T-cell-dependent responses. GA-MOF(+) treatment improved T cell function via antigen presentation, as evidenced by enhanced infiltration of memory T cells and improved tumor antigen-specific antitumor responses. The combination of GA-MOF(+) with αPD-L1 extends this local treatment regimen to systemic antitumor effects. We used bilateral tumor models to mimic patients with distant metastases that are not amenable to localized RT treatment. Blockade of the PD-1/PD-L1 axis not only reinvigorates T cells and eradicates local tumors, but also reduces the infiltration barrier of T cells to distant tumors and elicits robust abscopal effects.

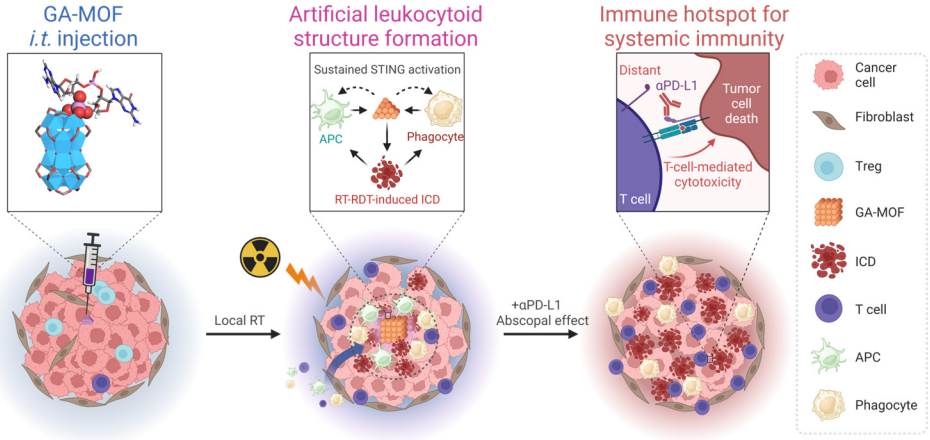

Figure 7-29. Proposed mechanism for systemic antitumor responses induced by RT treatment of ALS.GA-MOF attracts infiltration of phagocytes and antigen-presenting cells (APCs). Sustained GA release activates STING in the local TME. MOF-mediated RT-RDT induces ICD of cancer cells to expose antigens for antigen processing and presentation. After GA-MOF(+) treatment, the distant untreated tumor also exhibits active immune infiltration with tumor-specific immune responses. Combination with ICB reinvigorates T cells for adaptive clearance of tumors.

7.3 Conclusions

In this Chapter, we designed a bifunctional nanoplatform for simultaneous STING activation and radiosensitization. GA-MOF prolongs GA retention in tumors and elicits strong and sustained STING activation. GA-MOF forms ALS rich in immune cells, which are converted to immune hotspots upon X-ray irradiation. GA-MOF(+) greatly ameliorates the immunosuppressive TME and demonstrates great local tumor control in four tumor models. Further combination with αPD-L1 elicits a robust abscopal effect, extending this local tumor control to systemic antitumor responses. With the ability to induce ALS, MOFs can not only enhance RT but also provide a unique mechanism for immune cell infiltration and *in situ* vaccination. MOFs thus represent a unique nanoplatform for developing innovative cancer treatments.

7.4 Methods

Synthesis and characterizations of MOF and GA-MOF. DBP-Hf MOF was synthesized according to a previous literature report.[11] Briefly, to a 1-dram glass vial, 2 mg $HfCl_4$, 1 mg H_2DBP, 75 μL AA, and 1 mL DMF were added. The mixture was sonicated and heated in a 90 °C oven for 3 days. The resulting dark brown solid was collected by centrifugation, washed with DMF and ethanol, and stored as ethanol dispersions in the dark. TFA-modified DBP-Hf (MOF) was then synthesized as previously reported.[19] DBP-Hf suspension in EtOH was washed sequentially with CH_3CN and benzene by sonication and centrifugation. Hf_{12}-DBP-Hf suspension in benzene (2 mM) and a 10-fold excess of TFA-TMS were stirred for 12 hours to obtain MOF. The suspension was washed with CH_3CN and EtOH sequentially and stored in EtOH for further use. GA-MOF was prepared by vortexing a mixture of MOF at a Hf concentration of 2.5 mM and 1 μg 2'3'-GA in 100 μL nuclease-free water for 15 minutes. The concentrations of Hf were detected by an

Agilent 7700x ICP-MS and analyzed using an ICP-MS Mass Hunter version 4.6 C.01.06. The crystallinity of MOF and GA-MOF was examined by PXRD on a Bruker D8 Venture diffractometer using a Cu Kα radiation source (λ = 1.54178 Å). The sizes and ζ-potentials were measured by a Malvern Nano Series ZetaSizer. The morphologies were observed by TEM on a TECNAI Spirit TEM and AFM on a Bruker V/Multimode 8 instrument.

Release profiles of GA-MOF. The concentration of GA was quantified by LC-MS on an Agilent 6540 Q-Tof MS-MS with 1290 UHPLC (5 μm Agilent C_{18} reverse phase column). GA-MOF was freshly prepared and redispersed in the same volume of 10× PBS, 1× PBS, and 0.1× PBS (100 μL/tube) in 1.5 mL Eppendorf tubes (3 replicates for each time point), respectively. The ep tubes were transferred onto a 37 °C heat block, and the supernatants (80 μL/tube) were collected at 0 h, 1 h, 2 h, 4 h, 8 h, 12 h, 24 h, 36 h, and 48 h by centrifugation at 14000 g. The supernatants were directly analyzed by LC-MS. The release percentages were fitted by the Hill function in Origin Lab software.

X-ray irradiation. For test tube and *in vitro* experiments, an RT250 orthovoltage X-ray machine (Philips, USA) with fixed setting at 250 kVp, 15 mA, and a built-in 1 mm Cu filter was used (dose rate = 0.02564 Gy/second). For irradiating animals *in vivo*, an X-RAD 225 image-guided biological irradiator (Precision X-ray Inc., USA) was used with voltage at 225 kVp, current at 13 mA, 0.3 mm Cu filter, and 15 mm collimator (dose rate = 0.04167 Gy/second).

GR assay. Cells were first seeded in 6-well plates at a density of 1×10^5 cells/well and cultured overnight. The cells were incubated with PBS or MOF (50 μM Hf) for 8 hours, and then irradiated with 0, 2, 4, or 8 Gy X-ray. The cells were washed with PBS twice and then trypsinized to afford single-cell suspensions. The cells were counted, diluted to 1500-3000 cells/mL, and reseeded in 24-well plates. The plates were put in an IncuCyte S3 live-cell analysis system (Essen BioScience)

and continuously observed by a 10× objective in phase contrast mode for up to 5 days at a 6-hour interval. The phase contrast images were collected and analyzed by IncuCyte 2021A software to obtain time-dependent confluence in each well (25 tiles per well, 6 replicates for each treatment group). $GIF_{10\%}$ was calculated based on a previous literature report.[26]

Immunofluorescence microscopy

All antibodies used in immunofluorescence experiments were purchased from Cell Signaling Technology except anti-mouse CD11c-PE/Cy5.5 (Invitrogen). Acti-stain™ 488 was purchased from Cytoskeleton, Inc. Hoechst 33342, and ProLong™ glass antifade mountant was purchased from ThermoFisher Scientific. The cells were seeded in 6-well plates or 12-well plates with a coverslip at the bottom of each well. The cells were treated with different conditions and fixed with 4% paraformaldehyde (pH = 7.2) at room temperature for 20 minutes. For intracellular staining, the cells were washed with PBS, blocked, and permeabilized by 5% FBS + 0.3% Triton-X in PBS at room temperature for 1 hour. After blocking the cells were incubated with primary antibodies in 1% BSA + 0.3% Triton-X in PBS at 4°C overnight (phospho-STING (Ser365) (D1C4T) rabbit mAb #62912, 1:200). The cells were then washed by PBS and incubated with secondary antibodies in 1% BSA + 0.3% Triton-X in PBS at room temperature for 1 hour (anti-rabbit IgG (H+L), F(ab')2 fragment (Alexa Fluor® 647 conjugate) #4414, 1:1000). For staining of surface markers, the cells were blocked by PBS with 5% FBS and stained with dye-conjugate antibody 1:100 in PBS with 1% BSA. Both cells were washed by PBS and further incubated with 1:500 Acti-stain™ 488 and 1:3000 Hoechst 33342 in PBS for 30 min. After washing with PBS, the coverslips were mounted on glass slides with ProLong™ glass antifade mountant, cured at 4°C overnight, sealed by nail polish, and observed on a Leica Stellaris 8 confocal microscope. The data were analyzed with Fiji ImageJ (NIH).

Isothermal titration calorimetry. The interaction between GA and MOF was analyzed on a MicroCal iTC_{200} system (Malvern Instruments) equipped with reference and sample cells (V = 400 μL). All titrations were carried out using a 40 μL syringe at 298.15 K with a stirring rate of 250 rpm. The aqueous dispersion of MOF (900 μM Hf) was titrated with 300 μM GA aqueous solution. A first injection of 0.4 μL was followed by 20 injections of 2 μL at intervals of 150 s. Data analysis was performed using the MicroCal iTC_{200} software, and all data were fitted to an independent single-site model.

Bone marrow-derived dendritic cells and macrophages. 6 to 8-week-old female C57BL/c mice were euthanized, and bone marrow cells were flushed out from the femur and tibia using insulin syringes with RPMI-1640. Red blood cells were lysed by sterile ACK buffer (Corning), and the rest of the cells were cultured in RPMI-1640 full medium + 20 ng/mL recombinant mouse granulocyte-macrophage colony-stimulating factor (GM-CSF, R&D Systems) + 10 ng/mL recombinant murine interleukin-4 (IL-4, PeproTech). On day 2, half of the medium was discarded, and fresh prewarmed medium with 40 ng/mL GM-CSF and 20 ng/mL IL-4 was added. On day 4, the entire medium was discarded and replaced by fresh and warm medium with 20 ng/mL GM-CSF and 10ng/mL IL-4. On day 8, the semi-suspended and loosely attached cells were collected by gently pipetting, and the medium suspension was collected as BMDCs. The adherent cells were gently scraped off by cell scrapers as BMDMs. The purity of the cells was confirmed by flow cytometry with CD11c-PE/Cy5.5 (N418) and F4/80-PerCP/Cy5.5 (BM8) antibodies, respectively. The phosphorylated STING and IRF-3 were also stained and visualized for BMDCs and Raw264.7, respectively.

STING activation *in vitro*. THP1-Dual™ KO-MyD88 reporter cells were used to quantify STING activation by GA and GA-MOF *in vitro*. The cells were seeded in 96-well plates at a

density of 2×10^5 cells/mL (N=3), and up to 139.2 μM GA or GA-MOF was added and incubated for 24 hours. The stimulation of the IRF pathway was quantified by QUANTI-Luc (InvivoGen) assay on a Synergy HTX plate reader. The cytokines secreted in the medium were quantified by LumiKine™ Xpress mIFN-β 2.0 (InvivoGen), TNFα mouse ELISA kit, and IL-6 mouse ELISA kit (Invitrogen).

Phagocytosis. In 6-well plates with collagen-coated coverslips, BMDCs or BMDMs (1 mL RPMI-1640 full medium, 500,000 cells/well) were seeded and incubated at 37 ℃. Eight hours later, CFSE-labeled MC38 cells (1 mL RPMI-1640 full medium, 250,000 cells/well) were added together with GA (0.1 μg/mL), MOF (25 μM Hf), or GA-MOF (0.1 μg/mL GA and 25 μM Hf). Four hours later, the plates were irradiated with 2 Gy X-ray and incubated for another 24 hours. The cells were then fixed by 4% PFA and stained with CD11c-PE/Cy5.5 (N418) or F4/80-PerCP/Cy5.5 (BM8) to visualize BMDCs or BMDMs with a Leica Stellaris 8 confocal microscope, respectively.

Cell viability assays. The cytotoxicity of MOF and GA-MOF to immune cells was evaluated in splenocytes, BMDMs, and BMDCs by CellTiter 96 AQ_{ueous} One Solution Cell Proliferation Assay (MTS assay, Promega, USA). The cells were seeded in 96-well plates at a density of 10,000 cells/well and cultured overnight. MOF or GA-MOF was added at a Hf concentration of 0, 0.2, 0.4, 0.8, 1.6, 3.1, 6.3, 12.5, 25, 50, and 100 μM and incubated for 8 hours. The cells were then irradiated with 0-8 Gy X-ray and allowed to incubate for another 3 days (N=3). The cell viability was determined by MTS assay.

Pharmacokinetics of GA-MOF in rats. SD/CD female rats (6 weeks, 160–200 g) were anesthetized and subcutaneously injected with GA-MOF. The rats were anesthetized at 5 min, 30 min, 1 h, 2 h, 4 h, and 24 h, and the blood was drawn from the retro-orbital plexus. The whole

blood was immediately centrifuged at 2,000 g at 4 ℃ for 15 minutes. The clear top layer was immediately transferred, aliquoted into 1.5 mL ep tubes, and tested by GA ELISA Kit (Cayman Chemical) for GA concentration.

GA retention in tumors. 6~8-week-old CT26-bearing BALB/c mice were anesthetized and *i.t.* injected with GA-MOF in 20 μL saline. The mice were anesthetized at 5 min, 30 min, 1 h, 2 h, 4 h, 24 h, 48 h, 96 h, and 168 h, and the blood was drawn by eyeball removal. The mice were then euthanized. The tumors were excised and kept on ice. Each tumor was then immersed in an individual 15 mL ep tube filled with 2 mL 10x PBS (on ice). The tumor tissues were then homogenized with a probe sonicator (500 W, 20 kHz) with 30% power for 1 minute on ice. The mixture was centrifuged at 4 ℃ at 14,000 g for 15 minutes. The supernatants were collected, aliquoted into 1.5 mL ep tubes, and tested by GA ELISA Kit (Cayman Chemical) for GA concentration.

***In vivo* antitumor efficacy.** The antitumor efficacy of GA-MOF was evaluated on subcutaneous CT26 tumor-bearing BALB/c, MC38 tumor- and Panc02 tumor-bearing C57BL/6, and SCC7 tumor-bearing C3H mouse models. For the single tumor model, 2×10^6 CT26 cells, SCC7 cells, MC38 cells, and Panc02 cells were subcutaneously injected into the right flanks. When the tumors reached 75-100 mm^3, MOF (0.5 μmol Hf), GA-MOF (0.5 μmol Hf, 2 μg GA), GA (2 μg GA), or PBS was *i.t.* injected into the mice. Eight hours later, the mice were anesthetized with 2.5 % (v/v) isoflurane/oxygen, and the tumors were irradiated with X-ray at the following doses: CT26, 2 Gy × 3 (N=8); MC38, 4 Gy × 3 (N=7); Panc02, 3 Gy × 3 (N=5); SCC7, 3 Gy × 3 (N=6). The tumor volumes (length×$width^2$/2), body weights, and health conditions of the mice were monitored, and the mice were euthanized according to the protocol limit.

Intratumoral cytokine levels. 6~8-week-old MC38 tumor-bearing C57BL/6 mice were treated in the same way as the efficacy study. Three days after the last RT dose, the mice were euthanized, and the tumors were excised and kept on ice. Each tumor was then immersed in an individual 15 mL ep tube filled with 2 mL RIPA buffer (on ice). The tumor tissues were homogenized with a probe sonicator (500 W, 20 kHz) with 30% power for 30 seconds on ice. The mixture was centrifuged at 4 ℃ at 14,000 g for 15 minutes. The supernatants were collected, aliquoted into 1.5 mL ep tubes, and tested by respective ELISA kits (Invitrogen) for cytokine concentrations.

Abscopal effect. The abscopal effect of GA-MOF plus αPD-L1 was evaluated in two bilateral subcutaneous mouse models. For the bilateral CT26 or MC38 tumor model, 2×10^6 CT26 or MC38 cells were subcutaneously injected into the right flanks, and 8×10^5 CT26 or MC38 cells were injected into the left flanks of BALB/c or C57BL/6 mice, respectively (N=6). When the primary tumors (right) reached 100-125 mm^3, the primary tumors were injected with GA-MOF, GA, or PBS. The mice received X-ray treatment on the primary tumors at 2 Gy × 3 for CT26 and 4 Gy × 3 for MC38. The CT26 model in αPD-L1, GA + αPD-L1, or GA-MOF + αPD-L1 group was *i.p.* injected with 75 μg/mouse αPD-L1 on day 3 and 6 after the first X-ray treatment. The MC38 model in αPD-L1, free GA + αPD-L1, or GA-MOF + αPD-L1 group was *i.p.* injected with 100 μg/mouse αPD-L1 on day 2, 4, and 6 after the first X-ray treatment. The tumor volumes, body weights, and health conditions of the mice were monitored, and the mice were euthanized according to the protocol limit.

Immune cell profiling. MC38 tumor-bearing C57BL/6 mice (N=6) received *i.t.* injections and X-ray doses, and the tumors and TDLNs were harvested on day 13 or day 25 for immune cell profiling by flow cytometry. The tumors and TDLNs were digested by RPMI-1640 + 10% FBS +

0.5 mg/mL collagenase I (Gibco) + 200 μg/mL collagenase IV (Gibco)+ 50 μg/mL Dnase I (Sigma-Aldrich) cocktail at 37 °C for 45 minutes. The digests were gently ground and filtered through sterile cell strainers (40 μm, Corning) to obtain single-cell suspensions. The cells were washed by ice-cold FACS buffer and stained first with eFluor™ 506-Fixable Viability Dye (ThermoFisher Scientific, 1:1000). The cells were then washed with FACS buffer, blocked by anti-CD16/32 antibody (clone 93, 1:100) at 4 °C for 15 minutes, and stained with the following fluorochrome-conjugated rat anti-mouse antibodies 1:200 (1:500 for CD45-BV421) at 4 °C for 45 minutes: CD45-BV421 (30-F11), CD45-AlexFluor488 (30-F11), CD45-PacificBlue (30-F11), CD11b-SB600 (M1/70), CD11b-FITC (M1/70), NK1.1-PE/Dazzole594 (PK130), F4/80-PerCP/Cy5.5 (BM8), Gr-1-PE (RB6-8C5), Gr-1-APC/eFluor780 (RB6-8C5), CD86-PE (GL1), CD206-APC (C068C2), CD11c-PE/Cy5.5 (N418), CD11c-BV421 (N418), MHCII-PE (M5/114.15.2), MHCII-PE/Cy7 (M5/114.15.2), CD3-PE/eFluor610 (145-2C11), CD3-PE/Cy7 (145-2C11), CD3-SB600 (145-2C11), CD4-APC/H7 (GK1.5), CD4-AlexaFluor488 (GK1.5), CD8-PerCP/eFluor710 (53-6.7), CD8-APC/eFluor780 (53-6.7), B220-APC (RA3-6B2), B220-PE/Cy5 (RA3-6B2), CD44-PE (IM7), CD62L-FITC (MEL-14), CD62L-APC (MEL-14), Tbet-PE/Cy5 (4B10), PD1-PE/Cy7 (J43), FoxP3-APC (FJK-16s), CD25-PE (12-0251-82). CD45-BV421 was from BD Bioscience. CD206-PE/Cy7, NK1.1-PE/Dazzole594 and CD3-PE/Cy7 were from BioLegend. Others were from eBioscience. The cells were finally washed and resuspended in FACS buffer and analyzed on an LSR Fortessa 4-15 flow cytometer.

NanoString analysis. SCC7 tumors were digested in the same way as immune cell profiling to afford single-cell suspensions of tumor cells. The RNA was extracted and purified with the Rneasy Mini Kit (QIAGEN). The RNA concentration was normalized to 20 ng/μL in nuclease-free water with a NanoDrop Eight spectrophotometer (Thermo Fisher Scientific). The RNA was

then hybridized with the Gene Expression CodeSet of the nCounter PanCancer Immune Profiling Panel (NanoString) in a thermal cycler (Bio-Rad), and processed and imaged with the nCounter MAX/FLEX system (NanoString). The data was analyzed with ROSALIND.

Immunohistochemistry analysis. For the FFPE samples, the tumors and major organs were harvested from the treated mice, washed with PBS, and fixed with 10% neutral buffer (4% PFA) for 24 hours and 70% ethanol for 24 hours. The tissues were processed, embedded in paraffin, sectioned, and stained (H&E, IBA-1, CD3e) by the Human Tissue Resource Center at the University of Chicago. Briefly, the slides were deparaffinized and rehydrated through xylenes and serial dilutions of ethanol to distilled water. Then the slides were treated with antigen retrieval buffer (S1699, DAKO for CD3e; S2367, DAKO for IBA-1) and heated in a steamer over 97°C for 20 minutes). After washing, the slides were incubated with primary antibodies (anti-CD3, Abcam (ab5690), 1:100; anti-IBA-1, Cell Signaling (E4O4W), 1:600) at room temperature for 1 hour in a wet chamber. The slides were washed with TBS, then CD3 and IBA-1 slides were incubated with biotinylated anti-rabbit IgG (1:200, BA-1000, Vector Laboratories) and anti-rabbit-polymer (Bond Polymer refine Detection, Leica Biosystems, DS9800) at room temperature for 30 minutes, respectively. The antigen-antibody binding was detected by Elite kit (PK-6100, Vector Laboratories) and DAB (DAKO, K3468) system. Tissue sections were then immersed in hematoxylin for counterstaining and e covered with cover glasses. The slides were scanned on a Cri Pannoramic SCAN 40x whole slide scanner by Integrated Light Microscopy Core at the University of Chicago. The images were analyzed by QuPath-0.4.2 software.[63]

IFN-γ ELISPOT assay. A Multiscreen HTS-IP plate (Millipore Sigma) was activated by 70% ethanol, washed with PBS, coated with anti-mouse IFN-γ capture antibody (BD Biosciences) at 37 °C for 8 hours, and blocked with sterile 1% BSA in PBS at room temperature for 2 hours.

The spleens were harvested from the treated bilateral CT26 tumor-bearing BALB/c and MC38 tumor-bearing C57BL/6 mice, and then gently grinded and filtered through sterile cell strainers to afford single cell suspensions. Red blood cells were then lysed by sterile ACK buffer (Corning), and splenocytes were counted and seeded in the plate at a density of 2×10^5 cells/well in RPMI-1640 full medium (6 mice each treatment group and each mouse with 3 replicates). CT26 tumor-associated antigen SPSYVYHQF (AH1) or MC38 tumor-associated antigen KSPWFTTL (KSP) was added to each well at a concentration of 10 μg/mL except for negative control wells. The splenocytes in positive control wells were directly stimulated with anti-mouse CD3Ɛ (145-2C11) and anti-mouse CD28 (37.51) antibodies (eBioscience, 1:1000). The splenocytes were incubated at 37 °C for 48 hours and culture media were discarded. The plates were then washed and incubated with biotinylated anti-IFN-γ detection antibody, streptavidin-HRP conjugate, and AEC substrate following the manufacturer's specification (BD Biosciences). The plate was air-dried and analyzed by a CTL ImmunoSpot® S6 Analyzer.

7.5 References

(1) Chandra, R. A.; Keane, F. K.; Voncken, F. E. M.; Thomas, C. R., Contemporary radiotherapy: present and future. *Lancet* **2021,** *398* (10295), 171-184.

(2) Huang, R.-X.; Zhou, P.-K., DNA damage response signaling pathways and targets for radiotherapy sensitization in cancer. *Signal Transduct. Target. Ther.* **2020,** *5* (1), 60.

(3) Formenti, S. C.; Demaria, S., Systemic effects of local radiotherapy. *Lancet Oncol.* **2009,** *10* (7), 718-726.

(4) Price, J. M.; Prabhakaran, A.; West, C. M. L., Predicting tumour radiosensitivity to deliver precision radiotherapy. *Nat. Rev. Clin. Oncol.* **2023,** *20* (2), 83-98.

(5) Schaue, D.; McBride, W. H., Opportunities and challenges of radiotherapy for treating cancer. *Nat. Rev. Clin. Oncol.* **2015,** *12* (9), 527-540.

(6) Oronsky, B. T.; Knox, S. J.; Scicinski, J., Six Degrees of Separation: The Oxygen Effect in the Development of Radiosensitizers. *Transl. Oncol.* **2011,** *4* (4), 189-198.

(7) Lawrence, T. S.; Blackstock, A. W.; McGinn, C., The mechanism of action of radiosensitization of conventional chemotherapeutic agents. *Semin. Radiat. Oncol.* **2003,** *13* (1), 13-21.

(8) Kuncic, Z.; Lacombe, S., Nanoparticle radio-enhancement: principles, progress and application to cancer treatment. *Phys. Med. Biol.* **2018,** *63* (2), 02TR01.

(9) Xu, Z.; Ni, K.; Mao, J.; Luo, T.; Lin, W., Monte Carlo Simulations Reveal New Design Principles for Efficient Nanoradiosensitizers Based on Nanoscale Metal–Organic Frameworks. *Adv. Mater.* **2021,** *33* (40), 2104249.

(10) Yom, S. S.; Takacsi-Nagy, Z.; Liem, X.; Salas, S.; Debard, A.; Finzi, L.; Vivar, O. I.; Farber, L. A.; Gogishvili, M.; Kristesashvili, G.; Makharadze, T.; Hoffmann, C.; Tourneau, C. L., NANORAY-312: A Phase III Pivotal Study of NBTXR3 Activated by Investigator's Choice of Radiotherapy Alone or Radiotherapy in Combination with Cetuximab for Platinum-Based Chemotherapy-Ineligible Elderly Patients with Locally Advanced HNSCC. *Int. J. Radiat. Oncol. Biol. Phys.* **2022,** *114* (3, Supplement), e313.

(11) Lu, K.; He, C.; Guo, N.; Chan, C.; Ni, K.; Lan, G.; Tang, H.; Pelizzari, C.; Fu, Y.-X.; Spiotto, M. T.; Weichselbaum, R. R.; Lin, W., Low-dose X-ray radiotherapy–radiodynamic therapy via nanoscale metal–organic frameworks enhances checkpoint blockade immunotherapy. *Nat. Biomed. Eng.* **2018,** *2* (8), 600-610.

(12) Lenders, V.; Koutsoumpou, X.; Sargsian, A.; Manshian, B. B., Biomedical nanomaterials for immunological applications: ongoing research and clinical trials. *Nanoscale Adv.* **2020,** *2* (11), 5046-5089.

(13) Barker, H. E.; Paget, J. T. E.; Khan, A. A.; Harrington, K. J., The tumour microenvironment after radiotherapy: mechanisms of resistance and recurrence. *Nat. Rev. Cancer* **2015,** *15* (7), 409-425.

(14) Bakhoum, S. F.; Ngo, B.; Laughney, A. M.; Cavallo, J.-A.; Murphy, C. J.; Ly, P.; Shah, P.; Sriram, R. K.; Watkins, T. B. K.; Taunk, N. K.; Duran, M.; Pauli, C.; Shaw, C.; Chadalavada, K.; Rajasekhar, V. K.; Genovese, G.; Venkatesan, S.; Birkbak, N. J.; McGranahan, N.; Lundquist, M.; LaPlant, Q.; Healey, J. H.; Elemento, O.; Chung, C. H.; Lee, N. Y.; Imielenski, M.; Nanjangud, G.; Pe'er, D.; Cleveland, D. W.; Powell, S. N.; Lammerding, J.; Swanton, C.; Cantley, L. C., Chromosomal instability drives metastasis through a cytosolic DNA response. *Nature* **2018,** *553* (7689), 467-472.

(15) Liang, H.; Deng, L.; Hou, Y.; Meng, X.; Huang, X.; Rao, E.; Zheng, W.; Mauceri, H.; Mack, M.; Xu, M.; Fu, Y.-X.; Weichselbaum, R. R., Host STING-dependent MDSC mobilization drives extrinsic radiation resistance. *Nat. Commun.* **2017,** *8* (1), 1736.

(16) Koshy, M.; Spiotto, M.; Feldman, L. E.; Luke, J. J.; Fleming, G. F.; Olson, D.; Moroney, J. W.; Nanda, R.; Rosenberg, A.; Pearson, A. T.; Juloori, A.; Weinberg, F.; Ray, C.; Gaba, R. C.; Chang, P. J.; Janisch, L. A.; Xu, Z.-Q.; Lin, W.; Weichselbaum, R. R.; Chmura, S. J., A phase 1 dose-escalation study of RiMO-301 with palliative radiation in advanced tumors. *J. Clin. Oncol.* **2023,** *41* (16_suppl), 2527-2527.

(17) Wang, C.; Wang, W.; Tan, J.; Zhang, X.; Yuan, D.; Zhou, H.-C., Coordination-based molecular nanomaterials for biomedically relevant applications. *Coord. Chem. Rev.* **2021,** *438*, 213752.

(18) Banerjee, S.; Lollar, C. T.; Xiao, Z.; Fang, Y.; Zhou, H.-C., Biomedical Integration of Metal–Organic Frameworks. *Trends Chem.* **2020,** *2* (5), 467-479.

(19) Luo, T.; Ni, K.; Culbert, A.; Lan, G.; Li, Z.; Jiang, X.; Kaufmann, M.; Lin, W., Nanoscale Metal–Organic Frameworks Stabilize Bacteriochlorins for Type I and Type II Photodynamic Therapy. *J. Am. Chem. Soc.* **2020,** *142* (16), 7334-7339.

(20) Ni, K.; Lan, G.; Chan, C.; Quigley, B.; Lu, K.; Aung, T.; Guo, N.; La Riviere, P.; Weichselbaum, R. R.; Lin, W., Nanoscale metal-organic frameworks enhance radiotherapy to potentiate checkpoint blockade immunotherapy. *Nat. Commun.* **2018,** *9* (1), 2351.

(21) Luo, T.; Nash, G. T.; Jiang, X.; Feng, X.; Mao, J.; Liu, J.; Juloori, A.; Pearson, A. T.; Lin, W., A 2D Nanoradiosensitizer Enhances Radiotherapy and Delivers STING Agonists to Potentiate Cancer Immunotherapy. *Adv. Mater.* **2022,** *34* (39), 2110588.

(22) Guo, N.; Ni, K.; Luo, T.; Lan, G.; Arina, A.; Xu, Z.; Mao, J.; Weichselbaum, R. R.; Spiotto, M.; Lin, W., Reprogramming of Neutrophils as Non-canonical Antigen Presenting Cells by Radiotherapy–Radiodynamic Therapy to Facilitate Immune-Mediated Tumor Regression. *ACS Nano* **2021,** *15* (11), 17515-17527.

(23) Ni, K.; Lan, G.; Guo, N.; Culbert, A.; Luo, T.; Wu, T.; Weichselbaum, R. R.; Lin, W., Nanoscale metal-organic frameworks for x-ray activated in situ cancer vaccination. *Sci. Adv.* **2020,** *6* (40), eabb5223.

(24) Lu, K.; He, C.; Lin, W., Nanoscale Metal–Organic Framework for Highly Effective Photodynamic Therapy of Resistant Head and Neck Cancer. *J. Am. Chem. Soc.* **2014,** *136* (48), 16712-16715.

(25) Luo, T.; Fan, Y.; Mao, J.; Jiang, X.; Albano, L.; Yuan, E.; Germanas, T.; Lin, W., Metal-Organic Layer Delivers 5-Aminolevulinic Acid and Porphyrin for Dual-Organelle-Targeted Photodynamic Therapy. *Angew. Chem. Int. Ed.* **2023,** *62* (22), e202301910.

(26) Xu, Z.; Luo, T.; Mao, J.; McCleary, C.; Yuan, E.; Lin, W., Monte Carlo Simulation-Guided Design of a Thorium-Based Metal–Organic Framework for Efficient Radiotherapy-Radiodynamic Therapy. *Angew. Chem. Int. Ed.* **2022,** *61* (46), e202208685.

(27) Bowen, J. W.; Levinson, C., Phosphate concentration and transport in Ehrlich ascites tumor cells: Effect of sodium. *J. Cell. Physiol.* **1982,** *110* (2), 149-154.

(28) Baker, S. B.; Worthley, L. I., The essentials of calcium, magnesium and phosphate metabolism: part I. Physiology. *Crit. Care Resusc.* **2002,** *4* (4), 301-6.

(29) Xu, C.; Dobson, H. E.; Yu, M.; Gong, W.; Sun, X.; Park, K. S.; Kennedy, A.; Zhou, X.; Xu, J.; Xu, Y.; Tai, A. W.; Lei, Y. L.; Moon, J. J., STING agonist-loaded mesoporous manganese-silica nanoparticles for vaccine applications. *J. Control. Release* **2023,** *357*, 84-93.

(30) Demaria, O.; Cornen, S.; Daëron, M.; Morel, Y.; Medzhitov, R.; Vivier, E., Harnessing innate immunity in cancer therapy. *Nature* **2019,** *574* (7776), 45-56.

(31) Veiseh, O.; Doloff, J. C.; Ma, M.; Vegas, A. J.; Tam, H. H.; Bader, Andrew R.; Li, J.; Langan, E.; Wyckoff, J.; Loo, W. S.; Jhunjhunwala, S.; Chiu, A.; Siebert, S.; Tang, K.; Hollister-Lock, J.; Aresta-Dasilva, S.; Bochenek, M.; Mendoza-Elias, J.; Wang, Y.; Qi, M.; Lavin, D. M.; Chen, M.; Dholakia, N.; Thakrar, R.; Lacík, I.; Weir, Gordon C.; Oberholzer, J.; Greiner, D. L.; Langer, R.; Anderson, D. G., Size- and shape-dependent foreign body immune response to materials implanted in rodents and non-human primates. *Nat. Mater.* **2015,** *14* (6), 643-651.

(32) Anderson, J. M.; Rodriguez, A.; Chang, D. T., Foreign body reaction to biomaterials. *Semin. Immunol.* **2008,** *20* (2), 86-100.

(33) Dievernich, A.; Achenbach, P.; Davies, L.; Klinge, U., Characterization of innate and adaptive immune cells involved in the foreign body reaction to polypropylene meshes in the human abdomen. *Hernia* **2022,** *26* (1), 309-323.

(34) von Andrian, U. H.; Mempel, T. R., Homing and cellular traffic in lymph nodes. *Nat. Rev. Immunol.* **2003,** *3* (11), 867-878.

(35) Adusei, K. M.; Ngo, T. B.; Sadtler, K., T lymphocytes as critical mediators in tissue regeneration, fibrosis, and the foreign body response. *Acta Biomater.* **2021,** *133*, 17-33.

(36) Chu, C.-L.; Lowell, C. A., The Lyn Tyrosine Kinase Differentially Regulates Dendritic Cell Generation and Maturation1. *J. Immunol.* **2005,** *175* (5), 2880-2889.

(37) Kabashima, K.; Shiraishi, N.; Sugita, K.; Mori, T.; Onoue, A.; Kobayashi, M.; Sakabe, J.-i.; Yoshiki, R.; Tamamura, H.; Fujii, N.; Inaba, K.; Tokura, Y., CXCL12-CXCR4 Engagement Is Required for Migration of Cutaneous Dendritic Cells. *Am. J. Pathol.* **2007,** *171* (4), 1249-1257.

(38) Rawat, K.; Tewari, A.; Li, X.; Mara, A. B.; King, W. T.; Gibbings, S. L.; Nnam, C. F.; Kolling, F. W.; Lambrecht, B. N.; Jakubzick, C. V., CCL5-producing migratory dendritic cells guide CCR5+ monocytes into the draining lymph nodes. *J. Exp. Med.* **2023,** *220* (6).

(39) Zhang, L.; Wei, X.; Wang, Z.; Liu, P.; Hou, Y.; Xu, Y.; Su, H.; Koci, M. D.; Yin, H.; Zhang, C., NF-κB activation enhances STING signaling by altering microtubule-mediated STING trafficking. *Cell Rep.* **2023,** *42* (3), 112185.

(40) Iwamoto, S.; Iwai, S.-i.; Tsujiyama, K.; Kurahashi, C.; Takeshita, K.; Naoe, M.; Masunaga, A.; Ogawa, Y.; Oguchi, K.; Miyazaki, A., TNF-α Drives Human CD14+ Monocytes to Differentiate into CD70+ Dendritic Cells Evoking Th1 and Th17 Responses. *J. Immunol.* **2007,** *179* (3), 1449-1457.

(41) Chen, S.; Saeed, A. F. U. H.; Liu, Q.; Jiang, Q.; Xu, H.; Xiao, G. G.; Rao, L.; Duo, Y., Macrophages in immunoregulation and therapeutics. *Signal Transduct. Target. Ther.* **2023,** *8* (1), 207.

(42) Yang, H.; Lee, W. S.; Kong, S. J.; Kim, C. G.; Kim, J. H.; Chang, S. K.; Kim, S.; Kim, G.; Chon, H. J.; Kim, C., STING activation reprograms tumor vasculatures and synergizes with VEGFR2 blockade. *J. Clin. Investig.* **2019,** *129* (10), 4350-4364.

(43) Yang, K.; Han, W.; Jiang, X.; Piffko, A.; Bugno, J.; Han, C.; Li, S.; Liang, H.; Xu, Z.; Zheng, W.; Wang, L.; Wang, J.; Huang, X.; Ting, J. P. Y.; Fu, Y.-X.; Lin, W.; Weichselbaum, R. R., Zinc cyclic di-AMP nanoparticles target and suppress tumours via endothelial STING activation and tumour-associated macrophage reinvigoration. *Nat. Nanotechnol.* **2022,** *17* (12), 1322-1331.

(44) La-Beck, N. M.; Islam, M. R.; Markiewski, M. M., Nanoparticle-Induced Complement Activation: Implications for Cancer Nanomedicine. *Front. Immunol.* **2021,** *11*.

(45) Guo, S.; Yao, Y.; Tang, Y.; Xin, Z.; Wu, D.; Ni, C.; Huang, J.; Wei, Q.; Zhang, T., Radiation-induced tumor immune microenvironments and potential targets for combination therapy. *Signal Transduct. Target. Ther.* **2023,** *8* (1), 205.

(46) Begg, A. C.; Stewart, F. A.; Vens, C., Strategies to improve radiotherapy with targeted drugs. *Nat. Rev. Cancer* **2011,** *11* (4), 239-253.

(47) Vogelzang, N. J., Continuous infusion chemotherapy: a critical review. *J. Clin. Oncol.* **1984,** *2* (11), 1289-1304.

(48) Wang, Y. H.; Yao, N.; Wei, K. K.; Jiang, L.; Hanif, S.; Wang, Z. X.; Pei, C. X., The efficacy and safety of probiotics for prevention of chemoradiotherapy-induced diarrhea in people with abdominal and pelvic cancer: a systematic review and meta-analysis. *Eur. J. Clin. Nutr.* **2016,** *70* (11), 1246-1253.

(49) Choi, J.; Kim, G.; Cho, S. B.; Im, H.-J., Radiosensitizing high-Z metal nanoparticles for enhanced radiotherapy of glioblastoma multiforme. *J. Nanobiotechnol.* **2020,** *18* (1), 122.

(50) Guidolin, K.; Zheng, G., Nanomedicines Lost in Translation. *ACS Nano* **2019,** *13* (12), 13620-13626.

(51) Ngoune, R.; Peters, A.; von Elverfeldt, D.; Winkler, K.; Pütz, G., Accumulating nanoparticles by EPR: A route of no return. *J. Control. Release* **2016,** *238*, 58-70.

(52) Sindhwani, S.; Syed, A. M.; Ngai, J.; Kingston, B. R.; Maiorino, L.; Rothschild, J.; MacMillan, P.; Zhang, Y.; Rajesh, N. U.; Hoang, T.; Wu, J. L. Y.; Wilhelm, S.; Zilman, A.; Gadde, S.; Sulaiman, A.; Ouyang, B.; Lin, Z.; Wang, L.; Egeblad, M.; Chan, W. C. W., The entry of nanoparticles into solid tumours. *Nat. Mater.* **2020,** *19* (5), 566-575.

(53) Ouyang, B.; Poon, W.; Zhang, Y.-N.; Lin, Z. P.; Kingston, B. R.; Tavares, A. J.; Zhang, Y.; Chen, J.; Valic, M. S.; Syed, A. M.; MacMillan, P.; Couture-Senécal, J.; Zheng, G.; Chan, W. C. W., The dose threshold for nanoparticle tumour delivery. *Nat. Mater.* **2020,** *19* (12), 1362-1371.

(54) Yuan, J.; Khilnani, A.; Brody, J.; Andtbacka, R. H. I.; Hu-Lieskovan, S.; Luke, J. J.; Diab, A.; Marabelle, A.; Snyder, A.; Cao, Z. A.; Hodi, F. S., Current strategies for intratumoural immunotherapy – Beyond immune checkpoint inhibition. *Eur. J. Cancer* **2021,** *157*, 493-510.

(55) Vincent, M. P.; Bobbala, S.; Karabin, N. B.; Frey, M.; Liu, Y.; Navidzadeh, J. O.; Stack, T.; Scott, E. A., Surface chemistry-mediated modulation of adsorbed albumin folding state specifies nanocarrier clearance by distinct macrophage subsets. *Nat. Commun.* **2021,** *12* (1), 648.

(56) Jiang, X.; Du, B.; Zheng, J., Glutathione-mediated biotransformation in the liver modulates nanoparticle transport. *Nat. Nanotechnol.* **2019,** *14* (9), 874-882.

(57) Du, B.; Yu, M.; Zheng, J., Transport and interactions of nanoparticles in the kidneys. *Nat. Rev. Mater.* **2018,** *3* (10), 358-374.

(58) Wang, S.; Chen, Y.; Wang, S.; Li, P.; Mirkin, C. A.; Farha, O. K., DNA-Functionalized Metal–Organic Framework Nanoparticles for Intracellular Delivery of Proteins. *J. Am. Chem. Soc.* **2019,** *141* (6), 2215-2219.

(59) Wang, S.; McGuirk, C. M.; d'Aquino, A.; Mason, J. A.; Mirkin, C. A., Metal–Organic Framework Nanoparticles. *Adv. Mater.* **2018,** *30* (37), 1800202.

(60) Sun, X.; Zhang, Y.; Li, J.; Park, K. S.; Han, K.; Zhou, X.; Xu, Y.; Nam, J.; Xu, J.; Shi, X.; Wei, L.; Lei, Y. L.; Moon, J. J., Amplifying STING activation by cyclic dinucleotide–manganese particles for local and systemic cancer metalloimmunotherapy. *Nat. Nanotechnol.* **2021,** *16* (11), 1260-1270.

(61) Sun, X.; Zhou, X.; Lei, Y. L.; Moon, J. J., Unlocking the promise of systemic STING agonist for cancer immunotherapy. *J. Control. Release* **2023,** *357*, 417-421.

(62) Teplensky, M. H.; Evangelopoulos, M.; Dittmar, J. W.; Forsyth, C. M.; Sinegra, A. J.; Wang, S.; Mirkin, C. A., Multi-antigen spherical nucleic acid cancer vaccines. *Nat. Biomed. Eng.* **2023**.

(63) Bankhead, P.; Loughrey, M. B.; Fernández, J. A.; Dombrowski, Y.; McArt, D. G.; Dunne, P. D.; McQuaid, S.; Gray, R. T.; Murray, L. J.; Coleman, H. G.; James, J. A.; Salto-Tellez, M.; Hamilton, P. W., QuPath: Open source software for digital pathology image analysis. *Sci. Rep.* **2017,** *7* (1), 16878.